Summer 2022

Molecular Theoretical Model for Lipid Bilayers: Adsorption of Lipidated Proteins on Lipid Bilayers as a Function of Bilayer Composition and Curvature

Shauna Celeste Kennard

MOLECULAR THEORETICAL MODEL FOR LIPID BILAYERS:

ADSORPTION OF LIPIDATED PROTEINS ON LIPID BILAYERS AS A FUNCTION OF BILAYER COMPOSITION AND CURVATURE

by

Shauna Celeste Kennard

Bachelor of Science
University of Florida, 2012

Submitted in Partial Fulfillment of the Requirements

For the Degree of Doctor of Philosophy in

Chemical Engineering

College of Engineering and Computing

University of South Carolina

2022

Accepted by:

Mark J. Uline, Major Professor

Melissa A. Moss, Committee Member

R. Michael Gower, Committee Member

Tarek Shazly, Committee Member

Tracey L. Weldon, Vice Provost and Dean of the Graduate School

ABSTRACT

Protein localization on biological membranes is motivated by either highly selective recognition of specific target membrane components or nonspecific attraction to general physical properties of the membrane, such as charge, lipid heterogeneity, and curvature. Here we discuss the interaction between lipidated proteins and lipid bilayer membranes from a comprehensive examination of how features of the membrane and its lipid constituents, including lipid composition, headgroup size, degree of tail saturation, tail length (bilayer thickness), and membrane geometry, affect the adsorption ability of the proteins. Of key importance is the strong interconnection among these compositional and morphological elements of the membrane in mediating the adsorption behavior of lipidated proteins. As a model protein, we use the dual lipidated (palmitoyl and farnesyl) anchoring motif of the signaling GTPase, N-Ras (tN-Ras). We find marked augmentation in tN-Ras adsorption with increasing degree of membrane curvature — a trend that is tightly regulated by the bilayer characteristics mentioned above. Experimental results from collaborative research laboratories are fully reproduced by our molecular-level mean-field theoretical model of the systems under study.

Of note, the theory suggests an explicit dependence of the selective adsorption behavior of tN-Ras, with respect to membrane composition and curvature, on the unique lateral pressure profile through the width of a given bilayer. We propose the membrane's heterogeneous distribution of lateral pressure to be an important mechanism that governs the membrane-protein interaction. Another primary contribution of this work is the revelation that changes in the local Gaussian curvature of the bilayer, independent of mean curvature, motivates a substantial response in the lateral pressure profile through the bilayer's width, and thus the adsorption trends of the tN-Ras protein. The Gaussian curvature has traditionally been a quantity neglected in theoretical studies involving membrane curvature, stemming from the approximation of the lipid bilayer as an infinitely thin, two-dimensional sheet. The results herein have demonstrated that the structural heterogeneity that exists at the atomic scale through the membrane's core provokes macroscopic consequences that determine biological function. Thus, an over-arching theme of this work is a message conveying that the width of the bilayer is an essential dimension to be considered in the physics of membrane shape transitions.

TABLE OF CONTENTS

LIST OF TABLES

LIST OF FIGURES

CHAPTER 1
A MATTER OF MEMBRANES—GENERAL INTRODUCTION

The mechanical and thermodynamic properties of biological membranes are of keen interest within the scientific and commercial communities because of the membrane's governing role in diverse biological processes. There is a broad spectrum of scientific activity within the domain of membrane research. Studies on the membrane range from resolving the details of lipid organization and their connection to membrane function on a fundamental level, to the large-scale development of lipid-based technologies. Substantial attention is focused on discovering the mechanisms by which proteins interact with the membrane, leading to improved diagnostic methods and treatments for diseases caused by mutations in membrane-associated proteins.

This thesis presents a theoretical analysis of model membranes that answers questions regarding the physicochemical properties of the membrane's lipid constituents on a molecular level and how their behavior evolves into macroscopic membrane phenomena. The mechanisms that govern the interaction between the membrane and lipidated proteins are explored. The theory evaluates the systems under consideration on the scale of the small monomer, comprehensively

including the physics of the configurational details and molecular chemistry involved. Chapter 2 provides a general introduction, comprising a summary of the history of membrane research, basic information about eukaryotic membranes, the current paradigm for the membrane as a functional, dynamic entity, the applications emerging from the study of biological membranes, and a brief review of several experimental and theoretical techniques used to investigate membrane properties. Chapter 3 describes the principal tools used to develop molecular theories such as ours – an overview of classical density functional theory (DFT) and statistical mechanics. We also lay out a general overview of the energetic and entropic contributions that we include in our theory, the types of molecules we incorporate in our models, environmental conditions of the system, and what facets of membrane biology we wish to investigate.

Chapter 4 presents specifics on the formulation and details of our molecular theory. Here, we discuss the curvature theory from differential geometry that we use to describe the geometry of our model membranes, the elasticity of biological membranes, and the reorganizational capabilities of membrane lipids. At the end of Chapter 4, we have our first results section *(Results I.I)*, which demonstrates our findings regarding the membrane's composition-dependent elastic properties and the curvature-mediated diffusion of its lipid constituents. Our analysis reveals that some elements of lipid dynamics (e.g., lipid transbilayer diffusion and the

variation in the timescale of membrane relaxation among different lipid compositions and membrane curvatures) tightly govern membrane organization and should be considered in the interpretation of experimental studies. It is shown that even minute alterations in compositional asymmetry between a membrane's inner and outer leaflets provoke drastic changes in internal membrane properties, such as chemical potential, and the membrane's bulk characteristics, such as the bending modulus.

Chapter 5 introduces lipidated proteins and how they are integrated theoretically into the model membrane system. We present our second results section *(Results I.II)* at the end of Chapter 5, which shows how the synergistic relationship between membrane curvature and composition modulates the degree of protein adsorption on pure component and binary model lipid bilayers. Findings indicate that such proteins are curvature sensitive and that their adsorption tendencies are dramatically influenced by the kinds of lipid dynamics discussed in Chapter 4. We discover that the underlying driving factor for the selectivity of protein enrichment in different membranes is the lateral pressure field within the membrane's hydrophobic core.

Chapters 6 and 7 rework the formulation of our theory to describe a membrane in a system that is expanded to include a surrounding aqueous environment of physiologically relevant pH and salt concentration. We add an

explicit model for the (previously phenomenologically treated) lipid headgroup and glycerol backbone and examine how the additional hydrophobic interactions, density distributions of solution components, and electrostatic contributions to the system affect membrane properties and the adsorption behavior of lipidated proteins. Whereas earlier chapters focus on curvature effects caused by changes in diameter of spherical membranes, these two chapters examine such effects in membranes of different shapes. We also specifically explore the direct impact of Gaussian curvature on the system through comparisons of model membranes with strategic differences in membrane geometry.

Many of the types of lipid membranes chosen for this work have been used in experimental studies investigating the properties and interactions outlined above. The theoretical results demonstrate excellent agreement with experimental work. This establishes the theory as a credible instrument to be used in the evaluation of those systems of interest without available experimental data. The benefit of such a tool is considerable – it can be applied to test endless lipid systems, of various compositions, geometries, and environmental conditions, for the design and optimization of lipid-based devices without the large expenses of materials, equipment, and time required for experimental methods. As demonstrated in this work, the theory also provides insight into the mechanisms

that drive biological phenomena that may be observed, but not fully understood, in an experimental setting.

CHAPTER 2
A BRIEF HISTORY OF BIOLOGICAL MEMBRANE RESEARCH

2.1 FROM A PASSIVE HOMOGENEOUS MEDIUM TO A DYNAMIC FUNCTIONAL ENTITY

Studies on the functionality of cell membranes have increasingly developed, launched by the milestone in membrane research introduced in 1972 [1] by S.J. Singer and G.L. Nicolson with the 'fluid mosaic' model for the membrane framework. Reflecting findings rendered by improvements in electron microscopy techniques at the time, the model presented an elegant description of the plasma membrane as a homogeneous, multicomponent, fluid bilayer of lipids, which accommodated both integral and peripheral proteins *(Figure 2.1)* [2]. One of the many novelties proposed by the model was the portrayal of cell membranes as *dynamic* systems, allowing for the lateral mobility of the lipid constituents and embedded proteins via Brownian diffusion. The rejection of the former depiction of the membrane as a simple, static protective barrier, in favor of the flexible dynamic character introduced by the fluid mosaic model, laid the foundation for a newly animated initiative in membrane research, where such dynamics were conceived to be fundamentally connected to membrane function.

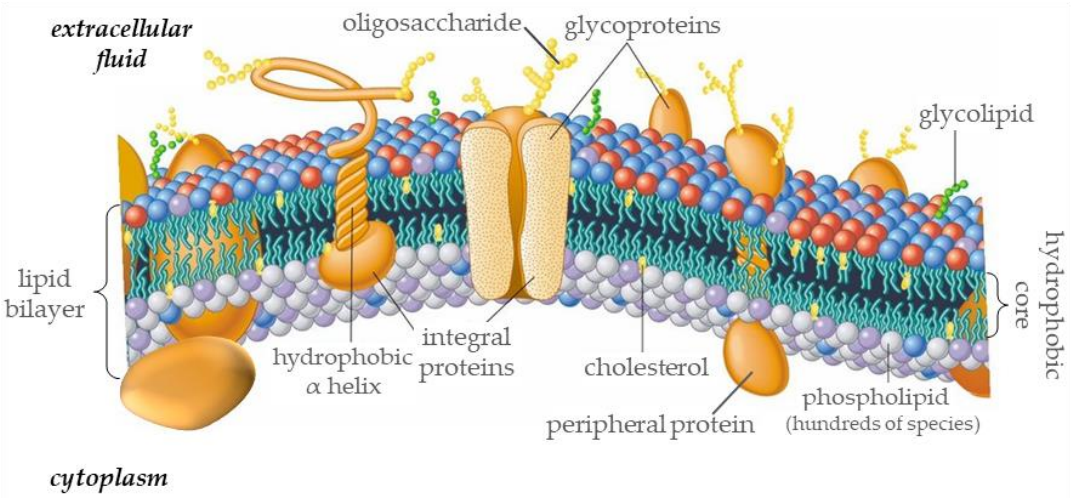

Figure 2.1) **Fluid mosaic model for membrane structure.** The fatty acid chains in the interior of the membrane form a fluid, hydrophobic region. Integral proteins float in this "sea" of lipid, held by hydrophobic interactions with their nonpolar amino acid side chains. Both proteins and lipids are free to move laterally in the plane of the bilayer. *Image adapted from* [2].

Enthusiasm continued to be fueled by recognition of the broad range of essential cellular processes with which the membrane was involved and the tendency of membrane proteins to form assemblies in various regions of the bilayer. However, the *lipids* that construct cell membranes were still largely regarded as only passive contributors to cellular activity, collectively acting as an inert medium in which proteins could partake in their own functional processes. Subsequent decades saw vast improvements in biophysical imaging techniques that granted several important corrections to the original fluid mosaic model [3-11]. Optical tweezers [9], Fluorescence Recovery After Photobleaching (FRAP) [8,10], and Single-Particle Tracking (SPT) [11] were among the experimental tools that aided in the revelation that diffusion of membrane proteins is appreciably

complex and varied, rather than ubiquitously Brownian as previously purported. The composition of the bilayer lipids themselves were also discovered to be heterogeneous in their distribution, both with respect to local regions within a given monolayer, or *leaf*, as well as in their partitioning between the two membrane leaflets. Heterogeneity in the membrane's organization of its lipid constituents established a new paradigm in fields of research with ties in biophysics, biochemistry, thermodynamics, and bioengineering [12-23]. Particularly within the past couple decades, interest in the dynamics of lipid bilayers has surged with growing evidence that this heterogeneity actually confers an operative purpose to the membrane itself. Biological membranes are in fact incredibly purposefully active, and the lipid constituents have been found to *directly* regulate the execution of varied cellular processes.

Much progress has been made in uncovering the complexities and organizational tendencies of membrane architecture that engender its physiological activity. The culmination of these scientific endeavors has set a new baseline for the analysis of biological membranes that acknowledges the myriad of processes for which the membrane is directly responsible, including enzymatic activity, cell-cell recognition, signal transduction, intercellular joining, endo- and exo-cytosis and other modes of transport, etc. This standard for current theories aiming to interpret membrane environments recognizes the self-association and

partitioning of lipids into assemblies of certain components, uniquely designed to support specific proteins and thereby effectuate deliberate cellular functions.

2.2 Mechanisms of Membrane Activity—Form to Function

Perhaps the most cogent model to advance a description of biological membranes, capable of reconciling the structure-to-function coupling evinced by experimental observations is the so-called *raft hypothesis*. The name reflects the tendency of cholesterol in the bilayer to preferentially aggregate with saturated lipids, creating an inhomogeneous mixture of different liquid *phases* composed of saturated lipid- and cholesterol-enriched domains, or *rafts*, residing in a largely unsaturated lipid medium, as illustrated in *Figure 2.2*.

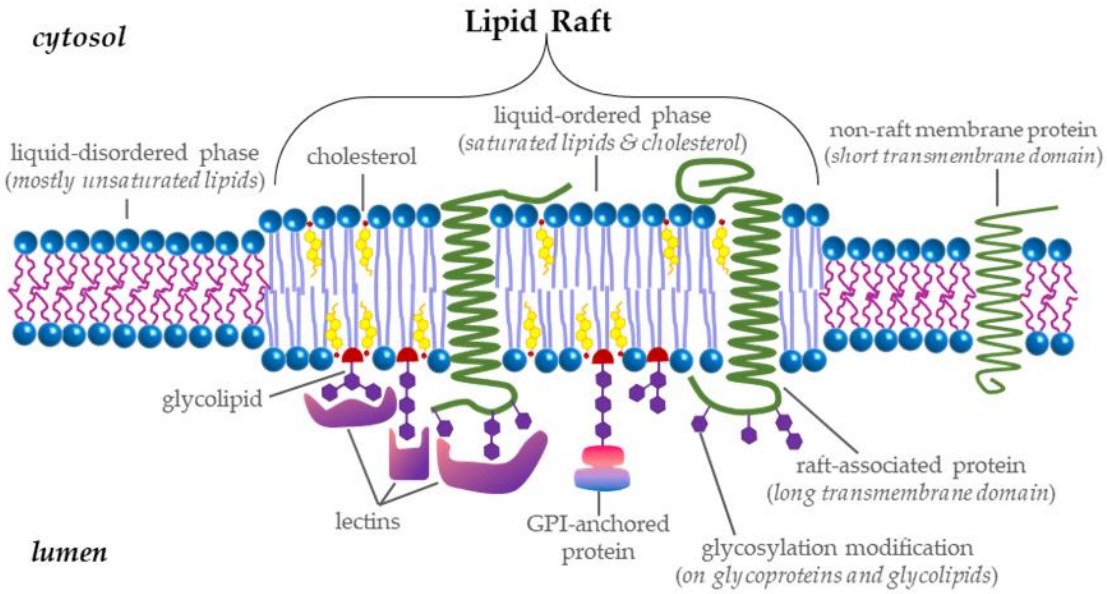

Figure 2.2) **Schematic of lipid-disordered and raft regions of the membrane.** Raft domains are capable of accommodating various proteins, including those with long transmembrane domains, which preferentially partition into the lipid rafts due to the thickening of the bilayer in these regions.

The concept of the 'lipid domain' that eventually gave rise to the raft model had its origins in results obtained from K. Simons and G. van Meer in 1988 [24], demonstrating a variation in lipid composition between the apical and basolateral membranes of epithelial cells. The concept further developed as observations of lipid partitioning became widespread. The term 'lipid raft' was first introduced by K. Simons and E. Ikonen in 1997 [25], who sought to capture the collection of experimental findings of lipid differentiation under a coherent, unified principle of membrane subcompartmentalization.

The *phase separation* described by the raft model is motivated by the dichotomy in lipid architecture among the membrane's lipid species, particularly regarding the varying degrees of organization attainable by the hydrocarbon chain, or *tail*, regions constituting the bulk of the hydrophobic membrane core. High melting temperature saturated lipid tails are built of singly bonded CH_2 groups that extend as unbranched, open aliphatic chains *(Figure 2.3, left)*. The chains of adjacent saturated lipids are capable of ordering into densely packed, viscous regions in areas of the bilayer where these components are in high concentration; under certain conditions, these regions may become sufficiently compact as to form distinct local domains referred to as the *liquid-ordered (lo)* phase, or even the solid-like (unphysical) *gel* phase.

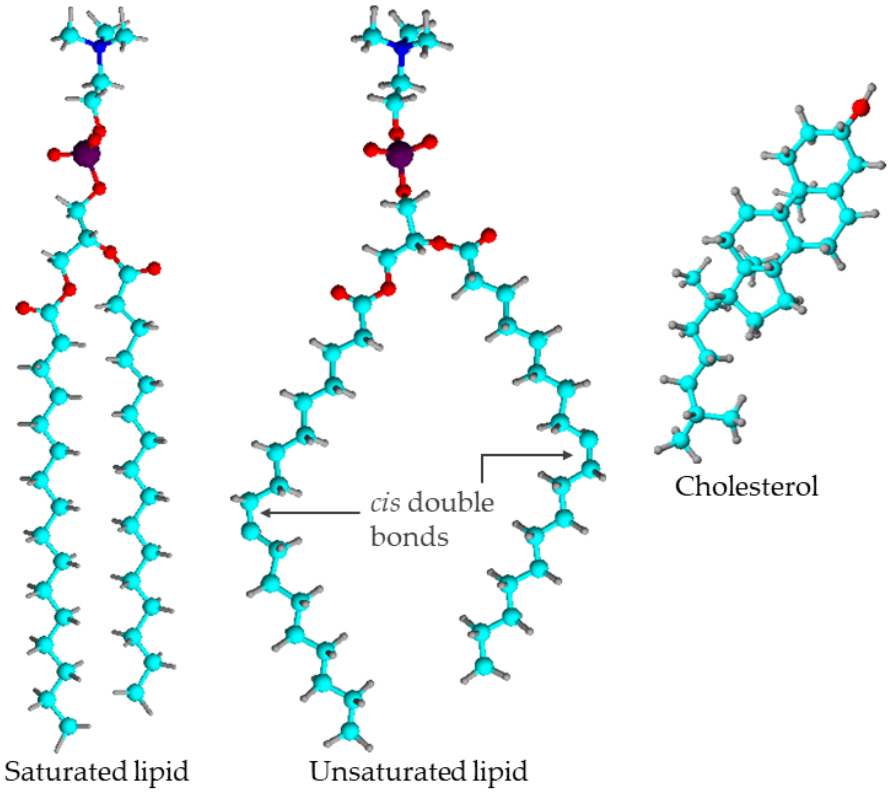

Figure 2.3) **Lipid structures.** ***Left****:* saturated dipalmitoyl-phosphatidylcholine (DPPC), ***middle****:* unsaturated dioleoyl-phosphatidylcholine (DOPC), ***right:*** cholesterol. Hydrophilic regions are decorated with large red oxygens; those closer to the tails are part of the glycerol backbone and those at the top belong to the phosphate group in the first two images. Phospholipids have large headgroups and either fully saturated tails or kinked, unsaturated tails, causing unsaturated lipids to generally have a larger molecular area. Cholesterol has a small hydroxyl headgroup that facilitates tighter packing between saturated lipids in the membrane.

In contrast, unsaturated lipid tails *(Figure 2.3, center)* bear a double bond between one or more pairs of their carbon monomeric units, which are nearly always in the *cis* conformation. These *cis* double bonds create kinks that disrupt the elongation of the chain, significantly lowering the lipid's melting temperature

and sterically preventing the same degree of alignment capable of saturated tails. Likewise, branched lipids are hindered from ordering into packed assemblies, regardless of their saturation state. The added bulk of the branches reduces their melting temperature, relative to unbranched saturated lipids. Both the kink created by the double bonds of unsaturated lipids and branches off the main-chain motivate a more fluid, loosely packed environment, rich in these types of lipids, known as the *liquid-disordered (ld)* phase (also referred to as the *liquid-crystalline (lc)* phase).

Eukaryotic membranes include hundreds of different lipidic species that fall under one of three classes: phospholipids, glycolipids, and sterols, which are themselves divided into several different subclasses – hence the profound compositional complexity of biological membranes. Phospholipids are the compositionally dominant species of lipid in biological membranes and are the type we incorporate in the model membranes used for this study. They feature two hydrophobic fatty acid tails, covalently bonded to glycerol (referred to as the *glycerol backbone*), which serves to link the tails to a large hydrophilic 'head' region composed of a phosphate group and an additional group that varies, depending on the specific sub-type of phospholipid, as illustrated in *Figure 2.4*.

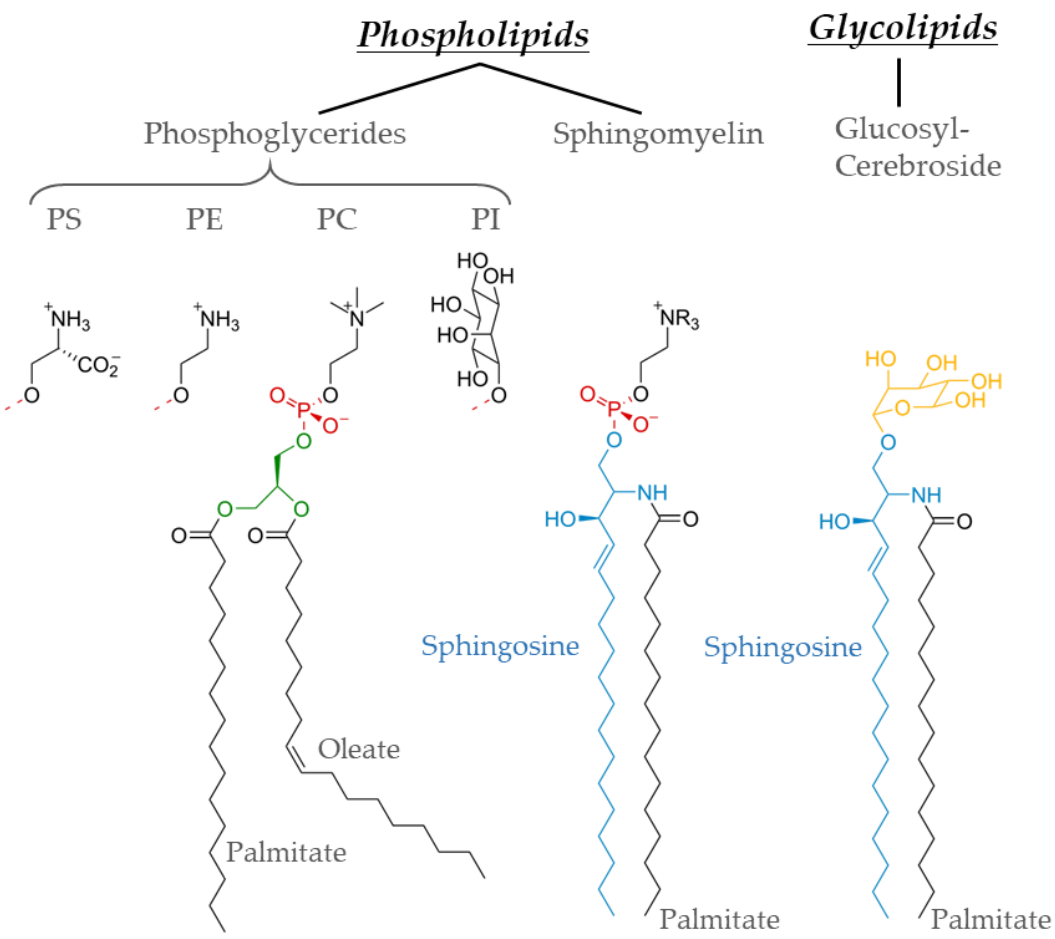

Figure 2.4) **Major types of lipids.** Phospholipids ***(left)***, glycolipids ***(right)***, and cholesterol *(not shown)* are the three major categories of lipids in humans. Examples of different types of phospholipid headgroups: PS (phosphatidylserine), PE (phosphatidylethanolamine), PC (phosphatidylcholine), PI (phosphatidylinositol).

Cholesterol, on the other hand, which is the most prevalent sterol in animals, has a small hydrophilic region composed of a single hydroxyl group *(Figure 2.3, right)*. Cholesterol attractively interacts with other lipids, due to hydrophobic and van der Waals forces, and the difference in headgroup size allows for cholesterol to pack neatly within the voids between phospholipid

molecules. The rigid, planar structure of cholesterol's hydrophobic region, nestled between the fatty acid chains of other membrane lipids, reduces the freedom of the adjacent chains to rotate about their carbon-carbon bonds. Within certain concentration ranges, pairing cholesterol with unbranched saturated lipids can result in a compact, inverse conical arrangement that has the effect of enhancing the degree of alignment assumed by the saturated tails, forcing the hydrocarbon chains into their fully extended conformation and promoting the local lateral compression of the hydrophobic region. Under these circumstances, the saturated lipid tails progressively expel the bulky structure of nearby unsaturated or branched lipids, effectively reducing the local lateral area further. The increasing incongruity between mixture components raises the internal energy of (destabilizes) the system. When the discrepancy in the organization of the lipids reaches a critical point, the system adapts to the upset in the tenuously conserved balance between energetics and entropics via a miscibility gap, dividing the 'ordered' and 'disordered' components. This accomplishes a reduction in the free energy that maintains stability and yields two distinct *lo*- and *ld*- (or *lc*-) phases over a range of lipid concentrations *(Figure 2.5)*, with lipid rafts as possible features of the former.

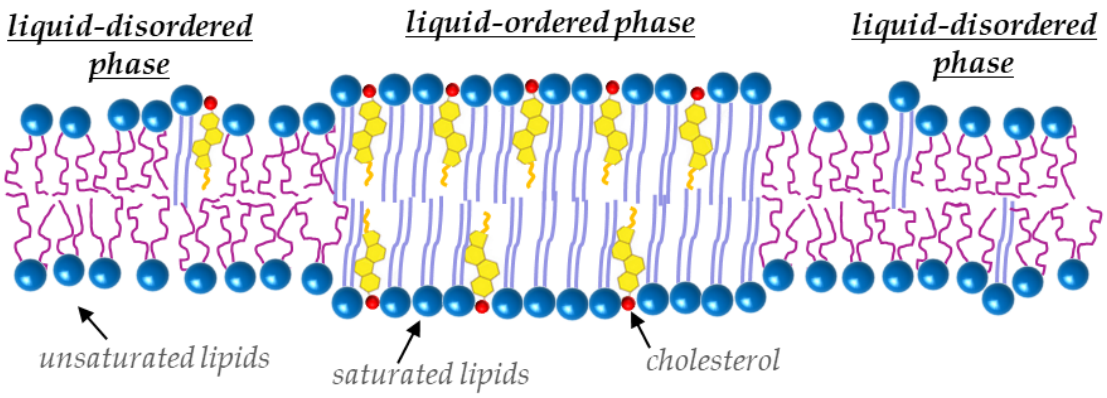

Figure 2.5) **Liquid-order–liquid-disorder phase separation.** Cholesterol fits neatly in the voids between adjacent saturated lipids, aligning the lipid chains. As saturated lipids and cholesterol aggregate, they expel the bulky unsaturated lipids, ultimately causing the demixing of the species into ordered (saturated lipid- and cholesterol-rich) and disordered (unsaturated lipid-rich) phases.

Cholesterol constitutes roughly 20-45% of plasma membrane lipids (and is present in lesser amounts, ~5%, in smaller structures, such as the inner mitochondrial membrane or the endoplasmic reticulum) [26, 27]. The likelihood that lipid rafts have specialized physical properties due to their enrichment in cholesterol was a concept inspired by J. H. Ipsen *et al.* (1987) [28], who originally reported on the direct influence cholesterol concentration had on manifesting the coexistence of the ordered and disordered regions under certain conditions. It has now been well documented that a condition for liquid–liquid phase coexistence is the system's inclusion of high (saturated) and low (unsaturated/branched) melting-temperature lipids and a sterol. Therefore, information about a biological membrane's phase behavior can be gathered from analyses of *model membranes* that

contain these three molecular varieties.[1]

It is important to note that while cholesterol can promote the alignment of unbranched saturated lipid tails under certain concentration ranges, there is a maximum limit to the local cholesterol concentration that fosters this ordering effect, beyond which the trend reverses. High enough local percentages of cholesterol – the precise number depending on factors such as local composition of other membrane lipids and temperature – actually destabilize ordered formations, as the rigid ring-structure of cholesterol's hydrophobic region begins to crowd the saturated lipid tails, preventing sufficient condensation to organize a distinct liquid-ordered phase. *Figure 2.6* illustrates this trend with fluorescence microcopy micrographs taken by S. L. Veatch *et al*. (2005) [29]. In these images, cholesterol is mixed in a 1:1 dipalmitoyl-phosphatidylcholine:dioleoyl-phosphatidylcholine (DPPC:DOPC) giant unilamellar vesicle (GUV). The plots accompanying the micrographs show that above ~50% cholesterol, the vesicle membrane exists in a homogenous, liquid-disordered state over the entire range

[1] The complexity of biological membranes, both cellular and of organelles within eukaryotic cells, is tremendous. Therefore, *model* systems are created, experimentally and in theory/simulation, which retain essential lipid bilayer structure but simplify the system to clearly ascertain the roles of individual components and features such as size and geometry, as well as to isolate the effects of environmental factors such as temperature, solution p*H*, and salt concentration on the system. Many studies use spherical model membranes for analyses that are broadly categorized into three classifications based on their diameter: *small unilamellar vesicles* (SUVs; 20-100 nm), *large unilamellar vesicles* (LUVs; 100-1000 nm), and *giant unilamellar vesicles* (GUVs; 1-200 μm), the latter of which is often used for better visualization of membrane characteristics.

of temperatures studied, exemplifying that a high enough local cholesterol density fosters the dominance of entropic forces in the system, preventing the coalescence of ordered domains. Below ~50% cholesterol, mixture heterogeneity arises with the presence of *ld*- and *lo*-phases by either decreasing temperature *(Figure 2.6, top panel)* or decreasing cholesterol concentration *(Figure 2.6, bottom panel)*, within certain ranges. Observing these plots, the reader might find curious that sufficiently reducing either temperature or percentage of cholesterol causes the vesicle membrane to ultimately transition into a third type of phase-state. At the extreme low temperature/cholesterol limit, a type of membrane heterogeneity exists that contains not only a liquid phase, but a solid-like gel phase as well.

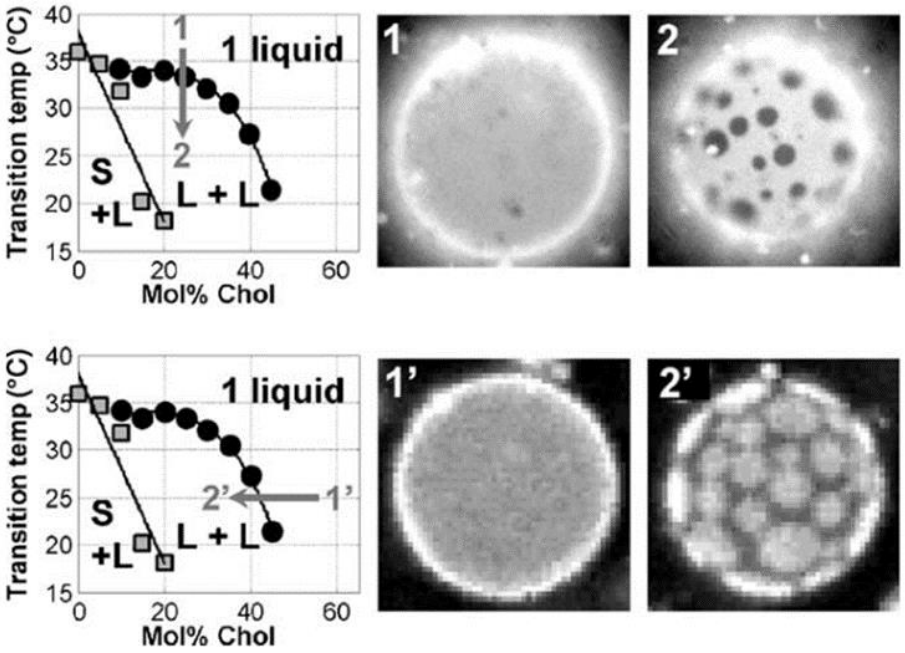

Figure 2.6) **Effect of temperature and cholesterol content on membrane phase-state in GUVs.** The miscibility phase transition boundary is crossed either by lowering temperature ***(top)*** or lowering cholesterol composition ***(bottom)***. ***Top*****:** A GUV of 1:1 DOPC:DPPC+25% cholesterol contains one uniform liquid phase at high temperature *(micrograph 1)*. Coexisting liquid domains form in the same vesicle as temperature is lowered *(micrograph 2)*. ***Bottom*****:** A GUV of 1:1 DOPC:DPPC+60% cholesterol is in one uniform liquid phase at room temperature *(micrograph 1')*. After treatment with β-cyclodextrin to reduce cholesterol, coexisting liquid phases appear *(micrograph 2')*. Data in each graph are transition temperatures measured by fluorescence microscopy in GUVs of 1:1 DOPC:DPPC with varying fractions of cholesterol. *Images and caption obtained from* [29].

Without cholesterol's regulation of lipid organization, high melting temperature lipids are capable of excessively condensing into these gel-phase regions at high enough concentrations, even at biological temperatures, as is illustrated in the binary phase diagram below *(Figure 2.7)* [30]. If this were to occur in living systems, the result would be cell death. Due to cholesterol's role in both

promoting the alignment of lipid tails that engenders the formation of biologically active, liquid-ordered membrane domains and preventing excessive chain ordering that would otherwise result in inelastic, static local gel-phase regions, cholesterol is known as the '*great mediator of bilayer fluidity*'. Fluidity is an essential aspect of biological membranes that preserves its biochemical activity and is integral to life continuity.

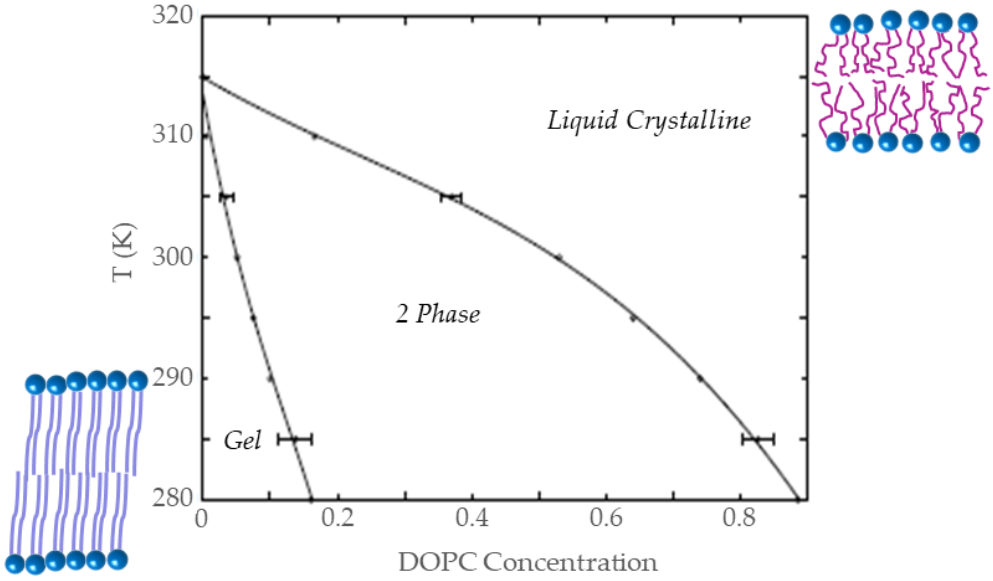

Figure 2.7) **Binary saturated-unsaturated lipid phase diagram; gel–liquid-disordered phase separation**. Calculated phase diagram for a bilayer composed of DPPC and DOPC as a function of the volume fraction of DOPC using a molecular field theory. Error bars are estimates of the uncertainty in the calculations introduced by discretization. *Image and caption adapted from* [30].

2.3 The Current (and Controversial) Membrane Model

The raft hypothesis has developed to provide a compelling explanation for the inhomogeneity of biological membranes [24, 25, 28-52]. The theory is able to reconcile the observations of bi-leaflet lipid asymmetry, apical- to basolateral-

membrane lipid polarization, lateral inhomogeneity, and the lipid differentiation consistent among sorting organelles such as the Golgi complex and endosomes, with a well-defined mechanism of lipid self-assembly. Therefore, it has been maintained as the most prominent and well-accepted description of the membrane system to date. The essence of the raft hypothesis lies in its promotion of the raft as a lipid-regulated *stable* (though perhaps quite transient) platform, which, by virtue of this stability, is proposed to be influential in most all aspects of membrane operations. For example, enzymatic activity and the assemblage of signal complexes are hypothesized to occur at the raft site itself. The elongation of the aligned, saturated tails constituting the raft structure causes a thickening of the bilayer in these regions, capable of accommodating the accumulation of certain proteins, especially those with long transmembrane domains and those that depend on the assembly of large protein complexes to achieve their functional purpose *(see Figures 2.2 and 2.8)*.

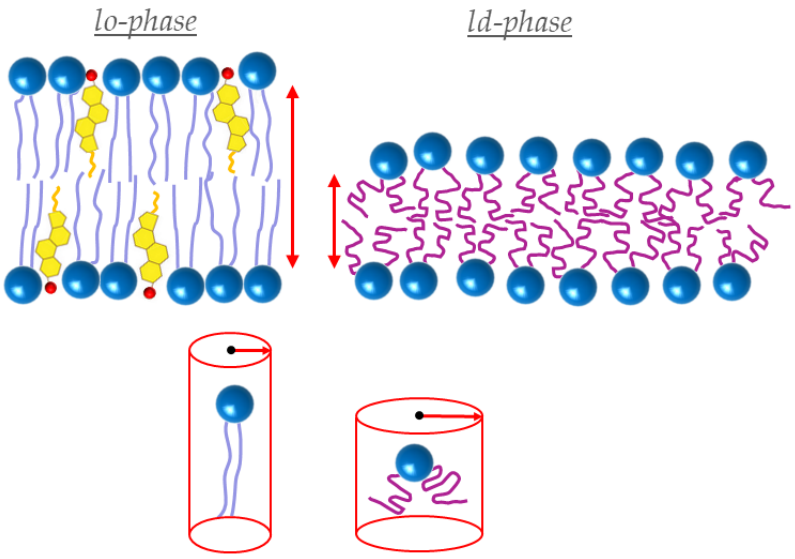

Figure 2.8) **Lipid chain architectures in different membrane phases result in different membrane thicknesses and areas per lipid.** ***Left panel:*** In the liquid-ordered phase, rich in saturated lipids and cholesterol, the lipid tails are elongated, thickening the width of the bilayer ***(top)*** and narrowing the molecular area ***(bottom)***. ***Right panel:*** In the liquid-disordered state, composed mostly of unsaturated or branched lipid tails, the width of the bilayer is reduced ***(top)*** and lipid tails sample a greater lateral area, increasing the area per molecule ***(bottom)***.

These proteins are thought to use the platforms as sites to initiate biochemical processes. An intriguing idea promoted by the model is that lipid rafts convey precise selectivity among proteins that increases the probability of interaction between membrane receptors and certain proteins that may be limited in availability. Furthermore, rafts have been implicated in effectuating viral infection and triggering inflammatory responses [53].

Though many studies have presented evidence [29, 32, 45, 47, 48, 54] in support of lipid rafts and their physiological function, their exact definition and their very existence are still topics of fervent controversy. A large number of

experiments conducted using model membranes, built of representative biological membrane constituents, demonstrate the macroscopic phase separation that gives rise to raft evolution; yet conclusive observation *in vivo* is still lacking. Most of these studies have captured raft phases in giant unilamellar vesicles (GUVs), as in *Figures 2.6* and *2.9* [29], which are often much larger in size (up to hundreds of micrometers in diameter) than biological vesicle formations, allowing features of interest to be visible with traditional fluorescence microscopy.

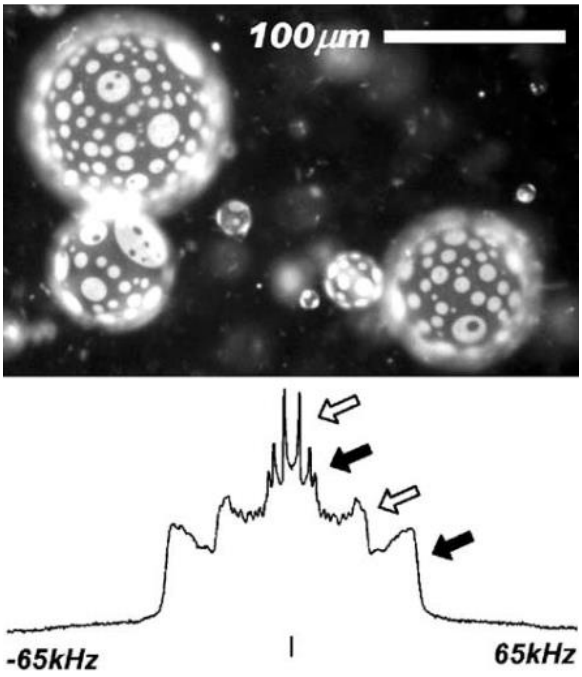

Figure 2.9) **Liquid-order–liquid-disorder phase separation in GUVs.** ***Top*:** Immiscible liquid phases are directly visualized on the surface of giant unilamellar vesicles by fluorescence microscopy. ***Bottom*:** Distinct superposition of ^{2}H NMR spectra demonstrates that liquid-disordered *(ld)* and liquid-ordered *(lo)* phases coexist in vesicle membranes. Distinguishing features of *ld* and *lo* spectra are denoted by white and black arrows, respectively, as described in [46]. Membrane compositions are ***(top)*** 1:1 DPhyPC:DPPC+50% cholesterol at 26°C and ***(bottom)*** 1:1 DOPC:DPPCd62 +20% cholesterol at 20°C. *Images and caption obtained from* [29].

The questions arise then: is detection of liquid–liquid phase separation mostly limited to GUVs, only due to the inadequacy of resolution in present imaging technology? If existent in biological membranes, this phenomenon would indeed occur at incredibly small size-scales. Or, do these lipid-cholesterol structures not exist as stable domains in living cell membranes at all? Other than GUVs, experimentalists often study rafts in blebs [47], which are vesicles extracted from the membranes of living cells. Thus, blebs retain all the compositional complexity of living cell membranes, without any of the cell's cytoplasmic components. Some argue that the underlying cytoskeletal network that adheres to the inner membrane leaflet of biological cells exerts a tension on the bilayer, disrupting the formation of stable, distinct phases. From this perspective, the development of rafts in blebs is possible due to the lack of this skeletal network and the tension it incurs. Additionally, the spatial- and temporal-scales of raft formation remain to be determined. Some critics suggest that the thermodynamic fluctuations in lipid composition are too fleeting to generate a local equilibrium that could endure in the dynamic environment long enough to activate feasible substrates for cellular activity. Such fluctuations may instead ensue from *non-equilibrium* conditions, and perhaps provoke states of the system more aptly regarded as *metastable*.

The ambiguity surrounding raft morphology has roused several

interpretations about what the details of the raft hypothesis entail. Some credit the occurrence of lipid demixing to a fine-tuning in membrane composition strategically close to critical miscibility points of the system. Near-critical fluctuations at these compositions, as have been observed in membrane phase studies [55, 56], would accordingly induce similarly fluctuating nano-scale assemblies – which, in the context of this representation, would define the 'lipid rafts'. An alternative model of membrane organization presents a definition of a 'raft' in the context of an equilibrium, reversible reaction between cholesterol and saturated phospholipids that forms a *condensed chemical complex* of the two species: $nqC + npS \rightleftarrows C_{nq}S_{np}$, where C and S in this case refer to cholesterol and saturated lipid, respectively, n is an oligomerization (cooperativity) parameter, and q and p are stoichiometric integers [57]. The model expands on the thermodynamics of *regular solutions*, with the additional concept of 'condensed complex' formation to account for deviations from the ideality inherent to regular solution theory. As is apparent from the reversibility of the proposed reaction, these complexes are small, ephemeral domains, considered to embody a fluctuating liquid-ordered phase. Segregation into a complex-rich phase is dependent on a strong cooperative binding between the reactants as well as their relative concentrations at a given temperature. High quantities of certain neighboring proteins are posited to have the potential for interacting with the lipid species engaged in the

reaction. Such interactions could develop protein–lipid complexes of augmented life-span and sufficient spatial breadth for macroscopic phase separation.

Regardless of the specific definition attributed to regions of local activity that are possibly modulated by distinct liquid phases, there is a consensus among the scientific community that lipid composition plays a vital role in the mechanics and thermodynamics of the membrane. The new era of membrane science attributes many biological functions of the cell to the organizational characteristics of the membrane's lipids – characteristics that vary widely among different lipid types and mixtures. This thesis probes the variation in membrane properties and its interactions with important proteins with changes in bilayer composition, size, and geometry using a molecular theory that explicitly incorporates the minute details of lipid atomic structure that deliver a powerful impact on cellular health and performance. Though the calculations in this work are performed for lipid membrane systems within the liquid-disordered phase, the theory presented here includes the appropriate terms to account for the condensed liquid-ordered and gel phases as well, along with a discussion on the formulation of these terms and how to apply them.

2.4 Bendy Bilayers and Lively Lipids

In addition to lipid concentration and the liquid–liquid phase separation discussed above, it is important to consider other bulk properties in analyses

regarding membrane characteristics, functionality, and interactions with external molecules. The local contour and elastic characteristics of the bilayer have been shown to influence the mechanics and thermodynamics associated with, for example, the stability of integral proteins, membrane fusion, activity of ion channels, and, as is the focus of this work, lipid reorganization across the bilayer and the adsorption trends of lipidated proteins [58]. Because of the membrane's fluidic constitution, it is highly *elastic*, which grants it the capacity to undergo structural fluctuations and large deformations if subject to appropriate stimuli. This property is essential for a cell's health and ability to function. A particularly conspicuous example conveying the value of bilayer flexibility is endocytosis *(Figure 2.10)*, where a signal prompts a depression in the plasma membrane, toward the cell's cytoplasm, ultimately budding into the cell to form an intracellular vesicle. Others include exocytosis, cell division, migration, apoptosis, and protein interactions.

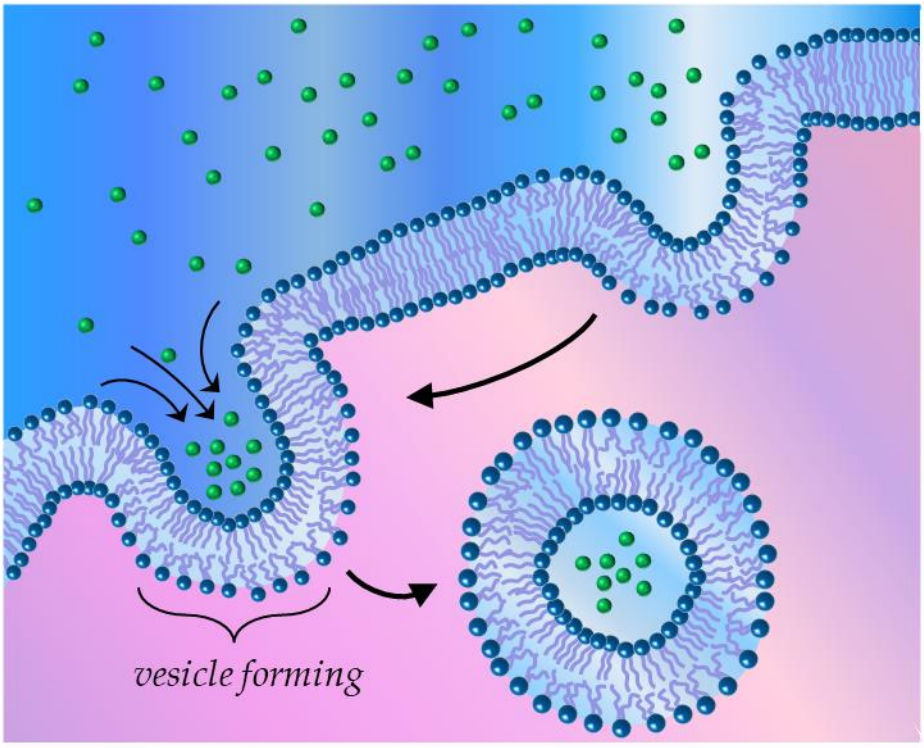

Figure 2.10) **Schematic of endocytosis.** The image illustrates the importance of membrane flexibility, which is imperative to numerous membrane functions, including vesicle formation during endocytosis as shown here.

There is a strong structure-to-function relationship within the membrane – a membrane's particular shape, which is influenced in a collaborative manner by factors such as lipid composition and membrane elasticity, is essential to the functional role of the cell or organelle it encapsulates, as is portrayed in *Figure 2.11* [59-62]. Nerve cells exhibit long, thin extensions (axons and dendrites) that facilitate their ability to make connections and pass chemical and electrical messages quickly between other nerve cells and their environment. Epithelial cells develop into a few different structures, but all are tightly packed to assemble into

near continuous sheets with minimal intercellular space, promoting the epithelial tissue's function as a protective barrier between the inside of the body and the environment. The biconcave shape of human red blood cells, and the high degree of reversible elastic deformation of their membranes, are ideal for the transportation of oxygen/carbon dioxide and passing through miniature capillary pathways [63]. The long, thin cells of muscle tissue facilitate immediate response and repair when tears form in the membrane from physical activity.

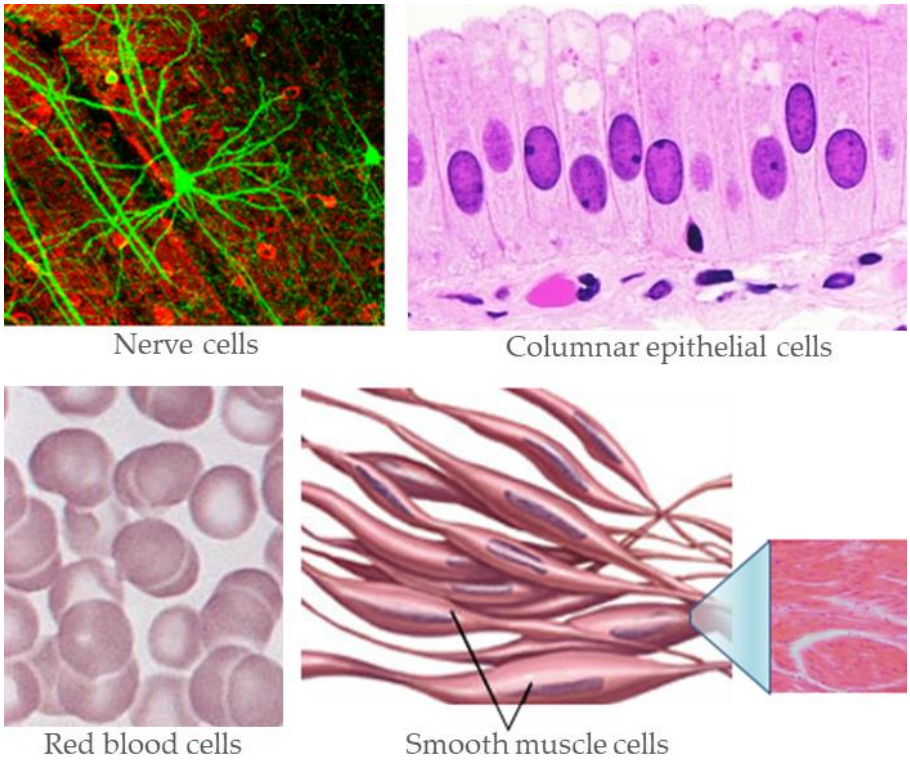

Figure 2.11) **Different types of cells have different shapes.** The shape of the membrane dictates the shape of the cell. Different membrane shapes are tuned to the specific functions of a given type of cell. *Images obtained from* [59-62].

Distortion in the shape of a cellular membrane can be indicative of various diseases. For example, as depicted in *Figure 2.12* [64], while normal red blood cells

are smooth and have the flexibility to change their shape when squeezing through blood vessels, sickle cell disease is indicated by a distortion in the membrane of red blood cells into rigid sickle, or crescent, structures that become trapped in blood vessels, interfering with normal blood flow.

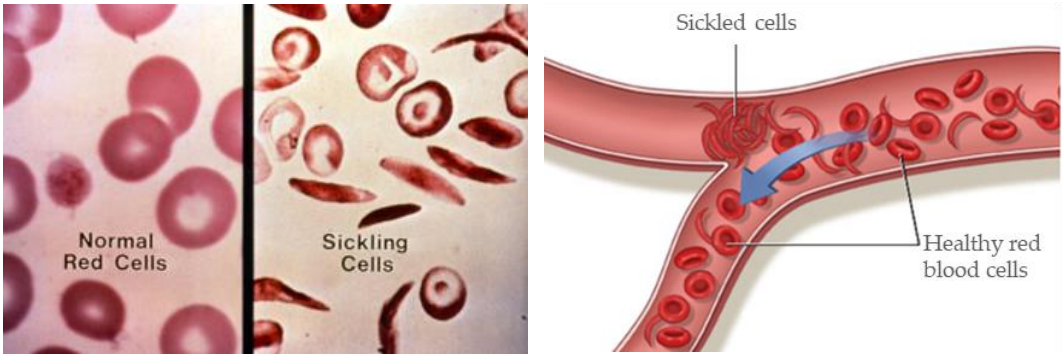

Figure 2.12) **Distortion of cell membranes is indicative of disease.** The change in shape and flexibility of a red blood cell to a rigid, sickle, or crescent, structure is the trademark of the sickle cell anemia disease. *Images obtained from* [64].

Lipid membranes serve not only as the outermost boundary of a cell (the plasma membrane), but also as the surrounding structure of organelles residing within a cell's cytosol. Each of these lipid membranes retains its own unique architecture that facilitates specific biological operations. The series of stacked, compositionally variable compartments, or cisternae, of the Golgi apparatus, each bound by tightly curved regions to form a narrow, flattened midsection, are imperative to the Golgi's capacity for the modification, sorting, and transport of materials, such as phospholipids, proteins, and biological polymers [65]. The helicoidal surface connecting adjacent ER sheets is thought to be an energetically

favorable structure that facilitates the dense packing of the sheets to accommodate maximum protein synthesis in secretory cells [66, 67]. When the structure of one organelle is disrupted, there are repercussions for the biochemical processes performed by that organelle, as well as those performed within other cellular compartments with which it interacts. Organelles also undergo necessary shape changes in response to the needs of the cell and under stress conditions. Mitochondria have been observed to elongate when nutrients are scarce to avoid degradation during autophagy; elongated mitochondria display increased density of cristae, stimulating ATP production to sustain cell vitality [68]. Understanding the evolutionary purpose for the sizes and geometries of plasma and organelle membranes and resolving the biological processes affected by shape transitions largely remains elusive and is an ongoing enterprise in membrane research.

The dynamic shape variations of elastic membranes are also coupled to the dynamics of the membrane lipids themselves. As we have discussed, lipid freedom of motion promotes the flexibility of lipid bilayers and is vital to membrane vitality. Movement of the individual lipids is possible due to the noncovalent interactions between them. Lipids continuously undergo conformational changes, rotations, and 'up and down' translations within their own monolayer on incredibly fast timescales – ranging from picoseconds to nanoseconds *(Figure 2.13)*. Lipids also rapidly diffuse *laterally*, within the plane of

their respective leaflet, on a constant basis, travelling several micrometers per second, with diffusion coefficients of around 5-18 $\mu m^2 s^{-1}$ for phosphatidylcholine (PC) lipids [69, 70], which constitute the bulk of mammalian cellular membranes. *Transmembrane* ("*flip-flop*") diffusion, on the other hand, is much slower, on the order of 10^{-15} s^{-1}. This corresponds to, on average, a single lipid 'flip' or 'flop' event every 24 hours, if at all, in most membranes [71].

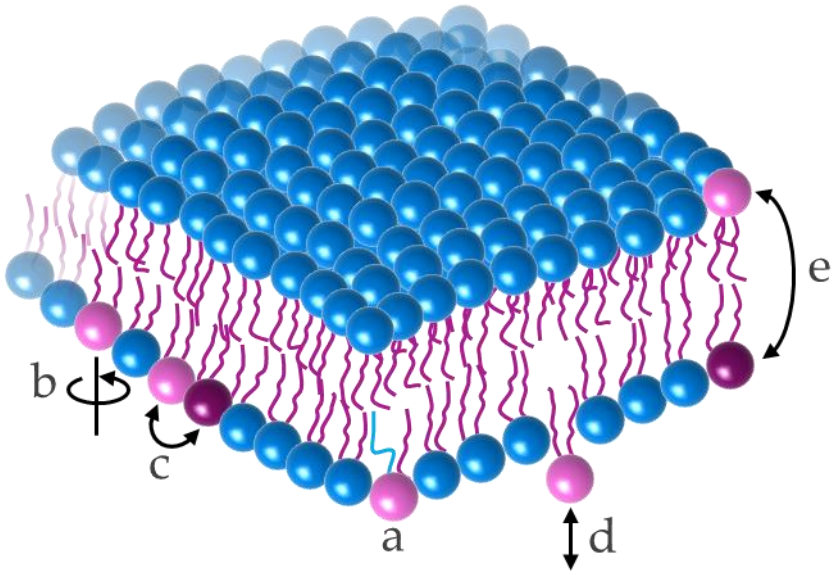

Figure 2.13) **Various motions of lipids in biological membranes.** Lipids continuously undergo **(a)** conformational changes, **(b)** rotations around the molecular axis, **(c)** lateral diffusion, and **(d)** protrusion out of the bilayer plane. Lipids rarely independently undergo **(e)** transbilayer diffusion (flip-flop) between lipid monolayers without a means of active transport or external stimulus.

There is a large energy barrier against lipid diffusion between the leaflets due to the hydrophilicity of the large phospholipid headgroups and the unfavorable increase in lateral pressure within the monolayer that must

accommodate the additional molecule. There are circumstances under which it is necessary for such movement, however. One such case is during lipid synthesis and transport in eukaryotic cells [72]. Lipids synthesized in the ER subsequently travel through the secretory system, where they must pass between the luminal and cytosolic leaflets of cellular compartments, either to maintain membrane stability or for appropriate placement in preparation for recruitment by other organelles, transport vesicles, or the plasma membrane. Another is the active maintenance of compositional asymmetry between the leaflets of the cell membrane itself. For example, plasma membranes generally contain a greater quantity of phosphatidylethanolamine (PE) and anionic lipids, such as phosphatidylserine (PS) and phosphatidylinositol (PI), in the cytosolic leaflet, whereas phosphatidylcholine (PC) and sphingolipids are preferentially retained in the exoplasmic leaflet – a distribution that must be actively regulated, using energy supplied by adenosine triphosphate (ATP) hydrolysis, and is lipid-specific. In these operations, two families of proteins – type IV, P-type ATPases (P4-ATPases), which is a type of *flippase* protein, and ATP-binding cassette (ABC) transporters, a type of *floppase* protein – are employed to facilitate the active transport of lipids from the exoplasmic to the cytosolic membrane leaf ('flip') or in the reverse direction ('flop'), respectively, providing a transmembrane path that catalyzes otherwise unfavorable transmembrane lipid diffusion [73, 74].

Changes in the phospholipid gradients between the membrane leaflets are tightly controlled. Regulated exposure of PS lipids in the exoplasmic leaf stimulates blood coagulation reactions in red blood cells [75, 76] and serves as a signal during cell apoptosis, prompting the disposal of the cell by macrophages [77-79]. The general shapes of PC and sphingolipids lipids confer neutral to positive curvature formations, whereas the small head-to-tail ratio of PE lipids form regions of negative curvature, explaining the distributions of these lipids in the exoplasmic and cytosolic leaflets of the plasma membrane, respectively. Much of the information regarding lipid transbilayer movement has been discovered only within the last few years, and much of the details of the process, such as the evolution of the transport proteins, the mechanisms by which they operate, and the specific residues involved in lipid recognition and transport remain obscure.

Another interesting phenomenon is the change in lipid diffusion patterns upon an induced deformation in the membrane, and how this ties with membrane elasticity. Alterations in the local curvature of a membrane create regions of local compression, which accumulate a density-based stress large enough to partially overcome the energetic barrier to lipid transmembrane diffusion and thus motivate lipid migration to the opposite, expanded leaf – even without the aid of catalyzing transport proteins. This results in the decay of the density gradient, relaxation of the accumulated local bending energy, and stabilization of the

membrane. However, the considerable energy requirement for lipids to traverse the hydrophobic membrane core is thought to prevent *complete* equilibration of the curvature-induced differential densities in the deformed bilayer leaflets on biologically relevant timescales. This is a concept we discuss in detail and support with the results of this work in later chapters.

Cholesterol is recognized as an integral player during the membrane remodeling process because of the molecule's rapid inter-leaflet mobility relative to other lipid components, primarily due to the small size of its polar headgroup, which consists of a single hydroxyl group. Though the rate of cholesterol transbilayer diffusion has not been definitively resolved, despite extensive experimental [80-83] and molecular dynamics [84-89] studies that approximate timescales ranging from sub-milliseconds to minutes, its relative ease of unaided passage across the membrane compared to the largely obstructed phospholipids is clear, suggesting an evolutionarily designed purpose for cholesterol as a mediator of stress relaxation in the bilayer.

We have noted that the incredible capacity of a membrane to geometrically transform is owed to its high degree of elasticity. The elastic character of a lipid membrane can be described by two elastic constants, the *bending modulus* (or mean-curvature modulus), κ_c, and the *saddle-splay constant* (or Gaussian curvature modulus), $\overline{\kappa}$. These parameters, often represented in units of k_BT, are 'stiffness

factors', assigned to the two possible orthogonal radii of curvature, that define the energy required to bend the bilayer into a given form, and are proportional to the system's free energy. This relationship can be recognized using Helfrich's theory of curvature elasticity [90], connecting the degree of elasticity of a membrane to the difference in the free energy of the system under a given deformation, relative to that of its planar orientation. The elastic membrane theory is ubiquitous in theoretical and molecular modeling of lipid membrane systems and the functional processes they engage in [91-94]. The application of Helfrich's theory to this work is detailed in Chapter 4; however, one contribution of this study is the expansion of the purely elastic model to incorporate the time-dependent element of lipid transbilayer reorganization upon a morphological change in the membrane. Whereas lipid 'flip-flop' has been acknowledged in the literature regarding membrane curvature, little has been done to quantitatively incorporate the phenomenon in the elastic membrane model.

Examining the rheological properties of curved membranes from the perspective of a molecular theory can be particularly illuminating. There is an abundance of experimental observations of curvature-induced biomechanical processes, whereas a mechanistic understanding of *how* membrane deformation causes such biological developments is largely inaccessible experimentally, leaving many open questions in cellular research. The following sections in this

chapter briefly explore the real-world applicability of membrane research and how theoretical membrane models can be valuable tools for probing the unanswered questions in biology, uniquely suited to bridging the gap between empirical observations/experimental measurements and the underlying mechanisms that motivate them. We will then describe the formulation of our own molecular model and use it to expand on transmembrane diffusion, particularly in terms of how it affects the bending energies involved in membrane deformations, and explore the influence of membrane curvature on the thermodynamics, elastic properties, and interactions with proteins of different types of lipid bilayers.

2.5 TANGIBLE APPLICATIONS OF MEMBRANE RESEARCH

Undoubtedly, much work is needed to understand membrane lateral heterogeneity and its intimate connection to cellular operations. The nano-scale size of biological membranes presents experimental and theoretical difficulties in studying such systems; however, continued research on lipid membranes has the potential to facilitate tangible applications that are undeniably promising. The importance of delineating the mechanisms that motivate membrane organization lies in the direct applicability such insight would confer to the rational design of efficient drug delivery systems, imaging technologies, fine-tuned gene control, and the engineering of optimized biomimetic devices and materials. For example, many recent nano-scale drug delivery devices are composed of *liposomal carriers*,

injected with therapeutic agents [95-98]. *Liposomes* are artificially synthesized spherical bilayers that offer excellent solubility and solubilizing capability and, being composed of materials that are also fundamental components of the cell membrane, i.e., lipids, these carriers are naturally inert and non-toxic.

Much research is devoted to different methods of functionalizing these spherical lipid bilayers with protective (stealth) polymers (such as polyethylene glycol, or PEG), imaging components, and targeting moieties to visualize and optimize the biodistribution profile of the drugs they contain *(Figure 2.14)*. The development of targeting ligands to selectively target the areas intended for drug release (such as to cancerous tissue as opposed to healthy cells) requires intimate knowledge of the types of receptors expressed on these cells, and how the membranes of both the biological cells and the lipid-based carriers will respond upon ligand-receptor binding. Many other non-lipidic nano-devices (e.g., polymeric materials, gold nanoparticles, dendrimers) have also been developed for therapeutic and imaging purposes. The interaction between these nanomaterials and biological membranes is of critical consequence and must be fully understood to ensure the efficiency of the device's intended function and to prevent cytotoxicity during its egression from the extracellular region, through the cell membrane, and into the cytoplasm.

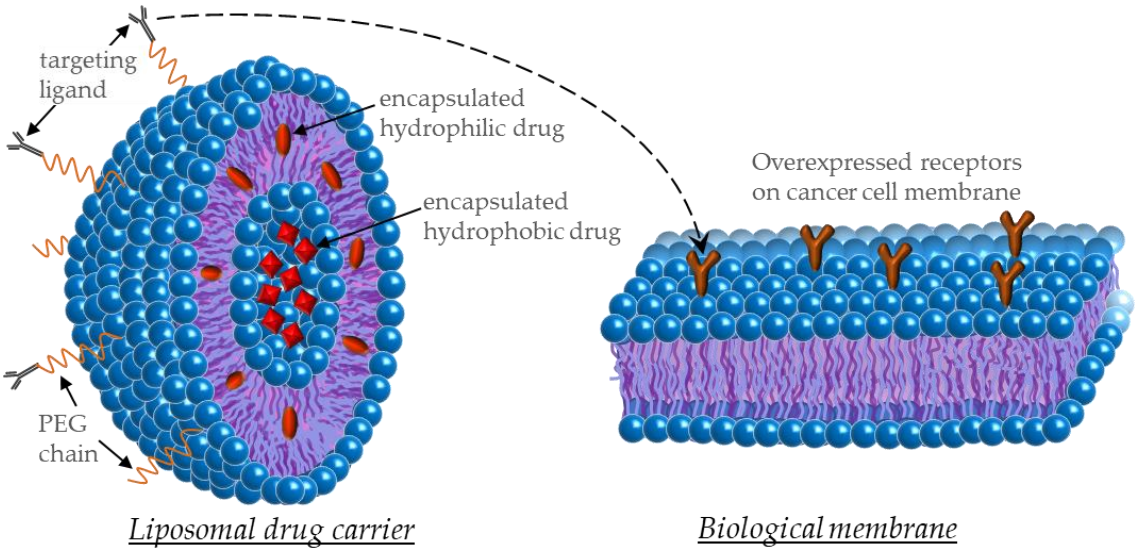

Figure 2.14) **Lipid-based technology.** Schematic representation of the use of targeting ligands and stealth polymers to enhance specificity and stability of liposome drug carriers.

Membrane research is also centrally tied to other biotechnological enterprises, such as the engineering of artificial cells, diagnostic reagents, energy transfer systems, and biosensors [99]. Multilayered membrane stacks are being used to increase bioelectrocatalytic activity of enzyme-containing bilayers [100]. *Intelligent nanostructures* are devised based on an understanding of lipid self-assembly, leading to the construction of acute bio-sensing devices [101]. Advanced molecular separation, water purification, and fuel production via biomimetic systems are all technologies inspired by analyzing the physicochemical operations of cellular membranes and the regulatory role of their lipids [102, 103]. A fundamental understanding of lipid membranes can also aid in the detection of certain disease states. For example, studies on the

nanomechanics of cells suggest that tumors or cancerous cells are softer and have a higher degree of deformability in terms of their elastic moduli compared to their healthy counterparts [104]. For all such applications, it is highly advantageous to develop predictive methods for investigating membrane behavior in the presence of nanomaterials and various environments to streamline successful experimental strategies for optimal performance and to reduce associated costs.

2.6 Experimental and Theoretical Methods for Studying Membranes, and their Limitations

The existing and developing applications stemming from the understanding of lipid systems mark momentous achievements for science, engineering, and the medical sector, establishing membrane research as a particularly salient area of current study. Ever more experimental discoveries inspire the drive for laboratory reproducibility, simulation-to-experiment compatibility, and mathematical modeling that would explain observed phenomena.

Refinements in the available experimental technology and novel methodologies for studying membrane activity have continued to provide valuable information. Electron microscopy is a powerful tool for visualizing membrane structural properties that can achieve resolutions of 0.05-2 nm – far more enhanced than other visualization techniques [105-107]. Several

architectural characteristics of the membrane have been distinguished using this method, such as the first direct observation of each of the membrane's monolayers [108]. However, samples viewed by the electron microscope must be fixed, and therefore dead, either under cryogenic conditions or vacuum. Studying lipid membranes in a dynamic state or within their natural environments is imperative for attaining knowledge about mechanistic sequences of operations occurring at the membrane in real time [109-111].

Atomic force microscopy (AFM), is another technique capable of gathering images of lipid membranes and their integral or peripheral structural complexes at the order of nanometers [112-114]. Specimens may be prepared at room temperature in ambient air or within aqueous environments. However, the studies are limited to the examination of supported lipid bilayers, on a surface that may alter the native properties of the membrane [115]. X-ray and neutron scattering are quite useful in detailing the size, shape, and even the conformation of molecular assemblies in solution. Information on phase transitions can be gathered from data on spatial averages between molecules (the density, or area per lipid, of regions of the membrane in one phase *versus* another) granted by these complementary procedures. Together, these scattering techniques have provided valuable improvements in the lipid area values used in molecular dynamics simulations [116, 117].

Fluorescence microscopy, where a number of membrane constituents are colored with a fluorescent dye molecule, has been most commonly used for imaging the dynamic behavior within live cells [118, 119]. A major advantage of fluorescence microscopy, including fluorescence energy resonance transfer (FRET) [120, 121] and fluorescence recovery after photobleaching (FRAP) [122], is the ability to study the dynamic localization and function of target molecules by following the targets in living cells, which is not possible by the other microscopy techniques. The predominant impediment faced by these methods is the relatively low degree of resolution, compared to that of electron and atomic force microscopes. Imaging is constrained to visible light wavelengths of 200 nm or larger, much larger than the thickness of the membrane and lipid microdomains. For this reason, micron-scale giant unilamellar vesicles (GUVs) or blebs are constructed to study membrane phase behavior, which yield lipid domains that are directly visible using the fluorescence-based techniques. Sarah Keller's research group has conducted many such studies, which have yielded enlightening evaluations of phase boundaries in various lipid and cholesterol ternary GUVs, and how reorganization of these boundaries ensues under variations in temperature, concentration, [29, 45, 48] and the presence of sugars [32].

The limitations of experimental applications highlight the efficacy of

theoretical approaches. Simulation and statistical-mechanical methodologies offer alternative perspectives that contribute intelligence inaccessible through experimental methods, or that support, refine, and interpret experimental results. Still, theoretical work remains comparatively sparse. Much of the theory that does exist is in the form of atomic level molecular dynamics (MD) simulations or coarse grained (CG) simulations. While these methods are valuable tools that complement experimentally drawn data with their contributions to structural information or qualitative interpretation, respectively, they also face prohibitive challenges that limit their utility. MD simulations are capable of gathering mechanistic details, such as the area per lipid, bilayer thickness, and other architectural quantities with a high degree of accuracy. However, they are highly dependent on the accuracy of the force field (inter-molecular interaction) parameters that are required as input to the system. Additionally, computer time is generally insufficient to equilibrate the lateral distribution of the lipids. Detailed molecular analysis is only realized at exceedingly high computational costs, especially when incorporating more than one lipid species. While most of the interesting membrane phenomena in biology transpire over a timescale on the order of microseconds up to seconds, evaluation of a simple membrane system requires close to a week of wait-time to capture but a few nanoseconds of real-time MD simulation. The CG models help illustrate qualitative trends over larger

system sizes and timescales than MD studies, yet they do not contain the molecular detail necessary to accurately represent such complex systems, even for simplified model membranes. This is also the deficiency of the phenomenological approaches that have been introduced.

Systematic characterization of a cell membrane's anatomical features is a necessary element in membrane research; however, purely structural models omit the linkage between the organizational motifs of membrane constituents and how these mobilize the biological activity of the cell. Molecular theoretical models, such as the model presented in this work, are derived from a statistical-mechanical framework of the membrane and its aqueous environment that connects the sub-nanoscopic details of the system to macroscopic behavior and grants access to greater size and timescales than the other theoretical methods of investigation, at reasonable computational cost. Furthermore, these molecular theories accommodate the need to delineate responses in membrane mechanics and thermodynamics to precise changes in various system variables and external conditions, an exercise imperative to revealing the nature of the relationship between form and function, with relative ease and efficiency.

CHAPTER 3
GENERAL OVERVIEW OF THEORETICAL METHODS —CLASSICAL DENSITY FUNCTIONAL THEORY—

3.1 STATISTICAL MECHANICS AND STATISTICAL ENSEMBLES

Classical density functional theories (DFTs) such as the one used in this work are used to investigate the structural and thermodynamic properties of complex molecular systems by employing the calculus of variations on a *thermodynamic functional*. This functional is a function, whose argument itself consists of functions describing the spatially-dependent density of particles. Such theories are rooted in a statistical mechanical foundation, which relates the system's microscopic, or even sub-nanoscopic, behavior to its observable macroscopic phenomena. Classically speaking, the position and momentum of each particle in the system together define the system's *microstate* (one of many possible microscopic configurations of the system's particles, each with its own probability), which in turn determines the system's total energy. Statistical mechanics links the analysis of what microstates are *possible* for the system to occupy, and what energies these states have, to the system's empirical thermodynamic properties by means of the statistical distribution of an *ensemble*

of microstates. There are different ensembles that are defined by the macroscopic constraints (or *canonical variables*) a given system is subject to. One example, the '*canonical ensemble*' describes an ensemble of microstates that are confined to a certain system volume, V, impermeable to the efflux of its constituent particles, N_i, (of type i) and the influx of external particles, and are in thermal contact with the environment, i.e., a system with canonical variables V, N_i, and temperature, T. Another, the '*grand-canonical ensemble*', likewise describes a system with a defined volume and temperature, however, molecules may freely pass through system boundaries; thus, this ensemble is constrained by the equivalency of a given species' chemical potential, μ_i, on either side of those boundaries (canonical variables of V, μ_i, and T). Other macroscopic physical requirements may be constant pressure, rather than constant volume, for a system consisting of, say, the contents of a vessel open to the atmosphere; alternatively, a system may be isolated such that insulation maintains a constant energy, rather than a constant temperature via heat exchange. From different macroscopic constraints, and thus different types of statistical ensembles, emerge distinct statistical characteristics.

A powerful statistical mechanical construct, unique to each of the many ensembles, is the *partition function*, which is a function of the system's particular set of canonical variables. The partition function is a statistical tool that is intimately related to the probability that the system occupies a certain microstate.

It encodes how the various probabilities are partitioned among the different microstates, based on their individual energies – essentially by summing over the *weighted* number of states a system may sample. In the classical limit where positions and momentums of particles are continuous, the sum is replaced by an integral. All macroscopic thermodynamic properties, for example heat capacities, pressure distributions, free energies, etc., may be expressed in terms of the partition function or its derivatives.

3.2 Mean Field Approximation and Thermodynamic Equilibrium

We have developed a theory, rigorously constructed from a molecular foundation, for describing the mechanics and thermodynamics in model membranes consisting of various lipid species. The theory precisely accounts for the architecture of the lipid chains, their headgroups, and solution components to realistically characterize the physics of the system on the scale of the monomer. This entails a description of the size and shape of each monomeric element and a comprehensive set of configurational states the system's molecules may assume. The momenta of the lipids, which are in continuous motion within biological membranes, are explicitly modeled in terms of their lateral, translational/kinetic degrees of freedom. The intra- and inter-molecular attractive energies, steric repulsions, and electrostatic contributions are the relevant internal and external (when applicable) potential energy contributions included in the model.

In its exact form, this approach forges a model system of a large number of various, interacting particles, giving rise to a vastly complicated, computationally difficult, many-body problem. When dealing with a system of many molecules, it is often not necessary, or even wise, to examine it by detailing the natural thermal fluctuations and trajectories involved in following the positions and momenta of each constituent particle. To reduce the challenges confronted when summing (integrating) over all energy states, rather than treating the inter-molecular interaction terms explicitly, where the influence exerted on a single lipid chain by neighboring molecules is via *direct* contact, interactions are accounted for within a *mean-field* approximation. That is, the interactions that N-1 system particles have with the N^{th} particle are approximated by a single, averaged effect. This spatially varying, *single-particle field potential* is representative of all states the system may assume. Such an approximation reduces the many-bodied system to a one-body system, consequently allowing the performance of thermodynamic calculations at a relatively low cost. In our theory, we treat each lipid chain individually. Intra-molecular interactions and architectural details of a given lipid chain are treated rigorously, as detailed in *Section 4.2*.

These contributions to our model are collected into a single expression, namely, the partition function, ultimately taking the form of a functional integral that encompasses fluctuations over all possible mean-field states of the system.

The functional integral can be approximately evaluated via the *saddle point method*, which amounts to the approximation of the integrand using a free energy functional – in our case, a density functional as introduced in *Section 3.1*. We formulate two different theories in this work, one which models an isolated membrane, to focus on the properties of its hydrophobic core, and one which encompasses a larger system, including an aqueous environment in which the membrane resides. The formulation of the first is developed within the canonical ensemble, subject to the thermodynamic constraints of constant volume (or area, A, in 2-D model systems or at interfacial regions), number of molecules, and temperature. This represents a biological system well, where we are concerned with a very small subsystem within a much larger biological entity that continuously exchanges energy with its surroundings and is metabolically regulated to maintain appropriate thermal conditions. In this context, the free energy functional represents the total Helmholtz free energy, $\mathcal{F}$, of the system (with canonical variables V, A, N_i, T):

$$d\mathcal{F} = -SdT - PdV + \gamma dA + \sum_i \mu_i dN_i \qquad \begin{matrix} \textit{differential Helmholtz free energy} \\ (\textit{canonical ensemble}) \end{matrix} \qquad (3.1)$$

We have included the total area as a canonical variable, independent of the system volume, to account for surface tension at the membrane boundary. The entropy (S), total pressure (P), surface tension (γ), and chemical potential of lipid species i

(μ_i), are the conjugate variables of T, V, A, and N_i, respectively.

With the inclusion of an aqueous environment surrounding the bilayer, we introduce a group of soluble molecules that are not bound to the membrane, in contrast to the membrane lipids. These solution components are mobile, able to freely pass the boundary between the system (the membrane and its direct aqueous environment) and the bulk solution, far from the membrane. As a consequence, these species are not subject to the constant molecule constraint enforced on the membrane lipids. In this case, a Legendre transform is performed on the free energy functional with respect to the mobile species, thereby lifting them from the requirement of maintaining constancy in number within the system and, instead, subjecting them to a constraint which enforces constancy of chemical potential at all positions. As noted previously, the statistical ensemble that represents the possible states of a constant volume system, in thermodynamic equilibrium with a reservoir (such as our bulk solution) with which it can exchange energy and particles, is referred to as the grand-canonical ensemble. The characteristic state function for this ensemble is the grand potential, sometimes referred to as the Landau free energy, Φ_G (with canonical variables T, V, A, and μ_m, where the subscript, m, indicates the mobile, aqueous species, which may include water, salts, and/or other biological water-soluble molecules):

$$d\Phi_G = -SdT - PdV + \gamma dA - \sum_m N_m d\mu_m \qquad \begin{matrix} differential\ Landau\ free\ energy \\ (grand\ canonical\ ensemble) \end{matrix} \tag{3.2}$$

Hence, the appropriate ensemble that accurately describes our 'membrane-plus-aqueous surroundings' system is a hybrid of the canonical and grand canonical ensembles, with a free energy functional that can therefore be regarded as a *semi-grand potential*, $\Phi_{S\text{-}G}$, with canonical variables T, V, A, N_i, and μ_m, where the subscript, i, refers to the particles confined to the membrane, namely the lipids, and m represents the mobile solvent molecules, ions, and any other components with the diffusive freedom to pass from the bulk solution to our system and make contact with the membrane:

$$d\Phi_{S\text{-}G} = -SdT - PdV + \gamma dA + \sum_i \mu_i dN_i - \sum_m N_m d\mu_m \qquad \begin{matrix} differential \\ semi-grand\ potential \end{matrix} \tag{3.3}$$

Thermodynamic information may be acquired from the theory via the *equilibrium states* of the system. There are an infinite number of states (e.g., set of density profiles, charge distributions, and configurational arrangements) that the system may technically sample; however, there will be one set of functions/states that will be overwhelmingly most probable – so much so that the system will most nearly always exist within this stable, equilibrium setting. We wish to represent our model in terms of these conditions, which yield the maximum probability, and may do so through minimizing our free energy functional with respect to the unknown variables in the system. *Functional minimization* delivers a set of self-

consistent, integrodifferential equations, used to obtain the expression for the system's equilibrium free energy and which are solved numerically, ultimately providing the avenue through which both structural and thermodynamic predictions can be made.

3.3 TWO THEORETICAL PLATFORMS: *GENERATION I* & *GENERATION II*

The research introduced in this work further develops a single-chain mean-field (SCMF) theory that stems from earlier theoretical models formulated by A. Ben-Shaul, W. Gelbart, and I. Szleifer [31, 123-128] and other gifted theorists. The field theory was later advanced by their students. Saliently, M. J. Uline, R. Elliott, M. Schick, and D. Grillo provided tremendous guidance in the formulation of the present model, directly or through their own related works [30, 35, 42-44, 129-131]. The foundation of the molecular theory has been expanded on and used to study both lipidic and non-lipidic systems (e.g., micelle formation of small surfactants [123-125, 132-134], the structure and thermodynamics of various tethered polyelectrolyte materials [135-142], and the phase behavior of lipid bilayers [30, 35, 42-44, 129-131, 143-147]).

Here, we have modified the theory to obtain a fundamental understanding of complex biological systems under two different perspectives, which we have entitled *Generation I* and *Generation II*. Model membranes in both versions are composed of different types of phosphatidylcholine (PC) and

phosphatidylethanolamine (PE) lipids (two of the most prominent classes of lipids in animal membranes). Those included are dioleoyl-phosphatidylcholine (DOPC), palmitoyl-oleoyl-phosphatidylcholine (POPC), dimyristoyl-phosphatidylcholine (DMPC), dilauroyl-phosphatidylcholine (DLPC), and dioleoyl-phosphatidylethanolamine (DOPE). Both PC and PE headgroups are *zwitterionic* – they contain one positive moiety and one negative moiety, resulting in a net-neutral, but polar hydrophilic region that creates an electrostatic dipole.

The first set of results of presented in this study are obtained using the *Generation I* model (Chapters 4 and 5) for a focused examination of the hydrophobic region's influence on membrane behavior. The conformations of the hydrocarbon tails are treated explicitly at the small monomeric level in accordance with Flory's Rotational Isomeric States (RIS) model [148] *(see Section 4.2)*. The steric packing interactions, or short-range repulsive forces, of the lipid tails are modeled by an incompressibility constraint – where the average molecular area *occupied* by the hydrophobic particles must equate to the average *available* molecular area within the hydrophobic core. In essence, this enforces a spreading of the monomeric units of the lipid chains, entropically driven to populate all available space. The incompressibility constraint also accounts for much of the long-range attractive potentials, such as van der Waals forces, by the requirement of a constrained system volume, preventing unlimited expansion of the system

particles. Excessive areal expansion of the lipids is also restricted by the attractive interactions of the lipid headgroups. Rather than modeling the headgroups explicitly in the *Generation I* theory, their effective interaction is treated using an oil-water surface tension term, following Tanford's opposing force model [149]. The oil-water interface accounts for attractive forces among the molecules on a phenomenological level by applying an energetic cost to a decrease in molecular density that would realistically cause unfavorable exposure of hydrophobic molecules to the surrounding aqueous environment. Opposing this attractive contribution from the headgroups are the steric repulsions among them. The counteracting forces between the repulsive interactions of the tails and bulky headgroup moieties and the molecular contraction caused by the headgroup interfacial tension result in a competition for the optimum areal density that would confer stability in the bilayer. The surface area may freely change to balance these internal forces.

To obtain the degree of ordering among the lipid tails necessary to drive the main chain transition from the liquid disordered phase to more condensed phases, the isotropic interactions based on packing are insufficient and an additional attractive energy term is needed. This term is written in the theory as a Maier-Saupe, pairwise interaction that relies on orientational ordering relative to the bilayer normal, which energetically favors chain conformations that are

more aligned. We note that the results presented in this work are obtained without the contribution from the Maier-Saupe attractive interaction terms, as they have negligible effect on the properties of membranes in the liquid-disordered state. All results of this study are obtained using systems well within the liquid-disordered phase. Systems that undergo phase transitions to liquid-ordered or gel states, however, are influenced significantly by the nematic ordering effected by these attractive interaction fields. Hence, we introduce the theory with the inclusion of the Maier-Saupe attractive terms and discuss their formulation in Chapter 4, for the sake of generality and to present a thorough description of an energetic contribution that would be quite relevant under different conditions.

The *Generation I* study concentrates on the physics of the lipid hydrocarbon chains, without the added complexity of electrostatic contributions from the polar lipid headgroups (other than the minimal representation based on the surface tension) and surrounding aqueous ionic solution. We confine this analysis to four pure-component lipid systems, and one binary lipid system, all evaluated above the main-chain transition temperature of the lipid(s) under consideration. This ensures a liquid-disordered medium, where the electrostatics of the headgroups are not necessary to capture important trends observed experimentally (though such contributions might be important for liquid-ordered systems [131]). We take the system to be isotropic in the *x*-*y* plane, such that inhomogeneities arise solely

along the z-direction, perpendicular to the lipid headgroup-tail interface, through the depth of the bilayer. We analyze the effects of curving the bilayers into spherical liposomes of assorted radii on important membrane properties and the behavior of membrane-associated proteins.

Generation II of our theory (Chapters 6 and 7) is generalized to include an aqueous environment of physiologically relevant pH and salt concentration surrounding the membrane. Here, electrostatic interactions among bulk solution salts and the zwitterionic lipid headgroups in the bilayer are accounted for. The volume, geometry, conformational freedom, and charge density of the ions, solvent, and lipid headgroups are considered explicitly. The conformations of the lipid tails are given the same rigorous consideration as in *Generation I*, using the isomeric states model of Flory [148] *(see Section 4.2)*. The elements that are incorporated in the incompressibility constraint now include all solution components and lipid headgroups, in addition to the hydrophobic lipid tails. We introduce an additional attractive term to fully represent the amphiphilic nature of the lipids that drives their self-assembly in an aqueous environment, where the lipid volume fraction is now dependent on all lipid and solution molecules in the system. We investigate membrane polymorphism with this theory by manipulating the radii of both spherical liposomes and cylindrical bilayers and comparing the corresponding changes in bilayer properties and interactions with

environmental proteins. These membrane geometries are widely expressed in biology, characteristic of, for example, spherical transport vesicles and plasma membranes of many cells and tubules found in highly curved organelles such as the ER and Golgi apparatus. Such a comparative geometrical analysis leads us to discover the crucial contribution from Gaussian curvature to membrane physics, often neglected in theoretical models.

Both generations of the theory are employed to study, primarily:

(1) Membrane elasticity

We examine the elastic character of model membranes with different lipid compositions and varying degrees of inter-leaflet asymmetry. There is much literature on experimental values of the bending modulus in pure component membranes, whereas multicomponent studies are fairly scarce. Thus, we primarily conduct our analysis on pure component bilayers.

(2) Lipid transbilayer diffusion

We explore the effects of membrane deformation on lipid transbilayer diffusion and how this is dependent on the elastic properties of the membrane. We discuss its significance to the interpretation of experimental data and in the development of theoretical models in studies that involve membrane curvature. Effects of curvature are inspected by explicitly modeling the dependency of the free energy on membrane geometry, using the symmetric planar bilayer as a

reference state.

(3) Protein–membrane interactions

We investigate the membrane-adsorption tendencies of lipidated proteins as functions of membrane composition, degree and mode of membrane curvature, and the asymmetry between bilayer leaflets caused by curvature-induced transbilayer lipid diffusion. Our analyses focus on the minimal membrane anchor of the ubiquitously expressed GTPase, N-Ras (tN-Ras). The goal is to obtain a mechanistic understanding of how the adsorption of the protein's lipid-anchor is modulated by these factors. We initially employ the first-generation of the theory, *Generation I*, to understand the relationship between the molecular structure of the hydrophobic lipid tails and the localization of lipidated proteins on spherical liposomes (Chapters 4 and 5). Due to the charged moieties on some proteins, ionic components in solution, and the charge distribution created by the charged groups of the lipid hydrophilic region in the bilayer, electrostatic contributions can be quite relevant. Therefore, we then perform a similar study with both spherical and cylindrical membranes using our expanded, second-generation model, *Generation II*, which includes an aqueous ionic medium surrounding our model membranes (Chapters 6 and 7). The protein studies are conducted in close collaboration with Dimitrios Stamou's experimental research group and collaborators from the University of Copenhagen, including Jannik B. Larsen, Soren L. Pedersen, Knud J.

Jensen, Nikos S. Hatzakis, Kadla R. Rosholm, Henrik K. Munch, Vadym Tkach, and Thomas Bjørnholm from the Department of Chemistry, and Poul M. Bendix from the Department of Physics. John J. Sakon and Keith R. Weninger from the Department of Physics at North Carolina State University also contributed to the experimental work. Comparing our theoretical findings with the results provided by our experimental counterparts demonstrates excellent agreement.

We have but one fitting parameter in both our models. The parameter is used as a free variable *only* in our study on membrane elasticity, to obtain theoretical values for the bending moduli of the various types of membranes that are in good agreement with experimental results. Experimental bending moduli are found in the literature, from independent laboratory groups not affiliated with our work or that of our experimental collaborators. We then apply the value for this parameter as a *set quantity* in our models for our studies on protein adsorption, such that there are technically no fitting parameters in these analyses, ensuring that theoretical results are derived independently of those obtained experimentally by our collaborators and without bias. This lends additional compelling evidence in support of the competency of our molecular theory in capturing the mechanical and thermodynamic qualities of lipid bilayers and their interactions with lipidated proteins.

CHAPTER 4
GENERATION I THEORY:
MODELLING THE MEMBRANE'S HYDROPHOBIC CORE

The following discussion details the mathematical construction of the 'first-generation' *(Generation I)* of our theory, which focuses on the contribution of the bilayer's hydrophobic region to the thermodynamic properties of the system. In Chapter 6, we present the 'second-generation' *(Generation II)* of our theory with a corresponding mathematical discourse that introduces a molecular description of the hydrophilic lipid headgroups and their electrostatic interactions with a surrounding ionic solvent.

4.1 INCOMPRESSIBILITY OF THE HYDROPHOBIC MEMBRANE CHANNEL

We begin with a description of a lipid bilayer of width, or thickness, $2l$ (along the z-axis in our coordinate system), which may comprise any type(s) of lipid species i, with number N_i, together totaling a number of N membrane lipids. These lipids are partitioned, with specified concentrations, between the two halves, or monolayers/leaflets, of the membrane. In curved bilayers, the monolayer in which the lipid headgroups line the concave surface is referred to as the *compressed leaflet*, while the monolayer of lipids whose headgroups line the

convex surface is referred to as the *expanded leaflet*, relative to the normal vectors projecting in opposite directions, stemming from the midplane. A biological membrane's inner and outer leaflets may be either locally convex/expanded or concave/compressed (or planar, for that matter), depending on the point of reference, as shown in *Figure 4.1* where an inward protrusion of the plasma membrane, called a caveola, dramatically changes the bilayer's curvature landscape.

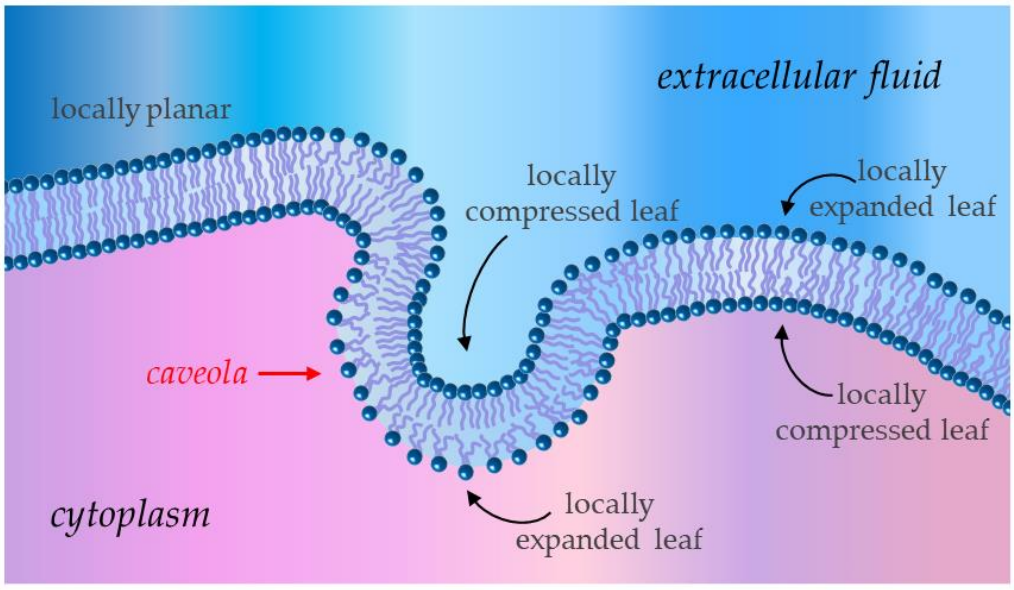

Figure 4.1) **Schematic of a membrane caveola.** A bilayer is composed of two monolayers, or leaflets, of lipids. In a curved bilayer the *expanded* and *compressed* leaflets correspond, respectively, to the locally convex and concave surfaces of curved membrane formations, relative to the normal vectors at the midplane. Cellular membranes constantly undergo local geometrical changes, such as in the case of caveola formation – an inward protrusion in the cell membrane that is involved in, e.g., signal transduction, endocytosis, and protection from mechanical stress – which changes the membrane's curvature landscape.

In our model, the hydrophobic core of lipid tails is considered transversely isotropic (in the x-y plane). Along the hydrophobic width of a single leaflet (parallel to the z-axis), however, there is an incredible degree of conformational heterogeneity of the hydrocarbon lipid chains. All lipid chain properties, and the thermodynamic quantities derived from them, are therefore functions of depth into the membrane (functions of z). In a planar bilayer, the two leaflets are symmetric about the bilayer midplane. When the theory is discretized, the lipid tail region is divided laterally into 'layers' of one angstrom each, as depicted in *Figure 4.2*, ensuring that all position-dependent properties are evaluated with a high degree of accuracy.

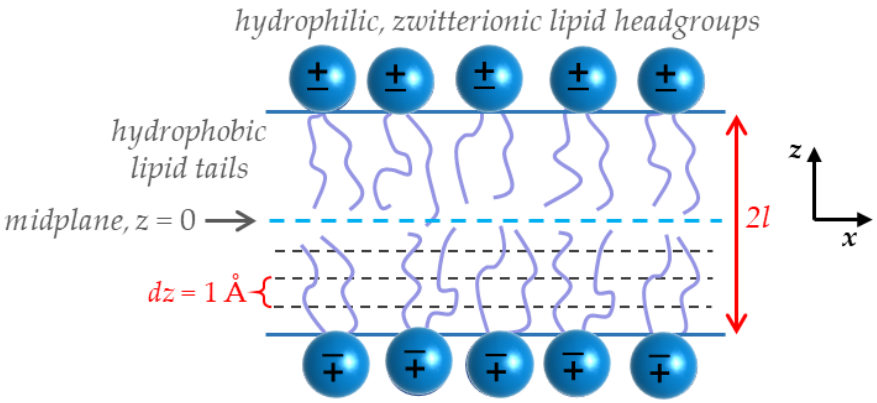

Figure 4.2) **Schematic of a model, planar lipid bilayer with zwitterionic lipid headgroups.** Inhomogeneities exist along the z-axis, through the width ($2l$) of the bilayer. The theory is discretized along the z-axis (parallel to the bilayer normal) into layers of 1 Å to capture the structural heterogeneity through the hydrophobic region. Planar model bilayers are symmetric across the midplane. All lipids considered in this study have zwitterionic headgroups, with one positive and one negative charged moiety, producing a net charge-neutral hydrophilic region (though the *Generation I* model treats this region minimally with a bare oil-water surface tension term).

This hydrocarbon membrane channel is an incredibly dense, fluid region, inhospitable to water or other polar molecules, and can therefore be justifiably treated as an incompressible fluid ($\nabla\cdot\vec{v}=0$). This imposes a constraint on the total volume of the system to consist entirely of the sum of all monomeric elements contributed by the lipid tails. For example, given a model membrane composed of a fully saturated phospholipid (*s*), an unsaturated phospholipid (*u*) with a specified number of double bonds, n_{db}, and cholesterol (*c*), the total volume, *V*, of the system would be:[2]

$$V=\sum_{\omega}^{n_i^{tails}}\left(N_s v_{CH_2}(n_{s,\omega}+1)+N_u\left(v_{CH_2}(n_{u,\omega}+1-2n_{db,\omega})+2v_{CH}n_{db,\omega}\right)+N_c v_c n_c\right) \qquad (4.1)$$

where N_i is the total number of lipids/cholesterol of component *i* (*i* = *s*, *u*, *c*) and the summation accounts for the multiple, possibly dissimilar, individual chains, ω, of lipid *i*, totaling n_i^{tails} (cholesterol has only one chain). The number of linked monomers extending from the glycerol-bound carbon constructing a single hydrophobic tail of a given lipid (not including the glycerol carbon) is designated $n_{i,\omega}$. Methylene (CH_2) groups in the saturated and unsaturated lipid chains are each given a volume of v_{CH_2} = 27.0 Å^3 and a bond length of 1.53 Å [150]. The number of

[2] The theory is well-equipped to analyze bilayers containing multicomponent membranes of various lipids, including cholesterol. While the membranes examined in this work are mostly pure component (with one binary system), and none of them containing cholesterol, we wish to present a generalized theory in this thesis, demonstrating its adaptability to multicomponent systems that may be of interest to other researchers and can be used in future studies.

double bonds in a given unsaturated lipid tail is $n_{db,\omega}$, and the *CH* group that forms half a double bond is assigned a volume of $v_{CH} = 0.8v_{CH_2}$. The terminal methyl (CH_3) groups of the lipid chains have a volume of 54.0 Å^3, twice that of the CH_2 units [35, 151-153]. If we were to assign the CH_2 and CH_3 volumes that compose the short cholesterol tail the same values as we have for the other two lipids, the result would be a disproportionate percentage of the total cholesterol volume being attributed to the extremity of its hydrophobic region, leaving cholesterol's aromatic ring structures with an inadequate volumetric contribution, roughly 30%. Therefore, an 'average' value, v_c, is applied to each of cholesterol's monomers, $v_c = {}^{v_{chol}}/_{n_c} \approx 21.0$ Å^3, where the total number of hydrophobic carbons in cholesterol is $n_c = 27$ and v_{chol} is cholesterol's total volume, less the 25.0 Å^3 of its polar hydroxyl headgroup [35, 125].

To obtain the bilayer's molecular area at the midplane, $a(0)$ (where $z = 0$), we divide the above equation by the total number of molecules, N, and the full width of the bilayer, $2l$:

$$\begin{aligned}\frac{V}{2lN} &= \frac{A(0)}{N} = a(0) \\ &= \sum_{\omega}^{n_l^{tails}} \left(\frac{x_s v_{CH_2}(n_{s,\omega}+1) + x_u\left(v_{CH_2}(n_{u,\omega}+1-2n_{db,\omega}) + 2v_{CH}n_{db,\omega}\right) + x_c v_c n_c}{2l} \right)\end{aligned} \tag{4.2}$$

where x_s, x_u, and x_c are the total concentrations of saturated lipid, unsaturated lipid,

and cholesterol within the membrane, respectively. For the planar bilayer, the midplane molecular area is representative of the molecular area for each discretized layer, or plane, of the membrane channel for any given increment along the *z*-axis, perpendicular to the bilayer interface. For curved systems, *Equation 4.2* describes the molecular area of the midplane only, while any digression in the positive or negative *z*-directions either increases or decreases the area per molecule as a function of the curvature and distance in *z* from the midplane, as given by the expansion about the midplane below:

$$\frac{A(z,\mathbf{c})}{N} = a(z,\mathbf{c}) = a(0)\left(1 + (C_1 + C_2)z + C_1C_2z^2\right) \tag{4.3}$$

Equation 4.3 describes the area per molecule, $a(z,\mathbf{c})$, in the *x-y* plane of the membrane at a distance *z* from the bilayer midplane, where the bilayer local geometry is defined by the *curvature tensor*, **c**, at the molecule's position. The expression is written in terms of the midplane molecular area, *a(0)*, and the *principal curvatures*, C_1 and C_2 [126]. The parameters C_i are the eigenvalues of the curvature tensor, $\mathbf{c} = [C_1, C_2]$, defined in terms of the *radii of curvature*, R_i $\left(C_i = {}^{1}/_{R_i}\right)$, which are considered positive for convex surfaces and negative for concave surfaces with respect to the bilayer normal *(Figure 4.3)*. The curvature tensor can fully describe how a surface bends, both in magnitude and direction, at a given point on a two-dimensional surface in three-dimensional space. We will discuss

the curvature tensor further in *Section 4.5*.

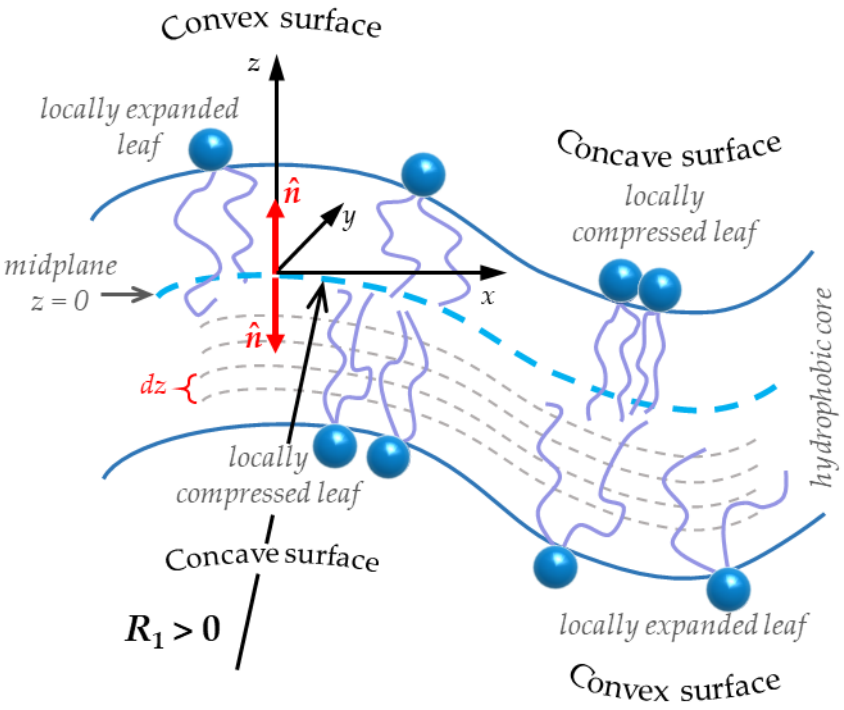

Figure 4.3) **Schematic of the coordinate system and curvature sign convention.** We take the radius, $R_i > 0$ for convex surfaces, and $R_i < 0$ for concave surfaces, with the normals projecting from the bilayer midplane, where $z = 0$.

The amount of volume in each discrete layer, *dz*, through the bilayer's hydrophobic region is calculated by integrating the area expression in *Equation 4.3* with respect to distance from the midplane along the *z*-axis in either the positive or negative direction, bounded by the upper and lower limits of a given discretized layer of length $\Delta = 1$ Å:

$$V(z',\mathbf{c}) = \int_{\Delta(z'-1)}^{\Delta z'} A(z,\mathbf{c})dz = A(0)\left(z + \left(C_1 + C_2\right)\frac{z^2}{2} + C_1C_2\frac{z^3}{3} \right)\Bigg|_{\Delta(z'-1)}^{\Delta z'} \tag{4.4}$$

where z' is the integer representation of a given discrete layer.

Imposing the incompressibility constraint on the system ensures that for any deformation of the membrane, the average area occupied by the molecules in a given lateral plane of the hydrophobic channel must remain equal the average available area. Such a constraint has a significant impact on the system, as it requires all particles to, on average, equally populate all regions of the hydrophobic membrane core. This forces chains to elongate in thicker bilayers, to sufficiently occupy the region near the bilayer midplane, thereby stifling their entropic freedom and consequently incurring an undesirable rise in the system's free energy. Thinner bilayers afford a greater entropic contribution, however, the highly coiled chains comprise a greater number of *gauche* conformational states *(see Section 4.2)*, at an unfavorable energetic cost. This competition between the energetic and entropic contributions to the system is at the heart of maintaining membrane stability, where the bilayer area is free to expand and contract to achieve optimum chain packing in the hydrophobic channel, based on a balance of these forces – this defines the equilibrium state in which the membrane will exist.

A generalized formulation of the incompressibility constraint can be obtained by *ensemble averaging (see Section 4.2)* over the configurations of the system's lipid particles and using the relationships given in *Equations 4.2-4.4*:

$$a(z,\mathbf{c}) = \sum_{i,\delta} x_i x_{i,\delta}(\mathbf{c}) \sum_{\omega}^{n_i^{tails}} \left\langle \overline{v}_{i,\omega,\delta}(z,\mathbf{c}) \right\rangle \qquad for\ -l < z < l \qquad \begin{matrix} Incompressibility \\ constraint \end{matrix} \tag{4.5}$$

where $\left\langle \overline{v}_{i,\omega,\delta}(z,\mathbf{c}) \right\rangle$ is the ensemble-averaged contribution to the volume of the hydrophobic core at z, per unit length, from the monomers of the ω^{th} chain of lipid species i, in the δ leaflet of a membrane with curvature, $\mathbf{c}$. Note that a summation over the number of lipids of species i, in leaflet δ, totaling $N_{i,\delta}$ lipids, has been performed *a priori* in the above equation, with subsequent division by the total number of molecules in the system, N, which sets the equation in terms of lipid concentration in the bilayer (such is done for all following equations in this work). We differentiate between the *total* concentration, x_i, of a molecule of species i (within the whole system) and the curvature-dependent concentration of a species within a *single bilayer leaflet*, $x_{i,\delta}(\mathbf{c})$, using the following definitions, respectively:

$$\left.\begin{aligned} x_i = \frac{N_i}{N} = \frac{N_{i,I}(\mathbf{c}) + N_{i,O}(\mathbf{c})}{N} \quad or \quad = \frac{N_{i,C}(\mathbf{c}) + N_{i,E}(\mathbf{c})}{N} \\ x_{i,\delta}(\mathbf{c}) = \frac{N_{i,\delta}(\mathbf{c})}{N_i} = \frac{N_{i,\delta}(\mathbf{c})}{N_{i,I}(\mathbf{c}) + N_{i,O}(\mathbf{c})} \quad or \quad = \frac{N_{i,\delta}(\mathbf{c})}{N_{i,C}(\mathbf{c}) + N_{i,E}(\mathbf{c})} \end{aligned}\right\} \; x_i x_{i,\delta}(\mathbf{c}) = \frac{N_{i,\delta}(\mathbf{c})}{N} \tag{4.6}$$

$$\begin{matrix} inner\ /\ outer \\ leaflet\ notation \end{matrix} \qquad \begin{matrix} compressed\ /\ expanded \\ leaflet\ notation \end{matrix}$$

This permits the specification of lipid concentration in a particular leaflet of our membrane model, needed in the event of curvature-driven compositional asymmetry via lipid diffusion across the bilayer midplane. The sum of the total concentrations of all species in the system equals unity, $\sum_i x_i = 1$. In the above

equation, $x_{i,I}(\mathbf{c})/N_{i,I}(\mathbf{c})$ and $x_{i,O}(\mathbf{c})/N_{i,O}(\mathbf{c})$ are the concentrations/number of molecules of species i in the $\delta = I$ (inner) and $\delta = O$ (outer) leaflets, respectively. In curved membranes, rather than 'inner' and 'outer', we refer to a bilayer leaflet as either locally 'compressed' ($\delta = C$) or locally 'expanded' ($\delta = E$), with corresponding concentrations/number of molecules: $x_{i,C}(\mathbf{c})/N_{i,C}(\mathbf{c})$ or $x_{i,E}(\mathbf{c})/N_{i,E}(\mathbf{c})$, respectively. Which set is used depends on context; when regarding planar membranes, the 'inner/outer' terminology may be used.

As discussed above, repulsive forces between the molecules are modeled as excluded-volume interactions, accounted for via the incompressibility constraint and imposed during minimization of our free energy functional. The constraint is enforced by the Lagrange multipliers, $\pi(z,\mathbf{c})$, which come to physically represent the lateral pressure fields in the membrane upon functional minimization (this is further explained in *Section 4.4*).

4.2 Ensemble Averaging of Configurationally Dependent Properties and the Rotational Isomeric States Model

The equalities in *Equations 4.3-4.5* couple the curvature dependence of the molecular area to all ensemble averaged properties, $\langle ... \rangle$, in the system. Ensemble averages calculate the mean of a quantity by averaging over all the microstate configurations realizable by the lipid chains, each weighted by its own probability. These averages may be written in terms of the probability, $P_{i,\omega,\delta}(\alpha_{i,\omega,\delta},\mathbf{c})$, that the ω

chain of species i, in leaf δ with a specified curvature, $\mathbf{c} = [C_1, C_2]$, will assume a certain configurational state, α, using the standard relation for the expectation of a discrete variable, for example:

$$\left\langle w(\mathbf{c}) \right\rangle = \sum_{\alpha} P(\alpha, \mathbf{c}) w(\alpha, \mathbf{c}) \tag{4.7}$$

where w, in this context, refers to any configuration-dependent system property. Therefore, the ensemble averaged volume per unit length, at z, of the membrane's constituent particles from *Equation 4.5*, takes the form:

$$\left\langle \overline{v}_{i,\omega,\delta}(z, \mathbf{c}) \right\rangle = \sum_{\alpha_{i,\omega,\delta}} P_{i,\omega,\delta}(\alpha_{i,\omega,\delta}, \mathbf{c}) \overline{v}_{i,\omega,\delta}(\alpha_{i,\omega,\delta}, z, \mathbf{c}) \tag{4.8}$$

Because ensemble averaged properties require summing over all configurational states, or positions, of every monomer on every tail of every molecule in both leaflets, their exact calculation is infeasible. However, as discussed previously, the probability of the system existing in the vast majority of available states is equal, or eminently close, to zero. There is a particular set of states, however, that is always highly probable at any given time. Therefore, the average that encompasses *all possible* states will very nearly be indistinguishable from that of the *most probable set* of states. The summation, then, may be reduced to account for this 'most probable' set of states only, without losing the physics of the system. The determination of the most probable set of states is achieved through functional minimization *(see Section 4.4)*.

The *configurational* state, α, of a chain in our model includes all possible *conformational* arrangements of the chain's monomers, in addition to a comprehensive set of both the *vertical*, *translational* degrees of freedom (up-and-down shifts of the entire chain) and solid body *rotations* of the chain about the bilayer normal. The conformations are formulated using Flory's Rotational Isomeric States (RIS) model [148]. The RIS model facilitates the calculation of the average values of conformation-dependent properties of a given chain, where averaging over a massive number of conformations is essential for adequate evaluation. The strength of the model lies in its unique combination of incorporating structural and energetic details of the given chain (individual bond lengths, bond angles, torsion/dihedral angles, and energetic contributions of different conformations, which are not required to be identical at each segment of the chain) with computational efficiency. The computational speed of the RIS approach is achieved from organizing the calculations as the serial product of a number of matrices, based on the number of segments in the chain.

In our application of the RIS model, each unique lipid tail conformation builds from the specified position of the anchoring, zeroth carbon of the chain, regarded as the *glycerol carbon* of the lipid tails, located at position, z_0, which is not included in the volume of the hydrophobic core but rather marks the position of the hydrophilic–hydrophobic interface (cholesterol is modeled somewhat

differently, as discussed at the end of this section). Stemming from the glycerol carbon, each consecutive k^{th} monomer along a single saturated chain, ω, of n total monomers (each with a volume, v_{CH_2} = 27.0 Å^3 or v_{CH_3} = 54.0 Å^3) is located by its position vector, $\vec{r}_{k,\omega}$, and bound covalently, 1.53 Å apart, with the angle between neighboring carbon segments taken to be 112° (θ = 68° as the supplement to that angle in *Figure 4.4*) [150]. Successive carbons may assume one of three possible orientations with respect to the bond-angle it forms with its predecessors. These *dihedral angles*, ϕ, are *gauche plus (+)* at ϕ = 120°, *gauche minus (-)* at ϕ = −120°, and *trans* at ϕ = 0° (these are the only three biologically accessible conformations of open, aliphatic hydrocarbons; *see Figure 4.4)*. The *cis-* double bond(s) in unsaturated chains slightly alters this construct by imposing a rigid kink in the chain about the location of the double bond(s). This kink prevents the same freedom of rotation capable about fully saturated segments; additionally, the volume of the *CH* groups linked by the double bond is reduced to $v_{CH} = 0.8v_{CH_2}$. These changes modify the configurations and corresponding energies of the segments associated with the double bond.

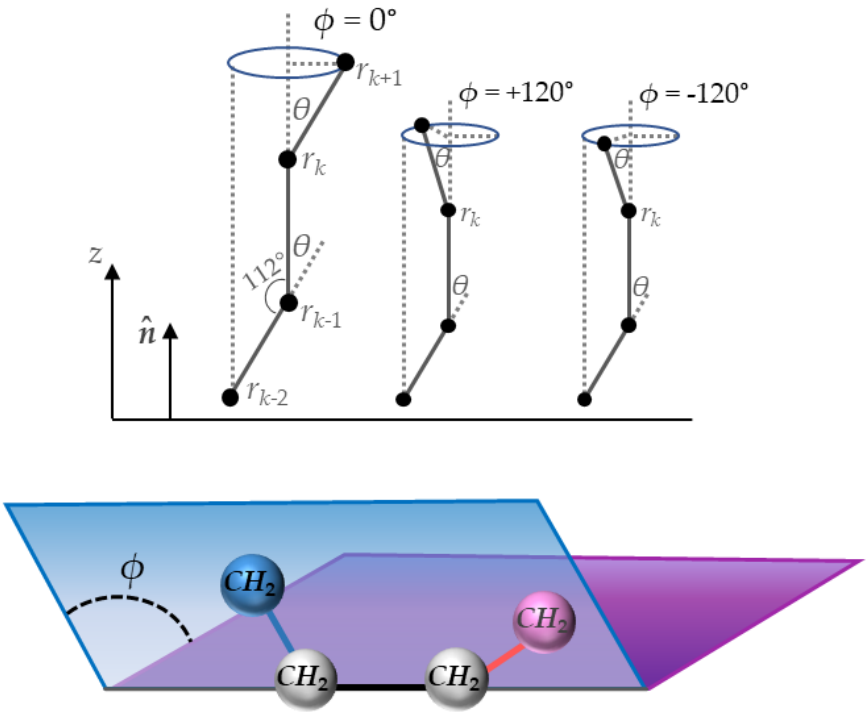

Figure 4.4) **Schematic of different dihedral angles.** A dihedral angle, ϕ, is the angle between two adjacent planes that are each made by a set of three consecutive monomeric units (each set of four monomers creates two planes and thus a dihedral angle). Open-chain hydrocarbon conformations can physically exist in three discrete states with dihedral angles of: *trans* (0°), *gauche (+)* (120°), and *gauche (−)* (−120°). Alkane sequences are taken to have a bond angle (between consecutive chain segments) of 112°, such that the supplement of that angle is $\theta = 68°$, and bond length of 1.53 Å.

A lipid tail with many *gauche* bonds is coiled, sampling many entropic degrees of freedom, whereas a lipid tail with an all *trans* conformation is highly stretched and entropically limited. Energetically, both ±*gauche* conformations are thermally excited states, which exist in energy wells that confer stability to these orientations, each contributing an increase in the internal energy by ε_g = 500 calories per mole ($\approx 0.8 k_B T$) [154]. The *trans* conformation has the lowest energy

level and is regarded as a reference state, with zero contribution to the internal energy *(Figure 4.5)*. Therefore, the conformational internal energy of a single, isolated chain for a given orientation is described simply as $\varepsilon(\alpha) = n^{gauche}(\alpha)\varepsilon_g$, where $n^{gauche}(\alpha)$ is the number of *gauche* bonds in a chain in configuration α.

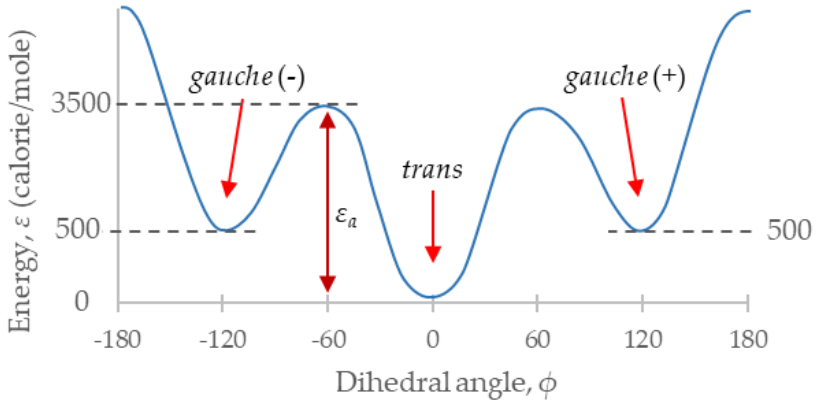

Figure 4.5) **The internal energy of the three possible aliphatic open-chain conformations.** Only *gauche* (+), *gauche* (-), and *trans* dihedral angles have low enough energy to be accessible as physical saturated hydrocarbon conformational states. *Trans* is the most energetically favorable and is taken as a reference state, with zero energetic penalty. Thermal fluctuations of the lipid chains are sufficient to overcome the activation energy, ε_α, required to access the *gauche* (+) and *gauche* (-) conformations, which exist in energy wells that confer stability to these states, though each incur an energetic penalty of 500 calories per mole.

The conformations defined by the three discrete dihedral angles are the only physical conformations of open aliphatic chains. Intermediate conformations do not represent orientations accessible by the chains in nature due to the excessive energetic cost they incur. There are other physical restrictions on the lipid configurations that are accounted for by the model, which reduce the spatial

sampling of the chains tremendously from what would otherwise encompass a total of 3^{n-1} configurations for each specified, initial bond orientation stemming from the glycerol carbon. First, all configurations that impose any part of a monomer's volume within the volume-space occupied by another monomer breeches the excluded volume requirement and are therefore eliminated. Self-interacting configurations are specified as those that place any two non-consecutive monomer centers closer together than the sum of their radii (assuming spherical monomer volumes). Second, the space extending into the aqueous region, beyond the hydrophobic–hydrophilic interfaces at $z > l$ and $z < -l$, is inaccessible to the lipid tails, hence, chains transgressing these bounds are excluded. Lastly, conformations that yield consecutive *gauche (+)* and *gauche (-)* dihedral angles along the chain experience large steric hindrances due to hydrogen-hydrogen overlaps, an event referred to as the *pentane effect* [154]. The substantial energetic penalty this effect provokes (~3000 cal/mole) prevents such arrangements in nature, thus, chains in violation of this constraint are also discarded.

For a capacious representation of the entire, physical configurational sample space within the bilayer, we add to the remaining set of conformational arrangements by performing both a series of Euler rotations on the hydrocarbon chains about the bilayer normal, according to random generation of sampling

angles, and vertical translations (perpendicular to the bilayer interface) of the lipid molecule as a solid body. Translations of the chains are established using the random generation of vertical displacements about the hydrophobic–hydrophilic plane within the interval $\{-\Delta z, \Delta z\}$, with $\Delta z = \left(1.5\ \text{Å} + {}^{1}/_{2}\, z_t\right)$, where $z_t = 2.53686$, the distance between every other carbon in an all trans chain conformation [150]. These rotations and translations are subject to the same steric and spatial restrictions as listed above. This compilation of configurational sequences of a single chain yield on the order of 10^8 configurations, which are used for the rigorous calculation of intra-molecular interactions for each type of lipid chain in the model bilayer.

Unlike the other lipids, cholesterol's conjoined aromatic rings constituting the bulk of its volume are rigid, and thus do not have the conformational degrees of freedom enjoyed by the lipid tails. Cholesterol is therefore modeled as two parts: the ring structure, which is constructed using coordinates from a protein databank, and the short, open, aliphatic 'tail' at the extremity of its hydrophobic region, which is analogous to a lipid tail and thus built according to the RIS model. The aromatic rings are given no internal degrees of freedom, are fixed in space with respect to one another, and are regarded as possessing no energetic contribution. The tail portion is afforded the same degrees of freedom as a saturated lipid chain, with a 1.53 Å bond length and *gauche*/*trans* conformational

states. Accommodation is made for the three terminal methyl groups protruding from the main-chain, placing them in a sequential manner based on the main-chain local conformation. Solid body rotations and translations are performed on cholesterol, as is done for the other lipid molecules – though, with fewer internal degrees of freedom, many more rotations are sampled for cholesterol than for the lipids (360 *versus* 36).

4.3 BUILDING THE FREE ENERGY FUNCTIONAL

There is a competition between entropy maximization and the minimization of internal energy as the system seeks optimal stability. Entropically, the system endeavors to sample as many configurations as possible. However, there is an energetic cost (increase) for assuming less favorable configurational states. This dynamic engagement is captured, beginning with the construction of our free energy functional. The free energy functional, which, for this application is derived within the confines of the canonical ensemble, depicts the interplay between the energetic and entropic contributions to the system, assuming the recognized form of the Helmholtz free energy:

$$\mathscr{F} = E - TS \tag{4.9}$$

where, E is the total internal energy, S is the total entropy, and T is the constant temperature of the system, maintained by the metabolically regulated 'heat reservoir' of the body.

Note that in this description, $\mathscr{F}$ represents a functional that includes fluctuations over all possible states, including those that are exceedingly improbable and highly unstable. The functional is rigorously constructed of the internal energy and entropy contributions that encompass all of these fluctuations, and is, therefore, exact. Formally, all these states should be accounted for, however, the integrals that arise from such a literal treatment are exceedingly difficult to evaluate. Fortunately, most of these states contribute infinitesimally or nothing at all to the observable, physical form in which the system will exist. On the other hand, there are also a set of states that will *most always* describe the system in any given space and time. These are the equilibrium, or most probable, states of the system, which may be accessed through functional minimization. The function procured from the minimization is the *equilibrium Helmholtz free energy*, in terms of the system's most probable set of configurational states, from which all thermodynamic quantities and distributions of interest may be evaluated.

Let us, then, assemble the functional by examining each relevant internal energy and entropy contribution and illustrate the procedure described above in mathematical terms. The total internal energy that is generated within our membrane arises from the configurational energy of each type of molecule in the system, $\langle \varepsilon_{conf}(\mathbf{c}) \rangle$, the intermolecular attractive energies among these molecules, $\langle \varepsilon_{attract}(\mathbf{c}) \rangle$, and the interfacial energy at the lipid headgroup region, $\langle \varepsilon_{heads} \rangle$. All

internal energy terms are expressed as ensemble averages over the system's configurational states; the curvature tensor, **c**, in the argument indicates dependency on membrane curvature of these properties. The total entropy of the system includes the entropy of the configurational arrangements sampled by the system's molecular constituents, $S_{conf}(\mathbf{c})$, and the translational entropy, $S_{trans}(\mathbf{c})$, which evolves from the momentums of system particles.

We can write the functional, expanded in these energetic and entropic contributions:

$$\beta\mathcal{F} = \beta\left\langle \varepsilon_{conf}(\mathbf{c})\right\rangle + \beta\left\langle \varepsilon_{attract}(\mathbf{c})\right\rangle + \beta\left\langle \varepsilon_{heads}\right\rangle - \frac{S_{conf}(\mathbf{c})}{k_B} - \frac{S_{trans}(\mathbf{c})}{k_B} \tag{4.10}$$

where we have made the equation dimensionless by multiplying both sides by $\beta = 1/k_B T$, with k_B as the Boltzmann factor and T the system's uniform temperature.

Molecular Configurational Energy and Entropy of the Hydrophobic Lipid Chains

Using the standard formalism for the expectation of a variable, we may express the ensemble-averaged molecular configurational energy generated by the lipids of the bilayer's δ leaflet in terms of the probability, $P_{i,\omega,\delta}(\alpha_{i,\omega,\delta},\mathbf{c})$, that a chain, ω, of lipid species i in this leaflet assumes a given configuration, α:

$$\frac{\beta\left\langle \varepsilon_{conf,\delta}(\mathbf{c})\right\rangle}{N} = \beta\sum_i x_i x_{i,\delta}(\mathbf{c})\sum_{\omega}^{n_i^{tails}}\sum_{\alpha_{i,\omega,\delta}} P_{i,\omega,\delta}(\alpha_{i,\omega,\delta},\mathbf{c})\varepsilon(\alpha_{i,\omega,\delta}) \tag{4.11}$$

We write our expressions on a per total molecule-basis so that they are in terms of

concentrations, x_i and $x_{i,\delta}$ (as defined in *Equation 4.6*), which are inputs to our model. As discussed in *Section 4.2*, each *gauche (±)* dihedral angle incurs an energetic penalty of 500 calories per mole more than that of the *trans* orientation, which is used as a reference state with zero energetic consequence.

The total molecular configurational entropy generated by the positional degrees of freedom accessible to the lipid chains in a single δ leaflet is:

$$\frac{S_{conf,\delta}(\mathbf{c})}{N} = -k_B \sum_i x_i x_{i,\delta}(\mathbf{c}) \sum_{\omega}^{n_i^{tails}} \sum_{\alpha_{i,\omega,\delta}} P_{i,\omega,\delta}(\alpha_{i,\omega,\delta},\mathbf{c}) \ln\left[P_{i,\omega,\delta}(\alpha_{i,\omega,\delta},\mathbf{c})\right] \tag{4.12}$$

Maier-Saupe Attractive Interaction Energy of the Hydrophobic Lipid Chains

Though the attractive dispersion forces between system molecules is partially accounted for, at least on a phenomenological level, by the limits on molecular expansion imposed by the incompressibility constraint and the interfacial tension of the bilayer, alone these contributions are not sufficient to motivate the considerable alignment of the lipid tails necessary to drive the transition from the liquid-disordered state to more condensed phases. This can be achieved by defining a composition-dependent potential that favors the local alignment of the chains. We incorporate these molecular attractions as local, pairwise interactions between tail segments, modeled following an approach similar to the Maier-Saupe theory [155-157], which quantifies the long-range attractive forces between molecules based on orientational ordering.

Therefore, it is first necessary to define the local orientation of a chain at a given position along the chain. We define the local orientation vector, $\hat{u}_{k,\omega}$, with a magnitude of unity, at the k^{th} monomer along chain ω of lipid species i as:

$$\hat{u}_{k,\omega} = \frac{\vec{r}_{k-1,\omega} - \vec{r}_{k+1,\omega}}{\left|\vec{r}_{k-1,\omega} - \vec{r}_{k+1,\omega}\right|}, \qquad k = 1...n_i - 1 \tag{4.13}$$

where the position vector of a monomer, $\vec{r}_{k,\omega}$, stems from the anchoring glycerol carbon at $\vec{r}_{0,\omega} \equiv z_0$, and $\hat{u}_{k,\omega}$ is specified for all non-terminal monomers of the lipid chain *(see Figure 4.6)*. For cholesterol, this method is used for the short, tail-like, base section of the molecule, while those monomers that are members of one of cholesterol's four aromatic rings are simply assigned the orientation vector between the base ring-carbon, bonded to the alkane tail, and the apex ring-carbon, bonded to the hydroxyl headgroup. The CH_3 monomers bonded to the ring structures are regarded as terminal monomers, taken to have no contribution to the ordering of the chain.

It is then necessary to define two functions: (1) a local density of these orientation vectors [158] as a function of position, z, and orientation, $\hat{u}$, in a specific configuration, α, assumed by each chain of lipid species, i, and (2) a pairwise interaction variable between the chains of species i and j that weights these orientations, relative to the bilayer normal, $\hat{n}$. These functions are denoted $\Psi_i(\alpha_i, z, \hat{u})$ and $V_{i,j}(\hat{u} \cdot \hat{n}, \hat{u}' \cdot \hat{n})$, respectively:

$$\Psi_i(\alpha_i, z, \hat{u}) = \frac{1}{A(0)} \sum_{\ell}^{N_i} \sum_{\omega}^{n_i^{tails}} \sum_{k=1}^{n_i - 1} v_{i,\omega}(k) \delta\left(z - z_{k,\omega}(\alpha_{i,\omega})\right) \delta\left(\hat{u} - \hat{u}_{k,\omega}(\alpha_{i,\omega})\right) \tag{4.14}$$

$$V_{i,j}(\hat{u} \cdot \hat{n}, \hat{u}' \cdot \hat{n}) \approx -J_{i,j} f(\hat{u} \cdot \hat{n}) f(\hat{u}' \cdot \hat{n}) = -J_{i,j} f\left(\cos(\theta_{\hat{u} \cdot \hat{n}})\right) f\left(\cos(\theta'_{\hat{u}' \cdot \hat{n}})\right) \tag{4.15}$$

The first summation in *Equation 4.14* runs over every lipid, ℓ, of species *i*, totaling N_i lipids of that species, the second runs over every chain, ω, on a lipid of species *i*, totaling the number of tails on that lipid, n_i^{tails}, and the third runs over every monomer, *k*, on chain ω, stemming from the glycerol carbon, totaling $n_i - 1$ non-terminal monomers. Each of these monomers is assigned an individual volume, based on the species of its host chain, and its place, *k*, in the sequence of monomers along the chain (i.e., $v_{i,\omega}(k) = v_{CH}$, v_{CH_2}, or v_{CH_3} depending on if the k^{th} monomer is a double-bonded *CH* group, a single-bonded CH_2 group, or a terminal CH_3 group, respectively, whereas $v_i(k) = v_c$ for any of cholesterol's monomeric units, as described in *Section 4.1*). The contributions to the orientation density are weighted by these individual volumes, causing the final form of the attractive energy to depend on the local volume fraction of lipids in the bilayer. The potential in *Equation 4.15* is approximated with the condition that its contribution to the free energy is determined by a chain's dependence on the bilayer normal, given by functions of $\hat{u} \cdot \hat{n}$ – their product reflecting that the interaction is pairwise. The particular form of this function is rooted in one originally devised by Wilhelm Maier and Alfred Saupe for predicting thermotropic, nematic-isotropic phase

transitions of liquid crystals [155, 156]. The model was adapted by Marcelja [159] to describe the ordering of lipid tails, further developed by Gruen [157], and later modified by R. Elliott *et al.* [30]:

$$f\left(\cos(\theta_{\hat{u}\cdot\hat{n}})\right) = \frac{2m+1}{m}\left(\cos^2(\theta_{\hat{u}\cdot\hat{n}})\right)^m \approx \left(\frac{m}{\pi}\right)^{1/2} \exp\left(-m\theta_{\hat{u}\cdot\hat{n}}^2\right) \tag{4.16}$$

which is approximately a Gaussian distribution, via expansion about the peak of the function, with standard deviation $(2m)^{-1/2}$.

A value of m can be decided by relating the standard deviation of the Gaussian to the angular range of $\theta_{\hat{u}\cdot\hat{n}}$ $\left(\theta_{\hat{u}\cdot\hat{n}} \in \left\{-(2m)^{-\frac{1}{2}}, (2m)^{-\frac{1}{2}}\right\}\right)$. The range of $\theta_{\hat{u}\cdot\hat{n}}$ can be coarsely estimated by considering that the spatial fluctuations of a lipid molecule are confined to a cylindrical shape, with a cross-sectional area given by the average molecular area of a lipid molecule, a_{ave}, with average radius, r_{ave}, and a length given as the average length of a typical bilayer leaf, l_{ave}. $\theta_{\hat{u}\cdot\hat{n}}^{max}$ is, then, taken to be the alignment angle, relative to the bilayer normal, made by the average orientation of an entire lipid chain within this cylindrical frame, and can be approximated as $\theta_{\hat{u}\cdot\hat{n}}^{max} = \tan^{-1}\left({}^{r_{ave}}/_{l_{ave}}\right)$. Comparison of this estimate to the Gaussian width, within one standard deviation, results in m ~ 14-19; we use m = 18 in our model [30]. The parameters $J_{i,j}$ represent the strength of the interaction between lipid species i and j. These lipid type-dependent interaction magnitudes

can be tuned for any combination of lipid species using available phase diagram data.

We can now write the dimensionless, orientation-dependent, local pairwise interaction energy between tail segments in terms of *Equations 4.14* and *4.15*; we include summations of these contributions over each pair-interaction between chains on lipids of type *i* and *j*, with configurations α and α', respectively, residing in the same bilayer leaflet ($\delta = \delta'$) or opposing leaflets ($\delta \neq \delta'$):

$$\beta\varepsilon_{attractive}^{orientation}(\alpha,\alpha') = \frac{A\beta}{2(4\pi)^2 v_{CH_2}} \sum_{i,j}\sum_{\delta,\delta'}\int\int\int \Psi_{i,\delta}(\alpha_{i,\delta}, z, \hat{u})\Psi_{j,\delta'}(\alpha'_{j,\delta'}, z, \hat{u}')V_{i,j,\delta,\delta'}(\hat{u}\cdot\hat{n}, \hat{u}'\cdot\hat{n})dzd\hat{u}d\hat{u}' \tag{4.17}$$

where the denominator corrects for the double-counting of the interaction and normalizes the value resulting from the integration over the full solid angle made by the orientation vectors. For convenience, we define the function:

$$\xi_{i,\omega,\delta}(\alpha_{i,\omega,\delta}, z) = \sum_{k=1}^{n_i-1} v_{i,\omega}(k)\delta\left(z - z_{k,\omega}(\alpha_{i,\omega,\delta})\right)f\left(\hat{u}_{k,\omega}(\alpha_{i,\omega,\delta})\cdot\hat{n}\right) \tag{4.18}$$

and calculate its average within the ensemble of configurations assumed by the single chain:

$$\begin{aligned}\left\langle \xi_{i,\omega,\delta}(z,\mathbf{c})\right\rangle &= \left\langle \sum_{k=1}^{n_i-1} v_{i,\omega}(k)\delta\left(z - z_{k,\omega}(\alpha_{i,\omega,\delta})\right)f\left(\hat{u}_{k,\omega}(\alpha_{i,\omega,\delta})\cdot\hat{n}\right)\right\rangle \\ &= \sum_{\alpha_{i,\omega,\delta}} P_{i,\omega,\delta}(\alpha_{i,\omega,\delta},\mathbf{c})\xi_{i,\omega,\delta}(\alpha_{i,\omega,\delta}, z)\end{aligned} \tag{4.19}$$

Taking the ensemble average of *Equation 4.17*, written in terms of the function formulated above, we obtain the functional form of the average, orientational

attractive interaction energy:

$$\frac{\beta\left\langle \varepsilon_{attractive}^{orientation}(\mathbf{c})\right\rangle}{N} = -\frac{\beta}{2a(0)v_{CH_2}}\sum_{\substack{i,j,\\ \delta,\delta'}} J_{i,j}x_i x_j x_{i,\delta}(\mathbf{c})x_{j,\delta'}(\mathbf{c})\sum_{\omega,\omega'}^{n_i^{tails},n_j^{tails}}\int\left\langle \xi_{i,\omega,\delta}(z,\mathbf{c})\right\rangle\left\langle \xi_{j,\omega',\delta'}(z,\mathbf{c})\right\rangle dz \tag{4.20}$$

where we have performed the integrals with respect to $\hat{u}$ and $\hat{u}'$ and the summations over the number of lipids, ℓ and ℓ', of a given species *i* and *j*, respectively. In performing these summations, $N_{i,\delta}$ and $N_{j,\delta'}$ are multiplied to the RHS of the expression; we divide by the total number of system molecules, *N*, to instead set the expression in terms of the lipid concentrations defined in *Equation 4.6*.

In summary, this is a cosine-based angle potential, where the local density of bonds contributed by a chain is weighted by its relative orientation to the bilayer normal; greater weight corresponds to chains taking a nematic-like orientation for efficient packing (preference of the chains to be parallel with respect to each other, and perpendicular to the bilayer normal, and thus highly aligned). This method successfully captures the liquid-crystalline to liquid-ordered or gel phase transitions that have been observed in GUVs.

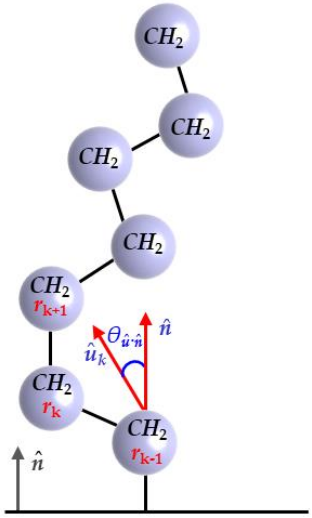

Figure 4.6) **Maier-Saupe attractive interactions modeled as a cosine-based angle potential.** Attractive interactions between hydrocarbon segments are based on a function of the cosine of the solid angle, $\theta_{\hat{u}\cdot\hat{n}}$, made between the orientation vector of a given segment, $\hat{u}_k$, and the bilayer normal, $\hat{n}$.

Opposing Forces of the Hydrophilic Lipid Headgroups

In this first generation of the theory, we treat the energetic contribution of the lipid headgroups, $\langle \varepsilon_{heads} \rangle$, phenomenologically in terms of the experimental value of the bare oil-water surface tension, $\gamma_0 = 0.12\ {}^{k_B T}/_{\text{Å}^2}$, and headgroup size:

$$\frac{\beta \langle \varepsilon_{heads} \rangle}{N} = \beta \gamma_0 a(0) \left(1 + \left(\frac{x_{PC} a_{PC} + x_{PE} a_{PE}}{a(0)} \right) \right) \tag{4.21}$$

The concept is borrowed from Tanford's opposing force model [149], which recognizes that the primary forces driving the self-assembly of amphiphiles, such as lipids, into various structures, including bilayers, stem from two contributions: (1) the immiscibility of the non-polar hydrocarbons with water, encouraging association of the hydrophobic molecules and a decrease in area per molecule, and

(2) the 'opposing force' of the hydrophilic headgroups that tend to increase the area per molecule due to steric repulsions. *Equation 4.21* couples the interfacial energy generated by the area of the aggregated lipid headgroups in contact with the surrounding aqueous solution, represented here by the bare surface tension, with a steric penalty (repulsion) for close packing. The term includes the contribution for both hydrophobic–hydrophilic interfaces of the bilayer. The magnitude of the excluded volume interactions depends on the size of the lipid headgroups included in the membrane and are weighted by their relative concentrations. Since we study bilayers that contain both PC and PE lipids in the *Generation I* model, the expression is written in terms of repulsive parameters for each, with units of area, which we take to be: $a_{PC} = 36.0\ \text{Å}^2/_{headgroup}$ and $a_{PE} = 30.0\ \text{Å}^2/_{headgroup}$, respectively.

<u>Molecular Translational Entropy of the Membrane Lipids</u>

The molecular translational entropy of the lipids in leaf δ is given by:

$$\frac{S_{trans,\delta}(\mathbf{c})}{N} = -k_B \sum_i x_i x_{i,\delta}(\mathbf{c}) \left(\ln\left[\frac{x_i x_{i,\delta}(\mathbf{c}) \lambda_i^2}{a(0)} \right] - 1 \right) \tag{4.22}$$

where λ_i is the thermal de Broglie wavelength of a lipid of species i. The translational entropy develops from the spatial distribution of the membrane components afforded by their lateral, translational degrees of freedom. This

contribution can be calculated exactly, as it depends solely on the kinetic internal energy of the molecules, which is determined by their momentums, independent of the positions or configurational states of the system.

4.4 Total Functional and Functional Minimization—Finding the Equilibrium Probability, Partition Function, and Helmholtz Free Energy

Together, *Equations 4.11*, *4.12*, and *4.20-4.22* construct the whole of our functional, which takes the form:

$$\begin{aligned}\frac{\beta\mathcal{F}}{N} = {} & \beta\sum_{i,\delta} x_i x_{i,\delta}(\mathbf{c})\sum_{\omega}^{n_i^{tails}}\sum_{\alpha_{i,\omega,\delta}} P_{i,\omega,\delta}(\alpha_{i,\omega,\delta},\mathbf{c})\varepsilon(\alpha_{i,\omega,\delta}) \\ & + \sum_{i,\delta} x_i x_{i,\delta}(\mathbf{c})\sum_{\omega}^{n_i^{tails}}\sum_{\alpha_{i,\omega,\delta}} P_{i,\omega,\delta}(\alpha_{i,\omega,\delta},\mathbf{c})\ln\left[P_{i,\omega,\delta}(\alpha_{i,\omega,\delta},\mathbf{c})\right] \\ & - \frac{\beta}{2a(0)v_{CH_2}}\sum_{i,j,\delta,\delta'} J_{i,j}x_i x_j x_{i,\delta}(\mathbf{c})x_{j,\delta'}(\mathbf{c})\sum_{\omega,\omega'}^{n_i^{tails},n_j^{tails}}\int_{-l}^{l}\left\langle\xi_{i,\omega,\delta}(z,\mathbf{c})\right\rangle\left\langle\xi_{j,\omega',\delta'}(z,\mathbf{c})\right\rangle dz \\ & + \beta\gamma_0 a(0)\left(1+\left(\frac{x_{PC}a_{PC}+x_{PE}a_{PE}}{a(0)}\right)\right) \\ & + \sum_{i,\delta} x_i x_{i,\delta}(\mathbf{c})\left(\ln\left[\frac{x_i x_{i,\delta}(\mathbf{c})\lambda_i^2}{a(0)}\right]-1\right) \\ & + \beta\sum_{i,\delta}\int_{-l}^{l}\pi(z,\mathbf{c})\left(x_i x_{i,\delta}(\mathbf{c})\sum_{\omega}^{n_i^{tails}}\left\langle\overline{v}_{i,\omega,\delta}(z,\mathbf{c})\right\rangle - a(z,\mathbf{c})\right)dz\end{aligned} \tag{4.23}$$

The last term is not inherently part of the functional but rather is imposed as the packing constraint introduced in *Section 3.3* and defined in *Section 4.1*, enforced by the Lagrange multipliers $\pi(z,\mathbf{c})$. The constraint represents the excluded volume (repulsive) interactions between the lipid monomers, while simultaneously acting

as a limit on excessive areal expansion of the membrane's constituents.

This functional is a manifestation of all possible probability distributions, including those that are exceedingly *improbable*, as discussed in Chapter 3 and *Sections 4.2* and *4.3*. From this functional, we may derive a single function (the free energy) that conveys the *equilibrium distribution*, which embodies the *most probable set* of configurational states with which to represent the nature of the system most aptly. Identification of the equilibrium probability distribution is achieved by means of *functional minimization*. Through this procedure, the contributions that influence the free energy are expressed by a set of coupled, self-consistent equations, providing the avenue through which we may interpret the non-trivial interplay between energetic and steric effects. Because our system in the *Generation I* model is built within the canonical ensemble (constant N, V, T), the equilibrium potential that arises by minimizing the functional is the equilibrium Helmholtz free energy.

While the system's total volume is a constrained quantity, the area is not. The stability of the membrane relies on a balance of the forces acting on it – the surface area is free to expand or contract, in accordance with the appropriate shortening or lengthening of the bilayer's width, to secure this balance. The system's internal forces include those regarding intermolecular chain packing and the interfacial tension (γ), much of which is accounted for via the incompressibility

constraint and the contributions of the lipid headgroups. The hydrophobic membrane core, though highly dense, is entirely fluid, owed to the high degree of flexibility of the lipid hydrocarbon tails. The lipid tails have a considerable number of thermally excited internal degrees of freedom; they prefer to exist in a highly disordered state and sample as many of the spatial distributions accessible to them as possible. Their conformational freedom is counteracted, however, by the aggregation of the lipids, such that the polar headgroups shield the hydrophobic tails from exposure to water, known as the *hydrophobic effect*. Thus, there is a competition between these forces – the steric repulsions of the lipid particles, causing expansion of the molecular area, and the interfacial tension forces acting at the hydrocarbon-water interface, which induces areal compression. The optimal areal density is attained by the modulation of the surface area to achieve membrane stability. In other words, a balance in the system's internal forces is realized at the minimum in the free energy with respect to the total area, which equates to a net surface tension of zero:

$$\left(\frac{\partial F}{\partial A}\right)_{T,V,N_i} = \gamma = 0 \tag{4.24}$$

Hence, the thermodynamic potential we derive from our functional in *Equation 4.23* is a *tensionless* Helmholtz free energy, ensuring thermodynamic equilibrium.

Before continuing with the derivation of our equilibrium thermodynamic

potential, we should consider the three equilibrium constraints that must be satisfied for *thermodynamic equilibrium*. These are, that the system must be in *thermal* equilibrium, *mechanical* equilibrium, and *chemical* equilibrium. Thermal equilibrium exists when there are no temperature differences within the system, nor between system and surroundings. We maintain constant temperature throughout system and environment in our model. Mechanical equilibrium is obtained when there is an absence of unbalanced forces acting on any part of the system, or on the system as a whole. Constraining the system at zero surface tension, as we have just discussed, balances the internal forces and, as no external forces are applied, we ensure mechanical equilibrium in our model. Chemical equilibrium is achieved when there are no chemical reactions that alter concentrations of system components, as is true for our model, and when there is no directional movement of particles from one part of the system to the other. Regarding this last point, subsequent sections in this chapter – on the topics of membrane elasticity and chemical potential – will discuss, in detail, the non-random, gradient-driven movement of lipids within the bilayer. This phenomenon is essential in analyses of curvature modulations within our model bilayers – one which prompts the examination of systems under *non-chemical equilibrium* conditions. For now, it is enough to say that via functional minimization, we obtain the thermodynamic potential for a system that satisfies

all equilibrium constraints and thus characterizes a system at thermodynamic equilibrium. For simplicity, we will use 'equilibrium' to generally appertain to 'thermodynamic equilibrium'.

Extremizing the functional with respect to the probability of the lipid chains assuming a particular configuration allows us to derive the equilibrium probability distribution function, used to obtain the function for the potential that describes the equilibrium state of the system. This procedure completes the set of equations needed to solve for the system's unknowns, namely $P_{i,\omega,\delta}(\alpha_{i,\omega,\delta},\mathbf{c})$, $\pi(z,\mathbf{c})$, and $\xi_{i,\omega,\delta}(\alpha_{i,\omega,\delta},z)$:

$$\begin{aligned}\frac{\partial\left(\beta\mathcal{F}/N\right)}{\partial\left(P_{i,\omega,\delta}(\alpha_{i,\omega,\delta},\mathbf{c})\right)} = 0 = {} & \beta x_i x_{i,\delta}(\mathbf{c})\varepsilon(\alpha_{i,\omega,\delta}) + x_i x_{i,\delta}(\mathbf{c})\left(\ln\left[P_{i,\omega,\delta}(\alpha_{i,\omega,\delta},\mathbf{c})\right]+1\right) \\ & -\frac{\beta}{a(0)v_{CH_2}}\sum_j J_{i,j}x_i x_j x_{i,\delta}(\mathbf{c})\sum_{\omega',\delta'}\int_{-l}^{l} x_{j,\delta'}(\mathbf{c})\left\langle\xi_{j,\omega',\delta'}(z,\mathbf{c})\right\rangle\xi_{i,\omega,\delta}(\alpha_{i,\omega,\delta},z)dz \\ & +\beta\int_{-l}^{l}\pi(z,\mathbf{c})x_i x_{i,\delta}(\mathbf{c})\overline{v}_{i,\omega,\delta}(\alpha_{i,\omega,\delta},z,\mathbf{c})dz\end{aligned} \tag{4.25}$$

From this, we solve for the equilibrium probability:

$$P_{i,\omega,\delta}(\alpha_{i,\omega,\delta},\mathbf{c}) = \exp\left[\begin{array}{l} -\beta\varepsilon(\alpha_{i,\omega,\delta}) \\ +\dfrac{\beta}{a(0)v_{CH_2}}\displaystyle\sum_j J_{i,j}x_j\sum_{\omega',\delta'}\int_{-l}^{l}x_{j,\delta'}(\mathbf{c})\left\langle\xi_{j,\omega',\delta'}(z,\mathbf{c})\right\rangle\xi_{i,\omega,\delta}(\alpha_{i,\omega,\delta},z)dz \\ -\beta\displaystyle\int_{-l}^{l}\pi(z,\mathbf{c})\overline{v}_{i,\omega,\delta}(\alpha_{i,\omega,\delta},z,\mathbf{c})dz - 1\end{array}\right] \tag{4.26}$$

The probability function must be constrained such that $\sum_{\alpha_{i,\omega,\delta}} P_{i,\omega,\delta}\left(\alpha_{i,\omega,\delta},\,\mathbf{c}\right) = 1$. To

impose the constraint, we introduce a normalization factor, which is the single-chain partition function, $q_{i,\omega,\delta}(\mathbf{c})$. Thus, the functional (normalized) form of the chain probability is:

$$P_{i,\omega,\delta}(\alpha_{i,\omega,\delta},\mathbf{c}) = \frac{\exp\left[\begin{array}{l} -\beta\varepsilon(\alpha_{i,\omega,\delta}) \\ +\dfrac{\beta}{a(0)v_{CH_2}}\sum_j J_{i,j}x_j \sum_{\omega',\delta'}\int_{-l}^{l} x_{j,\delta'}(\mathbf{c})\left\langle \xi_{j,\omega',\delta'}(z,\mathbf{c})\right\rangle \xi_{i,\omega,\delta}(\alpha_{i,\omega,\delta},z)dz \\ -\beta\int_{-l}^{l}\pi(z,\mathbf{c})\overline{v}_{i,\omega,\delta}(\alpha_{i,\omega,\delta},z,\mathbf{c})dz \end{array}\right]}{q_{i,\omega,\delta}(\mathbf{c})} \tag{4.27}$$

and the partition function is given by the sum:

$$q_{i,\omega,\delta}(\mathbf{c}) = \sum_{\alpha_{i,\omega,\delta}} \exp\left[\begin{array}{l} -\beta\varepsilon(\alpha_{i,\omega,\delta}) \\ +\dfrac{\beta}{a(0)v_{CH_2}}\sum_j J_{i,j}x_j \sum_{\omega',\delta'}\int_{-l}^{l} x_{j,\delta'}(\mathbf{c})\left\langle \xi_{j,\omega',\delta'}(z,\mathbf{c})\right\rangle \xi_{i,\omega,\delta}(\alpha_{i,\omega,\delta},z)dz \\ -\beta\int_{-l}^{l}\pi(z,\mathbf{c})\overline{v}_{i,\omega,\delta}(\alpha_{i,\omega,\delta},z,\mathbf{c})dz \end{array}\right] \tag{4.28}$$

We discussed in *Section 3.2* the construction of the theory in terms of a single, isolated chain, which experiences the effects of chain-chain contact interactions with proximal chains/molecules through effective fields representing the influence of neighboring molecules, rather than directly. One of these effective interaction fields, $\pi(z,\mathbf{c})$, arises from the incorporation of the incompressibility constraint. The high density of many molecules within a confined system, such as a biological membrane, serves as the basis for incompressibility in our model; by

enforcing the constraint, $\pi(z,\mathbf{c})$ manifests as the effective field representing the close-contact repulsions between these molecules. Another form of chain-chain contact in the system results from the attractive interactions among molecules, which serve to increase local molecular density and locally order the chains in the bilayer. In the context of a single-particle system, these interactions manifest through the ensemble-averaged, nematic-ordering functions $\langle \xi_{i,\omega,\delta}(z,\mathbf{c})\rangle$. To simplify the expressions for the equilibrium probability and partition function, we define the functions, $b_{i,\omega}(z,\mathbf{c})$, in terms of $\langle \xi_{i,\omega,\delta}(z,\mathbf{c})\rangle$ and corresponding magnitude, $J_{i,j}$, to represent the ordering fields acting on our single chain:

$$\beta b_{i,\omega}(z,\mathbf{c}) = -\frac{\beta}{a(0)v_{CH_2}} \sum_{j,\omega',\delta'} J_{i,j} x_j x_{j,\delta'}(\mathbf{c}) \left\langle \xi_{j.\omega',\delta'}(z,\mathbf{c}) \right\rangle \tag{4.29}$$

Substituting these field-variables into the probability and partition function (*Equations 4.27* and *4.28*, respectively), we have:

$$P_{i,\omega,\delta}(\alpha_{i,\omega,\delta},\mathbf{c}) = \frac{\exp\left[-\beta\varepsilon(\alpha_{i,\omega,\delta}) - \beta\int_{-l}^{l} b_{i,\omega}(z,\mathbf{c})\xi_{i,\omega,\delta}(\alpha_{i,\omega,\delta},z)dz - \beta\int_{-l}^{l} \pi(z,\mathbf{c})\overline{v}_{i,\omega,\delta}(\alpha_{i,\omega,\delta},z,\mathbf{c})dz \right]}{q_{i,\omega,\delta}(\mathbf{c})} \tag{4.30}$$

and

$$q_{i,\omega,\delta}(\mathbf{c}) = \sum_{\alpha_{i,\omega,\delta}} \exp\left[-\beta\varepsilon(\alpha_{i,\omega,\delta}) - \beta\int_{-l}^{l} b_{i,\omega}(z,\mathbf{c})\xi_{i,\omega,\delta}(\alpha_{i,\omega,\delta},z)dz - \beta\int_{-l}^{l} \pi(z,\mathbf{c})\overline{v}_{i,\omega,\delta}(\alpha_{i,\omega,\delta},z,\mathbf{c})dz \right] \tag{4.31}$$

The mean-fields, $b_{i,\omega}(z,\mathbf{c})$, encompass the average attractive interaction

exchanged between a chain, ω, on molecule of type i, at location z, and all other molecules in the system by acting on the orientation of the given chain with respect to the bilayer normal. Together, the incompressibility constraint and *Equation 4.29* (which comprises separate equations for each pair-interaction between chains of the same species and between chains of different species) provide a set of integrodifferential equations, which are converted into a set of coupled, nonlinear, self-consistent equations, solved numerically by discretization of space to obtain the solutions to the probability distribution function for each lipid species and the field variables, $\pi(z,\mathbf{c})$ and $b_{i,\omega}(z,\mathbf{c})$. Solving for these unknows grants access to the equilibrium lateral pressure distributions, energy profiles, and all structural and thermodynamic properties of interest.

Using the above equations, we can now construct the thermodynamically relevant, minimized Helmholtz free energy for a tensionless bilayer, *at thermodynamic equilibrium*, which on a per-molecule basis takes the form:

$$\begin{aligned}\beta f = &-\sum_{i,\delta} x_i x_{i,\delta}(\mathbf{c}) \sum_{\omega}^{n_i^{tails}} \ln\left[q_{i,\omega,\delta}(\mathbf{c})\right] \\ &+ \frac{\beta}{2a(0)v_{CH_2}} \sum_{i,j}\sum_{\delta,\delta'} J_{i,j} x_i x_j x_{i,\delta}(\mathbf{c}) x_{j,\delta'}(\mathbf{c}) \sum_{\omega,\omega'}^{n_i^{tails},n_j^{tails}} \int_{-l}^{l} \left\langle \xi_{i,\omega,\delta}(z,\mathbf{c}) \right\rangle \left\langle \xi_{j,\omega',\delta'}(z,\mathbf{c}) \right\rangle dz \\ &+ \beta\gamma_0 a(0)\left(1 + \left(\frac{x_{PC}a_{PC} + x_{PE}a_{PE}}{a(0)}\right)^2\right) + \sum_{i,\delta} x_i x_{i,\delta}(\mathbf{c}) \ln\left[\frac{x_i x_{i,\delta}(\mathbf{c})\lambda_i^2}{a(0)e}\right] \\ &- \beta\int \pi(z,\mathbf{c}) a(z,\mathbf{c}) dz\end{aligned} \tag{4.32}$$

or, in terms of the orientation field variable, $b_{i,\omega}(z,\mathbf{c})$:

$$\begin{aligned}\beta f = &-\sum_{i,\delta} x_i x_{i,\delta}(\mathbf{c}) \sum_{\omega}^{n_i^{tails}} \ln\left[q_{i,\omega,\delta}(\mathbf{c})\right] \\ &- \beta \sum_{i,\delta} \frac{x_i x_{i,\delta}(\mathbf{c})}{2} \sum_{\omega}^{n_i^{tails}} \int_{-l}^{l} b_{i,\omega}(z,\mathbf{c}) \left\langle \xi_{i,\omega,\delta}(z,\mathbf{c}) \right\rangle dz \\ &+ \beta\gamma_0 a(0) \left(1 + \left(\frac{x_{PC} a_{PC} + x_{PE} a_{PE}}{a(0)} \right)^2 \right) + \sum_{i,\delta} x_i x_{i,\delta}(\mathbf{c}) \ln\left[\frac{x_i x_{i,\delta}(\mathbf{c}) \lambda_i^2}{a(0) e} \right] \\ &- \beta \int \pi(z,\mathbf{c}) a(z,\mathbf{c}) dz\end{aligned} \tag{4.33}$$

<u>Membrane Surface Tension and Lateral Pressure</u>

As we discussed, this thermodynamic potential describes a membrane that maintains stability by optimizing the areal density of its lipid constituents via the hydrophobic effect, resulting in a net zero surface tension in the bilayer. Now that we have found the functional form of the equilibrium free energy, we can expand on *Equation 4.24* by writing the expression for the surface tension as the partial derivative of *Equation 4.32* or *4.33* with respect to the molecular area, holding all other canonical thermodynamic variables constant:

$$\left(\frac{\partial F}{\partial A} \right)_{T,V,N_i} = \left(\frac{\partial f}{\partial a} \right)_{T,V,N_i} = \gamma(T, A, V, N, \mathbf{c}) = 0 \tag{4.24}$$

$$\begin{aligned}\beta\gamma(\mathbf{c}) = &-\frac{\beta}{2a(0)^2 v_{CH_2}} \sum_{i,j,\delta,\delta'} J_{i,j} x_i x_j x_{i,\delta}(\mathbf{c}) x_{j,\delta'}(\mathbf{c}) \sum_{\omega,\omega'}^{n_i^{tails}, n_j^{tails}} \int_{-l}^{l} \left\langle \xi_{i,\omega,\delta}(z,\mathbf{c}) \right\rangle \left\langle \xi_{j,\omega',\delta'}(z,\mathbf{c}) \right\rangle dz \\ &+ \beta\gamma_0 \left(1 - \left(\frac{x_{PC} a_{PC} + x_{PE} a_{PE}}{a(0)} \right)^2 \right) - \frac{1}{a(0)} - \beta \int_{-l}^{l} \pi(z,\mathbf{c}) dz\end{aligned} \tag{4.34}$$

or

$$\beta\gamma(\mathbf{c}) = \frac{\beta}{2a(0)}\sum_{i,\delta} x_i x_{i,\delta}(\mathbf{c}) \sum_{\omega}^{n_i^{tails}} \int_{-l}^{l} b_{i,\omega}(z,\mathbf{c}) \left\langle \xi_{i,\omega,\delta}(z,\mathbf{c}) \right\rangle dz + \beta\gamma_0 \left(1 - \left(\frac{x_{PC} a_{PC} + x_{PE} a_{PE}}{a(0)} \right)^2 \right) - \frac{1}{a(0)} - \beta \int_{-l}^{l} \pi(z,\mathbf{c}) dz \tag{4.35}$$

The expression obtained for the surface tension provides the means to calculate an important property in membrane physics: the lateral pressure distribution through the membrane's width. The lateral pressure profile relays how the lateral stresses across the membrane core are distributed. These stresses include repulsive components, generated by the steric interactions between the tightly packed lipid molecules, and attractive components bringing about lipid cohesion, which segregates the hydrophobic molecules from the aqueous environment. These components are distributed inhomogeneously across the bilayer. Because the non-uniform lateral pressure profile reflects the internal structure of the membrane, it affects membrane interactions with membrane-inserting macromolecules in the environment and the conformation and stability of membrane-embedded proteins.

The lateral pressure, $\Pi(z,\mathbf{c})$, is a second-order tensor defined as the difference between its transverse, $P_T(z,\mathbf{c})$, and normal, $P_N(z,\mathbf{c})$, components [160-162]:

$$\Pi(z,\mathbf{c}) = P_T(z,\mathbf{c}) - P_N(z,\mathbf{c}) \tag{4.36}$$

which can be expressed in terms of the surface tension, for any geometry, by the

definition [163]:

$$\gamma(\mathbf{c}) = -\int_{-\infty}^{\infty} \left(P_T(z,\mathbf{c}) - P_N(z,\mathbf{c}) \right) dz = -\int_{-\infty}^{\infty} \Pi(z,\mathbf{c}) dz \tag{4.37}$$

To interpret *Equation 4.37* in the context of our *Generation I* model membrane system using the surface tension expression derived from our theory *(Equation 4.35)*, the limits of the integral, ranging from $-\infty$ to $+\infty$, must be partitioned to explicitly distinguish the domain that encompasses the hydrophobic core region of the bilayer (from $-l$ to l). We accomplish this by dividing the integral into three domains. The domain with boundaries of $-\infty$ and $-l$ represents the aqueous phase of the interior of the cell, or liposome, as well as the headgroups of the lipids lining the inner leaflet. The hydrophobic tail region of the membrane, our domain of interest, is bound by $-l$ at the tail-headgroup interface of the inner leaflet and by l at the tail-headgroup interface of the outer leaflet. Lastly, the boundaries which contain the lipid headgroups of the outer leaf and the extracellular aqueous environment range from l to $+\infty$. Combining *Equations 4.35* and *4.37*, the lateral pressure profile can then be written as:

$$\beta \int_{-\infty}^{-l} \Pi^{\text{aqueous}}_{\text{interior}}(z,\mathbf{c}) dz + \beta \int_{-l}^{l} \Pi^{\text{hydrophobic}}_{\text{tail region}}(z,\mathbf{c}) dz + \beta \int_{l}^{\infty} \Pi^{\text{aqueous}}_{\text{exterior}}(z,\mathbf{c}) dz = \tag{4.38}$$

$$\beta \int_{-l}^{l} \pi(z,\mathbf{c}) dz - \frac{\beta}{2a(0)} \sum_{i,\omega,\delta} x_i x_{i,\delta}(\mathbf{c}) \int_{-l}^{l} b_{i,\omega}(z,\mathbf{c}) \left\langle \xi_{i,\omega,\delta}(z,\mathbf{c}) \right\rangle dz - \beta\gamma_0 \left(1 - \left(\frac{x_{PC} a_{PC} + x_{PE} a_{PE}}{a(0)} \right)^2 \right) + \frac{1}{a(0)}$$

In our theory, the sum of the integrals ranging over the internal and external

aqueous domains of the lateral pressure (the first and last terms on the LHS of the above equation) are taken to be equivalent to the sum of the contributions to the surface tension from the lipid headgroups and translational free energy of the lipids (the last two terms on the RHS of the above equation).[3] The integral of the lateral pressure over the membrane's hydrophobic region (center term on the LHS) is then equal to the contributions from the incompressibility constraint and the orientational ordering potential. As explained in *Section 3.3*, the nematic ordering of chains accomplished by $\langle \varepsilon_{attractive}^{orientation}(\mathbf{c}) \rangle$ is only required in analyses of the condensed liquid-ordered or gel phases; here, we consider systems all well within the liquid-disordered state, in which the orientational attractive energy is unnecessary.[4] Finally, this leaves us with an important relationship between the

[3] In the *Generation I* version of our theory, emphasis is placed on the influence of the membrane's hydrophobic core to membrane thermodynamics and interactions with environmental macromolecules; thus, the lipid headgroups are treated only on a phenomenological level and can be considered as outside our system of focus. Therefore, the headgroup regions are reasonably absorbed into the 'aqueous domains' of the lateral pressure. The contribution from the translational entropy of the bilayer lipids is not as straightforward. Technically, we should incorporate this contribution in the expression for the lateral pressure in the membrane's hydrophobic domain. However, we model the translational entropy of the lipid as a whole and do not delineate its distribution as a function of depth into the bilayer. Hence, we can only include its contribution to the lateral pressure as an added constant. As this does not necessarily enhance the physics or detail of the system, it is not included in our analysis of the lateral pressure within the hydrophobic core.

[4] Note that, while the Maier-Saupe orientational ordering terms play a principal role in regulating the structural properties of the bilayer that distinguish between ordered and disordered phase states, and are thus necessary for the modeling of liquid-ordered or gel phase membranes, we find they have negligible contribution to the distribution of lateral pressure through the bilayer in our systems. These attractive field potentials have also been shown to have insignificant effect on the lateral pressure, even in liquid-ordered systems [164]. Therefore, in our *Generation I* model of an

lateral pressure profile through the width of the bilayer and the Lagrange multipliers, $\pi(z,\mathbf{c})$, governing the packing conditions through the membrane's core:

$$\beta\int_{-\infty}^{-l}\Pi^{\substack{\text{aqueous}\\\text{interior}}}(z,\mathbf{c})dz+\beta\int_{l}^{\infty}\Pi^{\substack{\text{aqueous}\\\text{exterior}}}(z,\mathbf{c})dz=\frac{1}{a(0)}-\beta\gamma_0\left(1-\left(\frac{x_{PC}a_{PC}+x_{PE}a_{PE}}{a(0)}\right)^2\right) \quad (4.39)$$

$$\begin{aligned}\beta\int_{-l}^{l}\Pi^{\substack{\text{hydrophobic}\\\text{tail region}}}(z,\mathbf{c})dz &= \beta\int_{-l}^{l}\pi(z,\mathbf{c})dz-\frac{\beta}{2a(0)}\sum_{i,\omega,\delta}x_i x_{i,\delta}(\mathbf{c})\int_{-l}^{l}b_{i,\omega}(z,\mathbf{c})\left\langle\xi_{i,\omega,\delta}(z,\mathbf{c})\right\rangle dz\\ &\approx \beta\int_{-l}^{l}\pi(z,\mathbf{c})dz\end{aligned} \quad (4.40)$$

The physical manifestation of the mean-field that enforces the incompressibility constraint as the lateral pressure within the membrane's hydrophobic channel now becomes clear. Because the lateral pressure profiles calculated by the *Generation I* molecular theory are zeroed at the bilayer midplane (where $z = 0$), we can refer to $\pi(z,\mathbf{c})$ as representing the *relative* lateral pressure as a function of distance (along the z-direction) from the midplane. This aids in the comparison of distributions in many types of lipid bilayers. The influence of the lateral pressure profiles in membranes of different lipid compositions comes to the forefront in our examination of the membrane-adsorption tendencies of lipidated proteins, which will be discussed in detail in our second results section of the *Generation I* study, *Results I.II* in *Section 5.3*.

---

isolated bilayer, the lateral pressure can justifiably be equated to the repulsive contribution of the term, given by $\pi(z,\mathbf{c})$.

Figure 4.7 demonstrates an example of the unnormalized lateral pressure profile within the hydrocarbon region of a planar POPC bilayer calculated by our *Generation I* theory *(solid black line)*, as well as a projection of how the profile would qualitatively appear if we were to extend our system boundaries to encompass the lipid headgroups and surrounding bulk solution *(grey dashed line)*, as we do explicitly in *Generation II*.

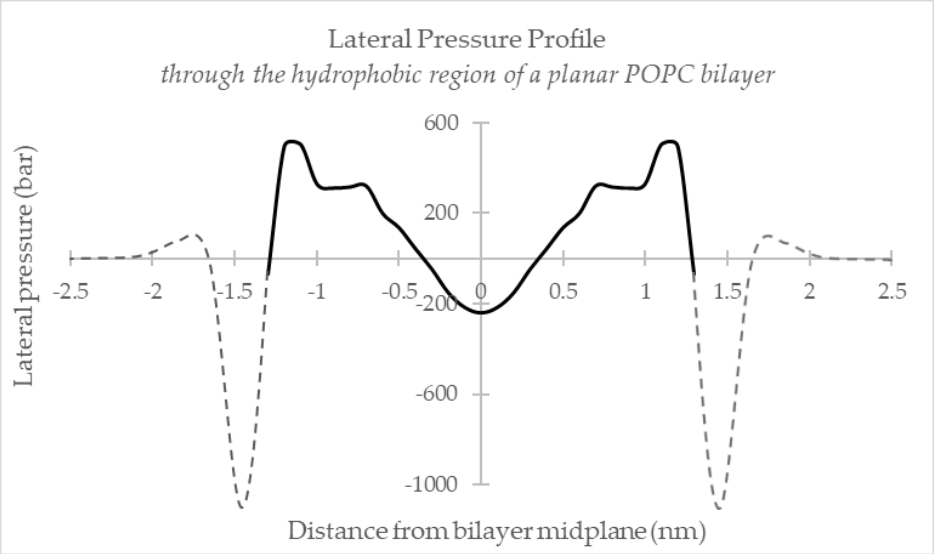

Figure 4.7) **Lateral pressure distribution of a planar POPC bilayer.** The lateral pressure profile calculated by the *Generation I* theory is confined to the hydrophobic region of the membrane *(black solid line)*. The profile demonstrates characteristic positive values within most of the hydrocarbon domain. A hypothetical projection of the full profile, which includes the lipid headgroups, is demonstrated by the dashed, grey lines.

Integrated over the entire system, the entropically-driven positive values of the lateral pressure, through most of the membrane's hydrophobic core, and the negative compression pressures centralized at the midplane (and the polar region in the projection of the extended model) balance one another to yield a net value

of zero – this is enforced by the requirement of a zero net surface tension, implemented in each of our bilayers to ensure mechanical stability in the membrane.

It is prudent to note the similarities and differences that would be observed from a comparison of lateral pressure distributions as calculated by our molecular theory and those determined by simulation and other recent theoretical approaches. One characteristic of the lateral pressure profiles depicted in more recent works [160-162, 165-168], but not in earlier models (earlier than ~2000) [126, 169-173] is a positive peak in the hydrophobic region centered about the bilayer midplane, the origin of which is still under debate [174]. Our model does not produce this central peak. The discrepancy is caused by slight alteration in the terms that are included in the calculation of the lateral pressure. As shown in the progression from *Equation 4.38* to *Equations 4.39* and *4.40*, our theory decouples the translational entropy contribution of the lipids (and, in *Generation I*, the influence of the lipid headgroups) from the lateral pressure within the lipid tail domain. This is because, in our theory, the translational and headgroup terms are constants that do not offer obvious insight as to the distribution of their values through the bilayer. Due to the net repulsive nature of these terms, they would lend a positive increase to the magnitude of the lateral pressure through the hydrophobic channel, possibly centralized about the midplane, were they accounted for in our

calculation.

The remaining steric contribution of the densely packed hydrocarbon tails is sufficient for our theory to calculate the lateral pressures within the membrane channel that reproduce the principal characteristic of a slightly oscillating, primarily positive distribution observed in simulation studies. Since our theory successfully delivers protein adsorption isotherms as functions of membrane curvature that are in excellent agreement with experimental observations (Chapter 5), which is our primary focus, the influence of the neglected terms is not deemed crucial.

There are three other characteristic features of lateral pressure profiles in lipid bilayer systems, as determined by simulation, that emerge from the direct impact of the hydrophobic–hydrophilic interfacial region and the headgroup domain extending into the aqueous medium. These are, (1) the precipitous decent to highly negative values localized at the interfacial planes due to the surface tension's effect of minimizing molecular area, serving to restrict exposure of the fatty acid tails to their aqueous surroundings, (2) the recovery of positive lateral pressure in the vicinity of the lipid headgroups, caused by their repulsive steric and electrostatic interactions and hydration, and (3) the attenuation of lateral pressure to values of zero in the bulk aqueous surroundings. As we focus our attentions on the bilayer's hydrophobic core in the *Generation I* theory, these

features are not exhibited in the *Generation I* lateral pressure profiles. However, these regimes are fully recapitulated in the lateral pressure profiles calculated using our *Generation II* model, which incorporates the full width of the membrane, explicitly accounting for the electrostatic interactions, hydrophobicity, and volume of the lipid headgroups, as well as an aqueous environment, into the system. The thermodynamics of our membrane systems are fully accounted for within the approximations used in the theory; hence, the theory would yield identical results to those given by simulation, from a thermodynamic perspective, should the same discretization size, correlations, and environmental and system conditions be applied.

The molecular theory is a powerful tool for discovering the responses that perturbations in system parameters provoke in a lipid membrane, and the mechanisms that drive them. Molecular theoretical models are uniquely efficacious to this end because of the ability to methodically tweak any single or combination of variables to an exact degree, with the assurance of timely results. Using our equilibrium Helmholtz free energy from *Equation 4.32/4.33*, we may calculate various desired thermodynamic distributions and quantities as functions of temperature, depth into the bilayer, chain length, degree of saturation, placement of double bond(s) in unsaturated lipid chains, composition, and any other environmental or system property of interest. One such property quite

relevant to biological membrane functionality is its geometry. We examine how the local curvature of a bilayer affects its internal structure and how it engages with the environment, beginning with the curvature theory introduced in the following section.

4.5 Curvature Theory and Membrane Elasticity

Detailed knowledge of a membrane's elastic properties is necessary for understanding membrane shapes and the morphological transformations a membrane undergoes during many important biological processes. Some obvious examples of these processes are endo- and exo-cytosis, cell division, the large morphological changes of the Golgi apparatus and endoplasmic reticulum, and autophagy. Earlier, we briefly discussed membrane curvature and the highly elastic nature of biological membranes. We introduced the parameters that govern these characteristics, namely, the principal curvatures, $C_1 = 1/R_1$ and $C_2 = 1/R_2$, and the elastic constants, $\bar{\kappa}$ and κ_c. We will now elaborate on these concepts and explain how we mathematically integrate them into our model.

For a brief introduction to the curvature theory from differential geometry that we apply to our analyses of curved lipid membranes, let us consider a curved surface, *S*, in three-dimensional space, such as shown in *Figure 4.8 a*, that can be described by a smooth function $z = f(x,y)$, and we wish to analyze the curvature at

a point, P, on this surface. We identify $\hat{n}$ as the unit normal vector to S, at point P; let us choose P to be the point at which the normal vector is oriented in the same direction as the z-axis. We can study the curvature of S by dividing the surface by planes containing $\hat{n}$ and P, as is done in *Figure 4.8 b*; these are called *normal planes*. The normal planes depicted in *Figure 4.8 b* can be rotated about the normal vector, to create any number of normal planes, as is shown in *Figure 4.8 c*. The resulting curves projected onto the surface, S, by a normal plane are the curves used to measure the *normal curvatures* on S at P; let us identify these as *normal curves* in *Figure 4.8 c*. Rotating our normal plane about the unit normal vector at P will yield one such plane orientation that results in the *maximum normal curvature* of S at P, and one that results in the *minimum normal curvature* – we illustrate the curves on S from which we can measure the maximum and minimum curvatures, denoted the *maximum* and *minimum normal curves*, respectively, in *Figure 4.8 d*. The radii of the *osculating circles* passing through P and along the normal curves are the *radii of curvature* (and their reciprocals are the corresponding *curvatures*) on S at P – those along the maximum and minimum normal curves are the *principal radii of curvature*, R_1 and R_2, and their reciprocals are the *principal curvatures*, C_1 and C_2, respectively, as shown in *Figures 4.8 e* and *f*. The unit vectors perpendicular to our normal vector at P (in the tangent plane) and in the planes along which we find the maximum and minimum curvatures are designated the *principal directions*,

which are orthonormal.

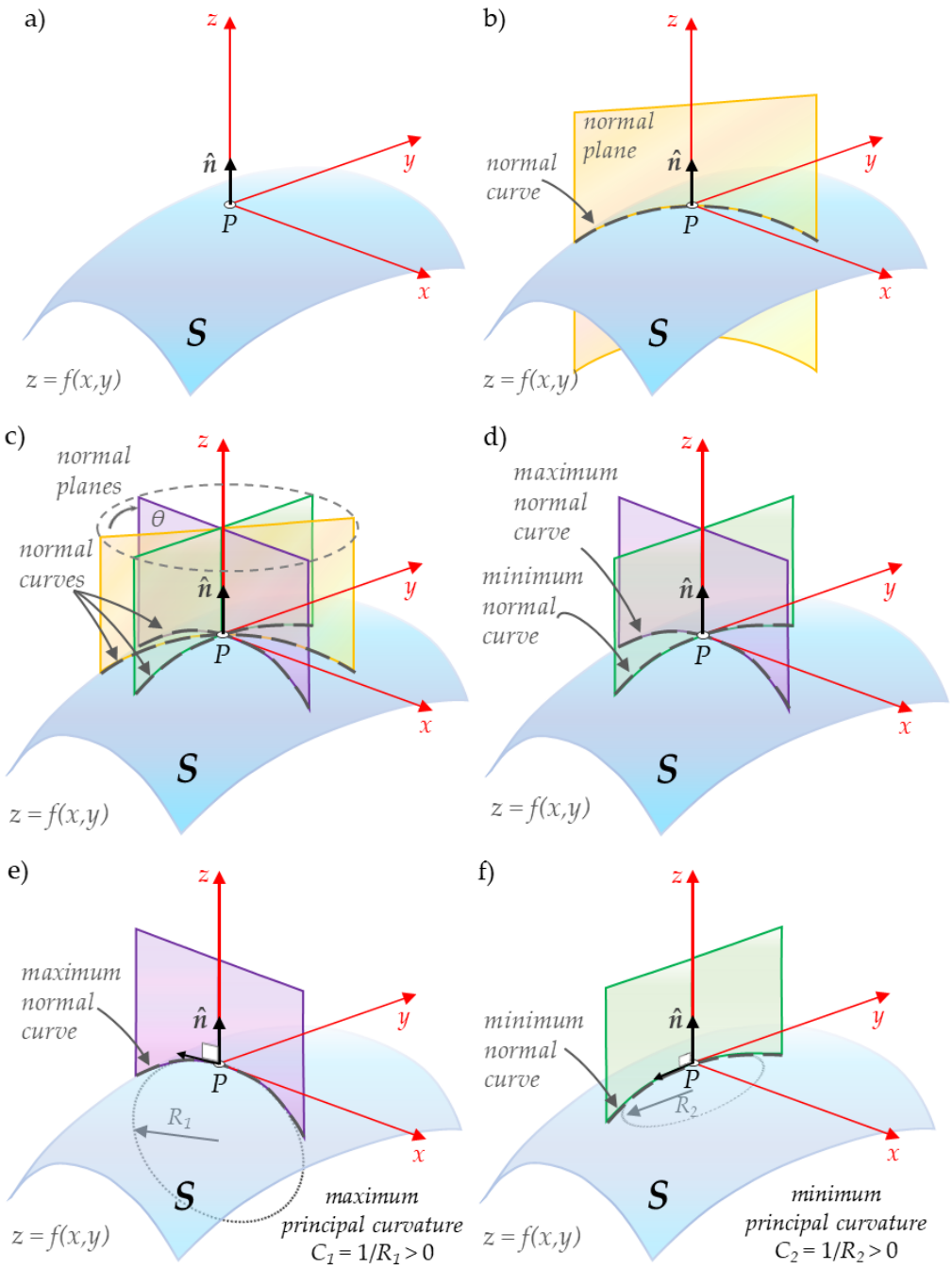

Figure 4.8) **Curvature theory from differential geometry: illustration of curvature conventions.** These schematics illustrate concepts from curvature theory, including normal planes, normal curves, the maximum and minimum normal curves, and the maximum and minimum principal curvatures. *See text for details on* ***(a)-(f)****.*

The principal curvatures and radii of curvature are taken to be positive if the curve is convex with respect to the chosen normal vector on the surface at P, and negative if the curve is concave with respect to the normal vector. For our illustrations in *Figure 4.8*, both principal curvatures are positive. *Figure 4.9* offers examples of the curvature sign convention applied to different types surfaces.

To obtain the values of these principal curvatures, let us again consider our function, $z = f(x,y)$, that describes our surface, S. We can perform a series expansion on z about our chosen point, P:

$$\begin{aligned} z = f(x_0, y_0) + \cancelto{0}{\left.\frac{\partial f}{\partial x}\right|_{x_0,y_0}}(x - x_0) + \cancelto{0}{\left.\frac{\partial f}{\partial y}\right|_{x_0,y_0}}(y - y_0) \\ + \left.\frac{\partial^2 f}{\partial x^2}\right|_{x_0,y_0} \frac{(x - x_0)^2}{2} + \left.\frac{\partial^2 f}{\partial y^2}\right|_{x_0,y_0} \frac{(y - y_0)^2}{2} \\ + \left.\frac{\partial^2 f}{\partial x \partial y}\right|_{x_0,y_0} \frac{(x - x_0)(y - y_0)}{2} + \left.\frac{\partial^2 f}{\partial y \partial x}\right|_{x_0,y_0} \frac{(x - x_0)(y - y_0)}{2} + \ldots \end{aligned} \tag{4.41}$$

where x_0 and y_0 are the values in the x- and y-directions, respectively, at our point P, and because our unit normal vector at P is parallel to the z-axis, the tangent plane at P is perpendicular to the z-axis and the first derivatives of our function with respect to x and y are zero. Let us refer to $f(x_0,y_0)$ as z_0 and rename our second derivatives $C_{i,j}$, as follows:

$$z = z_0 + C_{11}\frac{(x - x_0)^2}{2} + C_{22}\frac{(y - y_0)^2}{2} + C_{12}\frac{(x - x_0)(y - y_0)}{2} + C_{21}\frac{(x - x_0)(y - y_0)}{2} \tag{4.42}$$

Note that the second derivatives, $C_{i,j}$, of z with respect to x and y describe the

concavity of our surface, and thus give us information about the curvature of S. Indeed, $C_{i,j}$ are the components of a 2×2 real, symmetric curvature tensor, **c** (also referred to as the shape operator):

$$\mathbf{c} = -\begin{bmatrix} C_{11} & C_{12} \\ C_{21} & C_{22} \end{bmatrix} \tag{4.43}$$

The eigenvalues of this matrix are the principal curvatures, C_1 and C_2, that we described conceptually above, and the eigenvectors are the principal directions. There are two scalar invariants of the curvature tensor that fully characterize the curvature of a two-dimensional surface at P and cast the values of C_1 and C_2 into physical formations. These are the trace, Tr(**c**), and the determinant, det(**c**) of the tensor, defined as follows:

$$\mathrm{Tr}(\mathbf{c}) = C_1 + C_2 = \frac{1}{R_1} + \frac{1}{R_2} = 2H \quad \text{and} \quad \det(\mathbf{c}) = C_1 C_2 = \frac{1}{R_1 R_2} = K_G \tag{4.44}$$

The sum (C_1 + C_2) is often referred to as the extrinsic curvature, though a more specific measure of extrinsic curvature is the mean curvature, H, and the product (C_1C_2) is known as the Gaussian curvature, K_G.

$$\text{Extrinsic curvature} \equiv C_1 + C_2 \quad \textit{or} \quad \text{Mean curvature: } H = \frac{C_1 + C_2}{2}$$

$$\text{Gaussian curvature: } K_G = C_1 C_2$$

These important quantities will aid us in describing shape transitions in our model membranes and the effects they have on membrane properties, taking center-stage

in our in-depth investigation of how geometrical changes in the bilayer influence the adsorption of lipidated proteins using the *Generation II* version of our theory in Chapters 6 and 7.

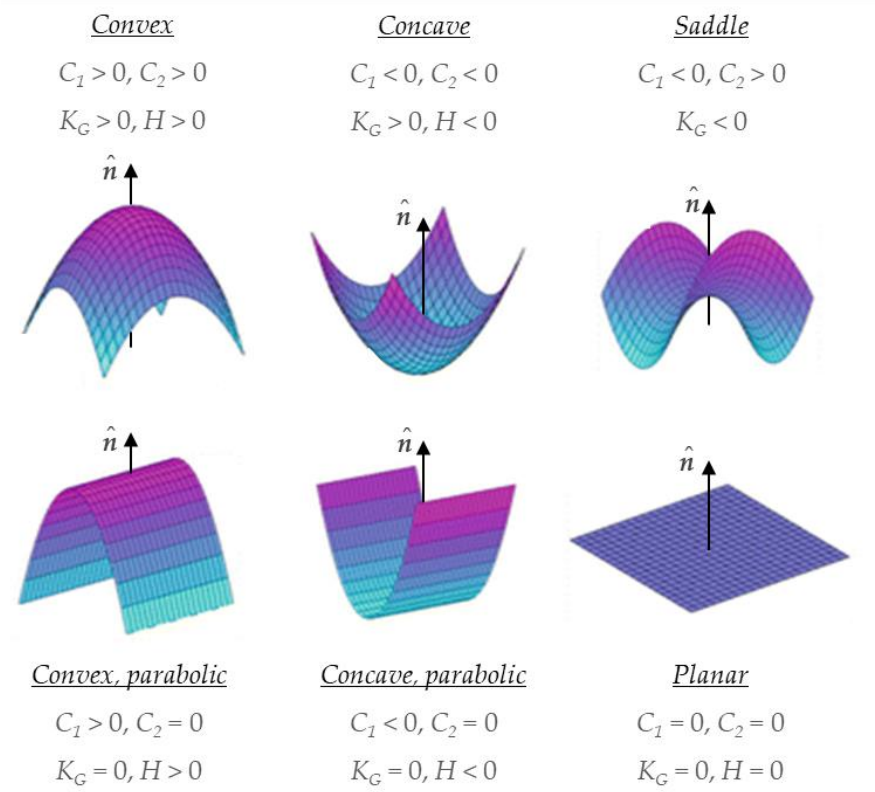

Figure 4.9) **Schematic of various surface types.** This schematic shows how the signs of the principal curvatures, C_1 and C_2, develop different surface geometries and change the Gaussian curvature, K_G, and the mean curvature, H.

For now, we refer back to *Equation 4.3*, where we used the principal curvatures to calculate the area per lipid in a plane, at z, of a curved membrane. The molecular area is dependent on the membrane's shape, or local curvature, and the particular distance, z, from the midplane within the hydrophobic core:

$$\frac{A(z,\mathbf{c})}{N} = a(z,\mathbf{c}) = a(0)\left(1 + (C_1 + C_2)z + C_1C_2z^2\right) \qquad (4.3)$$

Two possible membrane formations are of primary interest in this work – these are cylindrical structures, where $C_1 = {}^{1}/_{R}$ and $C_2 = 0$, and spherical structures, where $C_1 = C_2 = {}^{1}/_{R}$; R is the radius of the formation, extending from the center of curvature to the midplane of the bilayer. The area of each plane at z for these formations are, respectively:

$$a(z,\mathbf{c}) = a(0)\left(1 + C \cdot z\right) \qquad \begin{matrix} \textit{molecular area of} \\ \textit{cylindrical bilayers} \end{matrix} \tag{4.45}$$

and

$$a(z,\mathbf{c}) = a(0)\left(1 + 2C \cdot z + C^2 \cdot z^2\right) \qquad \begin{matrix} \textit{molecular area of} \\ \textit{spherical bilayers} \end{matrix} \tag{4.46}$$

Different membrane curvatures generate unique sets of lipid conformational states, due to a change in boundary conditions for each change in **c**. This results in a change in the cross-sectional area accessible to a lipid chain as a function of depth into the bilayer, from a cylindrical sample space in planar bilayers to a conical one, as well as an increase or decrease in the number of accepted lipid conformations based on the degree of negative or positive membrane curvature, respectively. Due to the large computational expense of calculating each new exhaustive set of lipid chain conformations for each perturbation in curvature, we implement an approximation, developed by Igal Szleifer [175], that neglects the effects caused by the change in boundary conditions upon bending. With this *pyramid approximation*, we may retain the

conformations generated for the original planar geometry and apply this set over all **c**. The deformations can then be represented solely by the 'shape' of the sample space, or available volume for a lipid chain, which varies according to **c** for each discretized layer constituting the width of the hydrophobic channel. The concept is illustrated by the 'pyramid-like' image on the right in *Figure 4.10* below.

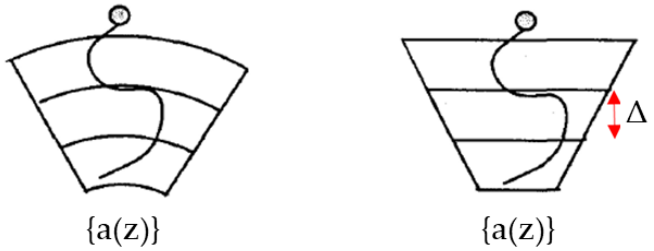

Figure 4.10) **Pyramid approximation.** ***Left:*** The boundary conditions and shape of the packing constraints of an arbitrary deformation. ***Right:*** The deformation in the pyramid approximation *(see the text)*. *Image and caption adapted from* [175].

The integration in the packing constraint has, in this way, been effectively discretized – the area per molecule of each discrete *x*-*y* plane of length $\Delta = 1$ Å, along the $\pm z$-direction from the midplane through the width of the membrane's leaflets, retains its value through a single Δ perturbation before being reevaluated at the next plane. Only the area of the midplane, or *surface of inextension*, is constant over all defined curvatures, while areas of all other discrete planes are variable as the membrane bends. The pyramid approximation has been tested by I. Szleifer *et al*. [126, 175] using a similar theoretical model in the context of its effect on the values of the bending modulus as a function of the midplane area per molecule (surface of inextension). A comparison was drawn between these values when

evaluated subject to the approximation and when obtained from the rigorous calculation.[5] As shown in *Figure 4.11*, the results of this comparison indicate that the differences in bending moduli between these approaches are less than 10% (within experimental error), providing confidence that such an approximation is a legitimate approach for the study of membrane elasticity.

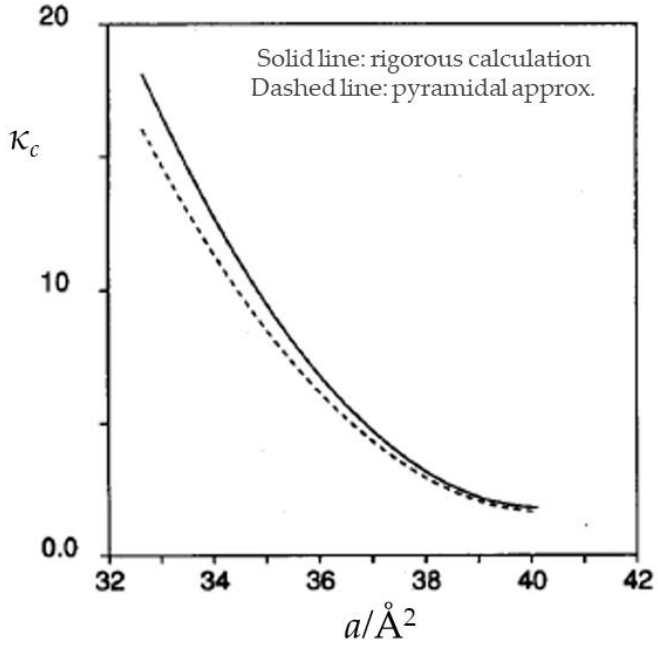

Figure 4.11) **Comparison of bending moduli, κ_c, using the pyramid approximation and rigorous calculation.** Constant area bending constants (in k_BT units) of a planar bilayer composed by C_{12} chain molecules, as a function of the average area per molecule. The full line corresponds to the full calculations while the dashed line is evaluated using the pyramid approximation. *Image and caption adapted from* [175].

[5] I. Szleifer *et al.* conducted the analysis using the *constant area bending modulus*, referring to a type of membrane deformation in which lipid diffusion occurs so as to maintain an equivalent average area per lipid for both membrane leaflets, at all curvatures. We discuss different *modes of membrane deformation* and a quantity that determines them, denoted the *relaxation ratio*, in the next section *(Section 4.6)*. For now, we will simply state that 'constant area bending' corresponds to a relaxation ratio equal to one.

The free energy of a membrane is coupled to the curvature dependence of the molecular area. There is an energy requirement for any change in membrane contour, which is governed by the intrinsic elastic constants of the membrane and dependent on how the membrane's geometry changes, as represented by the principal curvatures. This relationship is expressed through Helfrich's curvature theory, used to evaluate the differential of the change in free energy, δf, of a differential piece of area on a curved membrane:

$$d\left(\delta f(\mathbf{c})\right) = \left(\frac{1}{2}\kappa_c(2H - C_0)^2 + \bar{\kappa}K_G\right)da$$

$$or \tag{4.47}$$

$$d\left(\delta f(\mathbf{c})\right) = \left(\frac{1}{2}\kappa_c(C_1 + C_2 - C_0)^2 + \bar{\kappa}C_1C_2\right)da$$

Membranes may bear a characteristic curvature, C_0, referred to as the *spontaneous curvature*. A non-zero spontaneous curvature signifies a membrane whose natural form does not rest in a planar state, but rather 'spontaneously' curves into whichever form secures the minimum in the system's free energy. Such a situation occurs (for example) when the inner and outer bilayer leaflets are asymmetric, caused by compositional heterogeneity of lipids and/or proteins between the two leaflets, as is common in biology. We have designed our system such that our model membranes have a planar *reference state*, with bi-leaflet compositional symmetry, where $C_0 = 0$. Therefore, the thermodynamic equilibrium given by the 'global' minimum in free energy, over all shapes the membrane may assume, rests

in the planar state. In our analysis of curved membranes, we bend the bilayer out of this global equilibrium, disrupting bi-leaflet symmetry. The system must then adjust to a new equilibrium state, subject to the imposed deformation, facilitated by the consequent lipid transbilayer diffusion patterns dictated by experimental factors.

The integration of *Equation 4.47* results in the total change in free energy caused by an induced membrane deformation (out of planarity) over the total surface area of the bilayer's midplane. This procedure equips us with the expression used to calculate the elastic constants, given the free energy outputs, $f(\mathbf{c} = 0)$ and $f(\mathbf{c})$, obtained by evaluating our model membrane in planar and curved formations, respectively:

$$\frac{f(\mathbf{c}) - f(\mathbf{c}=0)}{a(0)} = \frac{1}{2}\kappa_c(2H - C_0)^2 + \bar{\kappa}K_G$$

$$or \qquad (4.48)$$

$$\frac{f(\mathbf{c}) - f(\mathbf{c}=0)}{a(0)} = \frac{1}{2}\kappa_c(C_1 + C_2 - C_0)^2 + \bar{\kappa}C_1C_2$$

Though the elastic constants stem from molecular origins, they communicate the overall rigidity of the membrane and can be regarded as bulk properties. This means that their values do not change with alterations in the membrane's macroscopic structure. Therefore, we may first consider cylindrical bilayers (C_2 = 0), which reduces the above formula to an expression that fully describes the bending energy in terms of a single unknown variable, κ_c, which may then be

evaluated:

$$\frac{f(\mathbf{c}) - f(\mathbf{c}=0)}{a(0)} = \frac{1}{2}\kappa_c C^2 \qquad \begin{matrix} \textit{cylindrical} \\ \textit{deformations} \end{matrix} \tag{4.49}$$

Spherical deformations include an additional dimension to the flection of the membrane, with symmetry in the curvature radii, $C_1 = C_2 = C$. The resulting change in bending free energy is governed by both elastic constants, κ_c and $\bar{\kappa}$:

$$\frac{f(\mathbf{c}) - f(\mathbf{c}=0)}{a(0)} = \left(2\kappa_c + \bar{\kappa}\right)C^2 \qquad \begin{matrix} \textit{spherical} \\ \textit{deformations} \end{matrix} \tag{4.50}$$

With the bending modulus of a given bilayer known from the analysis of the cylindrical membrane system, the saddle-splay constant can be calculated for the same type of bilayer using the above expression.

The Gaussian term *(from Equation 4.48)* is often estimated to be negligible in membranes with sufficiently low curvatures $\left(< 1/150 \text{ nm}^{-1}\right)$, because the magnitude of the term becomes exceedingly small in this limit. Furthermore, as established by the Gauss-Bonnet theorem from differential geometry, in the integration of *Equation 4.47* the surface integral over the Gaussian curvature term depends only on the topology and boundary of the membrane patch under study. Therefore, it is often concluded that unless there is some local change in the topology (such as pore formation) or membrane boundary, the K_G term becomes a constant that does not influence the ensuing physics, rendering the saddle-splay

constant inconsequential (though we challenge this assumption with our *Generation II* theory).[6] Measurement of the splay constant relies on either of these surface changes to obtain an experimental signal sensitive to $\overline{\kappa}$. Its measurement is further hindered by the difficulty in controlling situations involving transformations in membrane geometry, both experimentally and in simulation [176]. Hence, values for the splay constant in the literature are almost nonexistent. Estimations for the bending modulus, however, are not subject to the same hinderances, making them more prevalent in the literature (though, other complications are involved; *see Section 4.7*).

The bending modulus is consequently regarded as the most relevant elastic constant and is of primary interest in our analysis of membrane elasticity using the *Generation I* model. Positive values of the bending modulus relate a membrane's resistance to bending, directly corresponding to an energetically unfavorable rise in the free energy; the larger the value of κ_c, the more rigid the membrane. Under these circumstances, the system will only succumb to a forced deformation if the

[6] In *Generation II* of our theory, we explore the effect of membrane geometry on protein localization on the membrane, with the surprising finding that membrane-inserting proteins show pronounced discrimination between membranes of different geometry with the same mean curvature. As the mean and Gaussian curvatures completely define the geometry of a surface, our findings implicate the Gaussian term as a crucial parameter contributing to the regulation of protein segregation on the membrane – contrary to existing theoretical models for lipid bilayers, which neglect the term. We will discuss the influence of the Gaussian curvature term in Chapter 7.

available energy input exceeds the energetic cost.[7] Conversely, negative values of κ_c indicate the membrane's tendency to spontaneously curve, with the planar geometry existing as an energetically unfavorable state. All membranes considered in this study are made predominately of PC lipids, the cylindrical structures of which form planar, symmetric bilayers upon self-assembly in water. The bending moduli of these types of membranes are therefore greater than zero. These values vary significantly with the migration of lipids between the bilayer leaflets, which is induced by bending the membrane; membrane elasticity should thus be explained in the context of this kinetic element. Bending moduli calculated by our theory and experimental values from the literature are provided in *Section 4.7, Results I.I.*

4.6 Lipid Transbilayer Diffusion and the Chemical Potential

Flipping Lipids

The elastic moduli are intrinsic membrane properties and are therefore not affected by variations in a membrane's shape. However, they are strong functions of *lipid organization* within the membrane, which can vary widely depending on the *mode of deformation*. The particular mode of deformation pertains to how the

[7] Recalling the biological phenomenon of endocytosis, the characteristic deformation is only possible with an adequately large transfer of energy from an external source, e.g., adenosine triphosphate (ATP) or guanosine-5′-triphosphate (GTP).

lipids reorganize upon membrane bending, specifically via diffusion from one leaflet to the other. When the membrane undergoes a macroscopic change in structure, local regions of compression will emerge in one leaf, while the opposing leaflet expands. This agitation in the system causes a rise in free energy, leading to membrane instability – the system has been forced out of its thermodynamic equilibrium. For the membrane to maintain its new form, internal reorganization of the lipids in the bilayer occurs to mitigate the bending energy and partially relieve the local accumulation of stress in compressed regions as the system seeks to regain stability at a *new* equilibrium.

Though membrane components diffuse rapidly and continuously in the lateral direction within their resident membrane leaflets, transverse lipid diffusion ('flip-flop' between the leaflets) occurs, under normal circumstances, quite slowly. There is a large energetic penalty for exposing a lipid's hydrophilic headgroup to the hydrophobic tail region (~84,000 $J \cdot mol^{-1}$, roughly equivalent to the energy derived from the hydrolysis of three ATP molecules); however, the cost can be preferable to a greater energetic disturbance caused by a structural deformation. Lipids from the compressed leaf are thereby provoked to traverse the membrane channel to the expanded leaf, consequently relieving the destabilizing forces.

One type of 'mode of deformation' is *blocked exchange*, which refers to the case where all model membrane components are constrained from diffusing across

the midplane upon an induced disturbance in membrane geometry; this limiting condition is the most unstable. PC lipids have a cylindrical shape that causes them to preferentially assemble into planar structures when their concentrations in the bilayer leaflets are comparable. In our analysis of membrane curvature, we bend the bilayer from a tensionless, symmetric, planar reference state, at equilibrium. Under the constraints of a blocked exchange deformation, the concentrations of each leaflet retain their planar system values, such that $x_{i,\delta}(\mathbf{c}) \equiv x_{i,\delta} = x_{i,C} = x_{i,E}$ is fixed at 0.50 for any curvature.

At the other extreme, *free exchange* is a mode of deformation by which the system is free to relax completely, as molecules are permitted to migrate between the two leaflets to obtain the optimal packing conditions that confer greatest stability to the membrane. For a free exchange deformation, the concentrations within the leaflets are not predefined as inputs to the system but are, rather, free to adjust until thermodynamic equilibrium is realized. The concentrations are functions of curvature and bilayer thickness (determined by the membrane's composition). This dependency can be related by the following derivative, designated as the *relaxation ratio*, η_i, of species *i*:

$$\eta_i = \frac{2}{l}\left(\frac{\partial x_{i,E}(\mathbf{c})}{\partial(C_1 + C_2)}\right)_{0,0} \tag{4.51}$$

where l is half the width of the bilayer (one leaf) and because the molecular

fractions in only one of the membrane leaflets is independent (either $x_{i,C}(\mathbf{c})$, in the compressed leaflet, or $x_{i,E}(\mathbf{c})$, in the expanded leaflet), we have chosen the expression to be written in terms of the lipid concentration of species i in the expanded leaf.

As there is no change in leaflet concentration during a blocked exchange deformation, the relaxation ratio is set at zero $\left(\eta_i = 0\right)_{\substack{blocked \\ exchange}}$ under this condition. Under a free exchange deformation, the value of the relaxation ratio for each membrane component is dependent on the types of lipids in the bilayer and must be discovered through evaluating the curved system at its new equilibrium. Equilibrium is achieved when the extent of lipid diffusion from the compressed to the expanded leaf is such that the chemical potential of each type of constituent lipid is equivalent across the bilayer, corresponding to a minimum in the system's total free energy. This state is also marked by a minimum in the bending modulus with respect to the relaxation ratio/lipid concentration in a given leaf, for each membrane component. We will designate this *equilibrium relaxation ratio*, η_i^*, $\left(\eta_i = \eta_i^*\right)_{\substack{free \\ exchange}}$. Evaluating the derivative in *Equation 4.51*, we can solve for the concentration of a given species in the expanded leaf (and consequently the compressed leaf) of the bilayer for any relaxation ratio, which is taken to be constant for all membrane curvatures with respect to a given species of constituent

lipid. For spherical and cylindrical membranes, this concentration is given by the following expressions:

$$x_{i,E}(\mathbf{c}) = 0.5000 + \frac{\eta_i l}{R} \qquad \begin{matrix} spherical \\ bilayers \end{matrix} \tag{4.52}$$

$$x_{i,E}(\mathbf{c}) = 0.5000 + \frac{\eta_i l}{2R} \qquad \begin{matrix} cylindrical \\ bilayers \end{matrix} \tag{4.53}$$

Whatever the mode of deformation, the free energy of a membrane with zero spontaneous curvature that has undergone an induced contortion is always higher than that of its planar form, $f(\mathbf{c}) > f(\mathbf{c} = 0)$. Bending under blocked exchange corresponds to the highest increase in free energy for a given curvature, whereas free exchange incurs the least energetic cost, $f(\mathbf{c})_{\substack{blocked \\ exchange}} > f(\mathbf{c})_{\substack{free \\ exchange}} > f(\mathbf{c} = 0)$. This trend is reflected in the magnitude of the bending modulus *(see Results I.I)*. As indicated by *Equation 4.49*, the bending modulus is directly proportional to the change in free energy required to bend the bilayer from its planar state. Membranes that are relatively inelastic (have a larger bending modulus) require a greater degree of lipid transmembrane mobility to temper the energetic upset. As illustrated in the results section below, the bending modulus is highest under blocked exchange, and decreases precipitously as the number of lipids that diffuse to the expanded leaf increases, until the membrane has regained chemical equilibrium, under the condition of free exchange.

A Discussion on Chemical Potential

The driving force for the migration of lipids from one leaf to another is the difference in a lipid's chemical potential, $\mu_{i,\delta}(\mathbf{c})$, between the bilayer leaflets. Chemical equilibrium is identified in our system by the condition that the chemical potential of a given species must be equivalent in both leaflets of the bilayer. Local compression of one leaflet and dilation of the other upon bending of the membrane generates a *chemical potential gradient*, $\Delta\mu_i(\mathbf{c})$, across the midplane, increasing the free energy, and is the source of membrane destabilization. The chemical potential of a species, i, in the δ bilayer leaf defines differential changes in the system's Helmholtz free energy, F, with perturbations in the number of molecules, $N_{i,\delta}$, of that species in the specified leaflet, when all other independent variables (temperature, T, volume, V, and number of system molecules, other than $N_{i,\delta}$) are held constant:

$$\mu_{i,\delta}(\mathbf{c}) = \left(\frac{\partial F}{\partial N_{i,\delta}} \right)_{T,V,N_{j\neq i},N_{i,\delta'\neq\delta}} \tag{4.54}$$

To identify chemical equilibrium, we must calculate $\mu_{i,\delta}(\mathbf{c})$ by evaluating this derivative, using our derivation of the free energy from *Equation 4.32/4.33*:

$$\beta\mu_{i,\delta}(\mathbf{c}) = \ln\left[\frac{x_i x_{i,\delta}(\mathbf{c})\lambda_i^2}{a(0)} \right] - \sum_{\omega}^{n_i^{tails}} \ln\left[q_{i,\omega,\delta}(\mathbf{c}) \right] \tag{4.55}$$

where $x_i x_{i,\delta}(\mathbf{c}) \big/ a(0) = N_{i,\delta}(\mathbf{c}) \big/ A(0) = \rho_{i,\delta}(\mathbf{c})$, the areal density of component i in leaf δ

of the bilayer, and the single-chain partition function, $q_{i,\omega,\delta}(\mathbf{c})$, is derived in *Equation 4.31*. Inequality between $\mu_{i,C}(\mathbf{c})$ and $\mu_{i,E}(\mathbf{c})$ motivates molecular diffusion down the gradient, from regions of high to low potential. Such migration is accompanied by a net release in free energy. Thus, lipid transmembrane diffusion from the compressed to the expanded leaf is a spontaneous process that reduces the chemical potential gradient and helps restore balance to internal forces. Given enough time, and barring external influences, this lipid reorganization ultimately attenuates when the chemical potential gradient for each membrane component reaches zero, $\mu_{i,C}(\mathbf{c}) = \mu_{i,E}(\mathbf{c})$, also identified when $\eta_i = \eta_i^*$, marking the system's return to chemical equilibrium (albeit, a *new* equilibrium, unique to the membrane's acquired geometry, thermodynamically altered from that of the preferred planar state). Variation in the chemical potential gradient with lipid inter-leaflet diffusion in each of our model membranes is illustrated in the next section.

It is important to note that the extent of lipid transbilayer diffusion is dependent on the timescale by which the system is given to relax. As we have discussed, a substantial activation energy must be overcome for spontaneous mobilization of the large hydrophilic lipid headgroups to enter the hydrophobic membrane channel. Therefore, in unperturbed membranes, such an event occurs over a timescale on the order of days or weeks, or longer. Stressing the membrane

by bending provides the incentive for larger-scale transmembrane diffusion at a much faster rate, however, the immediate effect is incomplete. The amount of lipid diffusion across the midplane of a curved bilayer requires sufficient time to reach the optimal packing density. The pertinence of this concept to the interpretation of experimental observations, theoretical models, and biological processes is significant. It means that the time required for the system to relax to its new equilibrium is not necessarily within a timeframe relevant experimentally, or biologically – there is a *kinetic constraint* on membrane equilibration, with the degree of lipid transbilayer diffusion as the rate limiting step. Thus, scientists must consider the possibility of their results being obtained under *non-chemical equilibrium* conditions and theoretical models must be capable of accounting for such.[8] The two extremes in the mode of curvature-driven relaxation (blocked and free exchange) explicitly delineate the boundaries within which all experimental findings should lie (without the presence of any intervening external forces/sources of energy).

In regard to a biological process's timescale, a 'blocked exchange

[8] Remember, due to the hydrophobic effect, bilayers are subject to the *mechanical equilibrium* constraint of zero surface tension, unless subject to external forces, such as cytoskeletal stress. Lipid bilayers attain mechanical equilibrium faster than they do chemical equilibrium. Thus, while our model system is constrained to be at mechanical equilibrium, we allow for non-chemical equilibrium conditions for curved membranes due to the long timescale of lipid transbilayer diffusion, which may prevent the chemical potentials of lipids in physiological membranes from reaching equality between the leaflets.

deformation' can be considered to characterize the bilayer immediately upon a change in shape, before any organizational restructuring has transpired and lipid concentrations of the compressed and expanded leaflets remain equal to their pre-deformation values (in our model, 0.50). The time required for full 'free exchange' system relaxation varies depending on the type of lipids composing the membrane, thermodynamic factors such as temperature, and other environmental conditions (salt concentration, p*H*, etc.). The extent of lipid flipping that has occurred at the time a biological process of interest has completed or at which experimentalists retrieve their data can be represented by an intermediate relaxation ratio, which we will refer to as η_i^{bio}, somewhere between these bounds, $\eta_i^{blocked\ exchange} \equiv 0 < \eta_i^{bio} < \eta_i^* \equiv \eta_i^{free\ exchange}$. The values for η_i^{bio} that we apply to our theoretical calculations (listed in *Table 4.1*) are determined by those which output bending moduli, as calculated by our theory, that are in agreement with those obtained by experiment (this process is detailed further in the following section). In this sense, the relaxation ratio is used as the only fitting parameter in our study of membrane elasticity. We then apply these η_i^{bio} values as input to our theory for the independent examination of protein adsorption on different types of lipid bilayers, under the same system and environmental conditions. Hence, the relaxation ratio is *set* in our protein adsorption analyses (which eliminates all fitting parameters).

The excellent agreement between our results and those of our experimental collaborators, J. B. Larsen *et al*. [177], confirms the effectiveness of our method.

The next section presents our first set of results in this work, featuring our theoretical calculations for the membrane's elastic properties, the diffusional tendencies and chemical potential changes of the membrane's lipid constituents with changes in membrane geometry, and the relationships between them. Both the bending modulus and the localization of proteins on lipid membranes *(Chapter 5)* are strong functions of the degree of inter-leaflet asymmetry and, consequently, are quite sensitive to the timescales of biological and experimental processes. The theory is well-equipped to operate under this added kinetic element, capable of examining the physicochemical properties of the systems at all stages of the relaxation process, from the advent of membrane deformation through the full recovery of thermodynamic equilibrium.

4.7 Results I.I: The Bending Modulus and Chemical Potential Gradient as Functions of Membrane Leaflet Concentration.

This section displays our results for the elastic moduli calculated for the model membranes under study: pure component DOPC, POPC, DMPC, and DLPC lipid bilayers, as well as binary membranes with varying concentrations of DOPC and DOPE lipids. Also presented here are plots illustrating how the chemical potentials of lipids in the compressed and expanded leaflets of each

bilayer change as diffusion from one leaf to the other progresses after an induced membrane deformation. Structural quantities and distributions (membrane thickness, molecular area, lateral pressure, etc.) and the influence of membrane properties on the localization of the lipidated protein, N-Ras, are provided in the *Results I.II* section, after a discussion regarding these proteins in Chapter 5.

Our goal here is to use the value of the bending modulus for a given type of bilayer as a means of estimating the extent of lipid transbilayer diffusion that physically occurs within a timeframe relevant to experimental techniques used in lipid membrane research. The propensity of a lipid to migrate across the bilayer midplane in a membrane under an induced stress is lipid-specific. In our theory, the degree of this migration can be represented by a given lipid's relaxation ratio. We modulate the relaxation ratio, which is input to our model, to find reasonably good agreement between experimental bending moduli values from the literature and the value output by our theory. The relaxation ratios selected in this manner are subsequently considered as fixed parameters in our study of protein-membrane interactions; the theory is thus regarded as free from any fitting parameters for this application. As the bending modulus is a temperature-dependent property, the system temperatures used to examine membrane elasticity are set equivalent to those used in the protein adsorption analyses performed by our theory and our experimental counterparts. DOPC, DOPE, and

POPC systems are set to 295 K; DMPC and DLPC systems to 305 K. The higher temperature of the latter pair is necessary to accommodate the high transition temperature of DMPC (T_m^{DMPC} = 297 K), ensuring a liquid-disordered phase state, and to allow comparisons between these two systems in our protein study. Values of the calculated bending moduli are given in *Table 4.1*.

Table 4.1) **Relaxation ratio, theoretical change in chemical potential between the bilayer leaflets, theoretical bending modulus, and averaged experimental bending modulus for each lipid bilayer.** Each relaxation ratio is determined by finding the value which yeilds a bending modulus calculated by our theory that reasonabley matches the experimental bending modulus, averaged over those found in the literature from experiments run at or near the same temperature as our system, for each type of lipid bilayer. For the binary systems, the listed relaxation ratio is taken to be representative of both lipid components. The change in lipid chemical potential between the bilayer leaflets is calculated using the given relaxation ratio in spherical liposomes, 40 nm in diameter.

Lipid Bilayer	Relaxation Ratio, η^{bio}	Inter-leaflet Difference in Chemical Potential, $\Delta\beta\mu$ (1/*N*)	Calculated Bending Modulus, κ_c (10^{-19} J)	Ave. Experimental Bending Modulus, κ_c^{exp} (10^{-19} J)
DOPC	0.40	2.36	0.85	0.86^{α}
DOPC + 25% DOPE	0.40	- -	0.85	No exp. value
DOPC + 50% DOPE	0.40	- -	0.84	No exp. value
POPC	0.28	4.08	0.80	0.77^{β}
DMPC	0.35	3.23	0.71	0.71^{γ}
DLPC	0.24	3.93	0.69	0.66^{δ}

Values averaged from References α: [178, 179], β: [180], γ: [181-188], δ: [181, 186, 189].

It is important to acknowledge that experimental values of bending moduli in the literature vary widely for the same type of lipid bilayer at the same temperature, depending on the type of experimental procedure conducted, even for simple bilayers [37, 58, 179, 190, 191]. Regrettably, variation is also frequently found among values reported from different laboratories using the same experimental technique. As lipid bilayers are exceedingly thin (approximately 3-5 nm) and fluid, their bending rigidities are exceptionally small (on the order of 10 $k_B T$) and thus difficult to measure experimentally. The most common experimental methods for measuring the bending modulus are: (1) measurement of the force required to actively bend the membrane by micro-mechanical manipulations (MM) of GUVs via pipette aspiration, optical tweezers, an electric field, or a magnetic field, (2) more recent approaches based on scattering techniques (ST), which comprise diffuse x-ray scattering using highly oriented, multilamellar bilayer stacks, neutron spin echo (NSE) combined with dynamic light scattering (DLS) on extruded LUVs, or x-ray and neutron reflectivity on floating bilayers, and (3) the classical fluctuating shape analysis (SA) of GUVs (also referred to as 'flicker spectroscopy'), first used in 1975 by F. Brochard and J. F. Lennon [192], based on the observation by light microscopy of the thermal fluctuations of a membrane as a function of time and measuring the amplitudes of these fluctuations.

Table 4.2 lists values of the bending moduli obtained by the different experimental measurement techniques from several different research groups. It is clear from these and many other works[9] that shape analysis yields values substantially larger than those obtained by mechanical deformation or scattering methods, for the same lipid at the same temperature, typically by as much as a factor of two - a conclusion that is recognized in the literature [37]. Such a difference in the bending modulus translates to whether or not a thermally activated biological process is kinetically competent. Deciphering the origin(s) of the variation to achieve an accurate and accepted value of a membrane's bending rigidity, a quantity recognized to be central in membrane research, is clearly of some priority in biophysics and remains an ongoing endeavor. The addition of glucose and sucrose mediums (typically used in the MM studies), used for enhanced visualization and vesicle stabilization, is a possible cause for some of the variation; though, it does not explain the considerable differences reported among techniques that do not use the sugar solutions. Reference [195] demonstrates the significant affect buffering molecules and ions can have on the bending rigidity *(see Table 4.2)*, serving as a warning to experimentalists in regard to data interpretation in lipid studies including such additives.

[9] See References [58, 193, and 194] for extensive compilations of studies that measure bending moduli in lipid structures using various techniques, environmental conditions, and additives.

Other causes have been hypothesized, including the effect of lipid tilt angles on data analysis, the influence of different surface tension regimes [37], variations in the theory involved, differences in the length-scale of the experiments, and alternative interpretations of data between laboratories. J. F. Nagle *et al.* have written detailed reviews [37, 196] regarding the various techniques used to measure the bending modulus and have addressed the concerns about tilt and sugar concentration, with the conclusion that, while there has been evidence of decreasing κ_c with increasing sugar concentration [197-200], the use of sugars is not likely to account for the disparity among reported values and more research is necessary to explain the mystery [194, 201]. Nagle followed up this work in 2017 [186] with an article comparing many previously measured values of the bending modulus with new measurements based on a recent technique using diffuse x-ray scattering that accounted for lipid tilt, the only experimental method at the time capable of doing so [202]. The study showed that accounting for tilt raises the value of the bending modulus, particularly for lipids with a smaller tilt modulus. Note the effect is primarily relevant to x-ray scattering data, which is obtained at in-plane length scales small enough for the tilt modulus to influence membrane mechanics. The SA method is not at all affected by tilt, as measurements probe length scales in the plane of the membrane that are too large to detect tilt, and as the MM method spans a wide range of length scales, only the shortest would be

affected by tilt. Therefore, other explanations must be sought for the pervasive differences between the methods. Nagle concluded that the original bending moduli values obtained by scattering techniques, without consideration of lipid tilt, may be more appropriate for researchers interested only in the 'overall flexibility' of a membrane, while a tilt degree of freedom is important in analyses of processes at the short length-scale, like fusion, where tilt causes a greater increase in membrane flexibility.

We again refer the reader to [58, 193, and 194] for discussions on the various techniques used to measure the elastic constants and corresponding tabulated values, obtained from different laboratories, for a larger variety of lipid systems than presented here. We propose that a possible factor contributing to the wide range in reported bending moduli values can be attributed to the different timescales of the measurements, which, as we have discussed, would affect the degree of lipid transbilayer diffusion, consequently impacting membrane elasticity *(see Figure 4.12)*.

Table 4.2) **Bending moduli in the literature.** Illustrating the variation in experimental bending moduli values (in units of 10^{-19} J) obtained for the same bilayers using different experimental procedures and/or from different laboratories. ST: scattering techniques, MM: mechanical manipulation, SA: shape analysis; *see the text for more information*.

DOPC	***Temperature* (K)**				
Experimental method	**291**	**294**	**295**	**298**	**303**
ST (x-ray) [178]			0.80[10]		0.76 ± 0.05
ST (x-ray) [186]					0.81 ± 0.03
ST (x-ray) [37]					0.751 ± 0.113
ST (x-ray) [202]					0.83 ± 0.06
ST (x-ray)[11] [203]					0.8 ± 0.08, 0.85 ± 0.09
ST (x-ray) [204]					0.84 ± 0.06
ST (x-ray) [205]					0.63 ± 0.06
ST (x-ray) [206]					0.73 ± 0.04
MM (electro-deformation) [179]		0.926			
MM (micropipette aspiration) [188]	0.85 ± 0.10				
MM (micropipette aspiration) [200]				0.94 ± 0.09	
SA [179]		1.147			
SA [200]				0.76 ± 0.02	

[10] This value is adjusted to 295 K according to the temperature dependence of DOPC detailed in [178].

[11] Results for two *D* spacings.

POPC	*Temperature* (K)				
Experimental method	**293**	**295**	**297**	**298**	**303**
ST (NSE & DLS) [180]		0.77 ± 0.08			
ST (x-ray) [182]					0.85
ST (x-ray) [186]					1.08 ± 0.088
SA[12] [195]	1.599 ± 0.031, 1.448 ± 0.019, 1.255 ± 0.033, 0.9709 ± 0.013, 0.9960 ± 0.0518				
SA [207]		1.29 ± 0.04			
SA [208]			1.46		
SA [209]				1.58 ± 0.03	
SA [210]					1.00 ± 0.0126

DLPC	*Temperature* (K)		
Experimental method	**297**	**298**	**303**
ST (x-ray) [181]			0.55
ST (x-ray) [186]			0.853 ± 0.059
ST (x-ray) [189]			0.58 ± 0.02
SA [214]		0.96 ± 0.08	
SA [215]	0.92 ± 0.05		

[12] H. Bouvrais *et al*. presented findings in [195] regarding the effect of buffers used in lipid bilayer studies on the value of the bending modulus. The values listed here correspond to bending modulus values for POPC GUVs in (from top to bottom) pure water, 10 mM Tris, 100 mM NaCl, a combination of 10 mM Tris, 100 mM NaCl, and 2 mM EDTA, and lastly a combination of 10 mM Tris and 100 mM NaCl. Also reported in [195] are POPC bending modulus measurements in the presence of 10 mM of various buffers, including HEPES, Histidine, MES, MOPS, and PIPES (not shown here).

DMPC	*Temperature* (K)							
Experimental method	297	298	299	300	301	303	308	313
ST (x-ray) [181-183]	0.43	0.53	0.6 ± 0.03	0.65		0.69	0.69	0.63
ST (x-ray) [184]	0.38 ± 0.04	0.46 ± 0.05	0.48 ± 0.05	0.48 ± 0.05	0.49 ± 0.05	0.52 ± 0.05	0.48 ± 0.05	
ST (NSE) [185]						0.619 ± 0.33		
ST (x-ray) [186]						1.03 ± 0.042		
ST (x-ray) [187]						0.80		
ST (x-ray) [211]							0.765	0.778
MM (micropipette aspiration) [188]						0.56 ± 0.06		
SA [212]		0.8 ± 0.13	1.1 ± 0.1	1.52 ± 0.06		1.3 ± 0.08		1.27 ± 0.09
SA [213]						1.15 ± 0.15		

Because of the systemic variation in bending moduli in the literature, there is no clear 'representative' value with which to compare that calculated by our theory for each of the bilayers studied. We conclude that the most straightforward approach for choosing a characteristic bending modulus for each type of lipid bilayer is to obtain an average value based on all results found in the literature measured via the ST and MM methods, which generally agree, conducted at the same temperature as set in our system (or within two Kelvin if the sample size is too small at the appropriate temperature to obtain an average, as with DOPC). Because of the absence of multiple POPC experimental bending modulus values near the desired temperature, we cannot obtain an average and thus elect the only

available value, as reported in [180]. In regard to *Table 4.2*, numbers in red are the values used to obtain the characteristic (averaged) experimental bending modulus. The temperature marked in blue text is the *lo–ld* phase transition temperature for DMPC, T_m^{DMPC} = 297 K. Temperatures highlighted yellow indicate the *anomalous swelling region* of DMPC bilayers (temperatures directly above the transition temperature, which uniquely display an increase in the bending modulus with rising temperature, rather than the usual decrease in bending modulus with rising temperature outside of this 'anomalous' region).

The decision to include bending moduli measured by the ST and MM techniques, at the exclusion of the SA method, is based on our opinion that they offer bending moduli closer to the true values, whereas shape analysis yields results that are artificially large. Part of this assumption stems from considering the difference in length-scales between the methods. Scattering and mechanical manipulation approaches access shorter length-scales on the order of 10-100 Å and 10-10^5 Å, respectively; small wavelengths are not optically visible via shape analysis, which is sensitive only to long-wavelength thermal undulations on the order of 10 μm. Additionally, the ST and MM methods typically report values that are very similar, offering the confidence that comes with reproducibility between two very different experimental techniques.

Though the bending modulus is an equilibrium property that cannot,

therefore, depend on the timescale of systems *in equilibrium*, we hypothesize that the relevant system conditions of the experiments measuring a membrane's elastic properties may *not* be at chemical equilibrium, but somewhere between blocked and free exchange scenarios. *Figure 4.12* illustrates the considerable impact even small concentration differences between the membrane leaflets have on membrane elasticity. The minimum in the bending modulus curve indicates the most stable state of lipid organization, where the chemical potential of each membrane component is equivalent across the bilayer, marking the system's chemical equilibrium for a given membrane geometry. The inter-leaflet chemical potential gradient, $\Delta\mu_i(\mathbf{c})$, of a lipid *i* (shown in *Figure 4.13*) as a function of relaxation ratio portrays the relief in the energetic disturbance caused by curving the membrane as a decrease in the gradient during relaxation of the system to its optimal lipid packing conditions. Chemical equilibrium is reflected in these curves as the point at which the chemical potential gradient is eliminated ($\Delta\mu_i(\mathbf{c}) = 0$).

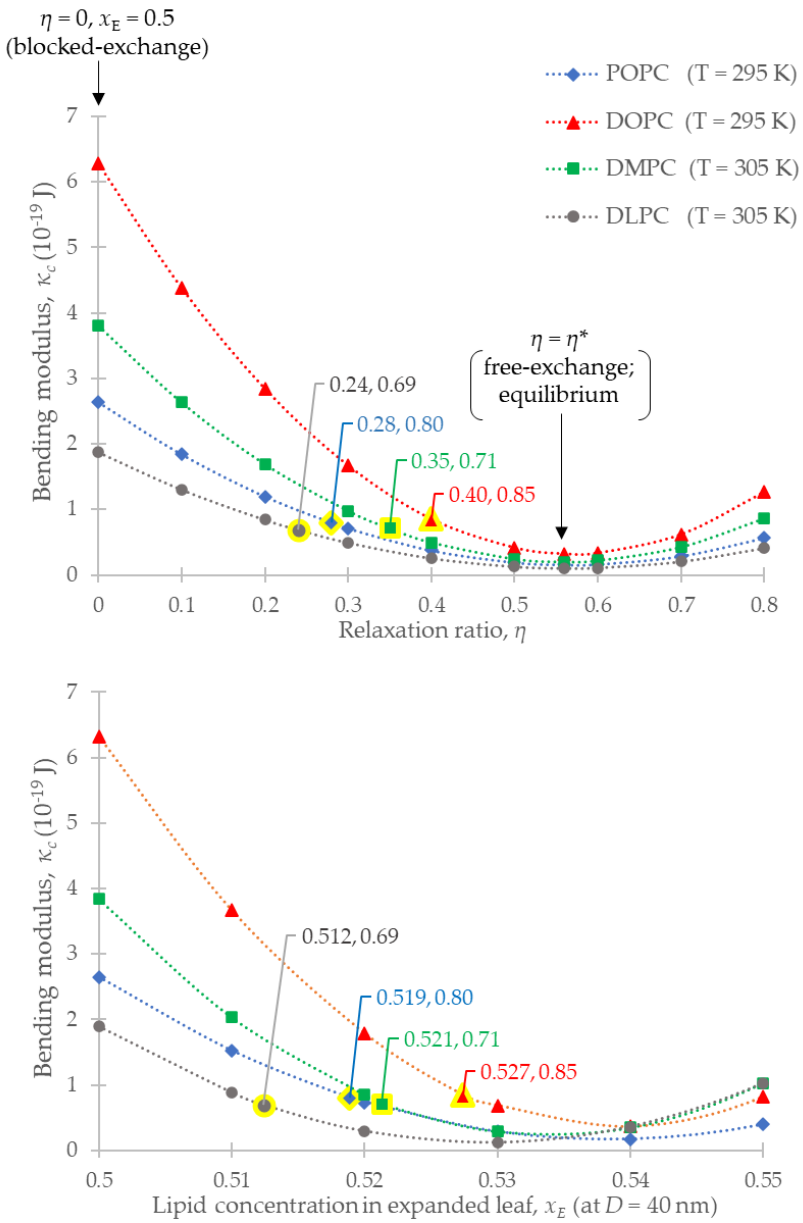

Figure 4.12) **Change in bending modulus with relaxation ratio and lipid concentration in the expanded leaf.** Shown here are the bending moduli of membranes composed of POPC *(blue, diamond markers)*, DOPC *(red, triangular markers)*, DMPC *(green, square markers)*, or DLPC *(grey, circular markers)* as functions of relaxation ratio ***(top)*** and expanded leaf lipid concentration in spherical liposomes 40 nm in diameter ***(bottom)***. The minimum in each curve represents the equilibrium state of the system; curiously, this occurs at $\eta^* \approx 0.56$ for each of the lipid bilayers. Data points highlighted yellow are the values of the bending moduli calculated by our theory that agree with experimental values; corresponding relaxation ratios are used in all calculations of curved membrane properties *(η^{bio} = POPC: 0.28, DOPC: 0.40, DMPC: 0.35, and DLPC: 0.24)*. These reflect the conditions we believe to be experimentally and biologically relevant.

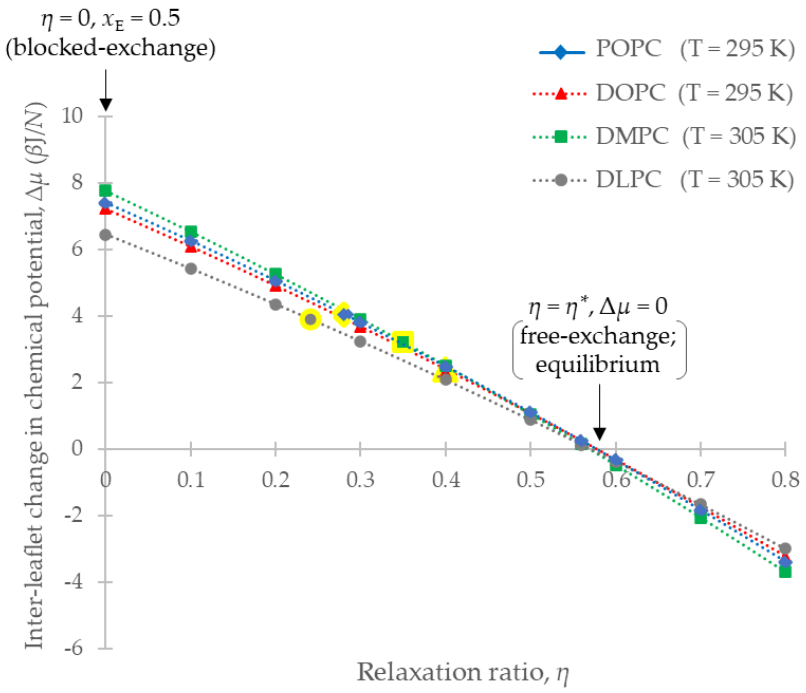

Figure 4.13) **Chemical potential gradient between membrane leaflets as a function of the relaxation ratio.** The difference in chemical potential between the leaflets decreases as the membrane relaxes after an induced deformation, as lipids diffuse from the locally compressed leaflet to the locally expanded leaflet – the degree to which is dictated by the composition-dependent relaxation ratio, η. Here we show the inter-leaflet chemical potential difference in spherical liposomes, 40 nm in diameter, composed of POPC *(blue, diamond markers)*, DOPC *(red, triangular markers)*, DMPC *(green, square markers)*, or DLPC *(grey, circular markers)* lipids. Lipid diffusion to the expanded leaf will continue passively until the gradient is fully eliminated (at equilibrium) at $\Delta\mu = 0$, $\eta = \eta^*$, if given infinite time; however, due to the kinetic constraint on lipid transbilayer diffusion, the system will only partially equilibrate within a relevant timescale, indicated by markers in yellow highlight *(η^{bio} = POPC: 0.28, DOPC: 0.40, DMPC: 0.35, and DLPC: 0.24)*. It is possible for lipids to continue to diffuse past the equilibrium point, only via the aid of an active transport system. In this case, the chemical potential gradient will switch directions, accompanied by a rise in free energy.

As expected, *Figure 4.12* indicates an inordinately large bending modulus under blocked exchange deformation, for all bilayers (marked by $\eta_i = 0$ in the top and $x_{i,E} = 0.50$ in the bottom graph). Interestingly, the equilibrium relaxation ratio

for all types of membranes lies at approximately $\eta_i^* \approx 0.56$. This relaxation ratio value defines a different *number* of lipids that diffuse to the opposite monolayer in different types of bilayers, as indicated in the bottom graph of *Figure 4.12*, yet the near equality of the equilibrium relaxation ratios indicates that the *rate* by which the lipid concentration in the expanded leaflet increases with perturbations in the extrinsic curvature, relative to the length of the lipid tails, is comparable for each type of lipid membrane approaching equilibrium (at least when the membranes comprise lipids with the same headgroup, PC in this case). Between blocked and free exchange conditions are our results for η_i^{bio} (also tabulated in *Table 4.1*), identified by markers highlighted in yellow in *Figures 4.12* and *4.13*. Beyond the equilibrium point in each of these graphs ($\eta_i > \eta_i^*$), the reader will notice a rise in the bending moduli and increasingly negative values of $\Delta\mu_i(\mathbf{c})$ with increasing relaxation ratio/expanded leaflet lipid concentration. This domain is characterized by a non-passive perpetuation of lipid diffusion, proceeding against the chemical potential gradient, which is opposite of its pre-equilibrium direction. This provokes a rise in system free energy. Such a phenomenon is only possible by the input of energy via an external source. As we touched on in *Section 2.4*, lipid flippases and floppases are examples of such active transport systems, which catalyze the relocation of lipids using ATP.

CHAPTER 5

GENERATION I THEORY:
ADSORPTION OF LIPIDATED PROTEINS ON THE MEMBRANE

It is a widely accepted theme within the biosciences that, integral to a biological membrane's role in cellular function, the lipid constituents of the membrane orchestrate their heterogeneity to accommodate the recruitment and partitioning of proteins in a highly coordinated scheme. This rational self-assembly of lipids may develop as macroscopic structural changes in the membrane, such as caveolae formation, to attract curvature-sensitive macromolecules. Alternatively, local lipid segregation might provoke the emergence of distinct liquid phases, operating on the affinity of phase-specific macromolecules. Presumably, enrichment of ordered phase-affiliated proteins precipitates the congregation of larger protein networks that can be functionalized. Clearly, the types of proteins that assemble along the bilayer are highly influenced by the nature of the membrane environment, as are the biochemical activities they engage in. Substantial attention from the bioscience and medical communities is focused on characterizing protein–membrane interactions and discovering the mechanisms that drive them. Such knowledge

promotes the improvement of diagnostic methods and the potential to control the activation/deactivation of membrane-associated proteins for therapeutic purposes. Still, the mechanistic basis for protein enrichment in the bilayer remains an outstanding question in membrane research.

In our present analysis of protein–membrane interactions, using *Generation I* of our theory, we examine how the recruitment of the lipidated protein, N-Ras, by the membrane is modulated by membrane composition, elasticity, and curvature. Subsequently, we generalize our study to investigate the explicit contributions of the lipid headgroups and electrostatic interactions within the framework of our extended, *Generation II* version of the theory. We will begin this section with a short introduction to lipidated proteins.

5.1 LIPIDATED PROTEINS

A *lipidated protein* is a type of integral monotopic protein (attached to only one side of the bilayer) that undergoes post- or co-translational covalent attachment to hydrocarbon chains, a process called *lipidation*, as means of interaction with a biological membrane. Often referred to as 'anchor molecules', or 'lipid-anchors', these hydrocarbon chains are responsible for attaching, or 'anchoring', the protein to the targeted membrane by inserting into the hydrophobic region of one of the membrane's leaflets. A protein may bind to multiple lipid-anchors of different types, particularly the long-chain acyl groups

myristate or palmitate, long-chain prenyl groups, or glycosyl-phosphatidylinositol (GPI) moieties *(Figure 5.1)* [216, 217].

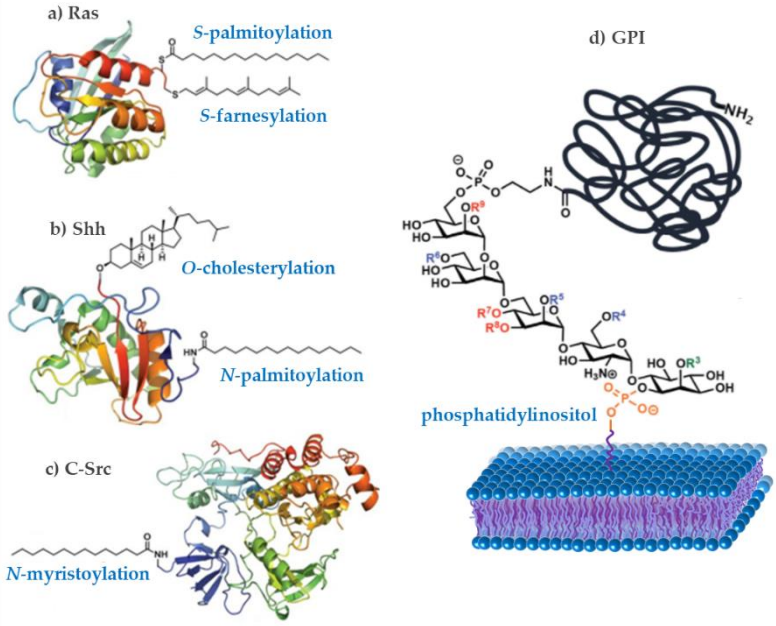

Figure 5.1) **Examples of lipid-anchored proteins.** Some examples of protein lipidation include **(a)** *S*-palmitoylation and prenylation (farnesylation), common in Ras-family proteins, **(b)** *N*-palmitoyation and cholesterylation of the Sonic hedgehog (Shh) protein, **(c)** *N*-myristoylation of C-Src proteins, and **(d)** the attachment of glycosyl-phosphatidylinisitol (GPI) anchors, illustrated here as the insertion of the protein's lipid-anchor into one leaf of the membrane, thereby tethering the protein to the bilayer where it engages in its functional activity. *Images adapted from* [216, 217].

The site of lipidation on the protein depends on the type of anchor molecule and the nature of the protein. A lipidated protein's function, localization, distribution, and hydrophobic character are often dictated by the kind of hydrocarbon moieties to which it is bound. Anchor molecules also facilitate protein–protein interactions and are actively involved in the regulation of signaling processes [218-220]. Lipid-anchored proteins are ubiquitous in animal, plant, and fungal life forms [221] and

participate in a broad array of essential biological processes; malfunction of these processes is often due to misregulation during lipidation, and commonly leads to various diseases, including cancer [222].

The Ras Family

Proteins of the *Ras family* are small GTPases that require membrane anchoring for their activation, undergoing lipidation to do so. Ras proteins are critical to biological function, acting as molecular switches in the initial stages of a vast number of signal transduction pathways that control eukaryotic cell proliferation, differentiation, and survival. There are three dominant, clinically relevant members of the Ras family, *N-Ras*, *H-Ras*, and *K-Ras*. These isoforms of the Ras gene are expressed throughout the entire developmental history of differentiated mammalian cells within all mammalian organs [222, 223]. While their bioactive roles are central to an organism's development, it was discovered in 1982 [224-229] that these members of the Ras family experience a high frequency of oncogenic mutation that inhibits their deactivation mechanism. The proteins consequently become locked in a permanently activated state that perpetuates their signaling to downstream effectors, despite the absence of incoming signals. Continuous Ras signaling causes overactive cell growth and division, contributing to several developmental syndromes [230] and can lead to tumor initiation and expansion.

N-Ras, H-Ras, and K-Ras are the most common oncogene proteins in human cancer – 20 to 30 percent of all human tumors contain the point mutations that cause perpetual activation of these Ras genes, and this percentage is much higher in certain varieties of cancer [231]. The kinds of tumors that develop from oncogenic misregulation of Ras activation/deactivation identify with specific Ras isoforms. For example, tumor cells in the pancreas [232, 233], colon [234, 235], and lungs [236] (three of the deadliest cancers in the United States [237]) are associated with mutations in K-Ras, whereas N-Ras mutations are found abundantly in acute leukemias [238] – though, the basis for such preferential tendencies is unclear.

Due to the prevalence of Ras mutations in cancer tissue, these proteins receive substantial attention from fields involving bioscience and medicine. Much has been learned regarding Ras architecture and biochemistry since the discovery of the Ras subfamily over fifty years ago [239-243]. Studies on Ras have directed investigations on the origins of cancer to the molecular level, considerably broadening the understanding of the pathogenesis of many forms of human cancer, and have aided in the development of possible treatments for cancer and other diseases associated with Ras overexpression (e.g., Ras inhibitors and viruses that target activated Ras pathways) [244-249].

Still, the observations of preferential aberrant activation of specific isoforms of Ras in distinct cancers remain a curiosity – in terms of the mechanisms that

would cause such selectivity and, more broadly, whether the specific *locations* where malignancy originates engender mutations in only individual isoforms of Ras, or if mutations in only *specific Ras isoforms* have the capacity to initiate specialized forms of cancer. Ongoing studies [250-258] seeking to address the issue suggest that the differences in cytosolic trafficking and intracellular localization of the Ras isoforms, precipitated by the disparity in their post-translational modifications and the variation in the shape and composition of the membranes with which they interact, are underlying causes of the biases.

Ras interacts with a variety of lipid membranes in the cytoplasm – particularly, those of the Golgi apparatus, the endoplasmic reticulum (ER), and the trafficking vesicles that mediate intracellular membrane transport of the proteins to the plasma membrane. Research has shown that the relationship between the lipid composition of these membranes and the necessary organization, sorting, and partitioning of the Ras proteins within cellular or subcellular compartments is crucial for proper signaling specificity [259].

All three Ras isoforms undergo post-translational prenylation, specifically *farnesylation*, which covalently binds the 15-carbon isoprenoid *farnesyl* at the cysteine residue membrane-targeting region of the C-terminal (CAAX-COOH). The farnesyl chain acts as an anchoring mechanism, tethering to its targeted lipid membrane. This modification occurs in the cytosol and enables the protein to first

insert into the cytosolic surface of the ER, thus commencing its migration along the secretory pathway to its ultimate destination on the inner leaflet of the plasma membrane, which is the activation site of the protein. Whether prenylation is followed by further modification depends on the particular type of Ras. N-Ras and H-Ras proteins are trafficked from the ER to the surface of the Golgi apparatus where they undergo *palmitoylation* on one (N-Ras) or two (H-Ras) cysteine residues, adjacent to the prenylated C-terminal. This process involves the covalent binding of the 16-carbon fatty acid *palmitoyl*, derived from palmitic acid, which increases the protein's hydrophobicity and, consequently, its capacity to associate with the plasma membrane's hydrophobic core. From the Golgi, the N- and H-Ras proteins are transported on vesicles of the secretory pathway to their targeted regions on the cell membrane. K-Ras does not receive additional processing after the prenylation step; rather, it is trafficked directly to the plasma membrane from the ER, relying on its farnesyl lipid-anchor and the electrostatic interactions between its positively charged, basic sequence of lysine residues and negatively charged lipid headgroups in the bilayer's inner leaf to secure its adsorption.

The whole of the anchor region is connected to the G-domain of a Ras protein by a linker sequence, which varies depending on the host life form and the isoform of the protein *(Figure 5.2)* [260]. Together, the anchor and linker domains comprise the *hypervariable region* (HVR), which is the only differentiating element

among the otherwise homologous sequencing of the canonical Ras family members and is the instrument by which protein structure, folding characteristics, cellular location/partitioning in different membrane microdomains, and functional specificity diverge among the Ras isoforms. The differences in the hypervariable region also influence the overall probability of mutation in a given isoform of Ras, the frequency of a particular missense mutation (at a specific position, or codon) for a given isoform, and the stage in the development of malignancy at which mutations in a given isoform arise.

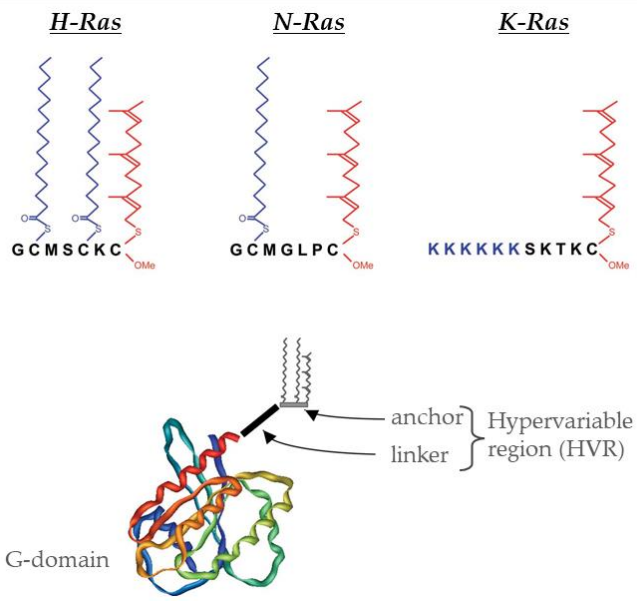

Figure 5.2) **Isoforms of the Ras family of proteins.** Each of the Ras proteins have identical G-domains but unique hypervariable regions. The blue lipid-anchor is palmitoyl and the orange lipid-anchor is farnesyl. *Image obtained from* [260].

While the hypervariable region predisposes a Ras protein to certain structural and functional properties, it is the protein's interaction with the lipid membrane that initiates and governs its conformationally regulated signaling

events. N. S. Hatzakis, *et al.* [261] demonstrated that increasing membrane curvature enhanced the localization of lipid-anchored proteins and amphipathic helices. This suggests that the curvature-sensing of these proteins is dictated by a higher density of binding sites resulting from curvature-induced defects in lipid packing, rather than by an augmented affinity inherent to the proteins. They concluded that membrane curvature-sensing was a property of the membrane itself, which universally recruited proteins containing hydrophobic (membrane inserting) moieties, and that affinity-regulated properties such as recognition motifs [262, 263], charged sites [264, 265], or phase domain-based partitioning [251, 266, 267] were mechanisms employed to fine-tune the curvature-selective proteins' sorting and localization.

More recently, the partitioning of various anchor motifs of lipidated proteins between liquid-disordered and liquid-ordered domains in planar, ternary lipid model membranes [42] and in spherical, ternary liposomes [164] has been studied to examine how anchor enrichment is influenced by phase-separated systems. These works highlight the important roles that the local compositions of a membrane's coexisting phases and the architecture of a protein's anchor play in the propensity of a lipidated protein to localize on the membrane. M. J. Uline *et al*. [42] demonstrates the inclination of saturated anchor molecules to favor the saturated, lipid-rich, ordered domains, and that the affinity for the ordered regions

of the membrane increases with increasing degree of saturation of the anchor, as well as with the number of anchors bound to the protein. Protein partitioning is shown to also be affected by the location of the double bonds along an unsaturated anchor's chain, with higher localization in the membrane's liquid-ordered phase for double bonds near the end of the anchor's chain, rather than near the middle *(see Figure 5.3)*.

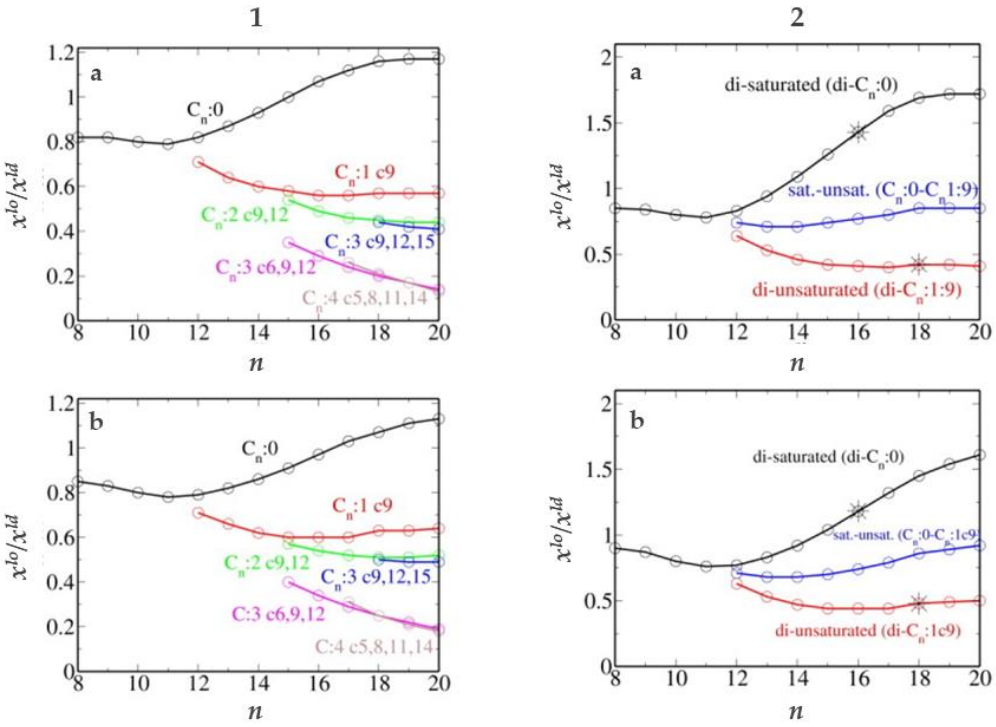

Figure 5.3) **Partition coefficient for various single anchor chains (1), and double-chain anchors (2), embedded in a membrane consisting of model DPPC, DOPC, and cholesterol.** The mole fractions of the chain anchors in the liquid-order and liquid-disorder phases are x^{lo} and x^{ld}, respectively. The number of carbons in the chain is n. **(*a*)** The temperature is 290 K. The concentrations of the *lo*-phase are $x_c = 0.48$, $x_s = 0.30$, and $x_u = 0.22$, whereas those of the *ld*-phase are $x_c = 0.27$, $x_s = 0.21$, and $x_u = 0.52$. ***(b)*** The temperature is 300 K. The concentrations of the *lo*-phase are $x_c = 0.52$, $x_s = 0.26$, and $x_u = 0.22$, whereas those of the *ld*-phase are $x_c = 0.32$, $x_s = 0.22$, and $x_u = 0.46$. The stars represent the values of the partition coefficient in the bulk lipid bilayer. *Image and caption obtained from* [42].

Furthermore, J. B. Larsen *et al*. [164] emphasizes the role of membrane curvature in the phase-partitioning of the N-Ras protein within spherical liposomes composed of dioleoyl-phosphatidylcholine (DOPC), *N*-palmitoyl-*D*-*erythro*-sphingosyl-phosphorylcholine (PSM), and cholesterol, using both theoretical and experimental analyses *(Figure 5.4)*. The study concludes that a curvature-induced relief in the local lateral pressure within the membrane leaflet in contact with protein-rich solution is the agent which determines the ability of the protein to interact with the membrane. The work illustrates that deviation in the degree of this lateral pressure change between liquid-ordered and liquid-disordered domains as the membrane bends causes the spatially-mediated enrichment of the N-Ras lipid-anchor on liposomes of variable radii.

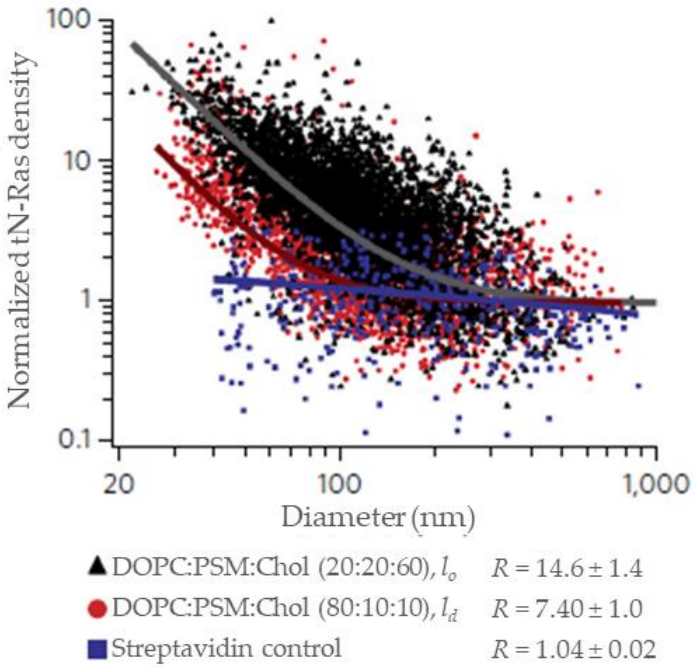

Figure 5.4) **Membrane curvature enables the association of tN-Ras anchor molecules with lo membrane phases.** Quantification of tN-Ras localization in liposomes of varied diameter. The increased recruitment of the protein by membranes in the *lo- (black triangles)* as compared to the *ld- (red dots)* phase is quantified via the increased *R*-value. *R* is reported as the average ± S.E.M. of n_{ld} = 6 and n_{lo} = 5 independent experiments. The negative control (streptavidin binding to biotinylated liposomes) showed no change in density as a function of diameter *(blue squares,* $n_{streptavidin} = 2$*). Image and caption obtained from* [164].

The theoretical approaches we have developed in our *Generation I* (Chapters 3-5) and *Generation II* (Chapters 6 and 7) models for delineating the fundamental properties of lipid membranes also provide the avenue through which we can explore the membrane's interaction with lipidated proteins. Here, we expand on [164] to investigate the cooperativity between the membrane's composition and degree of curvature to *selectively* recruit lipidated proteins. We find that there is indeed a synergistic relationship between these two organizational cues that

mediates the curvature sensitivity of the protein's lipid-anchor and gives rise to differences in protein adsorption density on different types of membranes. This coordination between composition and morphology parallels the kind of active conservation of membrane-specific localization of distinct lipid species observed in biology. Furthermore, we explore the effect of bilayer asymmetry, caused by the curvature-driven reorganization of lipids across the midplane, on the protein's adsorption behavior.

We focus our analysis on the adsorption tendencies of the minimal membrane anchor of N-Ras, tN-Ras. The following section describes the mathematical integration of tN-Ras into our theory, followed by our second set of results in this work, *Results I.II*, obtained within the framework of our *Generation I* thermodynamic membrane model. We achieve excellent agreement with our experimental counterparts in quantitatively capturing the density curves of tN-Ras on spherical lipid liposomes of varied composition as functions of liposome size. The theory's ability to mirror experimental trends regarding protein–membrane interactions, membrane elasticity, and fundamental structural characteristics of different types of bilayers, obtained from independent lab groups, demonstrates a consistent theoretical reproduction of experimental measurements on diverse biological quantities that reinforces the integrity of our molecular model. Moreover, the theory is able to discern the mechanistic forces

that engender observable phenomena at the atomic- or small monomeric-scale, granting access to valuable information inaccessible in an experimental setting.

Investigation of the physicochemical properties of a lipid membrane that motivate its recruitment of Ras proteins contributes to the kind of fundamental understanding that helps build a solid knowledgebase from which solutions to the many remaining questions surrounding these proteins can be developed. Coalescing intelligence on Ras, accumulated from both experimental and theoretical platforms and collected at all stages in the proteins' life cycle, lays the foundation for significant advancement in the design and optimization of diagnostic techniques and therapeutic procedures concerning Ras-associated diseases. This research proposes a mechanistic basis for lipidated protein localization to the membrane, which has previously been a topic of inquiry in membrane science.

5.2 Integrating Lipidated Proteins into our Generation I Theoretical Model

This section details the mathematical methods used to integrate an additional component, the minimal membrane anchor of N-Ras (tN-Ras), into our membrane system. Because the palmitoyl and farnesyl chains of N-Ras's hypervariable region are the only elements of the protein in contact and interacting with the membrane, it is sufficient to include only the protein's anchor motif in the

system with our model bilayer. We design the palmitoyl and farnesyl chains with the same rigorous treatment used to construct the lipid tails of the membrane, using Flory's Rotational Isomeric States model [148]. Incorporating the anchor's chains into our system is achieved using Widom's Potential Distribution Theorem [268] (also referred to as Widom's particle insertion principal), which has proved valuable for applications in almost all areas of equilibrium statistical mechanics. The method describes the insertion of a test, or 'ghost' particle (our lipid-anchor) into the membrane, where the thermodynamics of the molecule is affected by the mean-fields generated by all other membrane constituents in the absence of this molecule, without disturbance to these fields upon its insertion.

The physics of the anchor insertion is captured in the expression for the anchor's chemical potential, μ_{Anchor} (or μ_A for concision). The definition of μ_A is analogous to that of the chemical potential of the membrane's lipids from *Equation 4.54*:

$$\mu_A = \left(\frac{\partial F}{\partial N_A} \right)_{T,V,N_i} \tag{5.1}$$

where N_i is the number of lipids of species i that compose the targeted membrane. However, an explicit expression for the free energy of a system which includes the Ras proteins for the evaluation of the above derivative is not readily available. Hence, we take an alternative approach, following the methodology of Widom's

insertion principal. We take the concentration of protein in the system to be in the limit of infinite dilution, ensuring that its effect on the equilibrium state of the membrane is benign.[13] The definition of the chemical potential of the anchor region on a single Ras protein introduced to our membrane system may then be approximated as:

$$\mu_A = \left(\frac{\partial F}{\partial N_A} \right)_{T,V,N_i} \approx \left(\frac{F_N - F_{N-1}}{\Delta N} \right) = F_N - F_{N-1} = -k_B T \ln \left[\frac{Q_N}{Q_{N-1}} \right] \tag{5.2}$$

where F_N is the Helmholtz free energy of the lipid-plus-protein system of N total molecules, $N-1$ of which comprise the bilayer's lipid constituents, with the N^{th} molecule as the protein's anchor. F_{N-1} is the Helmholtz free energy of our original lipid bilayer system, without the protein. The above equation uses the statistical mechanical relation of the Helmholtz free energy in terms of the partition function, $F = -k_B T \ln[Q]$, for corresponding systems.

The definition of the classical, canonical partition function from statistical mechanics is:

$$Q = \sum_w \exp\left(-\beta E_w\right) \tag{5.3}$$

where the system may sample a set of discrete microstates, w, each with a

[13] Infinite dilution of the Ras protein is determined to be a reliable approximation, based on the good agreement found with experiments. If one wished to study a system containing a large concentration of proteins, an extension of the theory developed in Chapter 4 to explicitly include the additional components would be required. Such a calculation is straightforward but computationally costly, and unnecessary for the purposes of this work.

particular configurational arrangement, and E_w is the internal energy of the system existing in a given microstate. We can further expand this expression by decomposing the internal energy into its kinetic (or translational) and potential (or configurational) contributions:

$$E_w = KE_w + PE_w \tag{5.4}$$

where the kinetic energy of the particles in the system in microstate w is naturally given by $KE_w = \sum_{k=1}^{N} {p_k^2}/{2m_k}$, in terms of the momentum, p, and mass, m, of all the system's particles ($k = 1 \ldots N$) and the potential energy is a function of the position vectors of these particles, which for now will be expressed as, $PE_w = U_N(\{\vec{r}_k\})$. If the energy change corresponding to the step-size within the summation over the discrete states of the system in *Equation 5.3* is quite small relative to the system's total energy, then the function will be nearly smoothly varying. In this case, the sum may be replaced by an integral. This is valid for all biological (and most other) systems of interest, as the associated temperature and energies are sufficiently high (at cryogenic temperatures, this approximation is not adequate). Applying this approximation and using our expressions for the kinetic/translational and potential/configurational energies, we rewrite the partition function, generally, as:

$$Q_N = \frac{1}{h^{3N}} \int_{\{p_k\}} \int_{\{r_k\}} \exp\left[-\beta \left(\sum_{k=1}^{N} \frac{p_k^2}{2m_k} + U_N\left(\{\vec{r}_k\}\right) \right) \right] d^N\vec{p}\, d^N\vec{r} \tag{5.5}$$

where the h in the prefactor is the Planck constant, used to keep the expression

dimensionless.

In our system of N lipid-plus-anchor chains, the integrals over the position vectors are performed for every monomer on every chain in the system, as each chain and each monomer are independently varying (within the physical constraints of allowed conformational states). Integration over the momentums is performed for the number of chains only, as the translations of the monomeric units constructing a chain are not independent, but rather move with the chain as a whole, set in a given chain configuration. Translational diffusion in our system occurs within the x-y plane of a bilayer leaflet for a given chain origin, z_0, thus the momentum of each chain can be written in terms of its x- and y-components. The above expression, then, can be explicitly written as:

$$Q_N = Q_N^{translational} Q_N^{configurational} \tag{5.6}$$

$$Q_N^{translational} = \frac{1}{h^N} \int_{p_{x,1}} \int_{p_{y,1}} \dots \int_{p_{x,N}} \int_{p_{y,N}} \exp\left[-\beta \sum_k^N \left(\frac{p_{x,k}^2}{2m_k} + \frac{p_{y,k}^2}{2m_k} \right) \right] dp_{x,1} dp_{y,1}, \dots, dp_{x,N} dp_{y,N}$$

$$Q_N^{configurational} = \frac{1}{h^N} \int_{r_1} \dots \int_{r_{\upsilon_N,N}} \exp\left[-\beta U_N(\vec{r}_1, \dots, \vec{r}_{\upsilon_N,N}) \right] d\vec{r}_1, \dots, d\vec{r}_{\upsilon_N,N} \tag{5.7}$$

$$\text{where} \begin{cases} k = 1, \dots, N \ \ chains \\ \upsilon_k = 1, \dots, n \ monomers \end{cases}$$

In a multi-component membrane, we can write the translational part of the partition function as a product over each species, j. There is no restriction on the

limits of integration over the momentum, thus we evaluate these integrals from negative to positive infinity, which can be done exactly:

$$Q_N^{translational} = \prod_j \left[\left(\sqrt{\frac{2m_j \pi k_B T}{h}} \right)^{2N_j} \right] = \prod_j \left[\left(\frac{\sqrt{h}}{\lambda_j} \right)^{2N_j} \right] \tag{5.8}$$

where λ_j is the thermal de Broglie wavelength of species j and h is the Planck constant. We will continue our derivation in terms of a pure-component membrane for simplicity, as the methodology is the same and does not affect our end result.

Evaluation of the configurational part of the partition function is less straightforward. Let us separate the total potential energy into that generated from interactions involving the N^{th} molecule, our anchor, and the interaction energy of the *N−1* molecule system, without the anchor; we will denote these as $u_A(\vec{r}_1,\ldots,\vec{r}_{v_N,N})$ and $U_{N\text{-}1}(\vec{r}_1,\ldots,\vec{r}_{v_{N\text{-}1},N\text{-}1})$, respectively. We will further modify the argument of the anchor's potential energy by combining the position vectors of the anchor's individual monomeric units into whole-chain configurations, ς, converting the integrals over the monomer positions to a sum over each discrete, physical configurational state of the anchor's chain:

$$\begin{aligned} Q_N^{configurational} = \frac{1}{h^N} \int_{r_1} \ldots \int_{r_{v_{N-1},N-1}} & \exp\left[-\beta U_{N-1}(\vec{r}_1,\ldots,\vec{r}_{v_{N-1},N-1}) \right] \cdot \\ & \int_{\vec{r}_{0,A}} \sum_{\varsigma} \exp\left[-\beta u_A(\vec{r}_1,\ldots,\vec{r}_{v_{N-1},N-1},\vec{r}_{0,A},\varsigma) \right] d\vec{r}_1,\ldots,d\vec{r}_{v_{N-1},N-1},d\vec{r}_{0,A} \end{aligned} \tag{5.9}$$

The configurations of the anchor are treated explicitly using the RIS model, as we have described regarding the lipid tails in Chapter 4. Just as the lipid chains stem from a specified position of the glycerol carbon, at $\vec{r}_0 \equiv z_0$, the anchor chains also emanate from a 'head' molecule, which marks a chain's starting position, denoted $\vec{r}_{0,A}$ in the above equation.

As our system is homogeneous in the *x*-*y* plane, the interaction energy experienced by the anchor can be taken to be independent of the lateral position of its 'headgroup' molecule along the bilayer's interfacial plane. Therefore, we may leave the anchor's potential energy out of the integral over $\vec{r}_{0,A}$ and evaluate $\int d\vec{r}_{0,A}$, which yields, A_{Anchor}, the cross-sectional area occupied by the anchor molecule in the bilayer:

$$Q_N^{configurational} = \frac{1}{h^N} \int_{r_1} \cdots \int_{r_{\upsilon_{N-1},N-1}} \exp\left[-\beta U_{N-1}(\vec{r}_1,\ldots,\vec{r}_{\upsilon_{N-1},N-1})\right] \cdot A_{Anchor} \sum_{\varsigma} \exp\left[-\beta u_A(\vec{r}_1,\ldots,\vec{r}_{\upsilon_{N-1},N-1},\varsigma)\right] d\vec{r}_1,\ldots,d\vec{r}_{\upsilon_{N-1},N-1} \tag{5.10}$$

In order to further our evaluation of the anchor's chemical potential, we return to the expressions we developed in *Equation 5.2* and *5.6*:

$$\mu_A = -k_B T \ln\left[\frac{Q_N}{Q_{N-1}}\right] = -k_B T \ln\left[\frac{Q_N^{translational} Q_N^{configurational}}{Q_{N-1}^{translational} Q_{N-1}^{configurational}}\right] \qquad \textit{(5.2 \& 5.6)}$$

Analogous to the system of *N* lipid-plus-anchor molecules, the translational and configurational partition functions of the *N−1* molecule system in the absence of

the anchor are, respectively:

$$Q_{N-1}^{translational} = \prod_j \left[\left(\sqrt{\frac{2m_j \pi k_B T}{h}} \right)^{2\left(N_j - 1\right)} \right] = \prod_j \left[\left(\frac{\sqrt{h}}{\lambda_j} \right)^{2\left(N_j - 1\right)} \right] \tag{5.11}$$

and

$$Q_{N-1}^{configurational} = \frac{1}{h^{N-1}} \int_{r_1} \ldots \int_{r_{\upsilon_{N-1},N-1}} \exp\left[-\beta U_{N-1}\left(\vec{r}_1, \ldots, \vec{r}_{\upsilon_{N-1},N-1} \right) \right] d\vec{r}_1, \ldots, d\vec{r}_{\upsilon_{N-1},N-1} \tag{5.12}$$

Inserting *Equations 5.8, 5.10, 5.11,* and *5.12* into our expression for the chemical potential of the protein's anchor, we have:

$$\beta\mu_A = \ln\left[\lambda_A^2 \right] - \ln \left[\frac{A_{Anchor} \int_{r_1} \ldots \int_{r_{\upsilon_{N-1},N-1}} \exp\left[-\beta U_{N-1}(\vec{r}_1, \ldots, \vec{r}_{\upsilon_{N-1},N-1}) \right] \cdot \sum_{\varsigma} \exp\left[-\beta u_A(\vec{r}_1, \ldots, \vec{r}_{\upsilon_{N-1},N-1}, \varsigma) \right] d\vec{r}_1, \ldots, d\vec{r}_{\upsilon_{N-1},N-1}}{\int_{r_1} \ldots \int_{r_{\upsilon_{N-1},N-1}} \exp\left[-\beta U_{N-1}(\vec{r}_1, \ldots, \vec{r}_{\upsilon_{N-1},N-1}) \right] d\vec{r}_1, \ldots, d\vec{r}_{\upsilon_{N-1},N-1}} \right] \tag{5.13}$$

We can simplify the above equation by defining the probability, $P_{N-1}(\{\vec{r}_{\upsilon_k,k}\})$, of the $N-1$ system particles to exist in a specific arrangement, given by $\{\vec{r}_{\upsilon_k,k}\} \equiv (\vec{r}_1, \ldots, \vec{r}_{\upsilon_{N-1},N-1})$, in terms of the system's interaction energy, $U_{N-1}(\{\vec{r}_{\upsilon_k,k}\})$:

$$P_{N-1}(\{\vec{r}_{\upsilon_k,k}\}) = \frac{\exp\left[-\beta U_{N-1}(\vec{r}_1, \ldots, \vec{r}_{\upsilon_{N-1},N-1}) \right]}{\int_{r_1} \ldots \int_{r_{\upsilon_{N-1},N-1}} \exp\left[-\beta U_{N-1}(\vec{r}_1, \ldots, \vec{r}_{\upsilon_{N-1},N-1}) \right] d\vec{r}_1, \ldots, d\vec{r}_{\upsilon_{N-1},N-1}} \tag{5.14}$$

Equation 5.13 thus takes the form:

$$\beta\mu_A = \ln\left[\lambda_A^2\right] - \ln\left[A_{Anchor} \sum_{\varsigma} \int_{r_1} \cdots \int_{r_{\upsilon_{N-1},N-1}} P_{N-1}(\{\vec{r}_{\upsilon_k,k}\}) \exp\left[-\beta u_A(\vec{r}_1,\ldots,\vec{r}_{\upsilon_{N-1},N-1},\varsigma)\right] d\vec{r}_1,\ldots,d\vec{r}_{\upsilon_{N-1},N-1} \right] \quad (5.15)$$

Furthermore, observe that we may use the standard relation for the expectation of a continuous variable to define:

$$\left\langle \exp\left[-\beta u_A(\varsigma)\right] \right\rangle_{N-1} = \int_{r_1} \cdots \int_{r_{\upsilon_{N-1},N-1}} P_{N-1}(\{\vec{r}_{\upsilon_k,k}\}) \exp\left[-\beta u_A(\vec{r}_1,\ldots,\vec{r}_{\upsilon_{N-1},N-1},\varsigma)\right] d\vec{r}_1,\ldots,d\vec{r}_{\upsilon_{N-1},N-1} \quad (5.16)$$

so that we may write *Equation 5.15* as:

$$\beta\mu_A = \ln\left[\lambda_A^2\right] - \ln\left[A_{Anchor} \sum_{\varsigma} \left\langle \exp\left[-\beta u_A(\varsigma)\right] \right\rangle_{N-1} \right] \quad (5.17)$$

where the average enclosing the exponential is the canonical ensemble average of the contribution to the anchor's Boltzmann factor by its potential energy, $u_A(\varsigma)$. The average encompasses all configurations of the lipid membrane system, excluding the anchor, such that the configurations of the membrane's *N−1* lipid constituents are not influenced by the presence of the N^{th} test particle (anchor). The anchor's potential energy is therefore dependent on the spatial distributions of the membrane's lipids, whereas the summation over ς includes all configurations the specific *anchor* can physically assume.

We want to write the chemical potential of the anchor in terms of the anchor's areal density adsorbed to a single leaflet, δ, of the membrane, which may

be done simply by adding and subtracting $\ln\left[N_{A,\delta}/A_{anchor}\right]$ to the above equation:

$$\beta\mu_{A,\delta} = \ln\left[\rho_{A,\delta}\lambda_A^2\right] - \ln\left[\sum_{\varsigma_{A,\delta}}\left\langle \exp\left[-\beta u_{A,\delta}(\varsigma_{A,\delta})\right]\right\rangle_{N-1}\right] \tag{5.18}$$

To calculate the potential energy of the N-Ras anchor, we need to evaluate the ensemble average. Since $u_{A,\delta}(\varsigma_{A,\delta})$ depends on all possible positions of each monomeric unit of the membrane's lipid chains, to do this exactly would mean analytically expressing the interaction energy between every monomer in the system. As discussed in *Sections 3.2* and *4.2*, the computational expense of this calculation renders it infeasible – however, substituting this calculation with its mean-field approximation is both highly accurate and efficient. The sum inside the natural log of *Equation 5.18* can then be rewritten as the single-molecule, configurational partition function, $q_{A,\delta}$, of the protein's anchor inserted into a leaflet, δ, of the bilayer, within the canonical ensemble of the lipid membrane system. The potential energy of the anchor includes the contributions from the internal energy of the anchor's chains, which can be calculated microscopically using the RIS model without the need for approximations, and the fields generated from the interacting lipid constituents of the membrane acting on the anchor. Expanding $u_{A,\delta}(\varsigma_{A,\delta})$ in terms of these contributions gives us the functional form of the anchor's chemical potential:

$$\beta\mu_{A,\delta}(\mathbf{c}) = \ln\left[\rho_{A,\delta}(\mathbf{c})\lambda_A^2\right] - \sum_{\omega}^{n_A^{tails}} \ln\left[\sum_{\varsigma_{A,\omega,\delta}} \exp\left[\begin{array}{l} -\beta\varepsilon(\varsigma_{A,\omega,\delta}) \\ -\beta\int_{-l}^{l} b_L(z,\mathbf{c})\xi_{A,\omega,\delta}(\varsigma_{A,\omega,\delta},z)dz \\ -\beta\int_{-l}^{l} \pi(z,\mathbf{c})\overline{v}_{A,\omega,\delta}(\varsigma_{A,\omega,\delta},z,\mathbf{c})dz \end{array}\right]\right]$$

or (5.19)

$$\beta\mu_{A,\delta}(\mathbf{c}) = \ln\left[\rho_{A,\delta}(\mathbf{c})\lambda_A^2\right] - \sum_{\omega}^{n_A^{tails}} \ln\left[q_{A,\omega,\delta}(\mathbf{c})\right]$$

The total potential energy of the protein's anchor comprises the individual potential energies from each chain, ω, bonded to the anchor; therefore, in *Equation 5.19* we have generalized the potential energy term as a summation over the contributions from each distinct anchor chain, totaling n_A^{tails} independent chains (assuming anchor chains are independent of each other). We have also specified the dependency of the chemical potential on the curvature tensor for non-planar membranes. As discussed in *Section 5.1*, our lipidated protein of interest, N-Ras, features two distinct hydrocarbon chains bound to its anchor, palmitoyl and farnesyl. Writing *Equation 5.19* explicitly in terms of the partition functions of these individual chains, we have:

$$\beta\mu_{A,\delta}(\mathbf{c}) = \ln\left[\rho_{A,\delta}(\mathbf{c})\lambda_A^2\right] - \ln\left[q_{palmitoyl,\delta}(\mathbf{c})\cdot q_{farnesyl,\delta}(\mathbf{c})\right] \tag{5.20}$$

Equation 5.19/5.20 is of the same form as the chemical potential of the membrane's lipid constituents, given by *Equations 4.55* and *4.31*. The $\pi(z,\mathbf{c})$- and

$b_L(z,\mathbf{c})$-fields acting on the anchor's volume distribution and orientation function, respectively, are calculated for the lipid membrane system, in the absence of the anchor, and are thus inputs to the model with added protein. Therefore, once the configurations of the palmitoyl and farnesyl chains are generated using the RIS method, the partition functions of these chains are known quantities, which can be used in the calculation of the tN-Ras anchor density localized on the bilayer. The density of the membrane-adsorbed anchor can be determined by recognizing the role of the chemical potential in processes involving particle exchange between two or more phases coexisting at equilibrium – that is, the condition of equivalency in the chemical potential of a given species between these phases. In the present context, the 'particles' undergoing such an exchange are the N-Ras lipid-anchors and the 'phases' acting as mediums for the exchange are the bulk solution containing our proteins (reflecting the cell's cytoplasm, where the Ras anchor is synthesized) and the lipid membrane in which they insert. When a bulk solution component integrates with the cell membrane, thermodynamics requires the equality of its chemical potential between the bulk and membrane 'phases' at equilibrium. The rule holds regardless of the structural characteristics of the phases; thus, no matter the geometrical transitions a membrane may undergo, at equilibrium the chemical potential of a given protein's anchor residing in the membrane's aqueous environment is equivalent to the chemical potential of those

inserted into the bilayer's proximal leaflet, δ:

$$\mu_A^{bulk} = \mu_{A,\delta}(\mathbf{c}=0) = \mu_{A,\delta}(\mathbf{c}) \tag{5.21}$$

The terms composing the chemical potential (namely the density and configurational partition function of the given species), however, are modulated by the local physical form of the particular host medium. For the membrane-inserted anchor, under the direct influence of the mean-fields generated in the lipid membrane system, this means that these terms are functions of the local contour of the membrane and are governed by the architecture of the membrane's constituent lipids and the kinetically controlled degree of lipid transbilayer reorganization caused by membrane bending. How the adsorption tendencies of a lipidated protein change with perturbations in these structural elements is examined by combining the equilibrium condition of *Equation 5.21* with our expression for the anchor's chemical potential in *Equation 5.20*:

$$\mu_{A,\delta}(\mathbf{c}=0) = \mu_{A,\delta}(\mathbf{c}) \;\rightarrow$$

$$\ln\left[\rho_{A,\delta}(\mathbf{c}=0)\lambda_A^2\right] - \ln\left[q_{palmitoyl,\delta}(\mathbf{c}=0)\cdot q_{farnesyl,\delta}(\mathbf{c}=0)\right] \tag{5.22}$$
$$= \ln\left[\rho_{A,\delta}(\mathbf{c})\lambda_A^2\right] - \ln\left[q_{palmitoyl,\delta}(\mathbf{c})\cdot q_{farnesyl,\delta}(\mathbf{c})\right]$$

and solving for the density of the protein's anchor inserted into a membrane under an induced curvature, $\mathbf{c}$, relative to that on a planar membrane, $\mathbf{c} = 0$, in terms of the ratio of their corresponding single-chain partition functions:

$$\frac{\rho_{A,\delta}(\mathbf{c})}{\rho_{A,\delta}(\mathbf{c}=0)} = \frac{q_{palmitoyl,\delta}(\mathbf{c}) \cdot q_{farnesyl,\delta}(\mathbf{c})}{q_{palmitoyl,\delta}(\mathbf{c}=0) \cdot q_{farnesyl,\delta}(\mathbf{c}=0)} \tag{5.23}$$

Of course, the protein density need not be relative to that on a planar membrane; the same methodology can be applied for describing the protein adsorption density on a membrane of any geometry, relative to that on a membrane of any 'reference' geometry. For the quantitative comparison of the relative density of the membrane-localized N-Ras lipid-anchor calculated by our theory with the experimental results obtained by J. B Larsen *et al.* [177], we apply this method to obtain anchor densities on spherical liposomes over a range of liposome diameters, from 400 nm (which simulates locally near-planar bilayers) to highly curved liposomes 40 nm in diameter, all relative to the 400 nm value:

$$\frac{\rho_{A,\delta}(D)}{\rho_{A,\delta}(D=400\text{ nm})} = \frac{q_{palmitoyl,\delta}(D) \cdot q_{farnesyl,\delta}(D)}{q_{palmitoyl,\delta}(D=400\text{ nm}) \cdot q_{farnesyl,\delta}(D=400\text{ nm})} \tag{5.24}$$

The ratio which calculates the increase in peptide density on the membrane when liposome diameter is reduced by a factor of ten, $\rho_{A,\delta}(40\text{ nm}) \big/ \rho_{A,\delta}(400\text{ nm})$, is the designated quantitative measure for how anchor adsorption changes from membranes of low curvature to membranes of high curvature, used as the basis for comparison between different types of liposomes and between theory and experiment. We refer to the ratio given in *Equation 5.24* as the *relative recruitment ratio*, *RR*, and the value evaluated specifically at $D = 40$ nm as RR^{40}.

Information regarding the experimental materials and methods used by our affiliates at the University of Copenhagen can be found in [177]. Here, we provide a (very) brief explanation of experimental techniques employed to acquire the data used for comparison with our theoretical results. Liposomes are prepared using a lipid hydration method described in [177, 261, 269]. The protein used for the study is the minimal membrane anchor of the N-Ras isoform (tN-Ras), which comprises the N-terminal heptapeptide with palmitoyl and farnesyl lipid moieties. The Single Liposome Curvature (SLiC) assay is used for studying the effect of membrane composition on the preferential localization of tN-Ras. Single liposomes of various sizes are immobilized on a passivated glass surface, with adequate spatial distancing for optical resolution. tN-Ras, labelled with Alexa-488, is free to bind from solution and left to equilibrate. Liposome diameter and tN-Ras density on liposomes are quantified by measuring the integrated fluorescence intensity of individual fluorescently marked liposomes and tN-Ras with a combination of confocal microscopy and dynamic light scattering. The single liposome measurements allow for the calculation of the density of tN-Ras on individual liposomes as a function of membrane curvature. Error-weighted fitting of the experimental Ras adsorption data with an off-set power function is used to determine the curvature-dependent recruitment of tN-Ras by the bilayer, given by:

$$\rho_{tN-Ras} = D_0 + \chi \cdot (D_{liposome})^{\omega} \tag{5.25}$$

Where $\rho_{tN\text{-}Ras}$ is the peptide absolute density, D_0 is the off-set peptide density value, $D_{liposome}$ is the liposome diameter, and both χ and ω, in this context, represent fitting parameters. From the obtained fits, the adsorption density of tN-Ras on liposomes of any diameter (in nm), relative to that on liposomes 400 nm in diameter, can be calculated:

$$RR_{\exp} = \frac{\rho_{tN-Ras}^{D_{liposome}}}{\rho_{tN-Ras}^{400\,\mathrm{nm}}} = \frac{D_0 + \chi \cdot (D_{liposome})^{\omega}}{D_0 + \chi \cdot (400\ \mathrm{nm})^{\omega}} \tag{5.26}$$

Specifically, the experimental relative recruitment ratio for liposomes 40 nm in diameter, RR^{40}, is given by:

$$RR_{\exp}^{40} = \frac{\rho_{tN-Ras}^{40\,\mathrm{nm}}}{\rho_{tN-Ras}^{400\,\mathrm{nm}}} = \frac{D_0 + \chi \cdot (40\ \mathrm{nm})^{\omega}}{D_0 + \chi \cdot (400\ \mathrm{nm})^{\omega}} \tag{5.27}$$

The RR_{exp}^{40} value is reported as the average ± standard error of the mean (SEM) of N independent experiments; it is used to compare the curvature-mediated recruitment of tN-Ras by liposomes of different lipid compositions and between experimental and theoretical results.

5.3 Results I.II: Membrane Curvature and Lipid Composition Synergize to Regulate tN-Ras Adsorption via Changes in Lateral Pressure Fields

In this section we present the second set of results of this work using the

Generation I theory, displaying our calculations for bilayer structural quantities and distributions of interest (area per lipid, hydrophobic thickness, lateral pressure profiles) as well as the theoretical and experimental findings regarding the membrane-adsorption tendencies of the lipidated protein, tN-Ras. These properties are studied in membranes of various compositions, liposome sizes, and degrees of lipid inter-leaflet packing asymmetry. Experiments are conducted by Dimitrios Stamou's research group and collaborators at the University of Copenhagen.

Traditionally, it has been recognized that the sorting and trafficking of lipidated proteins is influenced by the unique compositional properties of distinct, local membrane domains [259, 270-278]. Membrane recruitment of lipidated proteins has also been recently discussed within the context of membrane morphology/curvature [164, 261]. The results presented here follow from investigating the integrated effects of bilayer composition and curvature, revealing a synergistic regulation of protein–membrane interactions by these highly conserved features of biological membranes. Specifically, we examine how the key structural elements of membrane lipids, namely the degree of saturation of the aliphatic tails, the length of the tails (bilayer thickness), and the size of the headgroup, modulate the agency of the membrane's curvature-induced recruitment of the tN-Ras anchor.

Additionally, we report our findings regarding an important mechanism driving the localization of the protein on the membrane, elucidated by our molecular field theory. This contribution is a central objective of this study, as such information is generally not accessible in an experimental setting and coarse-grained theories do not contain the level of detail necessary for insight into behaviors that are so strongly regulated at the atomic scale. For example, while macroscopic structural information, such as bilayer thickness, can be measured experimentally, technology with the sensitivity to determine atomic-scale distributions inside the hydrophobic region, arising from the conformational heterogeneity of the lipid tails, is lacking. The pressure profile through the depth of the membrane core is one such distribution, which has proved to be fundamental in delineating the motivations behind membrane–lipidated protein interactions. Our theory is able to capture organizational and thermodynamic characteristics of the systems that are crucial for determining how the membrane operates and interacts with its environment. The atomic- or small monomeric-level detail of the system provided by the theory grants a mechanistic understanding of how the curvature-mediated, selective recruitment of the tN-Ras anchor is influenced by the architecture of the membrane lipids.

Lipid Tail Saturation Modulates the Relative Adsorption Densities of the tN-Ras Anchor as a Function of Membrane Curvature

We first consider how tN-Ras anchor localization is affected by the combined influence of the degree of saturation of the lipid chains composing the targeted liposome membrane and changes in liposome diameter. Pure DOPC and POPC liposomes are used for comparison, as the two bilayers have similar average hydrophobic thicknesses (27.4 Å and 27.0 Å, respectively) and are distinguished by the one, fully saturated chain in the latter: DOPC has two oleoyl, eighteen carbon, monounsaturated chains (di$C_{18:1}$) and POPC contains one oleoyl chain and one palmitoyl, sixteen carbon, fully saturated chain ($C_{16/18:1}$). Both theoretical and experimental analyses of these systems are conducted in the liquid-disordered phase at a constant environmental temperature of 295 K. *Figure 5.5* presents plots of the normalized tN-Ras density on pure DOPC and POPC liposomes as a function of liposome diameter. The *normalized*, or *relative*, protein density refers to the density ratio of membrane-adsorbed tN-Ras anchor on liposomes of a given diameter to that on liposomes 400 nm in diameter (nearly planar), as given by *Equations 5.24* (theory) and *5.26* (experiment). Comparison of these relative densities facilitates a more effective measure of how the adsorption behavior of the protein is influenced by individual membrane features and provides a basis for the parallel analysis of theoretical and experimental results. Specifically, the ratio at D = 40 nm (RR^{40}), is used as a measure for comparing the effects of high membrane curvature on protein localization between different types of bilayers.

The lines through the experimental data points are the off-set power function fits, described previously, and the black (or red, for DLPC in a following subsection) markers overlaid on the plots are the relative protein densities calculated by our molecular theory.

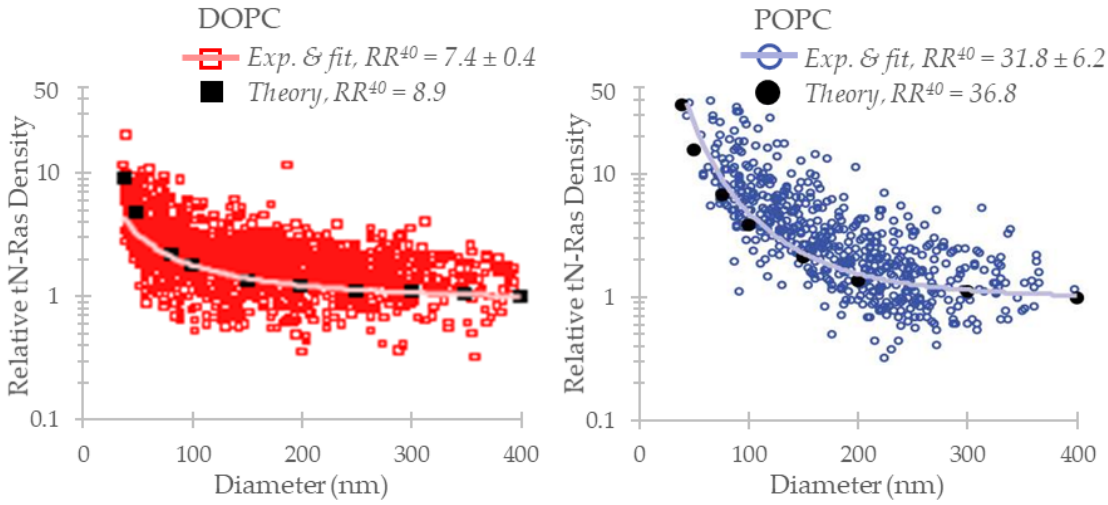

Figure 5.5) **Normalized tN-Ras adsorption density as a function of liposome diameter, modulated by lipid tail saturation.** Experimental tN-Ras density as a function of liposome diameter (normalized to the density at 400 nm in diameter) for liposomes prepared from DOPC lipids ***(left**, bright red markers)* with corresponding off-set power function fit *(pale red line)* and POPC lipids *(**right**, dark blue markers)* with corresponding off-set power function fit *(pale blue line)*. The black square and circular markers, respectively, represent the corresponding normalized densities of the tN-Ras anchor calculated by the molecular field theory for each type of liposome. The recruitment ratio, RR^{40}, represents the increase in tN-Ras density when reducing membrane diameter by a factor of 10 (a ratio of 40 nm to 400 nm in liposome diameter), as quantified either from power function fitting to the experimental data (RR^{40} is reported as the average mean ± SE of n_{DOPC} = 9 and n_{POPC} = 8 independent experiments) or from the theoretical calculations. The sensitivity of tN-Ras to membrane curvature is more pronounced in membranes comprised of lipids with a greater degree of tail saturation.

Both plots clearly demonstrate the strong sensitivity to curvature of tN-Ras, with a dramatic increase in adsorption, regardless of membrane type, as

membrane curvature increases (decreasing liposome diameter). Theoretical results closely agree with experimental observations. As expected, the magnitude of Ras adsorption and the degree of curvature sensitivity of the protein proves to be quite compositionally dependent. The recruitment ratios at D = 40 nm for DOPC ($RR^{40}_{theory} = 8.9$; $RR^{40}_{exp} = 7.4 \pm 0.4$) and POPC ($RR^{40}_{theory} = 36.8$; $RR^{40}_{exp} = 31.8 \pm 6.2$), a more than four-fold increase in POPC, with a 128% (theory) and 131% (experiment) difference between the two bilayers, indicate significant curvature-driven adsorption selectivity for membranes comprised of lipids with a higher degree of tail saturation.

By also considering the experimentally measured *absolute* adsorption densities of tN-Ras in the different membranes, we can decipher if the change in the bilayer's selective recruitment of the protein as a function of membrane curvature originates from dissimilarity in protein localization solely on curved membranes, solely on locally flat membranes, or both. For each individual data set, Larsen *et al*. [177] calculates the absolute density from the off-set power function fit at five specific liposome sizes. These values are used to calculate the average absolute density on pure DOPC and pure POPC membranes for the five liposome diameters, presented in *Figure 5.6*, along with the standard error of the mean (SEM) from $n_{DOPC} = 9$ and $n_{POPC} = 8$ independent experiments. For liposomes larger than roughly 90 nm in diameter, we find a greater absolute density of tN-

Ras on DOPC membranes than on POPC membranes, while in highly curved liposomes (diameters less than 90 nm), the absolute density of tN-Ras adsorbed on POPC membranes surpasses that on membranes comprised of DOPC. This highlights the complex interplay between membrane composition and curvature, demonstrating one aspect of why the influences from these features of organelle and plasma membranes couple to form a highly conserved and regulated phenotype – the specific combination of both properties accounts for the observed trends in Ras adsorption on the membrane.

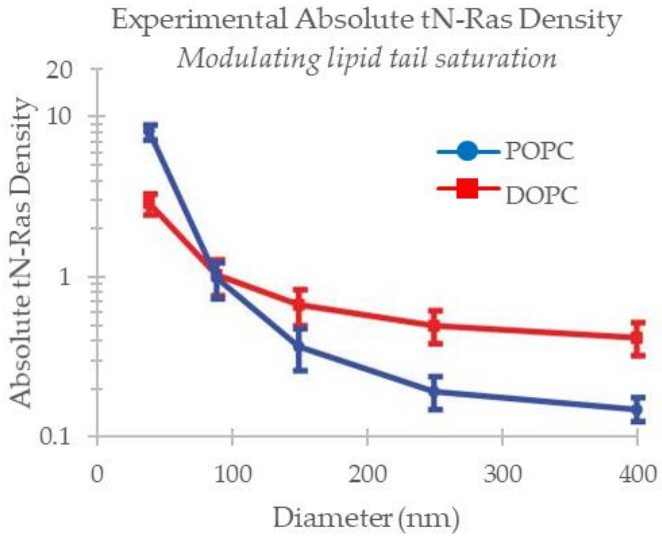

Figure 5.6) **Experimentally determined absolute density of tN-Ras as a function of liposome diameter, modulated by lipid tail saturation.** The average absolute tN-Ras density on POPC *(blue)* and DOPC *(red)* membranes, calculated from the power function fits to each individual experimental data set for five liposome diameters, demonstrating the coupling between membrane composition and shape in protein–membrane interactions. The plot indicates enhanced sensitivity of tN-Ras to membrane curvature on the more saturated POPC bilayers while a stronger protein–membrane interaction exists with the less saturated DOPC bilayers for diameters > 90 nm, or flatter membrane systems.

Lateral Pressure Profile in the Membrane as an Important Mechanism Driving the Recruitment of Lipidated Proteins

Before continuing with our findings for the other lipid systems, we address the question concerning how membrane composition and curvature might be 'sensed' by lipidated proteins to result in the preferential adsorption behavior of tN-Ras observed in the DOPC and POPC bilayers – in other words, what physical or chemical mechanism(s) drives a protein's curvature-mediated discrimination between different types of membranes? Fundamentally, the answer stems from the chemical potential of the protein's anchor, driven to equilibrate between the bulk and membrane-adsorbed states, as discussed in *Section 5.2*. Expanding the chemical potential, and consequently the partition function, of the anchor mathematically *(Equation 5.19)*, we can probe further into which contributions have a direct and meaningful impact on the protein's sensing ability. The two curvature-dependent contributions to the protein anchor's partition function are the orientational attractive interaction fields among the hydrophobic segments of the lipid tails, $b_{i,L}(z,\mathbf{c})$, and the product of the fields governing the molecular packing through the membrane's hydrophobic region, $\pi(z,\mathbf{c})$, and the volume of the anchor's chains, integrated over the thickness of the bilayer. Comparison of *Equation 5.19* with *Equation 4.40* clearly depicts the partition function of the protein's anchor as an explicit exponential function of the membrane's lateral

pressure profile. Hence, the differences in the adsorption trends of tN-Ras on membranes of varied size and lipid constituency can theoretically be attributed to changes in the lateral pressure generated by the lipids of the host membrane. Several examples of this connection are illustrated graphically in the following discussion and subsequent sub-sections below.

First, note that in *Section 4.4* we suggested an approximation to the lateral pressure expression that neglected the contribution from the Maier-Saupe attractive fields in a liquid-disordered system, in order to use the minimum physics required to efficiently capture the system's thermodynamics. In *Figure 5.7* we demonstrate that, in our current model, the effect of the attractive interactions on the behavior of our lipidated protein is also negligible. DOPC and POPC bilayers are used as example systems here, exhibiting near-equivalent adsorption densities of tN-Ras calculated with and without the inclusion of the $b_{i,L}(z,\mathbf{c})$-fields in the theory *(dark, solid lines versus pale, dashed lines, respectively)*, confirming the suitability of the approximation for our purposes. Though, it is important to remember that the Maier-Saupe orientational ordering terms play a principal role in engendering the structural properties of model bilayers that distinguish *liquid-ordered* and *gel* phases from the *liquid disordered* phase. We advise that accurate analyses of ordered phases in lipid membrane theoretical models require the inclusion of this attractive energy contribution [42, 161, 164].

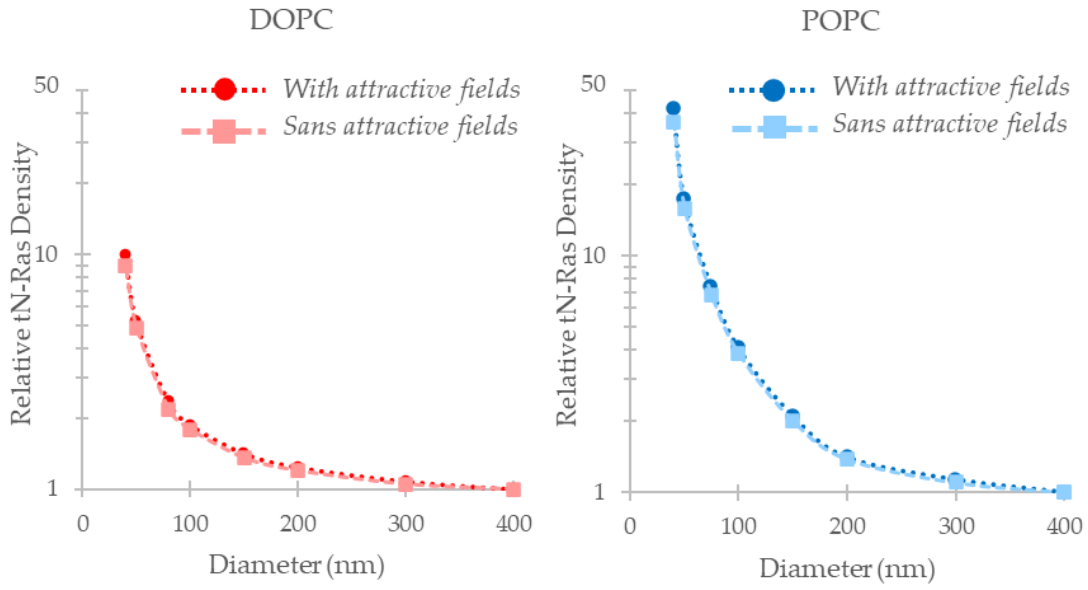

Figure 5.7) **Theoretical tN-Ras adsorption with and without attractive energy contribution.** The plots above demonstrate that for our model system, which isolates the lipid bilayer in the absence of an aqueous environment, attractive interactions among the hydrophobic lipid tails have a negligible effect on the adsorption of tN-Ras on lipid membranes in the liquid-disordered phase. Shown here are the curvature-dependent, normalized densities of tN-Ras on DOPC liposomes ***(left)*** and on POPC liposomes ***(right)***, as calculated by the molecular theory, including the attractive interaction component (*dark red circles in DOPC; dark blue circles in POPC)* and without the attractive energy term *(pale red squares in DOPC; pale blue squares in POPC)*; the dotted and dashed lines, respectively, are to guide the eye.

Attention, then, is turned to the distribution of lateral pressure through the width of the bilayer as the possible acting force motivating a lipidated protein's ability to discriminate membrane type and curvature. Theoretical [42, 44, 279] and experimental [94, 164, 280-282] studies have demonstrated the explicit dependence of protein partitioning in membranes on the lipid packing density within the bilayer. Lipid packing is expressed in our molecular field theory as the

combination of the area per lipid and the lateral pressure profile through the bilayer's width. As indicated in *Table 5.1* below, when curving a planar membrane to a spherical liposome 40 nm in diameter, our calculation of the corresponding relative increase in area within the hydrophobic–hydrophilic interfacial plane of the expanded leaf, per total number of bilayer lipids, is very similar between DOPC and POPC membranes (14.17% and 13.95%, respectively). This amounts to just a 1.56% difference in the areal response to curvature between these two bilayers. Moreover, whereas the POPC system demonstrates a much larger, curvature-driven protein recruitment ability, relative to the DOPC system, the changes in molecular area contradict this trend, with the molecular area in the POPC bilayer evincing lower sensitivity to membrane curvature (given by the calculated percent changes above). These data suggest that composition-dependent variation in the area per lipid within the membrane is likely not the primary underlying factor driving the observed pronounced differences in the recruitment of tN-Ras between the different types of bilayers as a function of membrane curvature. This conclusion is in agreement with previous studies on amphipathic helix insertion [283].

Perhaps a more germane measure of the 'change in molecular area' when curving a bilayer in which lipids may undergo transbilayer diffusion is the interfacial area *per lipid in the expanded leaf* $\left({}^{A(z=l,\,\mathbf{c})}\big/_{N_E}\right)$, which takes into account

the bilayer's composition-dependent relaxation ratio, rather than the interfacial area *per total number of lipids in the bilayer* $\left({}^{A(z=l,\,\mathbf{c})}/_{N}\right)$. The percent changes in ${}^{A(z=l,\,\mathbf{c})}/_{N_E}$ from planar bilayers to spherical liposomes 40 nm in diameter are 8.24% and 9.80% for DOPC and POPC, respectively. A 17.32% difference between these values demonstrates a higher degree of variation in the areal response to curvature than we see using the previous metric. Additionally, this response is stronger in the POPC system than in the DOPC system, correlating with the higher recruitment ability with curvature in the former. This indicates that curvature-driven changes in the interfacial molecular area of the expanded leaflet, when accounting for lipid transbilayer diffusion, could influence the selectivity of lipidated proteins for lipid type. However, whether this influence controls the selective adsorption of Ras to any meaningful degree can be better established by analyzing other relevant factors and evaluating additional types of lipid bilayers for a sufficient sample size.

Table 5.1) **Theoretical results for area per lipid, membrane thickness, integrated lateral pressure, and recruitment ratio (RR^{40}).** All calculated molecular areas are in excellent agreement with experimental findings [178, 182, 282]. Similarity in the percent change in molecular area from planar to spherical geometry between the bilayers being compared suggests differences in the integrated lateral pressure, $\Delta P_{geometry}$ (or simply ΔP here), rather than molecular area to be the more influential driving factor for differences in the membrane's ability to recruit lipidated proteins. The effects of membrane curvature on bilayer thickness are found to be negligible.

	Area per Lipid *(total)* **(nm²/molecule)**			**Area per Lipid** *(expanded leaf)* **(nm²/molecule)**			**Membrane Thickness (nm)**			**Integrated Lateral Pressure (bar·Å)**				RR^{40} *theory*
	Planar	*40 nm*	*% change*	*Planar*	*40 nm*	*% change*	*Planar*	*40 nm*	*% change*	*Planar*	*40 nm*	*-ΔP*	*-% change*	
DOPC	0.694	0.792	14.2	1.387	1.502	8.2	2.740	2.738	0.08	4800	3699	1101	22.9	8.9
DOPC + 25% DOPE	0.688	0.785	14.2	1.376	1.489	8.2	2.740	2.740	0.00	4560	3626	934	20.5	7.7
DOPC + 50% DOPE	0.681	0.777	14.2	1.362	1.474	8.2	2.740	2.740	0.00	4320	3507	813	18.8	6.5
POPC	0.672	0.766	14.0	1.344	1.476	9.8	2.699	2.688	0.41	5170	3197	1973	38.2	36.8
DMPC	0.621	0.699	12.5	1.243	1.341	7.9	2.433	2.428	0.22	4420	2929	1491	33.7	17.7
DLPC	0.627	0.693	10.6	1.253	1.352	7.9	2.068	2.061	0.37	4580	2620	1960	42.8	28.3

Considering the second contribution to membrane lipid-packing density, the lateral pressure, the theory reveals that by curving the bilayer, the symmetry in the lateral pressure profile becomes distorted, nonuniformly increasing the pressure in the compressed leaf and relieving the pressure in the expanded leaf, as shown in *Figure 5.8*.

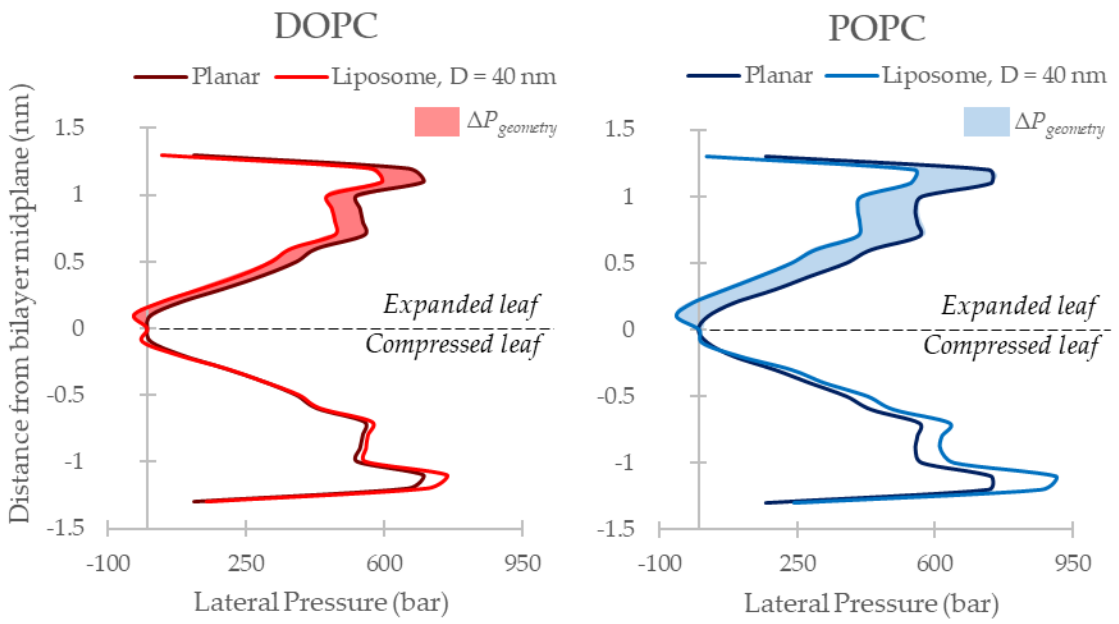

Figure 5.8) **Membranes composed of lipids with higher chain saturation demonstrate greater relief in lateral pressure in curved liposomes.** Lateral pressure profiles along the bilayer normal, through the hydrophobic width of DOPC ***(left**, red)* and POPC ***(right**, blue)* membranes, for both planar *(dark line)* and spherical (40 nm in diameter) *(pale line)* geometries. The top half of each graph represents the monolayer that expands and experiences a decrease in lateral pressure with curvature; the bottom half represents the monolayer that is compressed and experiences a rise in lateral pressure with curvature. The curvature-dependent relief in the lateral pressure in the expanded monolayer, $\Delta P_{geometry}$, is calculated as the total area between the curves *(shaded area)*. Molecular field theory calculations reveal a greater curvature-mediated relief in lateral pressure for POPC *versus* DOPC.

There are two metrics for the change in lateral pressure, integrated over the width of the expanded leaf (or of either leaf in planar bilayers, as they are symmetric), that are calculated by the theory to aid in visual comparative analyses between different lipid systems. These are $\Delta P_{geometry}$, referring to the drop in integrated lateral pressure that *occurs from bending* a planar bilayer to a spherical bilayer, 40 nm in diameter, within a given type of lipid membrane (e.g., DOPC *or* POPC)

(*Figure 5.9, bottom left*), and $\Delta P_{lipid\text{-}type}$, assigned to the difference in integrated lateral pressure *between different types of lipid bilayers* (e.g., between DOPC *and* POPC), for a given membrane curvature (specifically, for planar bilayers and for spherical bilayers 40 nm in diameter), (*Figure 5.10, bottom left*). The same methodologies used for these calculations are also applied to the two measures of molecular area discussed above (i.e., $\Delta a_{geometry}$, $(\Delta a/x_E)_{geometry}$, $\Delta a_{lipid\text{-}type}$, and $(\Delta a/x_E)_{lipid\text{-}type}$; *top panels of Figures 5.9 and 5.10, respectively*) to better perceive the correlations between the different bilayer properties and Ras adsorption behavior discussed in the text. Note that graphs depicting the change in integrated lateral pressure from planar to curved membranes or the difference in integrated lateral pressure between two types of bilayers, such as shown in *Figures 5.9* and *5.10* below, are presented as negatives of the values obtained from the corresponding calculations. This standardizes the effects of membrane curvature changes on all properties under consideration, for ease in visual comparisons (for example, an expansion of a membrane leaflet would result in an *increase* in molecular area but a *decrease* in lateral pressure).

$\Delta P_{geometry}$ in *Figure 5.9, bottom left*, quantifies the area of the shaded region in *Figure 5.8*, which is the position-dependent relief in the lateral pressure distribution experienced by the expanded leaf of a membrane that bends from planarity to, in this case, a 40 nm (diameter) spherical liposome.

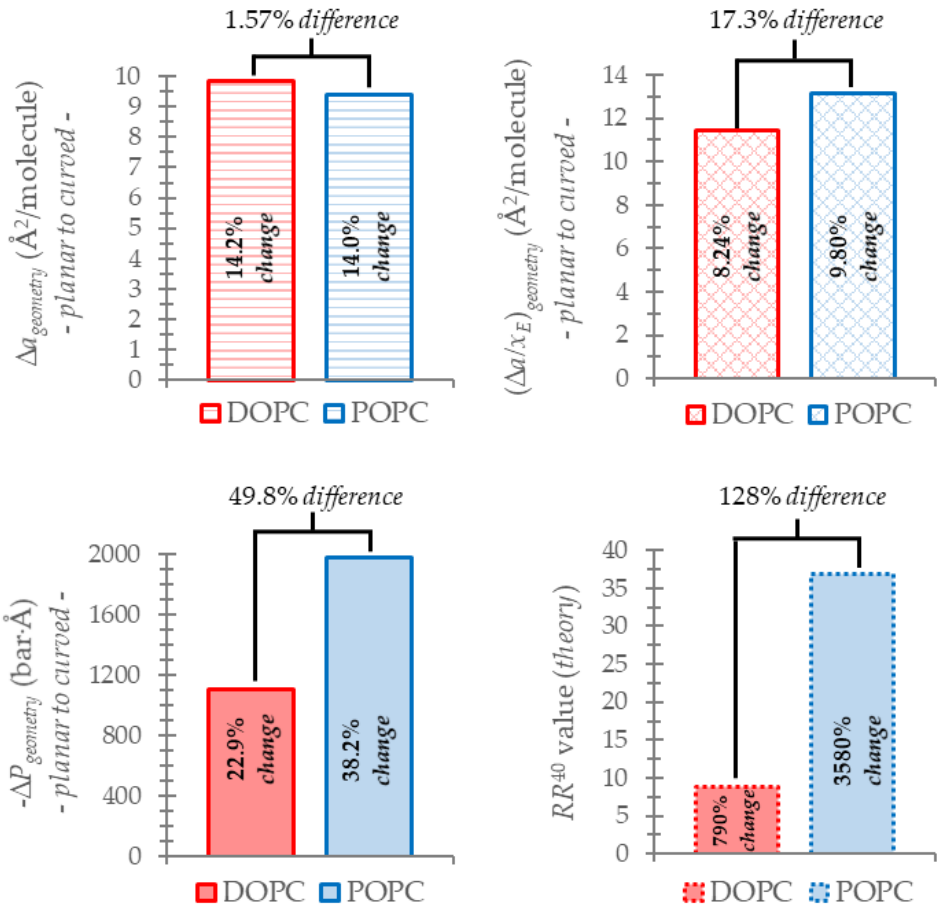

Figure 5.9) **Quantification of comparisons in area and lateral pressure changes with membrane curvature between DOPC and POPC bilayers.** Quantification of $\Delta a_{geometry}$ ***(top left)***, $\Delta(a/x_E)_{geometry}$ ***(top right)***, and $-\Delta P_{geometry}$ ***(bottom left)*** in the expanded leaflet from bending DOPC *(red)* and POPC *(blue)* membranes from a planar to a spherical (40 nm diameter) geometry. Both $\Delta(a/x_E)_{geometry}$ and $-\Delta P_{geometry}$ demonstrate a higher curvature-induced response in the more saturated POPC bilayers, with the latter demonstrating a much larger response and greater compositional variation than either of the areal metrics. This correlates with the higher RR^{40} value of tN-Ras in POPC, relative to DOPC membranes ***(bottom right)***.

We find a 22.9% decrease in integrated lateral pressure in DOPC bilayers (from planar to curved forms) and a 38.2% decrease in POPC. This results in a 49.8% difference between the two, a substantial disparity in the response of the lateral pressure to membrane curvature between the two systems, indicating a much

stronger correlation with the theoretical and experimental adsorption density trends in these membranes (from *Figure 5.5* and as quantified by the RR^{40} value in *Figure 5.9, bottom right*) than demonstrated by either of the molecular area metrics.

Next we examine the different curvature regimes of $\Delta P_{lipid\text{-}type}$, $\Delta a_{lipid\text{-}type}$, and $(\Delta a/x_E)_{lipid\text{-}type}$ with reference to the corresponding changes in the experimental absolute tN-Ras adsorption densities, $(\Delta\rho_{tN\text{-}Ras})_{lipid\text{-}type}$ (*Figure 5.9, bottom right; also see Figure 5.6*). Comparing $-\Delta P_{lipid\text{-}type}$ in planar *(pink)* bilayers with that in highly curved *(orange)* bilayers reveals a shift in the weight of the lateral pressure contribution between the compositionally different membranes. In the former, the integrated lateral pressure in POPC bilayers is greater than that in DOPC. As liposome diameter decreases, the degree of curvature-driven relief in lateral pressure diverges between the systems, with the effect more pronounced in POPC relative to DOPC bilayers – enough so to shift the lower lateral pressure to the POPC system in the highly curved membrane regime. This corresponds to the shift observed in the experimental absolute density curves in *Figures 5.6* and the absolute density changes quantified by $(\Delta\rho_{tN\text{-}Ras})_{lipid\text{-}type}$, an indication that the lower adsorption ability of the protein in a POPC *planar* bilayer, relative to DOPC, might be the result of the higher integrated lateral pressure in the former, while the augmented protein adsorption ability in a POPC, *highly curved liposome*, relative to DOPC, could be due to the sufficiently diminished integrated lateral pressure in

the POPC liposome, relative to DOPC in this regime. $\Delta a_{lipid\text{-}type}$, and $(\Delta a/x_E)_{lipid\text{-}type}$ do not exhibit such a correlation with the protein's adsorption profiles.

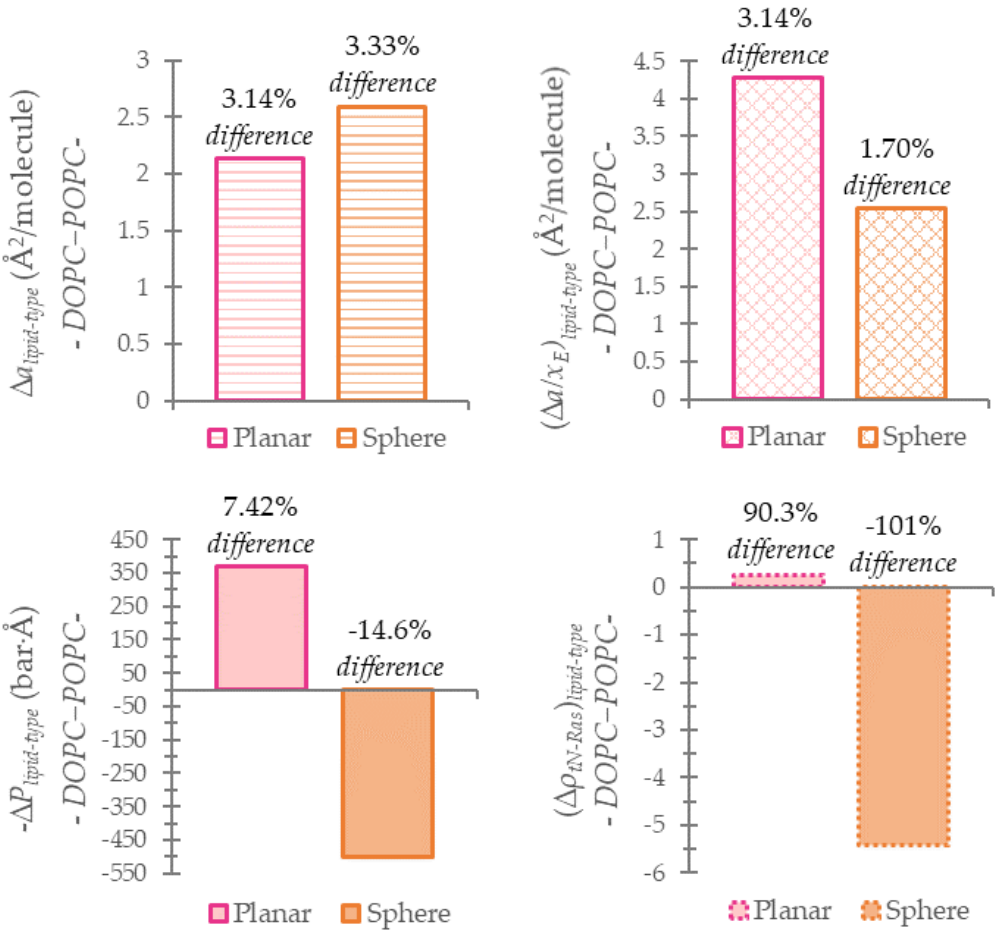

Figure 5.10) **Quantification of comparisons in area and lateral pressure changes with changes in membrane composition between planar and spherical bilayers.** Quantification of the compositional-dependent change, within the expanded leaflet, in the area per total number of lipids, $\Delta a_{lipid\text{-}type}$ ***(top left)***, the area per number of lipids in the expanded leaf, $\Delta(a/x_E)_{lipid\text{-}type}$ ***(top right)***, the integrated lateral pressure, $-\Delta P_{lipid\text{-}type}$ ***(bottom left)***, and the experimental absolute tN-Ras density, $\Delta(\rho_{tN\text{-}Ras})_{lipid\text{-}type}$ ***(bottom right)***, between DOPC and POPC membranes, comparing such for planar bilayers *(pink)* and spherical liposomes 40 nm in diameter *(orange)*. The trends in the integrated lateral pressure in both the planar and highly curved regimes correlate well with adsorption tendencies of the protein. The molecular area metrics do not exhibit such a correlation.

To summarize, the data thus far have indicated the possible causal relationship: greater curvature-induced relief in lateral pressure (larger overall reduction in lateral pressure in the expanded leaflet caused by bending the membrane) ≡ greater *curvature-sensitivity* of tN-Ras, which enhances the protein's adsorption ability.

The connection between the adsorption density of lipidated proteins in the membrane and the lateral pressure profile in the membrane's hydrophobic core can be intuitively and mechanistically interpreted in the context of the amount of *work* needed by the protein to insert its anchor into the densely packed lipid tail region of a bilayer leaflet. Recall that when the membrane bends, crowding of lipids in the compressed leaf causes a rise in the lateral pressure, while the expanded leaf experiences a relief in lateral pressure. The greater this relief, the easier it is (less work is required) for the anchor's chains to insert into the expanded leaf of the bilayer. Hence, the physics of protein recruitment by the membrane is tied to the amount of $P\Delta V$ work required for insertion of the anchor. For a given anchor motif, the change in volume upon insertion is equivalent in all types of host membranes, at all membrane curvatures. Therefore, mechanistically, differences in the work requirement are contingent only on the average lateral pressure within the bilayer leaflet in contact with the protein, with higher pressures corresponding to increased difficulty for anchor adsorption and greater curvature-induced *relief*

in pressure driving increased localization of the protein.

The above results demonstrate how the localization of tN-Ras may be fine-tuned by the synergistic coupling of a lipid membrane's macroscopic geometry and the composition of its lipid components, the latter of which is effectuated by variation in the degree of saturation of the lipid aliphatic tails. To assess the protein's behavior in different membrane environments, we next examine how the adsorption tendencies of tN-Ras are modulated by two other biologically relevant lipid shape factors: hydrocarbon tail length and size of the lipid headgroup. We begin with the former.

Lipid Chain Length Modulates the Relative Adsorption Densities of the tN-Ras Anchor as a Function of Membrane Curvature

Varying the number of methylene groups that construct the lipid chains effectively assigns different thicknesses to the hydrophobic region, a feature that, to our knowledge, has yet to be examined for its potential role in regulating curvature-dependent protein recruitment by the membrane. We analyze the relatively thicker pure DMPC (diC_{14}) membrane system for comparison with the likewise fully saturated, but thinner, pure DLPC (diC_{12}) system. The environmental temperature is raised for these systems to 305 K, to accommodate the high melting temperature of DMPC (T_m^{DMPC}= 297 K), ensuring all systems are well within the liquid-disordered phase. The hydrophobic thicknesses of DMPC

and DLPC have previously been measured at 303 K using a combination of small-angle X-ray and neutron scattering data to be 25.7 ± 0.5 Å and 21.7 ± 0.4 Å, respectively, with a ~16.9% difference between the two [284]. Our molecular model calculates a hydrophobic thickness of 24.3 Å for DMPC and 20.7 Å for DLPC bilayers (a 16.2% difference) under the same conditions, matching well with the experimental values *(see Table 5.1 for all membrane hydrophobic thicknesses, calculated by the theory)*.

The dependence of tN-Ras adsorption on liposome size that was observed in the POPC and DOPC systems is repeated in both the DMPC and DLPC membranes, as expected. The relative and absolute adsorption densities of the protein as functions of liposome diameter are plotted in *Figure 5.11*. We quantify the $D = 40$ nm recruitment ratio of DMPC as $RR^{40}_{theory} = 17.7$; $RR^{40}_{exp} = 15.4 \pm 2.9$ and of DLPC as $RR^{40}_{theory} = 28.3$; $RR^{40}_{exp} = 31.0 \pm 3.7$, indicating that decreasing membrane thickness by two carbon units causes an approximately two-fold increase in the curvature-driven, selective localization of tN-Ras, with a 48% (theory) and 70% (experiment) difference in the RR^{40} value between the two bilayers. The average absolute density plots shown in the bottom graph of *Figure 5.11*, obtained from $n_{DMPC} = 7$ and $n_{DLPC} = 6$ independent experiments for five liposome diameters, demonstrate similar tN-Ras densities on both DMPC and DLPC in large diameter liposomes, or locally near-planar membranes. As the membrane bends to higher curvatures

(decreasing liposome diameter), however, the density curves diverge, with greater protein adsorption on the short-tailed DLPC liposomes. The trends indicate distinctive sensitivity to curvature, tuned by bilayer thickness, as the origin of the increased RR^{40} value in the DLPC system, rather than differential affinity for a specific bilayer type alone. The molecular theory fully captures the curvature-dependence of tN-Ras in these systems and the preferential adsorption of the protein on DLPC liposomes as diameter decreases, relative to the DMPC system, albeit while following the lower range of the particular experimental data set shown *(Figure 5.11, top panel)*.[14]

[14] The experimental relative protein density plots presented in this work are representative data sets of a single, independent experimental run – and not necessarily that which best matches with the theoretical curves. Multiple experiments are performed for each bilayer (between 6 and 9 runs for the pure-component systems), from which the RR^{40} value is calculated as an average, based on the off-set power function fits through the data of each experiment. Therefore, a comparison of experimental and theoretical RR^{40} values is a better indicator of quantitative agreement than the displayed density plots, which are rather used to establish and compare trends in the data. Comparison of the RR^{40} values for all systems under study indicates excellent agreement.

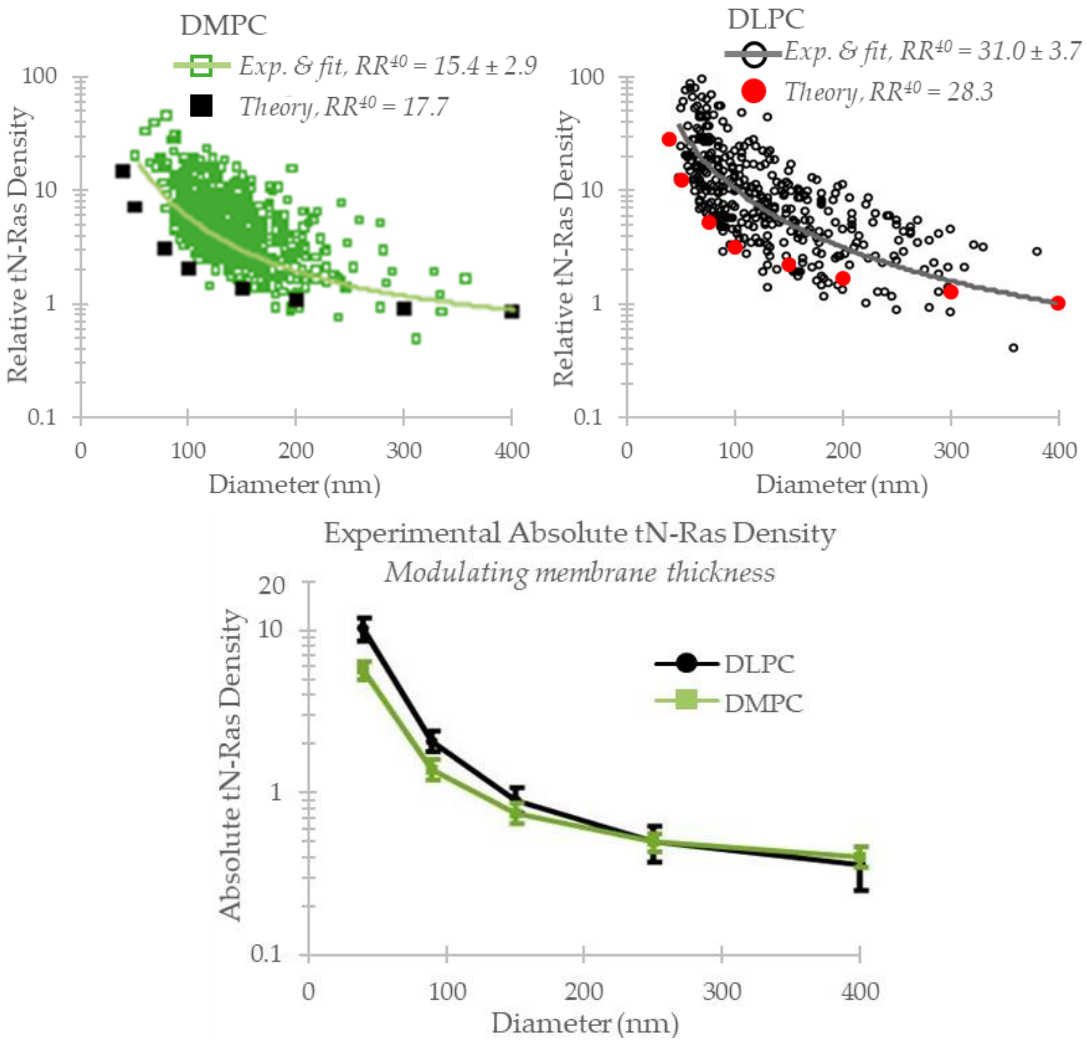

Figure 5.11) **Normalized tN-Ras adsorption density as a function of liposome diameter, modulated by lipid tail length.** Thinner membranes show increased recruitment of tN-Ras by membrane curvature. ***Top panel:*** Experimental tN-Ras density as a function of liposome diameter (normalized to the density at 400 nm in diameter) for liposomes prepared from DMPC lipids *(**left**, green markers)* and DLPC lipids *(**right**, black markers)* with corresponding off-set power function fits *(pale green line and grey line, respectively)*. The black square and red circular markers represent the corresponding normalized densities of the tN-Ras anchor calculated by the molecular theory for each type of liposome, respectively. The recruitment ratio value, RR^{40}, represents the increase in tN-Ras density when reducing membrane diameter by a factor of 10 (using the ratio of 40 nm to 400 nm in diameter liposomes), as quantified either from power function fitting to the experimental data (RR^{40}_{exp} is reported as the average mean ± SE of n_{DMPC} = 7 and n_{DLPC} = 6 independent experiments) or from the theoretical calculations. ***Bottom:*** The experimental average absolute tN-Ras density on DMPC *(green)* and DLPC *(black)* liposomes, for five liposome diameters, indicating enhanced sensitivity of tN-Ras to membrane curvature on the thinner DLPC bilayers.

Whereas the change in lipid tail saturation, from the comparisons drawn from DOPC *versus* POPC membranes, demonstrated a negligible percent difference in the areal response to membrane curvature on a 'per total molecule' basis, and a moderate difference in the areal response relative to the 'number of lipids in the expanded leaflet', variation in bilayer thickness effects the opposite relative results. The percent increase in the expanded leaflet's interfacial area per total lipid $\left({}^{A(z=l,\,\mathbf{c})}/_{N}\right)$ when curving planar, pure component DMPC and DLPC membranes to spheres 40 nm in diameter is 12.5% and 10.6%, respectively (*Table 5.1*). This results in a modest distinction in the responses to curvature, with a 16.7% difference between the two bilayers; however, the percent change in the DLPC system is less than that of the DMPC system, and thus does not correlate with the higher RR^{40} value of the former. The corresponding percent increases in the interfacial area per lipid in the expanded leaf $\left({}^{A(z=l,\,\mathbf{c})}\!\!\diagup_{N_E}\right)$ are 7.94% and 7.93% in DMPC and DLPC bilayers, respectively, resulting in a negligible, 0.125% difference.

The lateral pressure profiles through the hydrophobic width of DMPC and DLPC bilayers are given in *Figure 5.12*, illustrating the pressure relief experienced by the expanded leaflet upon bending from planarity to 40 nm diameter spheres.

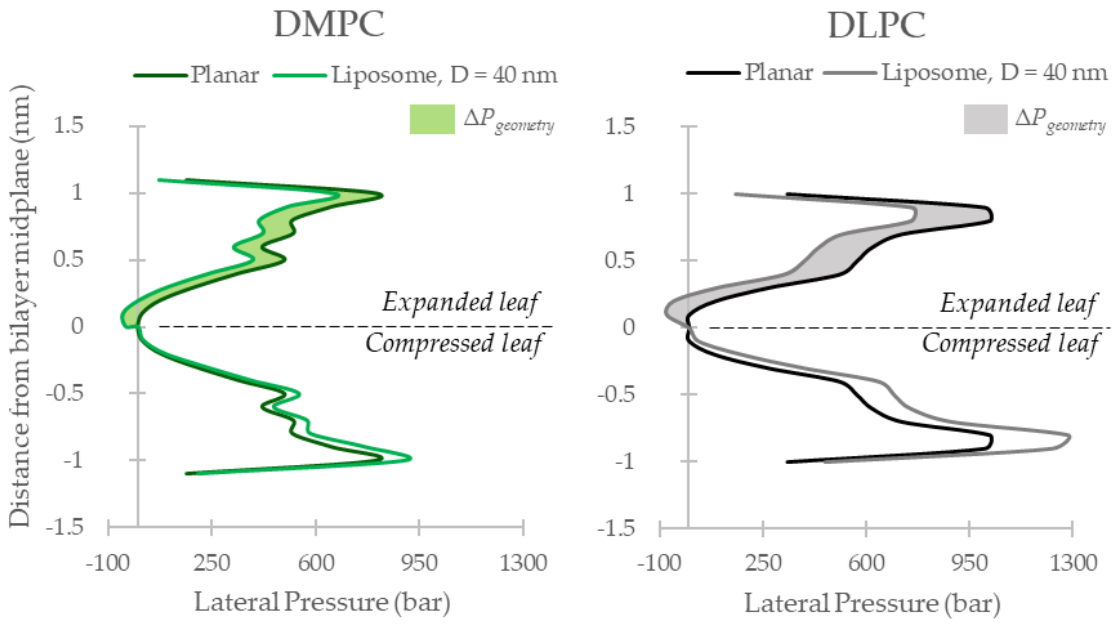

Figure 5.12) **Thinner membranes show greater relief in lateral pressure in curved liposomes.** Theoretically calculated lateral pressure profiles along the bilayer normal, through the width of the hydrophobic region, for thicker DMPC membranes *(**left**, green)* and thinner DLPC membranes *(**right**, black/grey)*, for planar bilayers *(dark line)* and spherical bilayers, 40 nm in diameter *(pale line)*. The shaded region between the curves in each graph indicates the degree of relief in lateral pressure ($\Delta P_{geometry}$) in the expanded membrane leaf (top half of each graph) when the membrane bends. DLPC bilayers experience a greater overall relief in lateral pressure in the expanded leaf as a function of membrane curvature, relative to DMPC bilayers.

The theory calculates a 33.7% and a 42.8% decrease in integrated lateral pressure from $\Delta P_{geometry}$ (*Figure 5.12, shaded region and 5.13, bottom left*) in DMPC and DLPC bilayers, respectively. This results in a 23.7% difference between these values, with the larger curvature-induced response in lateral pressure found in the DLPC, relative to the DMPC, system. These trends mirror the comparative behavior of the tN-Ras protein, which also displays enhanced curvature-sensitivity in the presence of the DLPC liposomes, marked by the system's higher RR^{40} value (as

shown in the theoretical and experimental relative density curves in *Figure 5.11, top panel* and quantified in *Figure 5.13, bottom right*). The curvature responses calculated from $\Delta a_{geometry}$ and $\Delta(a/x_E)_{geometry}$ are illustrated in *Figure 5.13, top right and left*, respectively, for comparison.

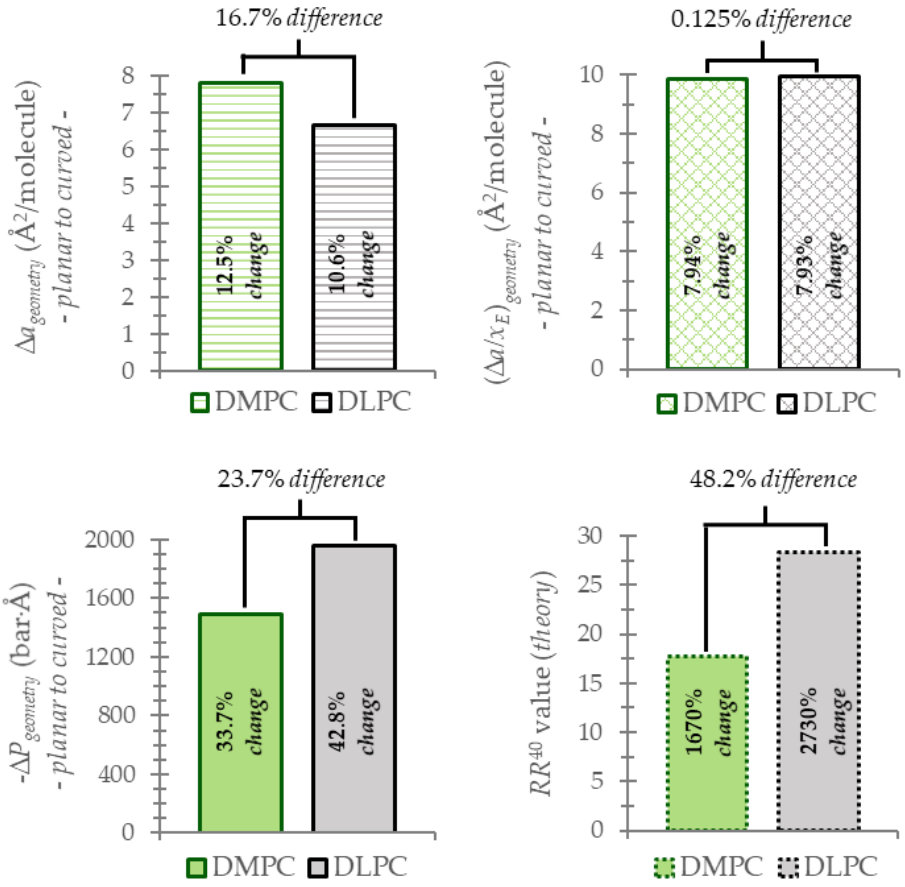

Figure 5.13) **Quantification of comparisons in area and lateral pressure changes with membrane curvature between DMPC and DLPC bilayers.** Quantification of the curvature-dependent change within the expanded leaflet in area per total number of lipids, $\Delta a_{geometry}$ ***(top left)***, area per number of lipids in the expanded leaf, $\Delta(a/x_E)_{geometry}$ ***(top right)***, and integrated lateral pressure, $-\Delta P_{geometry}$ ***(bottom left)***, from bending DMPC *(green)* and DLPC *(grey)* bilayers from a planar to a spherical (40 nm diameter) geometry. Only the trends in the lateral pressure correlate with those of tN-Ras adsorption ***(bottom right)*** in these systems.

Furthermore, we find a markedly larger discrepancy in the integrated lateral pressure between highly curved (40 nm) DMPC and DLPC liposomes, with lower pressure in the latter, than between the planar DMPC and DLPC systems, with higher pressure in the later, *(-$\Delta P_{lipid\text{-}type}$, Figure 5.14, bottom left)*. These trends correspond with the experimentally measured, average absolute tN-Ras density curves from *Figure 5.11*, from which $(\Delta\rho_{tN\text{-}Ras})_{lipid\text{-}type}$ is calculated *(Figure 5.14, bottom right)*. The density graphs feature greater tN-Ras density values in DLPC liposomes, relative to DMPC, in the highly curved membrane regime, and slightly lower values in the DLPC system in the near-planar membrane regime. These findings support the position that the membrane's lateral pressure profile might hold a fundamental, governing role in the capacity for successful interaction between a membrane and lipidated proteins, resulting in adsorption events. The molecular area metrics have thus far not exhibited consistent correlation with the protein's adsorption tendencies.

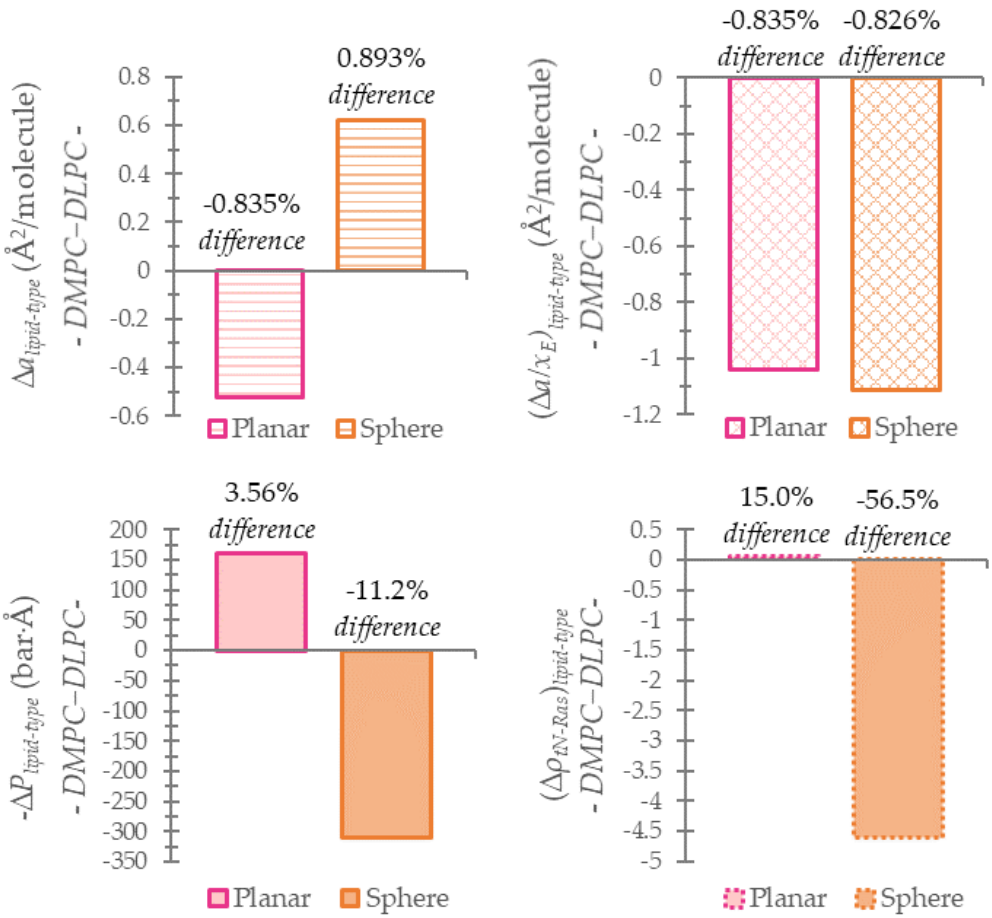

Figure 5.14) **Quantification of comparisons in area and lateral pressure changes with changes in membrane composition between planar and spherical bilayers.** Quantification of the composition-dependent change, within the expanded leaflet, in the area per total number of lipids, $\Delta a_{lipid\text{-}type}$ ***(top left)***, the area per number of lipids in the expanded leaf, $\Delta(a/x_E)_{lipipd\text{-}type}$ ***(top right)***, the integrated lateral pressure, $-\Delta P_{lipid\text{-}type}$ ***(bottom left)***, and the experimental absolute tN-Ras density, $\Delta(\rho_{tN\text{-}Ras})_{lipipd\text{-}type}$ ***(bottom right)*** between DMPC and DLPC membranes, comparing such for planar bilayers *(pink)* and spherical liposomes 40 nm in diameter *(orange)*. The trends in the integrated lateral pressure for both membrane geometries correlate well with the adsorption tendencies of the protein. The molecular area metrics do not exhibit such a correlation.

Lipid Headgroup Size Modulates the Relative Adsorption Densities of the tN-Ras Anchor as a Function of Membrane Curvature

We now examine the effects of modulating our final lipid shape parameter, lipid headgroup size, on the degree of lipidated protein localization on lipid bilayers. DOPC and DOPE lipids are well suited for this comparative analysis, as they both feature the same dioleoyl hydrocarbon tails, differing only in the size of their headgroup. DOPC features a large choline moiety at the extremum of its polar region, as shown in *Figure 5.15* which is replaced in DOPE by the relatively much smaller amine group.

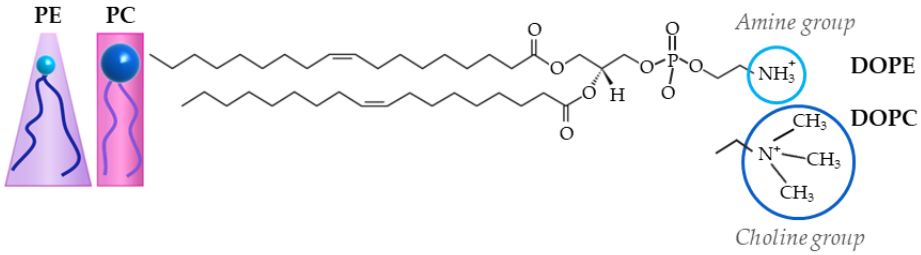

Figure 5.15) **Size differences between lipid headgroups cause differences in the shape of the overall lipids.** Lipids with a small headgroup relative to the large areal footprint of their hydrocarbon tails, such as PE, tend to assume a cone shape. Lipids that have a headgroup size comparable to the areal footprint of their tails, such as PC, take on a cylindrical shape. The different shapes of lipids influence where they tend to localize and affect the host membrane's structure, configuration, and local mechanical properties.

As is depicted in the above figure, the overall shape of the lipid molecule is affected by the size of its headgroup [285]. While PC lipids are fairly balanced in terms of cross-sectional area from head to tail regions, and thus generally maintain

a cylindrical shape, PE lipids take the form of an inverted cone, owed to their smaller head-to-tail volume ratio. This study tracks the changes in tN-Ras protein adsorption on binary DOPC+DOPE liposomes of varying diameter as the concentration of DOPE lipids is increased (100:0, 75:25, and 50:50 mole % DOPC:DOPE bilayers). Experimental and theoretical results show up-concentration of tN-Ras in each of the three bilayers as curvature increases, with decreasing curvature-sensitivity as the concentration of DOPE in the membrane rises. The $D = 40$ nm relative recruitment ratios of the binary membranes decrease from the 0%, to the 25%, to the 50% DOPE liposome concentration, with values of $RR^{40}_{theory} = 8.9$; $RR^{40}_{exp} = 7.4 \pm 0.4$, to $RR^{40}_{theory} = 7.7$; $RR^{40}_{exp} = 6.4 \pm 1.7$, to $RR^{40}_{theory} = 6.5$; $RR^{40}_{exp} = 5.1 \pm 0.2$, respectively *(see Figure 5.16 and Table 5.1)*. The 36% (theory) and 44% (experiment) difference between the largest and smallest of these values constitutes a small (relative to the other systems compared), yet significant reduction in the influence of liposome diameter on the selective recruitment of tN-Ras by the membrane when increasing the content of DOPE lipids.

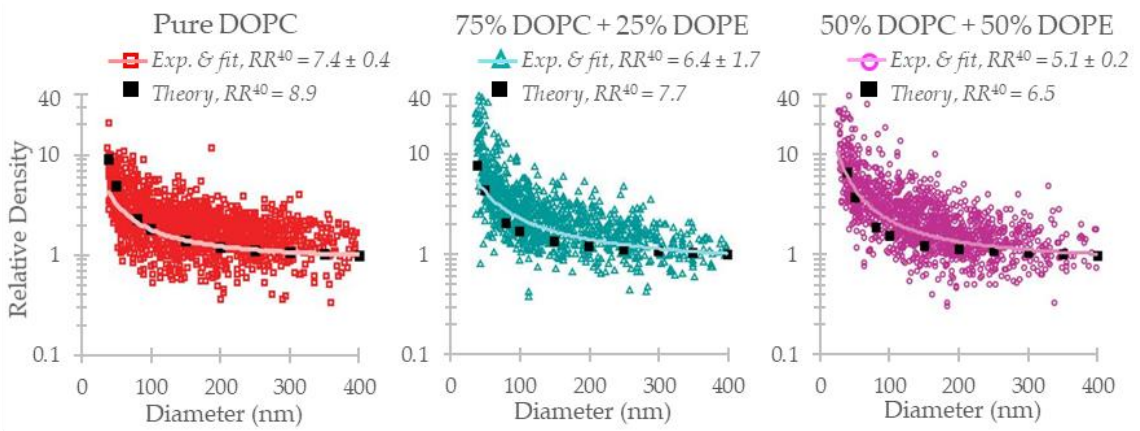

Figure 5.16) **Normalized tN-Ras adsorption density as a function of liposome diameter on DOPC membranes with increasing concentration of DOPE lipids.** The normalized tN-Ras density as a function of the diameter of liposomes composed of DOPC lipids, with increasing DOPE concentration, including systems of pure DOPC *(**left**, red)*, 75:25% DOPC:DOPE *(center, turquois)*, and 50:50% DOPC:DOPE *(**right**, purple)*. Values calculated by the theory *(black squares)* show excellent agreement with experimental results. The solid lines are the error-weighted fits to the experimental data. The experimental relative recruitment ratio, RR^{40}_{exp}, is reported as the average mean ± SE of $n = 9$, 3, and 6 independent experiments, respectively. Both experimental and theoretical RR^{40} values indicate a diminishing rate of increase in Ras adsorption as curvature increases on membranes with higher concentrations of lipids with smaller headgroup size (PE).

The absolute tN-Ras density curves, shown below in *Figure 5.17*, clearly exhibit the diminishing rate by which the protein's density on the membrane increases with membrane curvature as the concentration of DOPE lipids rises. We quantify an ~70% increase in absolute protein density in locally near-planar (400 nm diameter) 50:50 mol % DOPC:DOPE membranes, relative to pure DOPC bilayers of the same size, while a nonsignificant percent change in protein density is quantified between these membranes when they are highly curved, to less than

~80 nm in diameter. Hence, the smaller RR[40] values corresponding to higher DOPE concentrations originate from a DOPE-dependent rise in tN-Ras density within flatter membranes.

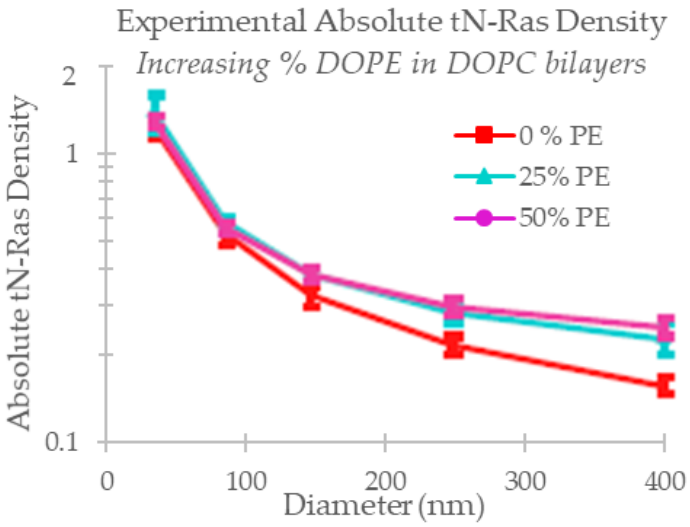

Figure 5.17) **Experimentally determined absolute density of tN-Ras on DOPC membranes with increasing concentration of DOPE lipids.** The average absolute tN-Ras density, calculated for five diameters of experimentally prepared liposomes comprised of pure DOPC *(red)*, 75:25% DOPC:DOPE *(turquois)*, and 50:50% DOPC:DOPE *(purple)* lipids, using $n = 9$, 3, and 6 independent experiments, respectively. The curves demonstrate that introducing lipids with reduced headgroup size (PE) into the bilayer increases the absolute tN-Ras adsorption on planar membranes and decreases the protein's sensitivity to membrane curvature.

As seen with the previous systems, the difference in the curvature-induced change in molecular area does not track with the differential adsorption trends of tN-Ras in these bilayers. In this case, there is near nonexistent variation in the areal response to curvature, with only a 0.012% difference calculated between the responses in both $A(z{=}l, \mathbf{c})/_{N}$ and $A(z{=}l, \mathbf{c})/_{N_E}$ in pure DOPC *versus* 50:50 DOPC:DOPE bilayers, when bending from planarity to 40 nm diameter spheres.

The percent changes are the same, within rounding, in each of the three bilayers for both metrics: 14.2% and 8.24%, respectively *(Table 5.1 and Figure 5.18, top panel)*.

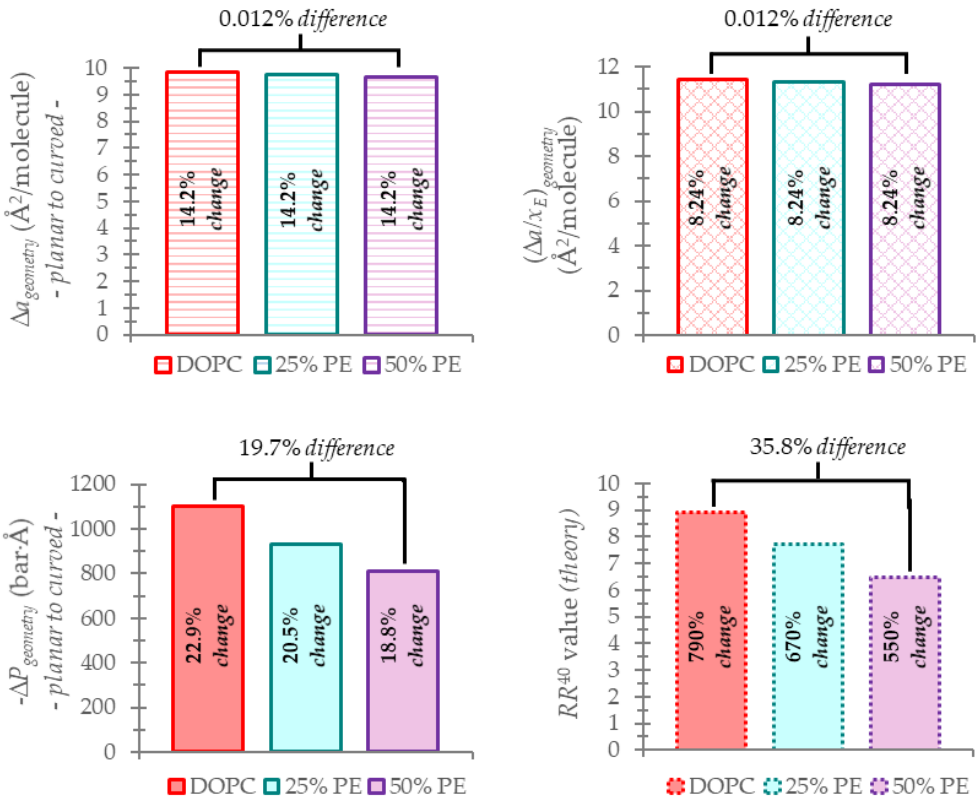

Figure 5.18) **Quantification of comparisons in area and lateral pressure changes with membrane curvature between DOPC bilayers with varying concentrations of DOPE.** Quantification of the curvature-dependent change within the expanded leaflet in area per total number of lipids, $\Delta a_{geometry}$ ***(top left)***, area per number of lipids in the expanded leaf, $(\Delta a/x_E)_{geometry}$ ***(top right)***, and integrated lateral pressure, $-\Delta P_{geometry}$ ***(bottom left)***, from bending membranes from a planar to a spherical geometry, 40 nm in diameter. Comparisons in these metrics are drawn from membranes composed of pure DOPC *(red, greatest curvature-induced relief in lateral pressure)*, 75:25 mole % DOPC:DOPE *(turquois)*, and 50:50 mole % DOPC:DOPE *(purple, least curvature-induced relief in lateral pressure)* lipids. The changes in lateral pressure trend with the observed tN-Ras behavior; the area metrics exhibit no correlation with protein adsorption.

The lateral pressure profile through the membrane, however, proves compelling as an agent which may control the observed changes in behavior of

tN-Ras in the presence of the different liposomes. We calculate consecutively lower degrees of curvature-induced relief in the integrated lateral pressure within the expanded leaflet with each increase in DOPE concentration, from a 22.9%, to a 20.5%, to an 18.8% decrease for pure DOPC, 75:25 mole % DOPC:DOPE, and 50:50 mole % DOPC:DOPE bilayers, respectively *(Figure 5.18, bottom left and Figure 5.19)*. This parallels the lower curvature-sensitivity of tN-Ras in the presence of bilayers with higher DOPE concentration, quantified by the consecutively diminishing RR^{40} values of the protein from the 0% to 50% PE systems *(Figure 5.18, bottom right)*.

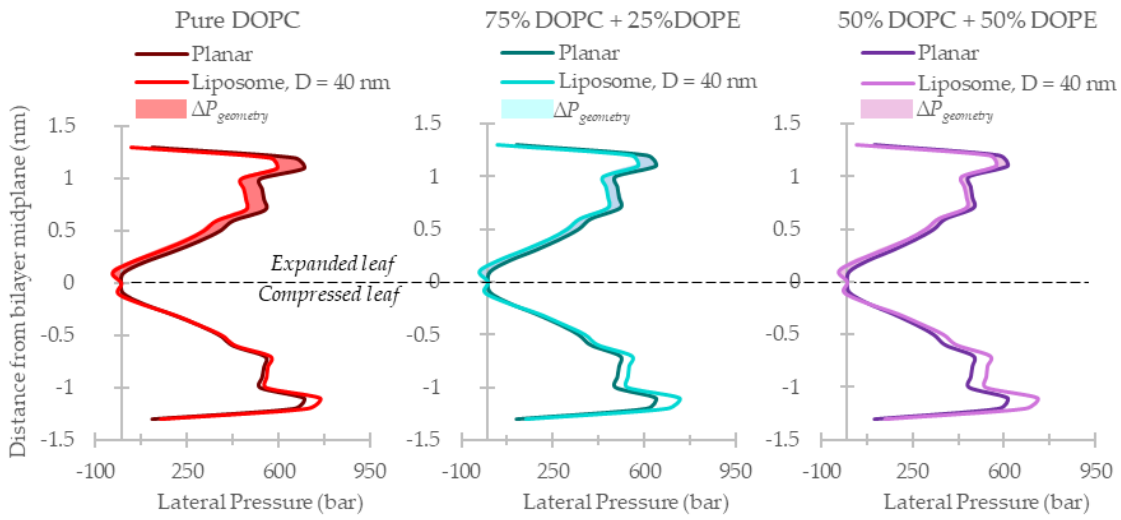

Figure 5.19) **Diminished curvature-induced relief in the lateral pressure in bilayers with increasing concentration of PE lipids.** Theoretically calculated lateral pressure profiles along the bilayer normal (through the width of the hydrophobic region) for increasing concentration of DOPE lipids (relatively smaller headgroup) within DOPC (relatively larger headgroup) bilayers: 0% PE *(**left**, red)*, 25% PE *(**center**, turquois)*, and 50% PE *(**right**, purple)* – showing the difference in distribution between planar bilayers *(dark line)* and spherical bilayers 40 nm in diameter *(pale line)*. The shaded region between the curves in each graph indicates the degree of relief in lateral pressure ($\Delta P_{geometry}$) in the expanded leaflet when the membrane is curved from a planar to spherical geometry.

Additionally, the theory returns a higher integrated lateral pressure in the pure DOPC bilayer than in either of the binary systems, which is notably more pronounced in the planar regime than in the highly curved regime *(-$\Delta P_{lipid\text{-}type}$; Figure 5.20, bottom left)*. This is consistent with the variation in the experimental tN-Ras absolute density values among the flatter bilayers (with the lowest density observed in those composed of pure DOPC) and the near convergence of these values with decreasing liposome diameter, illustrated in *Figure 5.17* and quantified as $(\Delta\rho_{tN\text{-}Ras})_{lipid\text{-}type}$ in *Figure 5.20, bottom right*.

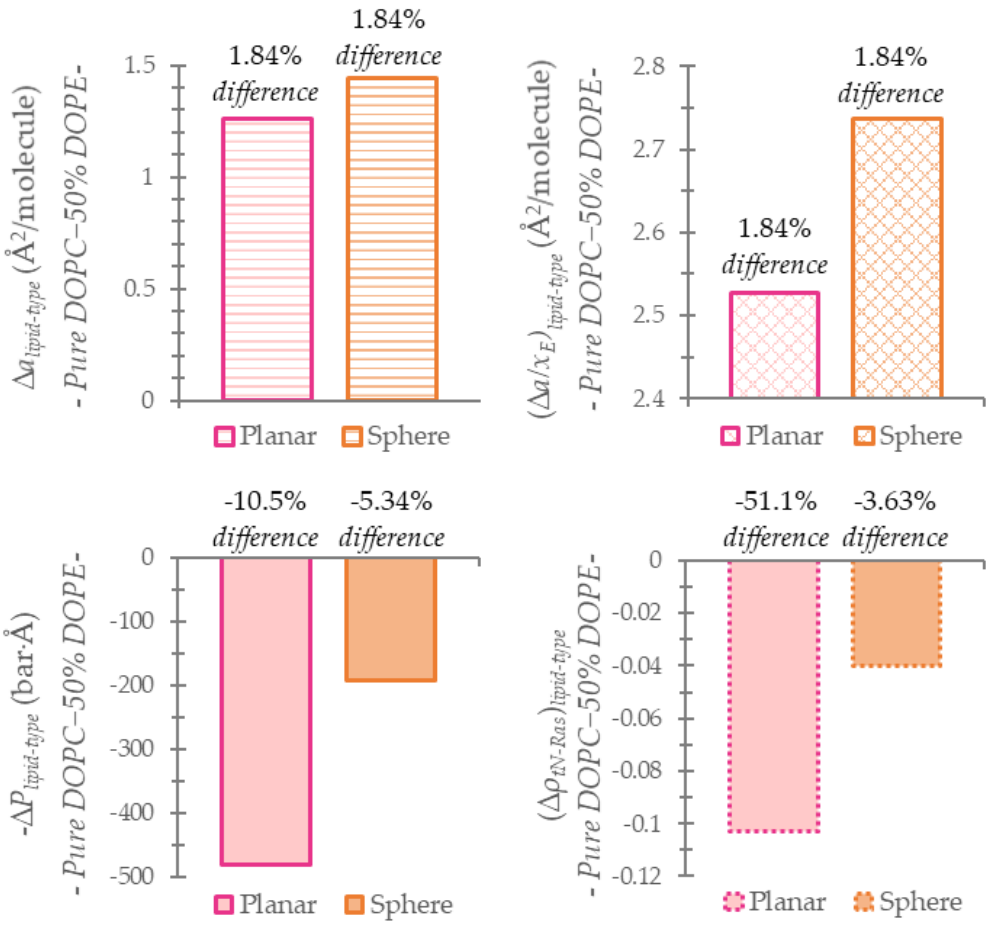

Figure 5.20) **Quantification of comparisons in area and lateral pressure changes with changes in membrane composition between planar and spherical bilayers.** Quantification of the composition-dependent change, within the expanded leaflet, in area per total number of lipids, $\Delta a_{lipid\text{-}type}$ ***(top left)***, area per number of lipids in the expanded leaf, $(\Delta a/x_E)_{lipid\text{-}type}$ ***(top right)***, integrated lateral pressure, $-\Delta P_{lipid\text{-}type}$ ***(bottom left)***, and the experimental absolute tN-Ras density, $(\Delta \rho_{tN\text{-}Ras})_{lipid\text{-}type}$ ***(bottom right)*** between pure DOPC and 50:50 DOPC:DOPE membranes. We compare these changes in planar bilayers *(pink)* to those in spherical 40 nm liposomes *(orange)*. As with the other lipid systems in this study, the lateral pressure trends correspond with the localization behavior of tN-Ras, whereas the molecular area metrics do not demonstrate consistent correlation.

The Whole Shebang

For a membrane property to demonstrate a possible curvature-driven, causal relationship with the ability of a protein to discriminate potential adsorption sites based on membrane composition, it should demonstrate *consistent* differential responses to membrane geometry between the types of bilayers compared that strongly correlate with the observed differential adsorption of the protein as a function of these shape changes. Comparing all types of bilayers studied in this work, we do not find such a consistent relationship between the expanded leaflet's areal responses to changes in membrane geometry, either relative to the total number of bilayer lipids or to the number of lipids in the expanded leaflet, and the observed discrimination of tN-Ras localization for bilayer composition as a function of membrane curvature. We do find, however, a direct relationship between the lateral pressure in the expanded leaflet of all bilayers studied, in all metrics used for comparisons, and the adsorption behavior of the protein, following the general rule that a greater relief in the lateral pressure of the membrane's expanded leaf upon bending induces enhanced adsorption ability of lipidated proteins in the vicinity.

Figure 5.21 visually portrays the degree of correlation between these membrane properties and protein adsorption by plotting the percent changes in each membrane property, resulting from bending a planar membrane to a 40 nm

(diameter) sphere, and the RR^{40} value of tN-Ras, for each bilayer studied. The correlation coefficient calculated from the entire range of bilayers quantifies the strength of these relationships. We find an express, near linear relationship between the curvature-induced percent change in the integrated lateral pressure of the membrane's expanded leaflet and the relative recruitment ratio of the protein, with a correlation coefficient of 0.91 using the RR^{40} values calculated by the molecular model and of 0.95 using those obtained by experiment *(see Figure 5.22 for the full range of theoretical and experimental RR^{40} values)*.

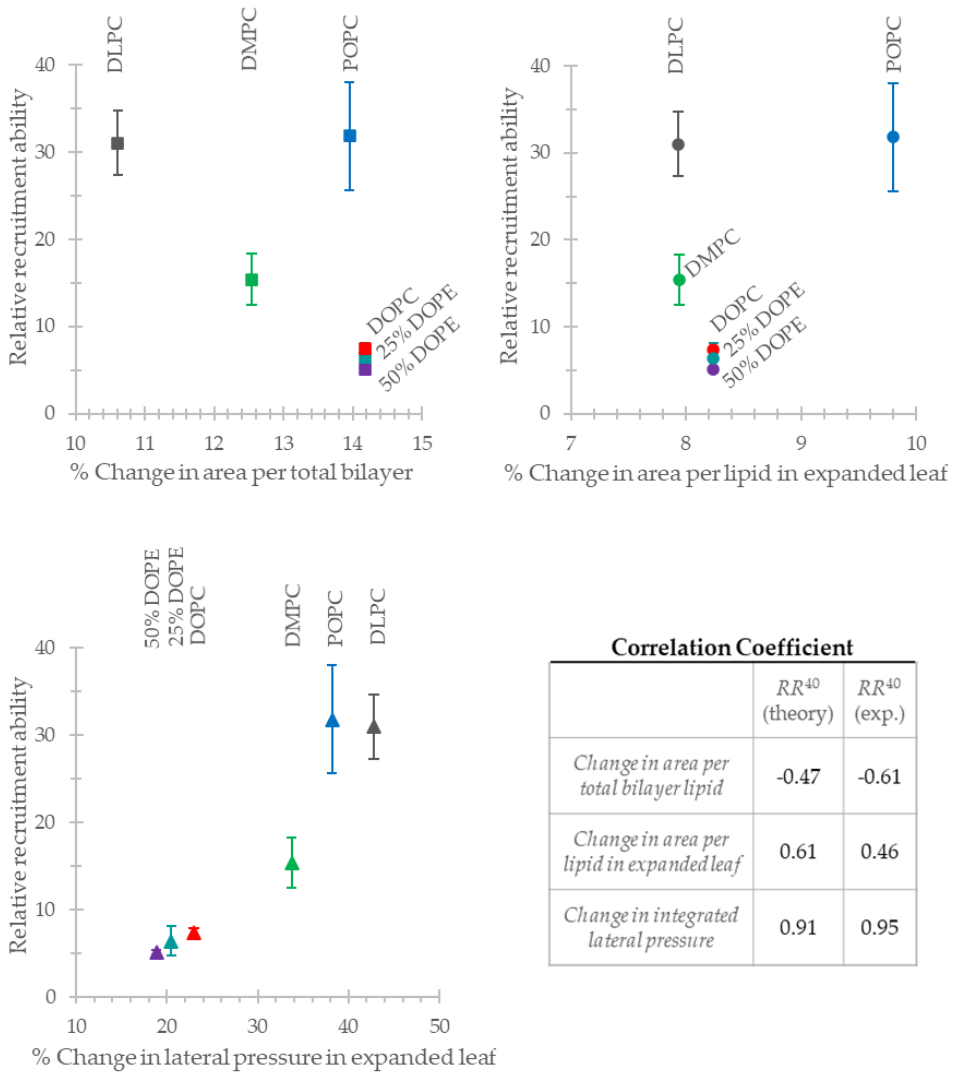

Correlation Coefficient

	RR^{40} (theory)	RR^{40} (exp.)
Change in area per total bilayer lipid	-0.47	-0.61
Change in area per lipid in expanded leaf	0.61	0.46
Change in integrated lateral pressure	0.91	0.95

Figure 5.21) **Correlations between the tN-Ras relative adsorption density and structural-mechanical properties of the membrane, among different types of lipid bilayers.** The experimentally determined RR^{40} values *versus* the theoretically calculated curvature-dependent percent change in the area per total number of lipids ***(top left)***, area per number of lipids in the expanded leaf ***(top right)***, and integrated lateral pressure ***(bottom graph)***, all quantified for the expanded leaf in membranes curved from planarity to liposomes 40 nm in diameter, for each type of bilayer studied: DOPC *(red)*, DOPC:DOPE 75:25% *(turquoise)*, DOPC:DOPE 50:50% *(purple)*, POPC *(blue)*, DLPC *(grey)*, and DMPC *(green)*. Correlation between the RR^{40} value and the percent change in either calculation of the molecular area is not significant, while a clear linear relationship is identified between the RR^{40} value and the percent change in the integrated lateral pressure.

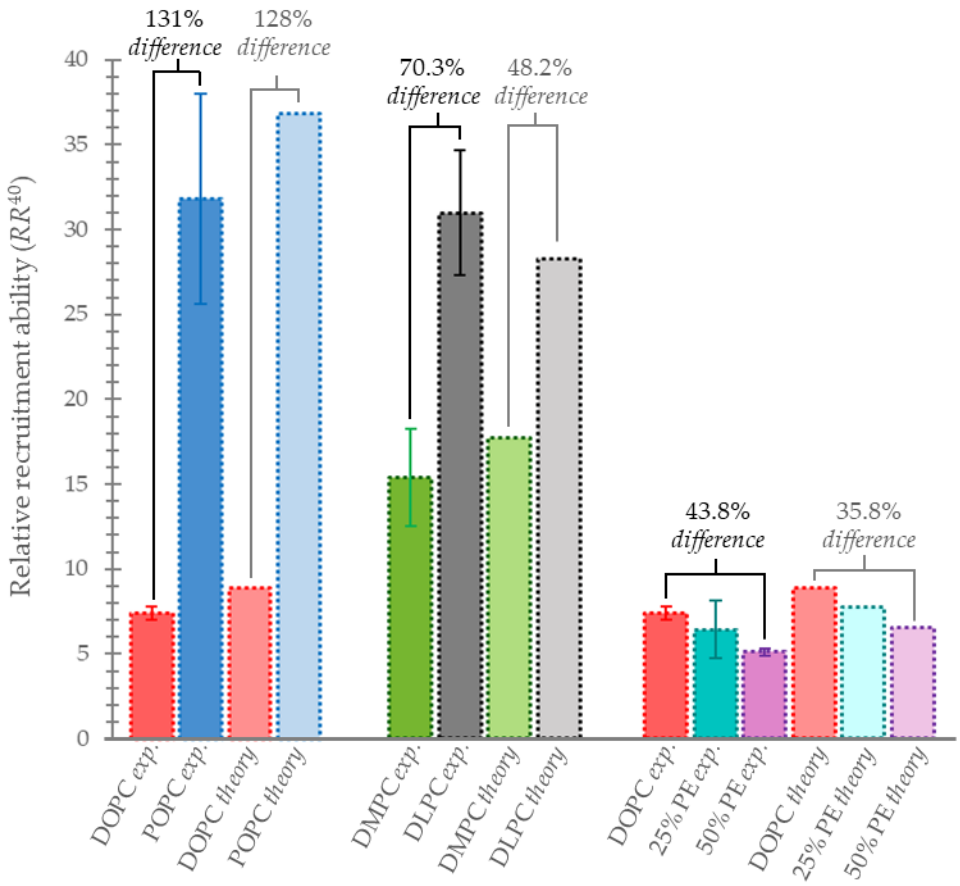

Figure 5.22) **Chart displaying all relative recruitment ratios calculated by the theory and experiment, for all bilayers studied.** The trends seen in the RR^{40} values demonstrate excellent agreement between those calculated by the theory and by experiment.

The strong correlation between the adsorption behavior of tN-Ras on membranes of assorted composition and size and the variation in the lateral pressure distributions of these membranes is meaningful because it extends the comparisons of protein localization from between two liposomal systems that vary by a single, controlled lipid shape factor to a comparative analysis drawn from the entire spectrum of lipid systems. This profoundly implicates the membrane's

lateral pressure distribution as a molecular mechanism that plays an important role in regulating the curvature sensitivity and compositional selectivity of lipidated proteins.

5.4 Some Compelling Correlations between our Findings and Biology

We have discussed the preferential association of the lipidated protein, N-Ras, with various membranes in the context of how membrane curvature-modulated adsorption of the protein is influenced by different shape characteristics of the membrane's lipid constituents. Our findings indicate a synergistic relationship between the local geometry of the targeted membrane and the atomistic orientation of its lipids that works to fine-tune protein recruitment, with the lateral pressure distribution through the bilayer's hydrophobic core as an underlying molecular mechanism driving protein–membrane interaction. Results are obtained through the analysis of model membrane systems; it is therefore prudent to address whether such findings are consistent with known biological characteristics and phenomena.

It is interesting to consider the geometrical variations of the organelles and vesicular carriers, and of the lipids they comprise, that constitute the secretory pathway. Ras proteins are synthesized, modified, and transported along this pathway from the endoplasmic reticulum (ER) to their activation sites on the

plasma membrane's cytosolic leaf [259, 273, 276, 286]. Transport of cellular material along the secretory pathway is bidirectional. Anterograde transport (along the exocytic pathway) of newly synthesized lipids and proteins originates at the ER, passes to the Golgi apparatus, and progresses through the cytoplasm via vesicular and possibly non-vesicular carriers, ultimately reaching the plasma membrane. Retrograde transport (along the endocytic pathway) moves from the plasma membrane to lysosomes, endosomes, and/or back to the Golgi or ER. The membranes living along these pathways (collectively referred to as endomembranes) maintain precisely regulated morphologies and compositions that dictate non-random directional trafficking of specific materials. Both lipids and proteins are laterally segregated along different regions of their host organelles and transport vesicles, based on their intended destination. Saturated lipids (namely, sphingolipids and saturated phospholipids) are purposefully transported unidirectionally from the ER and Golgi to the plasma membrane (where there is roughly two-fold greater lipid saturation in the exoplasmic leaflet), preserving a gradient of increasing fatty acid chain saturation in membranes along the exocytic pathway, whereas unsaturated phospholipids are preferentially included in transport vesicles moving toward the ER [287-290].

Ras proteins use these vesicular transport mechanisms to travel back and forth between the ER or Golgi and the plasma membrane in a cyclical manner,

undergoing several post-translational modifications at the CAAX motif on their C-termini to do so. The first of these modifications is the isoprenylation of the cysteine, resulting in the addition of a farnesyl chain that facilitates the protein's interaction with the ER. Farnesyl's branched, multi-unsaturated architecture is consistent with the loose packing of the ER membrane lipids and affords it a weak association with the membrane. Other modifications are required to improve the strength of insertion in subsequent bilayers on the protein's journey to the plasma membrane. For N-Ras, H-Ras, and the minor isoform of K-Ras, K-Ras4A, this involves the attachment of the saturated chain, palmitoyl (palmitoylation), at the Golgi. This hydrocarbon addition increases the hydrophobicity of the protein, ensuring its stable association with anterograde transport vesicles, at the exclusion of retrograde vesicles, and ultimately secures its position in the cytosolic leaf of the plasma membrane. Importantly, this modification is cleavable, enabling reversible, dynamic interactions with membranes of multiple subcellular compartments and facilitating the protein's cyclic translocation between the Golgi and cell membranes many times during its life span [291].

Our findings regarding the selective adsorption tendencies of tN-Ras are congruous with these biological trafficking mechanisms. The results obtained from our molecular field theory and from the experiments conducted by our collaborators show that the farnesyl and palmitoyl anchor motifs of tN-Ras

preferentially localize on small-diameter liposomes comprised of lipids with a relatively higher degree of chain saturation (by comparing POPC and DOPC model bilayers), analogous to the high saturated lipid content of biological, small (< 100 nm) secretory vesicles moving toward the plasma membrane. Furthermore, our larger diameter model liposomes recruit the tN-Ras anchor more readily when comprised of unsaturated lipids, reflecting biological N-Ras disassociation with the highly curved, highly saturated trafficking vesicles and integration with the locally flat, cytosolic leaf of the plasma membrane, which comprises a much higher percentage of unsaturated lipid species. Since de-palmitoylation of the plasma membrane-integrated N/H/K4A-Ras protein marks its dissociation from the membrane, initiating its migration through the endocytic pathway via retrograde vesicles, it would be interesting to replicate our experiments and theoretical analysis for Ras proteins bound to the farnesyl, but not the palmitoyl, chain anchor.

Membrane thickness increases by roughly 13% moving through the secretory pathway from the ER to the plasma membrane; anterograde transport vesicles budding from the ER and Golgi likewise feature membranes that are notably thinner than the plasma membrane [292]. These vesicles are also highly curved (50-100 nm in diameter). Such characteristics might indicate that Ras proteins preferentially associate with highly curved membranes that are relatively

thin, promoting the necessary sorting and integration of the protein into organelle-budding, anterograde transport vesicles. It can be similarly inferred that such selectivity regarding membrane thickness attenuates in the presence of larger diameter, or locally planar, membranes, to facilitate the fusion of the vesicular carriers and the adsorption of the passenger protein on the plasma membrane.

Comparable to the change in membrane thickness of the cellular components along the secretory pathway, our study involves the effects on protein–membrane interactions when modulating bilayer thickness by ~16%, achieved by changing the length of the constituent lipid tails by two carbon units (DMPC *versus* DLPC). Our findings are consistent with the trends observed in biological systems, demonstrating more pronounced curvature-sensitivity of tN-Ras within the thinner DLPC systems and fairly equivalent adsorption profiles within very large diameter, or flat, DLPC and DMPC membranes. Variation in membrane thickness has previously been suggested as a regulatory cue for the sorting of integral membrane proteins, attributed to the hydrophobic mismatch between the transmembrane segment and the bilayer [293]. Here, we have introduced the novel relationship between composition-based selectivity of lipidated proteins for a particular membrane (in this case manifesting as differences in bilayer thickness) and membrane curvature.

Lastly, our examination of how perturbations in lipid headgroup size affect

tN-Ras adsorption on the membrane is conducted using liposomes constructed from DOPC lipids with increasing concentrations of DOPE lipids from 0, to 25, to 50 mole %. Our analyses reveal variation in lipid headgroup size has a marked effect on protein localization in larger diameter liposomes (> 200 nm), which diminishes and ultimately nearly vanishes as liposome diameter decreases. Liposomes larger than ~200 nm in diameter demonstrate enhanced recruitment ability for the tN-Ras anchor when containing a greater percentage of PE lipids. Considering the compositional variations in the membranes of biological cells leads to an intuitive expectation of our results in this study. Eukaryotic membranes frequently feature non-random, asymmetric distribution of lipid species across the bilayer. The plasma membrane's cytosolic leaflet is characteristically rich in PE lipids, while sphingomyelin, glycophingolipds, and PC lipids, all with larger headgroups, are predominately housed in the exoplasmic monolayer [290]. We can therefore conclude that the assimilation of the vesicle-bound Ras protein with the cytosolic leaflet of the plasma membrane is facilitated by the protein's preferential interaction with flatter membranes containing relatively high concentrations of PE, congruent with our study. Our findings are also in accordance with previous observations of proteins anchored through shallow insertion of amphipathic helices [281, 283, 294, 295].

In this work, we have contributed evidence that modifying an individual

structural feature of membrane lipids, such as degree of chain saturation, chain length, or headgroup area, provokes variations in the curvature-mediated relief in lateral pressure, which we propose is an important molecular mechanism driving the selective recruitment of curvature-sensitive lipidated proteins. The results from our theory demonstrate a well-defined trend of greater protein localization on liposome membranes with a larger drop in the average lateral pressure within the bilayer's expanded leaf, induced by a decrease in liposome diameter. The trend holds for curvature manipulations within a single type of liposome membrane and when comparing different types of liposomes at a defined curvature. Our findings complement previous work headed by D. Stamou and M. J. Uline [164] suggesting a synergistic relationship between membrane curvature and phase-state working to actively regulate the membrane's adsorption of lipid-anchored proteins. A generalized conclusion that can be derived from these studies is that any extrinsic property or phenomenon that affects the membrane's lateral pressure distribution will, as a consequence, also change the degree of lipidated protein adsorption. Such an influence can be, for example, in the form of coat proteins that initiate endocytosis, scaffolding of the membrane by protein complexes, or cytoskeletal stress, all of which would coordinate in a nontrivial manner with membrane composition and curvature to tightly regulate the localized density of lipidated proteins.

CHAPTER 6
GENERATION II THEORY:
MODELLING LIPID MEMBRANES IN AN AQUEOUS ENVIRONMENT

We will now turn to *Generation II* of our theoretical membrane model, a generalization of the previous theory that introduces an aqueous, ionic environment around the membrane, providing a link between a membrane's architectural character (e.g., composition, shape, phase state) and the physicochemical nature of its surroundings. While the previous model captured the nanoscopic details of the bilayer's hydrophobic region that dominate its macroscopic structural behavior, we now wish to examine how the interaction between the membrane and its physical environment operates to fine-tune the membrane's thermodynamic properties and functionality. We introduce an explicit representation of the lipids' polar headgroups and the electrostatic interactions that arise between them and an aqueous solvent containing physically relevant salt ion concentrations. Acid-base equilibria, charge distributions, density distributions of aqueous species, and electrostatics are elements new to the theory, while the same rigorous treatment as presented previously to characterize the lipid hydrocarbon tails (e.g., molecular size, shape, and conformational details)

is extended to include all additional system components. As before, the intramolecular interactions are treated in detail at the scale of the small monomer, while intermolecular interactions are represented via a mean-field approach.

Much of the theoretical description of the membrane's hydrophobic region applied to the *Generation I* theory holds for the generalized, *Generation II* model, with a few key changes. One is the extension of our analysis of protein adsorption on spherical liposomes of varied *radii* to a comparison of the protein recruitment ability of membranes with varied *geometry*, focusing on two of the most abundant cellular/subcellular membrane shapes: spheres and tubules [296]. Biological membranes display broad polymorphism, taking on distinct shapes that have been observed to correlate with specific biological functions [296-299]. We noted several examples of the diverse structure-to-function relationships in the membranes of highly elastic, biconcave erythrocytes, spiky neurons, sheet-like formations of tightly packed epithelial cells, and the long, thin cells of muscle tissue in *Section 2.4*. Our study elucidates one such biological relationship: the regulation of protein localization, and thus protein activation, by membrane polymorphism and, on a fundamental level, the membrane geometry-dependent distribution of lateral pressure through the membrane's core. Notably, the comparisons of spherical and cylindrical membrane systems using *Generation II* of our molecular theory have uncovered an unexpected but crucial contribution from

the Gaussian curvature, a quantity often neglected in theoretical studies involving membrane curvature, to protein localization in the bilayer.

Another change between our *Generation I* and *Generation II* models is the inclusion of an explicit description for the lipid's hydrophilic headgroup and the glycerol backbone linking it to the fatty acid chains. In biological membranes, the large, bulky lipid headgroup region has a direct, physical impact on the packing of the lipid tails within the hydrophobic channel and influences the system's electrostatics, enabling a small volume fraction of water and salt ions into the region. There is also a hydrophobic contribution to the attractive energy from the *CH*, CH_2, and *CO* segments located between the phosphate and choline moieties of a PC lipid and incorporated in the lipid's glycerol backbone *(Figure 6.1)*.

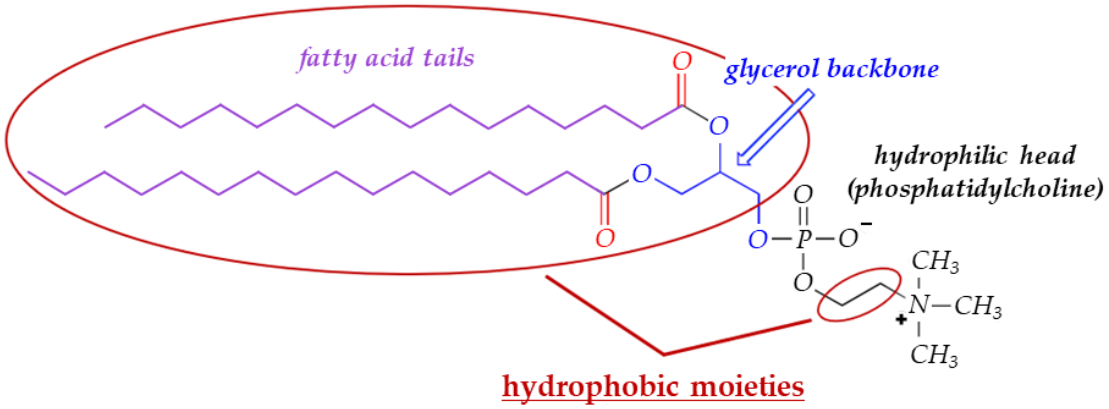

Figure 6.1) **Schematic of the hydrophobic moieties in a PC lipid.** The hydrophobic moieties of the tail, glycerol backbone, and headgroup regions of the lipid contribute to the attractive, hydrophobic interactions.

Previously, the contribution from the lipid head region to the interfacial energy

was represented by a phenomenological model in terms of the bare oil/water surface tension. The *Generation II* theory incorporates greater molecular detail for the headgroup and glycerol linker with a more complete model that accounts for their associated volumes, hydrophobicity, charge distribution, and set of configurational arrangements.

Variations of this molecular theory have been used to study acid-base equilibrium and the influence of hydrogen bonding in systems of grafted polymer chains. Others have adapted similar theoretical models to examine how membrane morphology is affected by the protonation state of p*H*-sensitive amphiphiles, how changes in local membrane composition are induced by the presence of functionalized proteins or nanoparticles, and how the electrostatic interactions between the headgroups of a membrane's lipids and an adsorbed, charged macro-ion causes a shift in the membrane's melting temperature [131, 135, 300-303]. However, the effects of membrane geometry, transbilayer lipid diffusion, and variation in lipid shape factors due to changes in membrane composition – and the non-trivial cooperativity among them – on how lipidated proteins interact with the membrane in an aqueous ionic environment have, to our knowledge, not yet been explored. The delineation of such is the goal of this work.

6.1 TOTAL FREE ENERGY FUNCTIONAL OF THE 'MEMBRANE-PLUS-IONIC

ENVIRONMENT' SYSTEM

The derivation of the theory follows a similar methodology as in *Generation I*, whereby all relevant energetic and entropic contributions are assembled into a free energy functional that fully describes all possible states of the system. In addition to the probability distribution of the hydrophobic segments in the lipid chains, the independent variables of the functional now include the probability distribution of the conformational states of the lipid headgroups, the density distributions of the free salt ions, water ions, and undissociated water molecules in the solution surrounding the membrane, and the electrostatic potential. The functional is minimized with respect to these unknown variables to solve for the potential that describes the equilibrium distributions for all species within the system in a particular physical and chemical state.

As with the *Generation I* theory, our *Generation II* membrane system is in thermal contact with a heat bath, indicative of the metabolic temperature regulation of endotherms, and maintains a defined volume. In contrast to the previous theory, however, because this volume consists of both a lipid membrane *and* its aqueous environment, rather than the system being closed to all particle exchange it is instead semi-permeable, where the number of lipids in the membrane is conserved while the aqueous species may freely pass between the system and a larger reservoir containing these species, i.e., the 'bulk' solution. To

maintain equilibrium, the chemical potential (rather than particle number) of each of these mobile components is a specified quantity, with the equilibrium requirement that it be constant at all positions within in the system and in the bulk solution. As discussed in *Section 3.2*, the potential that describes such a system is one developed within the *semi-grand canonical ensemble*, with canonical variables T, V, A, N_i, and μ_m, where the subscript, i, refers to the particles confined to the membrane, i.e., lipids, and m represents the mobile solvent and ions in the aqueous surroundings that may make contact with the membrane. Such a potential evolves from a partial Legendre transform of the Helmholtz potential, $\mathcal{F}$, that we applied to the previous theory, replacing the numbers of molecules of the mobile species with the corresponding chemical potentials as independent variables:

$$\Phi_{\text{S-G}} = \mathcal{F} - \sum_m N_m \mu_m \quad semi-grand\ potential \begin{pmatrix} partial\ Legendre\ transform \\ of\ the\ Helmholtz\ potential \end{pmatrix}$$

$$d\Phi_{\text{S-G}} = -SdT - PdV + \gamma dA + \sum_i \mu_i dN_i - \sum_m N_m d\mu_m \quad \begin{matrix} differential \\ semi-grand\ potential \end{matrix} \tag{6.1}$$

Analogous to *Equation 4.10* from the *Generation I* theory, we can expand the former expression in terms of all applicable energetic and entropic contributions to the system:

$$\beta\Phi_{\text{S-G}} = -\frac{S_{trans,lipid}(\mathbf{c})}{k_B} - \frac{S_{conf,lipid}(\mathbf{c})}{k_B} + \beta\left\langle \varepsilon_{conf,lipid}(\mathbf{c})\right\rangle + \beta\left\langle \varepsilon_{attract,lipid}(\mathbf{c})\right\rangle + \beta\left\langle \varepsilon_{electro}(\mathbf{c})\right\rangle - \frac{S_{mix}(\mathbf{c})}{k_B} + \beta F_{form}(\mathbf{c}) - \sum_m N_m \mu_m \tag{6.2}$$

The ensemble averaged electrostatic energy, $\langle\varepsilon_{electro}(\mathbf{c})\rangle$, generated from the charged particles, the mixing entropy, $S_{mix}(\mathbf{c})$, arising from the mobile species capable of intermixing between the system and the bulk, the free energy of formation, $F_{form}(\mathbf{c})$, contributed by the species capable of ionization, and the transform of the chemical potentials of the free species to independent (canonical) variables are elements unique to *Generation II*. The energetic and entropic terms associated with the membrane lipids also now explicitly incorporate both lipid chain and lipid headgroup. Further expanding each of these contributions, imposing the constraints of incompressibility and global charge neutrality, and dividing by the average lipid chain area, A (produced from performing the integrals over the x- and y-coordinates, as the system is homogeneous in the x-y plane), we obtain the operative form of our functional, per area, for a multi-component lipid bilayer within an aqueous bath containing a monovalent, fully ionized salt:

$$\frac{\beta\Phi_{\text{S-G}}}{A}=\sum_{i,\delta}\frac{x_{i,L}x_{i,L,\delta}(\mathbf{c})}{a(0)}\left(\ln\left[\frac{x_{i,L}x_{i,L,\delta}(\mathbf{c})\lambda_{i,L}^{2}}{a(0)}\right]-1\right) \tag{6.3}$$

$$+\sum_{i,\delta}\frac{x_{i,L}x_{i,L,\delta}(\mathbf{c})}{a(0)}\sum_{\omega}^{n_{i,L}^{tails}}\sum_{\alpha_{i,\omega,\delta}}P_{i,L-t,\omega,\delta}(\alpha_{i,\omega,\delta},\mathbf{c})\ln\left[P_{i,L-t,\omega,\delta}(\alpha_{i,\omega,\delta},\mathbf{c})\right]$$

$$+\beta\sum_{i,\delta}\frac{x_{i,L}x_{i,L,\delta}(\mathbf{c})}{a(0)}\sum_{\omega}^{n_{i,L}^{tails}}\sum_{\alpha_{i,\omega,\delta}}P_{i,L-t,\omega,\delta}(\alpha_{i,\omega,\delta},\mathbf{c})\varepsilon(\alpha_{i,\omega,\delta})$$

$$+\frac{\beta}{2}\sum_{i,j,\delta,\delta'}\varepsilon_{i,j,L-t}\int_{-l}^{l}\left\langle\rho_{i,L-t,\delta}(r,\mathbf{c})\right\rangle\left\langle\phi_{j,L-t,\delta'}(r,\mathbf{c})\right\rangle dr$$

$$-\frac{\beta}{2a(0)^{2}v_{CH_2}}\sum_{i,j,\delta,\delta'}J_{i,j,L-t}x_{i,L}x_{j,L}x_{i,L,\delta}(\mathbf{c})x_{j,L,\delta'}(\mathbf{c})\sum_{\omega,\omega'}^{n_{i,L}^{tails},n_{j,L}^{tails}}\int_{-l}^{l}\left\langle\xi_{i,L-t,\omega,\delta}(r,\mathbf{c})\right\rangle\left\langle\xi_{j,L-t,\omega',\delta'}(r,\mathbf{c})\right\rangle dr$$

$$+\sum_{i,\delta}\frac{x_{i,L}x_{i,L,\delta}(\mathbf{c})}{a(0)}\sum_{\sigma_\delta}P_{i,L-h,\delta}(\sigma_{i,\delta},\mathbf{c})\ln\left[P_{i,L-h,\delta}(\sigma_{i,\delta},\mathbf{c})\right]$$

$$+\frac{\beta}{2}\sum_{i,j,\delta}\varepsilon_{i,j,L-h}\int_{-\infty}^{\infty}\left\langle\rho_{i,L-h,\delta}^{hydrophobic}(r,\mathbf{c})\right\rangle\left\langle\phi_{j,L-h,\delta}^{hydrophobic}(r,\mathbf{c})\right\rangle dr$$

$$+\int_{-\infty}^{\infty}\left[\frac{\left\langle\rho_{q}(r,\mathbf{c})\right\rangle}{e}\psi(r)-\frac{1}{2}\varepsilon\left(\nabla\psi(r,\mathbf{c})\right)^{2}\right]dr$$

$$+\int_{-\infty}^{\infty}\rho_{w}(r,\mathbf{c})\left(\ln\left[\rho_{w}(r,\mathbf{c})v_{w}\right]-1\right)dr+\int_{-\infty}^{\infty}\rho_{H^+}(r,\mathbf{c})\left(\ln\left[\rho_{H^+}(r,\mathbf{c})v_{w}\right]-1+\beta\mu_{H^+}^{0}\right)dr$$

$$+\int_{-\infty}^{\infty}\rho_{OH^-}(r,\mathbf{c})\left(\ln\left[\rho_{OH^-}(r,\mathbf{c})v_{w}\right]-1+\beta\mu_{OH^-}^{0}\right)dr$$

$$+\int_{-\infty}^{\infty}\rho_{+}(r,\mathbf{c})\left(\ln\left[\rho_{+}(r,\mathbf{c})v_{w}\right]-1-\beta\mu_{+}''\right)dr+\int_{-\infty}^{\infty}\rho_{-}(r,\mathbf{c})\left(\ln\left[\rho_{-}(r,\mathbf{c})v_{w}\right]-1-\beta\mu_{-}''\right)dr$$

$$+\beta\lambda_{c.n.}\int\left\langle\rho_{q}(r)\right\rangle dr+\beta\int_{-\infty}^{\infty}\pi(r,\mathbf{c})\left(\begin{array}{l}\sum_{i,\delta}\left\langle\phi_{i,L-t,\delta}(r,\mathbf{c})\right\rangle+\sum_{i,\delta}\left\langle\phi_{i,L-h,\delta}(r,\mathbf{c})\right\rangle+\phi_{w}(r,\mathbf{c})\\+\phi_{+}(r,\mathbf{c})+\phi_{-}(r,\mathbf{c})+\phi_{H^+}(r,\mathbf{c})+\phi_{OH^+}(r,\mathbf{c})-1\end{array}\right)dr$$

For generality, the functional is written to accommodate a multicomponent lipid membrane, though for clear and direct mechanistic interpretations and computational simplicity, we focus on comparisons between spherical and cylindrical model membranes composed of pure DOPC in this study. Note that the use of scalar r, rather than $\vec{r}$, for position-dependent variables implies the

assumption of lateral homogeneity at each point in the system, with inhomogeneity explicitly accounted for only in the radial direction. Let us describe the functional term by term. The first three terms on the right-hand side are, respectively, the translational entropy of the lipids (headgroup and tail region as a single unit) and the configurational entropy and configurational energy of the lipid tails constructing the bilayer's hydrophobic region, per average lipid cross-sectional area. The details regarding these contributions mirror those of their counterparts from the *Generation I* theory, therefore, we will not repeat the more detailed explanation of these terms here, but rather give a brief description below and refer the reader to *Sections 4.2* and *4.3* for further discussion.

Areal Translational Entropy of the Membrane Lipids

$$\frac{S_{trans,L,\delta}(\mathbf{c})}{A} = -\frac{k_B}{a(0)}\sum_i x_{i,L}x_{i,L,\delta}(\mathbf{c})\left(\ln\left[\frac{x_{i,L}x_{i,L,\delta}(\mathbf{c})\lambda_{i,L}^2}{a(0)}\right]-1\right) \tag{6.4}$$

$x_{i,L}(\mathbf{c})$ is the total lipid (L) concentration of species i in the bilayer and $x_{i,L,\delta}(\mathbf{c})$ is the lipid concentration of species i in the δ (inner/outer or compressed/expanded, depending on context) leaflet, with the relationships defined in *Equation 4.6*. $a(0)$ is the average molecular area of the bilayer midplane, and $\lambda_{i,L}^2$ is the thermal de Broglie wavelength of a lipid of species i.

Areal Configurational Entropy of the Hydrophobic Lipid Chains

$$\frac{S_{config,L-t,\delta}(\mathbf{c})}{A} = -\frac{k_B}{a(0)} \sum_{i,\omega,\alpha_{i,\omega,\delta}} x_{i,L} x_{i,L,\delta}(\mathbf{c}) P_{i,L-t,\omega,\delta}(\alpha_{i,\omega,\delta},\mathbf{c}) \ln\left[P_{i,L-t,\omega,\delta}(\alpha_{i,\omega,\delta},\mathbf{c}) \right] \quad (6.5)$$

$P_{i,L\text{-}t,\omega,\delta}(\alpha_{i,\omega,\delta},\mathbf{c})$ is the probability that an individual chain, ω, of the lipid tail (L-t) region of species i in the δ leaflet exists in a given configuration, α. The summations run over all lipid species contained in a given membrane, the individual chains on each lipid, and the possible conformational states the lipid chains can physically assume.

Areal Configurational Energy of the Hydrophobic Lipid Chains

$$\frac{\beta \left\langle \varepsilon_{conf,L-t,\delta}(\mathbf{c}) \right\rangle}{A} = \frac{\beta}{a(0)} \sum_{i,\omega,\alpha_{i,\omega,\delta}} x_{i,L} x_{i,L,\delta}(\mathbf{c}) P_{i,L-t,\omega,\delta}(\alpha_{i,\omega,\delta},\mathbf{c}) \varepsilon(\alpha_{i,\omega,\delta}) \quad (6.6)$$

$\varepsilon(\alpha_{i,\omega,\delta}) = n^{gauche}(\alpha_{i,\omega,\delta})\varepsilon_g$ is the total energetic penalty incurred by a single fatty acid chain, ω, of a lipid of species i, in a particular configurational state, α, from the *gauche* (+) and *gauche* (−) dihedral angles that exist along the chain. The total number of gauche conformations along the given chain is $n^{gauche}(\alpha_{i,\omega,\delta})$, each causing a rise in the free energy by ε_g = 500 calories per mole.

Van der Waals & Hydrophobic Attractive Interaction Energy of the Hydrophobic Lipid Chains

The fourth term of our free energy functional accounts for the hydrophobic

forces generated by the attractive hydrogen bonding forces between the polar solvent molecules that drive lipid self-assembly and the weaker van der Waals (dispersion) attractive interactions, per total area, among the carbon monomers comprising the lipid chains:

$$\frac{\beta\left\langle \varepsilon_{attractive,L-t}^{hydrophobic}(\mathbf{c})\right\rangle}{A}=\frac{\beta}{2}\sum_{i,j,\delta,\delta'}\varepsilon_{i,j,L-t}\int_{-l}^{l}\left\langle \rho_{i,L-t,\delta}(r,\mathbf{c})\right\rangle\left\langle \phi_{j,L-t,\delta'}(r,\mathbf{c})\right\rangle dr \tag{6.7}$$

The attractive forces are represented by a contact potential between monomers on lipid chains existing in the same bilayer leaf or opposing leaflets. The potential is dependent on the volume fraction, $\phi_{i,L\text{-}t,\omega,\delta}(\alpha_{i,\omega,\delta},r,\mathbf{c})$, or number density, $\rho_{i,L\text{-}t,\omega,\delta}(\alpha_{i,\omega,\delta},r,\mathbf{c})$, of lipid tail monomers at each point (in each discretized layer) along the hydrophobic width of the bilayer in the δ leaflet, in a given configurational state, ensemble averaged over all physical configurations:

$$\left\langle \phi_{i,L-t,\delta}(r,\mathbf{c})\right\rangle=\left\langle \rho_{i,L-t,\delta}(r,\mathbf{c})\right\rangle v_{CH_2}=\sum_{\omega,\alpha_{i,\delta}}P_{i,L-t,\omega,\delta}(\alpha_{i,\omega,\delta},\mathbf{c})\rho_{i,L-t,\omega,\delta}(\alpha_{i,\omega,\delta},r,\mathbf{c})v_{CH_2} \tag{6.8}$$

where v_{CH2} is the volume of the CH_2 units constructing the lipid tails (27.0 Å^3) [150]. The conformation-dependent number density of a single chain, $\rho_{i,L\text{-}t,\omega,\delta}(\alpha_{i,\omega,\delta},r,\mathbf{c})$, is calculated by summing the number of its carbon atoms per unit length, $\bar{n}_{i,L\text{-}t,\omega,\delta}^{hydrophobic}(\alpha_{i,\omega,\delta},r,\mathbf{c})$, in each discretized layer through the membrane's hydrophobic channel, as determined by the RIS model:

$$\rho_{i,L-t,\omega,\delta}(\alpha_{i,\omega,\delta}, r, \mathbf{c}) = \frac{x_{i,L} x_{i,L,\delta}(\mathbf{c})}{a(0)} \overline{n}^{hydrophobic}_{i,L-t,\omega,\delta}(\alpha_{i,\omega,\delta}, r, \mathbf{c}) \tag{6.9}$$

The interactions are determined within the mean-field approximation, which is generated in a self-consistent manner from the average properties of the system's molecules. The strength of the interaction, $\varepsilon_{i,j,L\text{-}t}$, is dependent on the type(s) of interacting lipids, of species *i* and *j*. For a pure component bilayer, this parameter takes on a single value, $\varepsilon_{L\text{-}t}$, found by modulating the membrane's thickness and molecular area, within the range of accepted experimental values from the literature [178, 182, 282] (at equilibrium, in planar form, and under similar environmental conditions as used in our model), to solve the system under the constraint of zero membrane tension. In our pure DOPC model bilayer at room temperature (298 K), which is presently the system of focus, we find a bilayer hydrophobic thickness of 28.0 Å, a molecular area of 69.5955 Å^2, and an $\varepsilon_{L\text{-}t}$ set at $-5.0 k_B T$ as the conditions which yield a tensionless membrane.

Such a potential is well suited to characterize the association among particles in a liquid crystalline environment. Modeling the intermolecular attractive energy as a function that tracks the density of the hydrophobic particles at each position in space is a necessary addition to the *Generation II* theory, in which we introduce an aqueous medium. It serves to simulate the important hydrophobic-driven forces acting on the lipid tails, capturing the amphiphilic

nature of the lipids that drives their self-assembly in solution *(hydrophobic effect)*. Local areas where lipid tail carbon units are high in density necessarily cause a depletion of water in these regions, in compliance with the incompressibility constraint, lending a higher contribution to the free energy from the attractive interaction term. Our model also uses this type of potential to capture the small number of hydrophobic interactions contributed by the hydrophobic moieties within the lipid headgroup and glycerol backbone *(see Figure 6.1 and Equation 6.12)*.

A model relying on a density-dependent contact potential alone does not sufficiently motivate the alignment, or straightening, of the hydrocarbon chains to the degree necessary to reproduce the experimentally reported condensed liquid-ordered or gel phases, below the main chain transition temperature of the lipid. The fifth term of our functional compensates for this limitation by incorporating a potential based on the orientation of the chain, relative to the bilayer normal, which favors efficient, nematic-like chain packing. This potential is introduced and discussed in greater detail than provided here in *Section 4.3*, in the sub-section titled *Maier-Saupe Attractive Interaction Energy of the Hydrophobic Lipid Chains*.

$$\frac{\beta\left\langle \varepsilon_{attractive,L-t}^{orientational}(\mathbf{c})\right\rangle}{A}= -\frac{\beta}{2a(0)^2 v_{CH_2}}\sum_{\substack{i,j,\\ \delta,\delta'}} J_{i,j,L-t}x_{i,L}x_{j,L}x_{i,L,\delta}(\mathbf{c})x_{j,L,\delta'}(\mathbf{c})\sum_{\omega,\omega'}^{n_{i,L}^{tails},n_{j,L}^{tails}}\int_{-l}^{l}\left\langle \xi_{i,L-t,\omega,\delta}(r,\mathbf{c})\right\rangle\left\langle \xi_{j,L-t,\omega',\delta'}(r,\mathbf{c})\right\rangle dr \tag{6.10}$$

The orientational energy term interprets intermolecular attractions through the

function $\langle \xi_{i,L\text{-}t,\omega,\delta}(r,\mathbf{c}) \rangle$ *(see Equations 4.14-4.20)*, which is dependent on the average angle between the carbon-carbon vector from position $\vec{r}_{k\text{-}1}$ to $\vec{r}_{k+1}$ along the lipid chain and the bilayer normal *(Equation 4.13)*. This cosine-based angle potential favors chain orientations in the *trans* conformation, effectively driving the main chain transition under appropriate environmental conditions. This contribution is tuned by the values of $J_{i,j,L\text{-}t}$, which represent the strength of the interaction between the segments of lipid species *i* and *j*. The values of $J_{i,j,L\text{-}t}$ are adjusted for each combination of interacting species based on available experimental phase diagrams. This ensures the ability of the model to capture disorder-order-gel phase transitions in systems involving high melting temperature saturated lipids, without producing artificial phase separation in systems, mostly of unsaturated lipids, that have not been shown by experiment to do so. In practice, this orientation-based attractive potential need only be applied to systems modeling liquid-ordered or gel phases, which usually require sufficient concentrations of unbranched saturated lipid species (and more readily emerge with the addition of cholesterol) at low enough environmental temperatures. Though this study models only the liquid-disordered phase, we include the term here for generality.

Areal Configurational Entropy of the Lipid Headgroups and Glycerol Backbone

The sixth term of the functional describes the configurational entropy of the lipid headgroup (*L-h*) (with which we incorporate the lipid's glycerol backbone)

in terms of the probability, $P_{i,L\text{-}h,\delta}(\sigma_{i,\delta},\mathbf{c})$, of species i assuming a specific headgroup conformation, σ, in leaf δ:

$$\frac{S_{conf,L-h,\delta}(\mathbf{c})}{A} = -\frac{k_B}{a(0)}\sum_{i,\sigma_{i,\delta}} x_{i,L}x_{i,L,\delta}(\mathbf{c})P_{i,L-h,\delta}(\sigma_{i,\delta},\mathbf{c})\ln\left[P_{i,L-h,\delta}(\sigma_{i,\delta},\mathbf{c})\right] \qquad (6.11)$$

The expression is analogous to that for the lipid tails from *Equation 6.5*. It is important to consider the role of the lipid headgroups when investigating the response of the membrane to a liquid environment containing charged molecules. The electrostatic interactions that arise, which precipitate either the accumulation or repulsion of ionic solvent species near the membrane, have a marked effect on the local p*H*, creating a fluctuating p*H* distribution between the membrane surface and the bulk solution. Integral membrane proteins or other membrane-associated macromolecules may also be affected by these local p*H* changes, as consequential alterations in the pK_a of their charged residues potentially alter their biological activity.

The modelling of the charged phosphate (PO_4^-) and choline ($N(CH_3)_3^+$) moieties of the PC lipid headgroup is similar to the formulations developed by E. C. Mbamala *et al*. [304] and later expanded upon by D. Grillo *et al.* [131]. Mbamala *et al*. [304] described the electric character of zwitterionic phospholipid headgroups within a mean-field that accounted for variations in the orientation of their dipoles with respect to the hydrophobic–hydrophilic interface. However,

they approximated the molecules as point charges, neglecting a volume component, and did not involve the lipid chains. Grillo *et al.* [131] adapted Mbamala's headgroup model in a theoretical analysis of planar phospholipid bilayers, conferring spherical volumes and an arbitrary set of spatial orientations to the charged headgroup moieties. Rather than hard spheres, we incorporate the volume of the glycerol backbone into that of the phosphate group and model the glycerol-plus-phosphate and choline moieties as two adjacent cylinders of radius 3.58 Å and 2.82 Å, respectively, both with a length of 4 Å, to better capture the principal shape of the molecules and the distribution of their charges. The negatively charged phosphate group is bound to the glycerol linker, which is proximal to the hydrophobic region, while the positively charged choline group is at the most distal portion of the headgroup and is free to migrate around the phosphate moiety. We therefore model the glycerol-plus-phosphate moieties as an immobile cylinder stemming from the tail interface, its negative charge ($-1e$; e is the fundamental charge) taken to be a point charge set at its base, and assign a set of conformational states to the adjoining choline 'cylinder'. For adequate sampling of the choline moiety's conformations, we characterize each unique state by both the location of the choline group (i.e., the amount of volume it contributes to each discretized layer it occupies, based on its position around the phosphate group) and the variable orientation of its positive (point) charge ($1e$) within the

choline moiety itself (that would physically result from bond rotations). Each of these conformational states lends a distinct number of hydrophobic units to the discrete layers within the model membrane's headgroup region. These non-polar segments contribute an attractive energy to the functional, with a term analogous to that of the tails. Examples of different conformational states of the phospholipid headgroup in a planar membrane are illustrated in *Figure 6.2*.

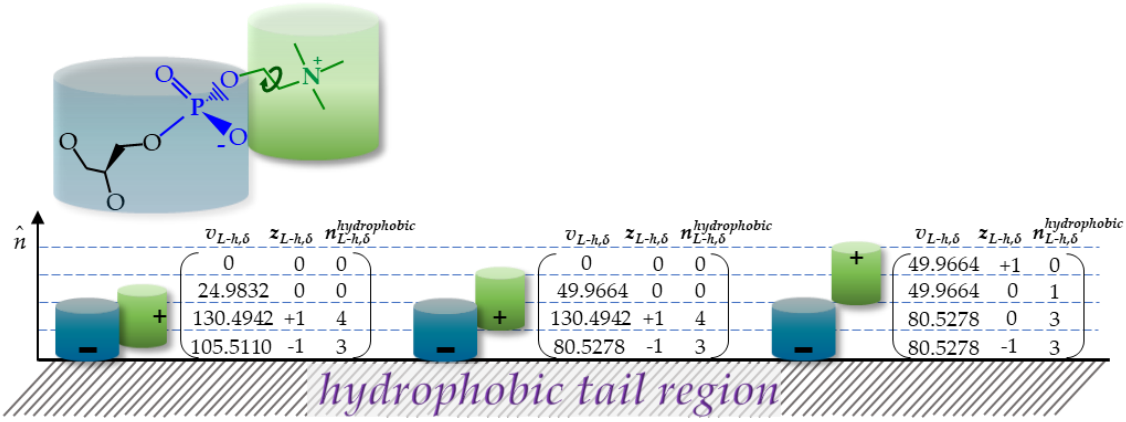

Figure 6.2) **Schematic representing three possible conformational states of the phosphatidylcholine headgroup and glycerol backbone of a PC lipid.** The PC headgroups are modeled as two adjoining cylinders representing a negatively charged phosphate moiety bound to the glycerol backbone *(blue)* and the positively charged choline moiety *(green)*. The phosphate group is fixed in space, with its negative (point) charge fixed at the first discretized layer above the hydrophobic–hydrophilic interface. The choline group is free to rotate about its covalent bond linking it to the phosphate group, yielding different conformational states, σ, that contribute different amounts of volume, $v_{i,L\text{-}h,\delta}(\sigma_{i,\delta},r,\mathbf{c})$, valence, $z_{i,L\text{-}h,\delta}(\sigma_{i,\delta},r,\mathbf{c})$, and number of hydrophobic monomers, $n^{hydrophobic}_{i,L\text{-}h,\delta}(\sigma_{i,\delta},r,\mathbf{c})$, to each discretized layer of our model.

In the above schematic, we show discretized layers along the bilayer normal, the first being at the interface of the hydrophobic lipid tail region and the

lipid's glycerol backbone, which links the fixed, negatively charged phosphate moiety of the PC headgroup. The choline group may migrate through the discretized layers, as illustrated, maintaining its covalent bond to the phosphate group; it may also rotate about that bond to a certain degree as dictated by its torsion angle, which confers the localization of positive charge to different regions of the moiety and thus to different discretized layers of our model membrane. The illustration presents three possible conformational states of the lipid headgroup, with corresponding values of the net volume, $v_{i,L\text{-}h,\delta}(\sigma_{i,\delta},r,\mathbf{c})$, valence, $z_{i,L\text{-}h,\delta}(\sigma_{i,\delta},r,\mathbf{c})$, and number of hydrophobic particles, $n_{i,L\text{-}h,\delta}^{hydrophobic}(\sigma_{i,\delta},r,\mathbf{c})$, contributed by the glycerol linker-plus-headgroup region in each discretized layer.

Phospholipid headgroups other than PC can be modeled using the same methodology described above. The cholesterol headgroup allows a simpler approach, as it comprises but a single hydroxyl group, which is uncharged and contains no conformational degrees of freedom. In systems including cholesterol, we assign a spherical volume to the hydroxyl group of 25.0 $Å^3$ [35, 125] and fix its position within the first discretized layer above the lipid hydrophobic–hydrophilic interface.

Van der Waals & Hydrophobic Attractive Interaction Energy of the Lipid Headgroup

The weak hydrophobicity of a lipid's headgroup and glycerol backbone is

accounted for by an energetic contribution given by the seventh term of the functional, analogous to that of the tails from *Equation 6.7*:

$$\frac{\beta\left\langle \varepsilon_{attract,L-h}^{hydrophobic}(\vec{c})\right\rangle}{A}=\frac{\beta}{2}\sum_{i,j,\delta}\varepsilon_{i,j,L-h}\int_{-\infty}^{\infty}\left\langle \rho_{i,L-h,\delta}^{hydrophobic}(r,\mathbf{c})\right\rangle\left\langle \phi_{j,L-h,\delta}^{hydrophobic}(r,\mathbf{c})\right\rangle dr \tag{6.12}$$

It captures the van der Waals and hydrophobic interactions among the small number of non-polar segments in these regions represented by a mean-field potential. For PC lipids, the majority of these segments include CH_2 groups, thus we choose a streamlined approach by approximating the total volume of each unit and the magnitude of the pair-wise interaction between them as equivalent to those used for the CH_2 monomers of the lipid tails: $v_{CH2} = 27.0$ Å^3 and $\varepsilon_{i,j,L\text{-}h} = -5.0k_BT$, respectively. The attractive potential is governed by the configuration-dependent density of the hydrophobic segments, $\rho_{i,L\text{-}h,\delta}^{hydrophobic}(\sigma_{i,\delta},r,\mathbf{c})$, in each discretized layer comprising the polar region of a lipid of species i in the δ leaflet, averaged over the ensemble of their accessible configurational states (σ), $\langle\rho_{i,L\text{-}h,\delta}^{hydrophobic}(r,\mathbf{c})\rangle$:

$$\begin{aligned}\left\langle \rho_{i,L-h,\delta}^{hydrophobic}(r,\mathbf{c})\right\rangle &= \sum_{\sigma_{i,\delta}} P_{i,L-h,\delta}(\sigma_{i,\delta},\mathbf{c})\rho_{i,L-h,\delta}^{hydrophobic}(\sigma_{i,\delta},r,\mathbf{c})\\ \left\langle \phi_{i,L-h,\delta}^{hydrophobic}(r,\mathbf{c})\right\rangle &= \left\langle \rho_{i,L-h,\delta}^{hydrophobic}(r,\mathbf{c})\right\rangle v_{CH_2}\end{aligned} \tag{6.13}$$

$P_{i,L\text{-}h,\delta}(\sigma_{i,\delta},\mathbf{c})$ is the probability of the lipid's glycerol-plus-headgroup existing in a given configuration, σ, and $\rho_{i,L\text{-}h,\delta}^{hydrophobic}(\sigma_{i,\delta},r,\mathbf{c})$ is defined in terms of the number of hydrophobic atoms per unit length, $\bar{n}_{i,L\text{-}h,\delta}^{hydrophobic}(\sigma_{i,\delta},r,\mathbf{c})$, in each discretized layer

through this region and the total concentration of the lipid in the δ leaf:

$$\rho_{i,L-h,\delta}^{hydrophobic}(\sigma_{i,\delta},r,\mathbf{c}) = \frac{x_{i,L}x_{i,L,\delta}(\mathbf{c})}{a(0)}\overline{n}_{i,L-h,\delta}^{hydrophobic}(\sigma_{i,\delta},r,\mathbf{c}) \tag{6.14}$$

Note that this density of *hydrophobic monomers*, localized in the otherwise generally *hydrophilic domain* of the lipid, is a different quantity than the *overall* density contributed by atoms (which may or may not be hydrophobic) of the lipid's glycerol backbone and headgroup, denoted $\rho_{i,L\text{-}h,\delta}(\sigma_{i,\delta},r,\mathbf{c})$, without the '*hydrophobic*' superscript of the former. Such a distinction is technically unnecessary in density-dependent terms involving the lipid chains, as *all* units in the tail region are hydrophobic.

Electrostatic Energy, per Area, Generated by the Charged Species

The eighth term in our functional depicts the total electrostatic energy arising from the potential field caused by the density distribution of all charged species in the system:

$$\frac{\beta\left\langle \varepsilon_{electro}(\mathbf{c})\right\rangle}{A} = \int_{-\infty}^{\infty}\left(\frac{\left\langle \rho_q(r,\mathbf{c})\right\rangle}{e}\psi(r,\mathbf{c}) - \frac{1}{2}\varepsilon\left(\nabla\psi(r,\mathbf{c})\right)^2\right)dr \tag{6.15}$$

where $\langle\rho_q(r,\mathbf{c})\rangle$ is the position-dependent, ensemble-averaged total charge density in the system, calculated by summing the individual charge densities of the system's charged components:

$$\left\langle \rho_q(r,\mathbf{c}) \right\rangle = \sum_{cations} \rho_+(r,\mathbf{c})q_+ + \sum_{anions} \rho_-(r,\mathbf{c})q_- + \rho_{H^+}(r,\mathbf{c})q_{H^+} + \rho_{OH^-}(r,\mathbf{c})q_{OH^-} + \sum_{\delta} \left\langle \rho_{q,i,L-h,\delta}(r,\mathbf{c}) \right\rangle$$

or

$$\left\langle \rho_q(r,\mathbf{c}) \right\rangle = \sum_{x} \rho_x(r,\mathbf{c})q_x + \sum_{\delta} \left\langle \rho_{q,i,L-h,\delta}(r,\mathbf{c}) \right\rangle \tag{6.16}$$

The electric charge, q_x, of the charged, mobile species ($x \equiv$ salt cations (+), salt anions (−), and the hydronium (H^+) and hydroxide (OH^-) ions of dissociated water), is defined as $q_x = z_x e$, where $e = 1.60217662 \times 10^{-19}$ C, the elementary charge, and z_x is the valence of charged particle x, positive for cations and negative for anions. The electric charge is weighted by the number density, $\rho_x(r,\mathbf{c})$, of its corresponding molecular species x, which is dependent on the particle's position within the system and membrane curvature but does not possess any conformational degrees of freedom. The lipid headgroup does experience conformational variations, thus, the local charge density of a lipid species i is averaged over the ensemble of its conformational states, $\sigma_{i,\delta}$, written as $\langle \rho_{q,i,L\text{-}h,\delta}(r,\mathbf{c}) \rangle$ and expressed in terms of its conformation-dependent number density, $\rho_{i,L\text{-}h,\delta}(\sigma_{i,\delta},r,\mathbf{c})$, and electric charge, $q_{i,L\text{-}h,\delta}(\sigma_{i,\delta},r,\mathbf{c})$, weighted by its corresponding probability distribution function, $P_{i,L\text{-}h,\delta}(\sigma_{i,\delta},\mathbf{c})$:

$$\left\langle \rho_{q,i,L-h,\delta}(r,\mathbf{c}) \right\rangle = \sum_{\sigma_{i,\delta}} P_{i,L-h,\delta}(\sigma_{i,\delta},\mathbf{c}) \rho_{i,L-h,\delta}(\sigma_{i,\delta},r,\mathbf{c}) q_{i,L-h,\delta}(\sigma_{i,\delta},r,\mathbf{c})$$

with: (6.17)

$$q_{i,L-h,\delta}(\sigma_{i,\delta},r,\mathbf{c}) = z_{i,L-h,\delta}(\sigma_{i,\delta},r,\mathbf{c})e$$

The valence of the lipid polar region, $z_{i,L\text{-}h,\delta}(\sigma_{i,\delta},r,\mathbf{c})$, is distributed as discussed previously, with examples shown in *Figure 6.2*.

The electrostatic energy is written in terms of the dimensionless electrostatic potential, $\Psi(r,\mathbf{c}) = \beta e \Phi_{\text{E.P.}}(r,\mathbf{c})$ and the prefactor, ε, is defined as:

$$\varepsilon = \frac{\varepsilon_0 \varepsilon_r}{\beta e^2} = \frac{1}{4\pi l_b} \tag{6.18}$$

where ε_0 = 8.854187817x10^{-12} F/m is the vacuum permittivity constant, ε_r is the relative dielectric permittivity of the salt-water bath, and l_b is the Bjerrum length. Technically, the relative dielectric permittivity of the bath includes the sum of the dielectric constants for each of the solution components weighted by their corresponding volume fractions at position, r:

$$\varepsilon_r(r) = \sum_{m=salts,water} \varepsilon_m \phi_m(r) \tag{6.19}$$

However, the dielectric properties of aqueous solutions have been shown to be noticeably affected only with local salt ion concentrations much higher than biologically relevant, e.g., at the molar range as opposed to physiological concentrations between 0.1 and 0.2 M (mole/liter) [147, 305]. We set our salt concentration to 0.1 M in our model; therefore, the bulk solution dielectric can be

taken to be equal to that of pure water: $\varepsilon_r = \varepsilon_w = 78.54$ [305], yielding a Bjerrum length of 0.714 nm.

A term analogous to *Equation 6.16* expresses the total charge density within the bulk solution, far from the membrane, in terms of the bulk number densities of the charged solution components:

$$\rho_q^{bulk}(r \to \infty) = \sum_{cations} \rho_+^{bulk} q_+ + \sum_{anions} \rho_-^{bulk} q_- + \rho_{H^+}^{bulk} q_{H^+} + \rho_{OH^-}^{bulk} q_{OH^-} \tag{6.20}$$

In our system, the number of cations and the number of anions in the bulk solution are equivalent, as are the magnitudes of their corresponding valences, and are distributed uniformly. Therefore, the bulk solution is inherently net charge-neutral, with $\rho_q^{bulk}(r \to \infty) = 0$. We extend the condition of charge neutrality from the bulk to our system with the imposition of a *global* electroneutrality constraint on our functional (which we discuss shortly), though the distribution of the system's charged species is nonuniform, creating *local* fluctuations in charge through the system.

The electrostatic properties of membranes are centrally involved in many membrane-mediated phenomena, such as the conductivity through ion channels, the membrane's interaction with charged proteins (which influences the protein's conformational state and functionality), and the membrane's response to therapeutic substances. There is some speculation that counterions near the

surface of anionic membranes, such as those with a high concentration of the PS lipids commonly found in the inner leaflet of biological bilayers, may alter the phase characteristics of the membrane by screening its interaction with sugar molecules present in the solution [32, 306]. Even lipids that are electrically net-neutral in physiological conditions, such as PC and PE lipids, generate electrostatic surface potentials from the dipole of their zwitterionic headgroups that create an electrostatic environment distinct from that of the bulk solution. The charges on lipid headgroups also alter concentration gradients due to the presence of counterions near the membrane surface. In the results section of Chapter 7 *(Section 7.3, Results II.I)*, we examine the equilibrium charge density distributions of the lipid molecules and ions in solution, obtained through the explicit modeling of the zwitterionic PC lipid headgroups.

Areal Mixing Entropy, Energy of Formation, and the Constant Chemical Potential Constraint

The next five terms of the functional (ninth through thirteenth) represent contributions from the mixing entropy of the mobile species, the formation energy of charged-regulated components, and the equilibrium requirement of global equivalency in chemical potential imposed on each of the mobile species.

The mixing entropy arises from the spatial inhomogeneity of all mobile components in the bulk solution that are in contact with the membrane, expressed

per total area as:

$$\frac{S_{mix}(\mathbf{c})}{A} = -k_B \sum_{m=\left(\substack{w,\ H^+,\ OH^-,\\ +,\ -}\right)} \int_{-\infty}^{\infty} \rho_m(r,\mathbf{c})\left(\ln\left[\rho_m(r,\mathbf{c})v_w\right]-1\right)dr \tag{6.21}$$

Note that we use the '+' and '−' symbols to broadly refer to any cationic and anionic salt ions, respectively, existing in the system; in our *Generation II* model, we include the salt *NaCl*, which we take to be completely dissociated into its monovalent ions, Na^+ and Cl^-. The local number densities of the mobile species, m, in the system at a location, r, are $\rho_m(r,\mathbf{c}) = \rho_w(r,\mathbf{c})$, $\rho_{H+}(r,\mathbf{c})$, $\rho_{OH-}(r,\mathbf{c})$, $\rho_+(r,\mathbf{c})$, and $\rho_-(r,\mathbf{c})$, corresponding to undissociated water, the hydronium and hydroxide ions of dissociated water, and the cations and anions of dissociated salts, respectively. The volume of a molecule of water is $v_w = 30.0$ Å^3; this value is also used to approximate the volumes of the H^+, OH^-, Na^+ and Cl^- ions.

The solvent water molecules continuously undergo self-ionization through the equilibrium reaction: $H_2O_{(l)} + H_2O_{(l)} \rightleftarrows H_3O^+_{(aq)} + OH^-_{(aq)}$. There is an *energy of formation*, F_{form}, associated with this process that is represented, per area, by the expression:

$$\frac{\beta F_{form}(\mathbf{c})}{A} = \beta \int_{-\infty}^{\infty} \rho_{H^+}(r,\mathbf{c})\mu^0_{H^+}dr + \beta \int_{-\infty}^{\infty} \rho_{OH^-}(r,\mathbf{c})\mu^0_{OH^-}dr \tag{6.22}$$

where $\mu^0_{H^+}$ and μ^0_{OH-} are the standard chemical potentials of the hydronium and hydroxide ions, respectively. We take the sodium chloride salt included in the

solution at 0.1 M to be completely dissociated, thus, it does not make any contribution to the energy generated from ongoing reactions in the system. Note that there would be additional terms contributing to the total formation energy if our system were to incorporate additional species involved in acid-base equilibrium reactions between charged and uncharged states. The charge-state of ionizable groups depends on their intrinsic pK_a and the pH of their local environment. The pK_a of a molecule, or its individual functional groups, may be considered as the pH at which the probabilities of the protonated and deprotonated states of the molecule are equal. At environmental pH values lower than a molecule's intrinsic pK_a, the molecule resides in a solution that is acidic relative to its own chemical nature and, due to the excess protons, the molecule predominantly exists in its protonated form; at pH values higher than a molecule's pK_a, the molecule is more acidic than its environment and is consequently unprotonated. While the headgroup of a PC lipid is capable of undergoing acid-base equilibrium reactions, within a physiological pH range the phosphate group (pK_a ~ 2) maintains its deprotonated form (with one negative charge), and the choline group (pK_a ~ 9) remains protonated (one positive charge) [307]. In this model, the concentration of solute in solution is sufficiently dilute and the effect of the ionic strength of the 1:1 *NaCl* electrolyte on the dissociation constant of water in the bulk solution, K_w, is negligible. Thus, we may take the activity of water to

be equal to unity and approximate the activities of the hydronium and hydroxide ions as their corresponding molar concentrations. We hence assume the bulk solution obeys the relation:

$$K_w = \left[H^+ \right] \left[OH^- \right] \tag{6.23}$$

such that:

$$\mathrm{p}K_w = -\log\left[K_w \right] = 14.0, \text{ at } 298.15 \text{ K} \tag{6.24}$$

and we set the bulk pH at 7.0. Under these conditions, it is not necessary to include protonation/deprotonation equilibrium reactions for the lipid components in our model.

At the top of this section, we discussed that in our choice of a statistical ensemble, in which our system is permeable to the efflux and influx of solution components to and from its surrounding aqueous 'bulk' reservoir, the equilibrium condition requiring equivalency in chemical potential of each of these mobile components between system and bulk manifests as an addition of $-\sum_m N_m \mu_m$ to our functional. The mobile species, m, include both solute and solvent, however, the relationship between the hydronium and hydroxide concentrations via the chemical equilibrium of water (discussed in the previous paragraph) and the implementation of two constraints, incompressibility and global electroneutrality (discussed in the following subsection), reduce the number of independent

thermodynamic variables by a total of three. We choose to eliminate the number of water, hydronium, and hydroxide molecules as independent variables. This procedure dismisses the need to explicitly specify the chemical potentials of these components, leaving our sum to encompass only the ions of dissociated salts in the system (presently, sodium and chloride ions). As the particle distribution in the system is inhomogeneous in the dimension normal to the bilayer, we integrate the term with respect to position and divide by constant area to obtain:

$$-\left(\beta \int_{-\infty}^{\infty} \rho_{+}(r,\mathbf{c})\mu_{+}''dr + \beta \int_{-\infty}^{\infty} \rho_{-}(r,\mathbf{c})\mu_{-}''dr \right) \tag{6.25}$$

as the effective expression resulting from the partial Legendre transform of $\mathcal{F}$. Note that the chemical potential of the aqueous sodium ions, μ_{+}'', and chloride ions, μ_{-}'', are in fact *exchange* chemical potentials (which we indicate with the double prime), due to the constraints that reduce the number of independent thermodynamic variables. The following subsection demonstrates the procedure for deriving these exchange chemical potentials.

Electroneutrality and Incompressibility Constraints

The final two terms included in the functional are not explicitly part of the functional but are, rather, imposed as constraints on the system to ensure global electroneutrality and local incompressibility. The former is written as the requirement that integration of the total charge density (defined in *Equation 6.16*)

over the entire system equates to zero:

$$\int_{-\infty}^{\infty} \left\langle \rho_q(r,\mathbf{c}) \right\rangle dr = 0 \tag{6.26}$$

The charge neutrality constraint is enforced by the Lagrange multiplier, $\lambda_{c.n.}$. After functional minimization (which is the topic of *Section 6.2*), this parameter gives a constant contribution to the lipid headgroup probability distribution function; consequently, its value can be absorbed in the partition function for the lipid headgroups. $\lambda_{c.n.}$ also appears in the equilibrium density functions of the charged solution species, however, as a constant, it cancels during the process of solving for the local density distributions using bulk solution quantities, as will be shown in the following section.

The second addendum to the functional, the incompressibility constraint, is understood on a macroscopic level to conserve total system volume; microscopically, it manipulates particle spatial distribution and conformational probabilities (of those molecules possessing conformational degrees of freedom) by ensuring that the volume between any position *r* and *dr* is filled completely by lipids, ions, or solvent, without overlap. By enforcing a particle's observation of the excluded volume of other system particles, the incompressibility constraint accounts for the average, short-range steric repulsions realistically existing in a confined system of highly dense molecules. Mathematically, the constraint sets

the sum of the volume fractions of all species included in the system (membrane and aqueous environment), at every position, to unity:

$$1 = \sum_{i,\delta} \left(\left\langle \phi_{i,L-t,\delta}(r,\mathbf{c}) \right\rangle + \left\langle \phi_{i,L-h,\delta}(r,\mathbf{c}) \right\rangle \right) + \phi_w(r,\mathbf{c}) + \phi_+(r,\mathbf{c}) + \phi_-(r,\mathbf{c}) + \phi_{H^+}(r,\mathbf{c}) + \phi_{OH^-}(r,\mathbf{c}) \quad (6.27)$$

The volume fractions of the lipid tails, $\phi_{i,L\text{-}t,\omega,\delta}(\alpha_{i,\omega,\delta},r,\mathbf{c})$, and lipid headgroup, $\phi_{i,L\text{-}h,\delta}(\sigma_{i,\delta},r,\mathbf{c})$, of species i, in the δ leaflet of the bilayer, are ensemble averaged over all their corresponding configurational states, α and σ, respectively, written as $\langle\phi_{i,L\text{-}t,\delta}(r,\mathbf{c})\rangle$ and $\langle\phi_{i,L\text{-}h,\delta}(r,\mathbf{c})\rangle$; solution components do not possess conformational degrees of freedom. The constraint is enforced during minimization of the functional by the Lagrange multipliers, $\pi(r,\mathbf{c})$. Via the incompressibility constraint, the field-variables $\pi(r,\mathbf{c})$ tie the forces acting within the membrane to the external forces generated by molecules existing on both sides of the bilayer. Though they are referred to as local parameters, $\pi(r,\mathbf{c})$ have important nonlocal contributions, as the constraints on molecular packing couple all positions in the system. After functional minimization, we find that these field variables come to physically represent the position-dependent osmotic pressures that arise to satisfy the condition of constant solvent chemical potential everywhere in the fluid; this is made clear in *Section 6.2*. Analogous to *Equation 6.27*, a constraint of incompressibility is imposed within the bulk fluid reservoir:

$$1 = \phi_w^{bulk} + \phi_+^{bulk} + \phi_-^{bulk} + \phi_{H^+}^{bulk} + \phi_{OH^-}^{bulk} \quad (6.28)$$

In the previous subsection, we noted that the implementation of the constraints on the system reduces the number of independent thermodynamic variables. Choosing the number of water molecules and the numbers of its dissociated ions to be the designated dependent quantities, the chemical potentials of these species need not be explicitly written, and the remaining solute chemical potentials consequently become exchange chemical potentials. Details of this process are as follows, beginning with writing the incompressibility constraint, *Equation 6.27*, in the form:

$$V = \sum_i v_{i,L} \left\langle N_{i,L}(\mathbf{c}) \right\rangle + \sum_m v_m N_m(\mathbf{c}) \tag{6.29}$$

In this example, we have consolidated the tails and headgroup of lipid species i into a single unit for simplicity, with total number, $N_{i,L}(\mathbf{c})$, within the membrane, each with a corresponding volume, $v_{i,L}$. The summation over m includes all of the mobile, aqueous components. Taking the differential of the above equation, we have:

$$dV = \sum_i v_{i,L} d\left\langle N_{i,L}(\mathbf{c}) \right\rangle + \sum_m v_m dN_m(\mathbf{c}) \tag{6.30}$$

In fulfilling this equation, the number of molecules in the system and the total system volume cannot all be independent. We begin by solving for the differential number of water molecules, $dN_w(\mathbf{c})$, in terms of the differential volume and number

of molecules of the other system species, to eliminate it from the expression for the Helmholtz thermodynamic potential:

$$dN_w(\mathbf{c}) = \frac{dV}{v_w} - \sum_i \frac{v_{i,L}}{v_w} d\left\langle N_{i,L}(\mathbf{c})\right\rangle - \sum_{m\neq w} \frac{v_m}{v_w} dN_m(\mathbf{c}) \tag{6.31}$$

$$dF = -SdT - \left(P - \frac{\mu_w}{v_w}\right)dV + \sum_i \left(\mu_{i,L} - \mu_w \frac{v_{i,L}}{v_w}\right) d\left\langle N_{i,L}(\mathbf{c})\right\rangle + \sum_{m\neq w}\left(\mu_m - \mu_w \frac{v_m}{v_w}\right) dN_m(\mathbf{c}) \tag{6.32}$$

The sum over $m \neq w$ now includes all aqueous components other than water. Let us define:

$$P' = P - \frac{\mu_w}{v_w} \tag{6.33}$$

as the *constrained pressure*, i.e., the total pressure of the system, which we take to be 1 bar, with respect to the solvent chemical potential, and:

$$\mu_k' = \mu_k - \mu_w \frac{v_k}{v_w} \tag{6.34}$$

as the *exchange chemical potential* of any system component of type, k, excluding water. The exchange chemical potential of species k is a measure of the work necessary to replace v_k/v_w solvent molecules by molecules of species k within the system.

We use the same methodology, this time applied to the electroneutrality constraint *(Equation 6.26)*, which we can write in the form:

$$0 = \sum_x q_x N_x(\mathbf{c}) \tag{6.35}$$

where x signifies the charged, mobile species in the system. Note that in integrating *Equation 6.26* over all space the lipid headgroup term is eliminated, as the equal and opposite electric charges of the headgroup's charged moieties together yield a net neutral molecule. As was done with the number of water molecules prior, we can solve for the total number of hydronium ions in the system, now using the above condition, and apply it to the 'constrained' Helmholtz potential derived in *Equation 6.32*, using the definitions of *Equations 6.33* and *6.34*, as so:

$$N_{H^+}(\mathbf{c}) = -\sum_{x \neq H^+} \frac{q_x}{q_{H^+}} N_x(\mathbf{c}) \quad \text{and} \quad dN_{H^+}(\mathbf{c}) = -\sum_{x \neq H^+} \frac{q_x}{q_{H^+}} dN_x(\mathbf{c}) \tag{6.36}$$

$$dF = -SdT - P'dV + \sum_i \mu'_{i,L} d\left\langle N_{i,L}(\mathbf{c}) \right\rangle + \sum_{x \neq H^+} \left(\mu'_x - \mu'_{H^+} \frac{q_x}{q_{H^+}} \right) dN_x(\mathbf{c}) \tag{6.37}$$

where the summation over $x \neq H^+$ includes all *charged* aqueous components other than hydronium. We denote the parenthetical quantity in the last term of *Equation 6.37* as:

$$\mu''_x = \mu'_x - \mu'_{H^+} \frac{q_x}{q_{H^+}} \tag{6.38}$$

which is the exchange chemical potential that measures the work required to replace solvent molecules by charged molecules of species x, under the constraint of charge conservation in the system. Replacing solvent molecules in the system

with charged molecules requires additional work than with neutral species, as the charge offset in the system caused by the introduction of a charged molecule, x, must be compensated by replacing additional solvent with protons if x is negatively charged, or vice versa should x be positively charged.

In addition to the two constraints, the self-dissociation reaction of water (discussed in the previous subsection) provides a relationship between the concentrations of hydronium and hydroxyl molecules that reduces the number of independent thermodynamic variables further. The chemical potentials of these two ions are, therefore, not independent of each other, leading to a system of equations that needs to be solved simultaneously. The chemical potentials of the remaining mobile components, which for our present system are sodium and chloride ions, are explicitly written in the functional (with the expression given in *Equation 6.25*) as a result of particle exchange of the system's aqueous species with the bulk solution.

6.2 Functional Minimization—Finding the Equilibrium Probability, Density, and Electrostatic Distributions and the Equilibrium Potential

Functional minimization provides access to the structural and thermodynamic properties that communicate information about membrane self-assembly, its chemical behavior, and how it interacts with environmental

compounds. The minimization is performed with respect to the independent, unknown variables in the model, subject to the constraints of local incompressibility and global charge neutrality, as well as the requirement for constant chemical potential of each of the aqueous species. This yields expressions for the equilibrium probability distributions of the phospholipid molecules, density distributions of all solution components, and electrostatic potential. These expressions, together with those formulated for the attractive interaction fields and the incompressibility constraint, provide a set of integrodifferential equations that illustrate the non-trivial coupling among all the physicochemical interactions operating within the complex system. The unknowns are solved for self-consistently, by discretizing space and converting these differential equations into a set of coupled, nonlinear, algebraic equations; the average properties of the system's molecules are numerically calculated and used to determine the mean-fields. The input necessary to solve the equations include the size of the system, the size, shape, and charge of all system particles, the possible conformational states of the lipids, the distribution of chargeable units of the lipid headgroups, the strengths of the attractive interactions between lipid molecules, the pK_a of species participating in acid-base equilibrium reactions, and the environmental conditions, i.e., temperature (298 K), bulk salt concentration (0.1 M), valency of the salt ions (+1 for Na^+, −1 for Cl^-), and bulk pH (7.0). The system of equations is

solved using the KINSOL software package, which specializes in solving systems of coupled, nonlinear equations, in the SUNDIALS suite. The equilibrium distributions are used to obtain the function for the potential that delineates the equilibrium physical and chemical states of the system. Derivatives of this equilibrium potential are used to calculate various desired thermodynamic properties. Below are the expressions for the unknown quantities of the system at equilibrium, obtained via minimization of the free energy functional:

Equilibrium Probability and Partition Function

of the Lipid Hydrocarbon Chains

The equilibrium probability that a lipid hydrocarbon tail, ω, of species i exists in a given conformation, α, in leaf δ of the bilayer, is:

$$P_{i,L-t,\omega,\delta}(\alpha_{i,\omega,\delta},\mathbf{c}) = \frac{1}{q_{i,L-t,\omega,\delta}(\mathbf{c})}\exp\left[\begin{array}{l} -\beta\varepsilon(\alpha_{i,\omega,\delta}) \\ +\dfrac{\beta}{a(0)v_{CH_2}}\displaystyle\sum_j J_{i,j,L-t}x_{j,L}\sum_{\omega',\delta'}\int_{-l}^{l} x_{j,L,\delta'}(\mathbf{c})\left\langle\xi_{j,L-t,\omega',\delta'}(r,\mathbf{c})\right\rangle\xi_{i,L-t,\omega,\delta}(\alpha_{i,\omega,\delta},r)dr \\ -\beta\displaystyle\sum_j \varepsilon_{i,j,L-t}\int_{-l}^{l}\overline{n}^{hydrophobic}_{i,L-t,\omega,\delta}(\alpha_{i,\omega,\delta},r,\mathbf{c})\sum_{\delta'}\left\langle\phi_{j,L-t,\delta'}(r,\mathbf{c})\right\rangle dr \\ -\beta\displaystyle\int_{-\infty}^{\infty}\pi(r,\mathbf{c})\overline{n}^{hydrophobic}_{i,L-t,\omega,\delta}(\alpha_{i,\omega,\delta},r,\mathbf{c})v_{CH_2}dr \end{array}\right] \quad (6.39)$$

The corresponding equilibrium partition function for a lipid hydrocarbon chain, denoted $q_{i,L\text{-}t,\omega,\delta}(\mathbf{c})$, is the normalization factor for the lipid chain probability distribution, such that $\sum_{\alpha_{i,\omega,\delta}} P_{i,L\text{-}t,\omega,\delta}(\alpha_{i,\omega,\delta},\mathbf{c}) = 1.0$, given by the sum:

$$q_{i,L-t,\omega,\delta}(\mathbf{c}) =$$

$$\sum_{\alpha_{i,\omega,\delta}} \exp\left[\begin{array}{l} -\beta\varepsilon(\alpha_{i,\omega,\delta}) \\ +\dfrac{\beta}{a(0)v_{CH_2}}\sum_j J_{i,j,L-t}x_{j,L}\sum_{\omega',\delta'}\int_{-l}^{l} x_{j,L,\delta'}(\mathbf{c})\left\langle \xi_{j,L-t,\omega',\delta'}(r,\mathbf{c})\right\rangle \xi_{i,L-t,\omega,\delta}(\alpha_{i,\omega,\delta},r)dr \\ -\beta\sum_j \varepsilon_{i,j,L-t}\int_{-l}^{l}\overline{n}^{hydrophobic}_{i,L-t,\omega,\delta}(\alpha_{i,\omega,\delta},r,\mathbf{c})\sum_{\delta'}\left\langle \phi_{j,L-t,\delta'}(r,\mathbf{c})\right\rangle dr \\ -\beta\int_{-\infty}^{\infty}\pi(r,\mathbf{c})\overline{n}^{hydrophobic}_{i,L-t,\omega,\delta}(\alpha_{i,\omega,\delta},r,\mathbf{c})v_{CH_2}dr \end{array}\right] \tag{6.40}$$

<u>Equilibrium Probability and Partition Function of the Lipid Headgroups</u>

The equilibrium probabilities of the lipid headgroups represent a set of conformations, σ, independent of those of the lipid chains, and are expressed as:

$$P_{i,L-h,\delta}(\sigma_{i,\delta},\mathbf{c}) =$$

$$\frac{1}{q_{i,L-h,\delta}(\mathbf{c})}\exp\left[\begin{array}{l} -\beta\sum_j \varepsilon_{i,j,L-h}\int_{-\infty}^{\infty}\overline{n}^{hydrophobic}_{i,L-h,\delta}(\sigma_{i,\delta},r,\mathbf{c})\left\langle \phi^{hydrophobic}_{j,L-h,\delta}(r,\mathbf{c})\right\rangle dr \\ -\int_{-\infty}^{\infty}\left(\psi(r,\mathbf{c})+\beta\lambda_{c.n.}e\right)\overline{n}_{i,L-h,\delta}(\sigma_{i,\delta},r,\mathbf{c})z_{i,L-h,\delta}(\sigma_{i,\delta},r,\mathbf{c})dr \\ -\beta\int_{-\infty}^{\infty}\pi(r,\mathbf{c})\overline{v}_{i,L-h,\delta}(\sigma_{i,\delta},r,\mathbf{c})dr \end{array}\right] \tag{6.41}$$

where $\overline{n}_{i,L\text{-}h,\delta}(\sigma_{i,\delta},r,\mathbf{c})$ and $\overline{v}_{i,L\text{-}h,\delta}(\sigma_{i,\delta},r,\mathbf{c})$ represent the conformation-dependent number of monomers and volume, respectively, of lipid species *i*, per unit length, at position *r* within the headgroup region of the δ leaflet. The headgroup partition function is the normalization factor for the headgroup probability distribution that fulfills the constraint, $\sum_{\sigma_{i,\delta}} P_{i,L\text{-}h,\delta}(\sigma_{i,\delta},\mathbf{c}) = 1.0$:

$$q_{i,L-h,\delta}(\mathbf{c}) = \sum_{\sigma_{i,\delta}} \exp\left[\begin{array}{l} -\beta \sum_j \varepsilon_{i,j,L-h} \int_{-\infty}^{\infty} \overline{n}_{i,L-h,\delta}^{hydrophobic}(\sigma_{i,\delta}, r, \mathbf{c}) \left\langle \phi_{j,L-h,\delta}^{hydrophobic}(r, \mathbf{c}) \right\rangle dr \\ -\int_{-\infty}^{\infty} \left(\psi(r, \mathbf{c}) + \beta\lambda_{c.n.} e\right) \overline{n}_{i,L-h,\delta}(\sigma_{i,\delta}, r, \mathbf{c}) z_{i,L-h,\delta}(\sigma_{i,\delta}, r, \mathbf{c}) dr \\ -\beta \int_{-\infty}^{\infty} \pi(r, \mathbf{c}) \overline{v}_{i,L-h,\delta}(\sigma_{i,\delta}, r, \mathbf{c}) dr \end{array}\right] \quad (6.42)$$

Note that the Lagrange multiplier, $\lambda_{c.n.}$, which enforces global charge neutrality, gives a constant contribution to $P_{i,L\text{-}h,\delta}(\sigma_{i,\delta}, \mathbf{c})$; its value can therefore be absorbed into $q_{i,L\text{-}h,\delta}(\mathbf{c})$.

Equilibrium Density Distributions of Water and Salt Ions

The equilibrium density distributions for water, the hydronium and hydroxyl ions from dissociated water, and the free salt cations and anions are, respectively:

$$\rho_w(r, \mathbf{c}) = \left(1/v_w\right) \exp\left[-\beta\pi(r, \mathbf{c}) v_w\right] \quad (6.43)$$

$$\rho_{H^+}(r, \mathbf{c}) = \left(1/v_w\right) \exp\left[-\beta\pi(r, \mathbf{c}) v_w - \beta\mu_{H^+}^0 - \psi(r, \mathbf{c}) \frac{q_{H^+}}{e} - \beta\lambda_{c.n.} q_{H^+}\right] \quad (6.44)$$

$$\rho_{OH^-}(r, \mathbf{c}) = \left(1/v_w\right) \exp\left[-\beta\pi(r, \mathbf{c}) v_w - \beta\mu_{OH^-}^0 - \psi(r, \mathbf{c}) \frac{q_{OH^-}}{e} - \beta\lambda_{c.n.} q_{OH^-}\right] \quad (6.45)$$

$$\rho_+(r, \mathbf{c}) = \left(1/v_w\right) \exp\left[-\beta\pi(r, \mathbf{c}) v_+ + \beta\mu_+'' - \psi(r, \mathbf{c}) \frac{q_+}{e} - \beta\lambda_{c.n.} q_+\right] \quad (6.46)$$

$$\rho_{-}(r,\mathbf{c}) = \left(1/v_w \right) \exp\left[-\beta\pi(r,\mathbf{c})v_{-} + \beta\mu''_{-} - \psi(r,\mathbf{c})\frac{q_{-}}{e} - \beta\lambda_{c.n.}q_{-} \right] \tag{6.47}$$

We have written the density expressions for water and its ions under the assumption that these molecules have equivalent volumes (30.0 $Å^3$). As was shown in *Section 6.1*, the constraints of incompressibility and global electroneutrality imposed on the system reduce the number of independent thermodynamic variables, making it unnecessary to explicitly specify the chemical potentials of water and its ions. The chemical potentials, μ''_{+} and μ''_{-}, are in effect *exchange* chemical potentials, as defined in *Equations 6.34* and *6.38*.

The values of the chemical potentials can be calculated based on the chemical conditions in the bath solution, facilitating the self-consistent determination of the equilibrium density distributions of the system's aqueous species. The process begins by considering the bulk solution counterparts to the in-system density expressions that were shown in *Equations 6.43-6.47* above:

$$\rho_{w}^{bulk} = \left(1/v_w \right) \exp\left[-\beta\pi^{bulk}v_w \right] \tag{6.48}$$

$$\rho_{H^+}^{bulk} = \left(1/v_w \right) \exp\left[-\beta\pi^{bulk}v_w - \beta\mu_{H^+}^{0,bulk} - \beta\lambda_{c.n.}q_{H^+} \right] \tag{6.49}$$

$$\rho_{OH^-}^{bulk} = \left(1/v_w \right) \exp\left[-\beta\pi^{bulk}v_w - \beta\mu_{OH^-}^{0,bulk} - \beta\lambda_{c.n.}q_{OH^-} \right] \tag{6.50}$$

$$\rho_{+}^{bulk} = \left(1/v_w \right) \exp\left[-\beta\pi^{bulk} v_{+} + \beta\mu_{+}''^{bulk} - \beta\lambda_{c.n.} q_{+} \right] \tag{6.51}$$

$$\rho_{-}^{bulk} = \left(1/v_w \right) \exp\left[-\beta\pi^{bulk} v_{-} + \beta\mu_{-}''^{bulk} - \beta\lambda_{c.n.} q_{-} \right] \tag{6.52}$$

Note that the electrostatic potential is zero in the bulk, which is a boundary condition placed on the model, hence the absence of the electrostatic term in the above equations. Quantitative calculations start with the calculation of the densities for the hydronium and hydroxyl ions in the bulk solution, using the bulk p*H* and equilibrium constant for water (*Equation 6.24* and *6.23*), respectively, while the bulk solution sodium and chloride ion densities can be obtained from their respective bulk concentrations, all of which are known input to the model. The incompressibility constraint imposed on the bulk fluid, *Equation 6.28*, is then used to obtain the density of water in the bulk, which is in turn used to calculate π^{bulk} via *Equation 6.48*. This provides the means by which to calculate the chemical potentials of the aqueous components using *Equations 6.49-6.52*. Because the bulk solution and system chemical potentials of a given component are equivalent at equilibrium, these values are input to the in-system density expressions given in *Equations 6.44-6.47*, leaving the system's inhomogeneous (local) osmotic pressures and electrostatic potential as the remaining unknowns needed to solve for the densities of the aqueous components within the system in a self-consistent manner.

Observing *Equation 6.43*, the physical meaning of the Lagrange multipliers enforcing the incompressibility constraint, $\pi(r,\mathbf{c})$, can be clearly related to the local osmotic pressure needed to maintain constant solvent chemical potential throughout the system, required for equilibrium. This interpretation of $\pi(r,\mathbf{c})$ is different from that drawn from the *Generation I* theory, where solvent is not present in the system. In the absence of solvent, $\pi(r,\mathbf{c})$ are the lateral pressures resulting from the repulsive interactions between the atoms of the lipid chains to fulfill the packing constraints, but they cannot represent osmotic pressures. Due to the thermodynamic equilibrium that is established within the system, there is potential for large local variations in p*H* and salt concentration to maintain a constant chemical potential of each species between 'local' and 'bulk' domains. The local densities of the free ions are therefore tied, not only to local molecular organization and the electrostatic potential, but also to the chemical potentials in the bulk solution.

Equilibrium Electrostatic Potential

Functional minimization of the free energy functional with respect to the local dimensionless electrostatic potential, $\Psi(r,\mathbf{c}) = \beta e \Phi_{E.P.}(r,\mathbf{c})$, yields the Maxwell equation for electrostatics, which, due to the assumption of a constant permittivity, reduces to the Poisson equation:

$$\nabla^2\psi(r,\mathbf{c}) = \frac{-\left\langle \rho_q(r,\mathbf{c}) \right\rangle}{\varepsilon e} = \frac{-\beta e^2}{\varepsilon_0 \varepsilon_r} \frac{\left\langle \rho_q(r,\mathbf{c}) \right\rangle}{e} \tag{6.53}$$

The Laplacian of the (dimensionless) electrostatic potential is derived, subject to the appropriate boundary conditions. As $r \to \pm\infty$, i.e., approaching the bulk solution, far from the membrane, the components of the aqueous medium in which the membrane resides approach their bulk solution concentrations. Here, the concentrations of the aqueous species are constant and the number of cations balances the number of anions of the same valency at all locations, resulting in a net charge-neutral environment at all r. In the bulk, the electrostatic potential is therefore constant and set to zero:

Electrostatic boundary conditions:

$$\psi(r \to \pm\infty) = \psi^{bulk} = 0$$

$$\frac{d\psi(r \to \pm\infty)}{dr} = 0$$

Periodic boundary conditions are inherently imposed on the electrostatic potential and all other spatially varying parameters, with respect to the plane parallel to the membrane's surface, due to the assumption of radial symmetry.

Total Equilibrium Potential of the 'Membrane-Plus-Environment' System

The expressions for the equilibrium distributions within the system, as listed above, together with those for the attractive interaction fields and the incompressibility constraint, yield a set of integrodifferential equations that can be

used to solve for the system's unknowns and determine the equilibrium potential as a function of lipid composition and environmental conditions, from which all thermodynamic parameters and average structural information of interest may be calculated. The expressions are first reconstructed into a set of coupled, nonlinear algebraic equations via discretization of space to be solved numerically, subject to the appropriate boundary conditions.

The molecular equilibrium potential, $\Phi_{\text{S.G.}}^{equilib}$ obtained from this process, divided by average area, takes the form:

$$\beta\frac{\Phi_{\text{S.G.}}^{equilib}}{A}=\sum_{i,\delta}\frac{x_{i,L}x_{i,L,\delta}(\mathbf{c})}{a(0)}\ln\left[\frac{x_{i,L}x_{i,L,\delta}(\mathbf{c})\lambda_{i,L}^{2}}{a(0)e}\right]-\sum_{i,\omega,\delta}\frac{x_{i,L}x_{i,L,\delta}(\mathbf{c})}{a(0)}\ln\left[q_{i,L-t,\omega,\delta}(\mathbf{c})\right] \qquad (6.54)$$
$$-\frac{\beta}{2}\sum_{i,j,\delta,\delta'}\varepsilon_{i,j,L-t}\int_{-l}^{l}\left\langle\rho_{i,L-t,\delta}(r,\mathbf{c})\right\rangle\left\langle\phi_{j,L-t,\delta'}(r,\mathbf{c})\right\rangle dr$$
$$+\frac{\beta}{2a(0)^{2}v_{CH_2}}\sum_{i,j,\delta,\delta'}J_{i,j,L-t}x_{i,L}x_{j,L}x_{i,L,\delta}(\mathbf{c})x_{j,L,\delta'}(\mathbf{c})\sum_{\omega,\omega'}^{n_{i,L}^{tails},n_{j,L}^{tails}}\int_{-l}^{l}\left\langle\xi_{i,L-t,\omega,\delta}(r,\mathbf{c})\right\rangle\left\langle\xi_{j,L-t,\omega',\delta'}(r,\mathbf{c})\right\rangle dr$$
$$-\sum_{i,\delta}\frac{x_{i,L}x_{i,L,\delta}(\mathbf{c})}{a(0)}\ln\left[q_{i,L-h,\delta}(\mathbf{c})\right]$$
$$-\frac{\beta}{2}\sum_{i,j,\delta}\varepsilon_{i,j,L-h}\int_{-\infty}^{\infty}\left\langle\rho_{i,L-h,\delta}^{hydrophobic}(r,\mathbf{c})\right\rangle\left\langle\rho_{j,L-h,\delta}^{hydrophobic}(r,\mathbf{c})\right\rangle v_{CH_2}dr$$
$$-\int_{-\infty}^{\infty}\frac{\left\langle\rho_{q}(r,\mathbf{c})\right\rangle}{2e}\psi(r,\mathbf{c})dr-\beta\int_{-\infty}^{\infty}\pi(r,\mathbf{c})dr$$
$$-\int_{-\infty}^{\infty}\left(\rho_{w}(r,\mathbf{c})+\rho_{H^{+}}(r,\mathbf{c})+\rho_{OH^{-}}(r,\mathbf{c})+\rho_{+}(r,\mathbf{c})+\rho_{-}(r,\mathbf{c})\right)dr$$

6.3 TENSION, PRESSURE, AND CHEMICAL POTENTIAL IMBALANCES — DAY IN THE LIFE OF A ~~PH.D. STUDENT~~ BIOLOGICAL MEMBRANE

Surface Tension of the Membrane

Due to the hydrophobic effect, a biological membrane reaches mechanical equilibrium quickly after a geometrical disturbance (caused by some biological process such as endo- or exocytosis, fusion of proteins or other lipids with the membrane, conformational changes induced by the formation of ion channels through the bilayer, etc.). The areal compression of lipids in the bilayer, induced by the hydrophobic effect, competes both with hydration and with the steric and electrostatic repulsions involving the lipid molecules, acting to expand molecular area. Balance of these forces acting at the bilayer's hydrophobic–hydrophilic interfaces eliminates mechanical stress, which would otherwise provoke a non-zero surface tension in the membrane, conceding that there are no external forces such as cytoskeletal stress. Analyses of our systems are conducted at mechanical equilibrium, i.e., under the constraint of zero surface tension. The area per molecule that yields a surface tension of zero in a planar membrane with a hydrophobic width of 28.0 Å sets the molecular area for the surface of inextension (surface of constant molecular area upon bending) for all systems, which is found to be at the bilayer midplane and equal to 69.5955 $Å^2$.

In the *Generation I* theory, the system consists entirely of the hydrophobic

membrane core; the expression for the surface tension in this case is calculated as the derivative of the equilibrium free energy with respect to membrane area. With the expansion of our theory in *Generation II* to include an aqueous medium surrounding the membrane, bilayer area and system volume become coupled and thermodynamics requires that the system length be explicitly separated from the volume to be held constant in the areal derivative of the minimized potential:

$$
\begin{aligned}
d\Phi_{\text{S.G.}}^{equilib} &= -SdT - P' \underset{d(A\cdot l)}{dV} + \gamma dA + \sum_i \mu'_{i,L} d\left\langle N_{i,L}(\mathbf{c})\right\rangle - \sum_{salt\ ions} N_{\substack{salt \\ ion}} d\mu''_{\substack{salt \\ ion}} \\
d\Phi_{\text{S.G.}}^{equilib} &= -SdT - P'(Adl + ldA) + \gamma dA + \sum_i \mu'_{i,L} d\left\langle N_{i,L}(\mathbf{c})\right\rangle - \sum_{salt\ ions} N_{\substack{salt \\ ion}} d\mu''_{\substack{salt \\ ion}} \\
d\Phi_{\text{S.G.}}^{equilib} &= -SdT - P'\cdot Adl + (\gamma - P'\cdot l)dA + \sum_i \mu'_{i,L} d\left\langle N_{i,L}(\mathbf{c})\right\rangle - \sum_{salt\ ions} N_{\substack{salt \\ ion}} d\mu''_{\substack{salt \\ ion}} \\
\left(\frac{\partial \Phi_{\text{S.G.}}^{equilib}}{\partial A}\right)_{T,l,N_{i,L},\mu''_{\substack{salt \\ ions}}} &= \gamma - P'\cdot l
\end{aligned}
\tag{6.55}
$$

This changes the calculation of the surface tension slightly. As shown in the final expression of the set given in *Equation 6.55*, the partial derivative of our minimized potential with respect to total area now thermodynamically equates to the surface tension, less the product of the 'constrained pressure' (defined in *Equation 6.33*) and system length. Evaluating this derivative, we can obtain the expression for surface tension:

$$
\gamma = \left(\frac{\partial \Phi_{\text{S.G.}}^{equilib}}{\partial A}\right)_{T,l,N_{i,L},\mu''_{\substack{salt \\ ion}}} + P'\cdot l \tag{6.56}
$$

$$\beta\gamma(\mathbf{c}) = -\frac{1}{a(0)} - \frac{\beta}{2}\sum_{i,j,\delta,\delta'}\varepsilon_{i,j,L-t}\int_{-l}^{l}\left\langle\rho_{i,L-t,\delta}(r,\mathbf{c})\right\rangle\left\langle\phi_{j,L-t,\delta'}(r,\mathbf{c})\right\rangle dr \tag{6.57}$$

$$+\frac{\beta}{2a(0)^2 v_{CH_2}}\sum_{i,j,\delta,\delta'}J_{i,j,L-t}x_{i,L}x_{j,L}x_{i,L,\delta}(\mathbf{c})x_{j,L,\delta'}(\mathbf{c})\sum_{\omega,\omega'}^{n_{i,L}^{tails},n_{j,L}^{tails}}\int_{-l}^{l}\left\langle\xi_{i,L-t,\omega,\delta}(r,\mathbf{c})\right\rangle\left\langle\xi_{j,L-t,\omega',\delta'}(r,\mathbf{c})\right\rangle dr$$

$$-\frac{\beta}{2}\sum_{i,j,\delta}\varepsilon_{i,j,L-h}\int_{-\infty}^{\infty}\left\langle\rho_{i,L-h,\delta}^{hydrophobic}(r,\mathbf{c})\right\rangle\left\langle\rho_{j,L-h,\delta}^{hydrophobic}(r,\mathbf{c})\right\rangle v_{CH_2}dr$$

$$-\int_{-\infty}^{\infty}\frac{\left\langle\rho_q(r,\mathbf{c})\right\rangle}{2e}\psi(r,\mathbf{c})dr - \beta\int_{-\infty}^{\infty}\pi(r,\mathbf{c})dr$$

$$-\int_{-\infty}^{\infty}\left(\rho_w(r,\mathbf{c}) + \rho_{H^+}(r,\mathbf{c}) + \rho_{OH^-}(r,\mathbf{c}) + \rho_+(r,\mathbf{c}) + \rho_-(r,\mathbf{c})\right)dr + \beta P'\cdot l$$

The surface tension, as well as other membrane properties derived from the equilibrium thermodynamic potential of the *Generation II* theory, such as the lateral pressure distribution and chemical potential, are significantly more complex than their counterparts from the *Generation I* model. In *Generation II*, these properties are not only regulated by the interactions that take place within the membrane's hydrophobic core, but are also tied to the local densities of the aqueous components in contact with the membrane, the electrostatic potential generated by the charged species, the hydrophobic interactions of the lipid headgroups, and the solvent chemical potential (via *P'*), in a non-trivial manner. To delineate the constrained pressure in terms of known quantities, we first derive the expression for the lateral pressure.

Lateral Pressure Distribution Through the Bilayer

Through the relationship between the surface tension and the lateral

pressure profile introduced in *Section 4.4* we can obtain the expression of the latter for any geometry:

$$\int_{-\infty}^{\infty} \Pi(r,\mathbf{c})dr = -\gamma(\mathbf{c}) \tag{4.37}$$

We formally extend all limits of integration in *Equation 6.57* to match *Equation 4.37* (from $-\infty$ to $+\infty$), as integration over terms describing lipid tails, outside the bounds of the hydrophobic region, will simply have a contribution of zero, which allows us to obtain:

$$\begin{aligned}
\beta\Pi(r,\mathbf{c}) &= \frac{\beta}{2}\sum_{i,j,\delta,\delta'} \varepsilon_{i,j,L-t}\left\langle \rho_{i,L-t,\delta}(r,\mathbf{c})\right\rangle\left\langle \phi_{j,L-t,\delta'}(r,\mathbf{c})\right\rangle \\
&- \frac{\beta}{2a(0)^2 v_{CH_2}}\sum_{i,j,\delta,\delta'} J_{i,j,L-t}x_{i,L}x_{j,L}x_{i,L,\delta}(\mathbf{c})x_{j,L,\delta'}(\mathbf{c})\sum_{\omega,\omega'}^{n_{i,L}^{tails},n_{j,L}^{tails}}\left\langle \xi_{i,L-t,\omega,\delta}(r,\mathbf{c})\right\rangle\left\langle \xi_{j,L-t,\omega',\delta'}(r,\mathbf{c})\right\rangle \\
&+ \frac{\beta}{2}\sum_{i,j,\delta} \varepsilon_{i,j,L-h}\left\langle \rho_{i,L-h,\delta}^{hydrophobic}(r,\mathbf{c})\right\rangle\left\langle \rho_{j,L-h,\delta}^{hydrophobic}(r,\mathbf{c})\right\rangle v_{CH_2} \\
&+ \frac{\left\langle \rho_q(r,\mathbf{c})\right\rangle}{2e}\psi(r,\mathbf{c}) + \beta\pi(r,\mathbf{c}) \\
&+ \rho_w(r,\mathbf{c}) + \rho_{H^+}(r,\mathbf{c}) + \rho_{OH^-}(r,\mathbf{c}) + \rho_+(r,\mathbf{c}) + \rho_-(r,\mathbf{c}) - \beta P'
\end{aligned} \tag{6.58}$$

where we have again decoupled the contribution from the translational motion of the membrane lipids from the functional form of the lateral pressure, as done in the *Generation I* theory. Evaluation of P' is straightforward by considering the expression for the lateral pressure distribution when applied to the inherently tension-free bulk solution, where the lateral pressure at all points is necessarily zero, which reduces *Equation 6.58* to:

$$\beta\Pi^{bulk} = 0 = \beta\pi^{bulk} + \rho_w^{bulk} + \rho_{H^+}^{bulk} + \rho_{OH^-}^{bulk} + \rho_+^{bulk} + \rho_-^{bulk} - \beta P' \tag{6.59}$$

Consequently, P' is the pressure that counteracts the forces acting on the system from the molecules in the fluid reservoir, needed to adjust the total pressure ($P = 1$ bar) such that the solvent chemical potential is constant:

$$P' = \pi^{bulk} + k_B T\left(\rho_w^{bulk} + \rho_{H^+}^{bulk} + \rho_{OH^-}^{bulk} + \rho_+^{bulk} + \rho_-^{bulk}\right) = P - \frac{\mu_w}{v_w} \tag{6.60}$$

As shown in *Figure 6.3*, there are large and widely varying stresses through the bilayer. Within the width of the hydrophobic region, the tendency of the lipid tails to maximize their entropy by occupying a greater volume creates a distribution of positive (outward pushing) pressure, peaking around 350-450 bar as given by our model (typical of PC lipids [160-162, 165-168]). The entropic lateral pressure attenuates as the lipid density drops towards the midplane, where the influence of constricting attractive dispersion forces increases.[15] Most of the lateral pressure accumulated by the entropic repulsion of the lipid tails is balanced by the inclination of the lipid headgroups to compress, in order to segregate the hydrophobic tails from the surrounding solvent. This compression is localized in

[15] As explained in *Section 4.4*, our model does not contain the positive peak in lateral pressure about the midplane, as is present in most works after ~2000, perhaps due to our exclusion of the translational entropy of the lipid molecules from the lateral pressure calculation. This is done because our theory is unable to delineate the distribution of the translational entropy's contribution to the lateral pressure through the bilayer. All other key features of the lateral pressure profile as obtained by simulation are reproduced using our theory and the translational term does not make any contribution to the comparison plots in *Figure 7.11*, since the lipid areal density at the midplane is constant in all calculations.

the narrow 4-5 Å width about the hydrophobic–hydrophilic boundary of the bilayer, which thrusts negative (compression) lateral pressures up to ~1000 bar in magnitude within this region. Small positive peaks in lateral pressure at the extrema of the headgroups emerge due to electrostatic and steric interactions that oppose the interfacial attraction. Asymmetry in these stresses arise across the midplane when the membrane curves out of a planar geometry, which affects lipid lateral and transbilayer diffusion, conformational ordering of the lipid tails, and consequently, bilayer structural integrity and functionality.

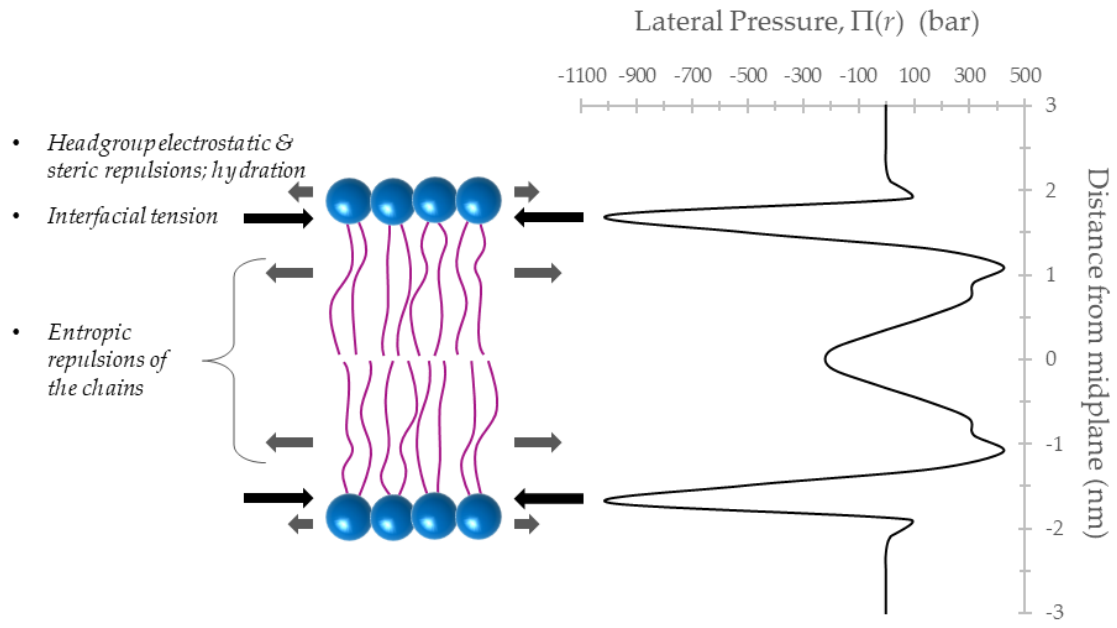

Figure 6.3) **Lateral pressure distribution through a planar, symmetric DOPC bilayer.** The heterogeneous lateral pressure profile through the width of the membrane, as calculated by the molecular field theory. The arrows represent the net position-dependent mechanical force vectors applied laterally within three domains through the width of the membrane.

One of the primary advantages of our theory is its ability to delineate this nonuniform distribution of lateral stress through the bilayer, which is quite challenging experimentally. Experimental determination of the lateral pressure profile requires measurements of local pressure differences on the order of angstroms inside a lipid bilayer; however, resolution on this scale is limited with current experimental tools. Extrinsic fluorescent probes using pyrene moieties attached to acyl chains of varying lengths have been used to measure lateral pressure at different depths into the bilayer [308]. However, three major issues with this technique are that the location of the probe in the membrane must be estimated, the behavior of the probe molecules inside the bilayer is not fully understood, and the probe's effects on the lateral pressure profile are unknown, making it challenging to discern valid measurements of a membrane property from artifacts caused by the perturbing effects of probe insertion into the bilayer [309]. It has been shown using atomistic simulations [310] that pyrene probes significantly disturb the packing and dynamics of nearby lipids within a few nanometers of the probe, though their specific effects on the lateral pressure profile have not yet been studied.

All-atom molecular dynamics (MD) simulations are well suited for the study of lateral pressure distributions in lipid membranes, as long as optimization of model parameters for the lipid chains is adequate enough to reproduce the

observed lipid order parameters. However, they are computationally taxing and inherently subject to statistical errors arising from insufficient sampling and to uncertainties in the applied intermolecular potentials. While computational algorithms, techniques (e.g., parallel computing), and hardware (e.g., GPUs and specialized computer chips) continue to improve, MD simulations are still subject to restricted trackable timescales, which prevent their ability to study certain phenomena. Additionally, though the body of work using MD simulations for the analysis of lipid bilayers is continuously growing in number and advancing scientifically, it is still limited to relatively few systems dependent on specific conditions.

Coarse-grained simulations accelerate calculations, though results are questionable as even small simplifications to the system can deviate results for quantities as sensitive as the lateral pressure profile. For example, results for simple, pure model membrane systems reported from coarse-grained simulations [172, 311] disagree with results from corresponding systems obtained using atomistic simulations [160, 312].

Monte Carlo simulations have been used to relate and compare the tangential pressure profiles in lipid bilayers calculated from the simulations to the lateral pressure profiles calculated using a mean field theory [170]. However, Monte Carlo models have difficulty with simulating particles in dense fluids and

non-rigid molecules/macromolecular assemblies, such as lipid bilayers, due to poor sampling efficiently caused by the rejection of high-energy steric clashes that frequently occur with intermolecular moves in such systems [313]. The demand for molecular theories, such as used in the present study, to investigate the lateral pressure distributions in lipid membranes reflects the difficulties posed by other methods.

Chemical Potential of the Membrane's Lipid Constituents

The chemical potential of each of the membrane's component lipids and of other membrane-associated molecules is an important thermodynamic property that can be used to evaluate the diffusional tendencies of the lipids between the membrane's leaflets and the interactions between membrane and protein. Relative to mechanical equilibrium, chemical equilibrium is attained at a much slower rate after an induced deformation of the bilayer. A large energetic barrier hinders the crossing of hydrophilic lipid headgroups through the hydrophobic membrane core, slowing inter-leaflet relocation of lipids as the membrane seeks to rebalance the chemical potentials of each of its constituents across its midplane. As a consequence, we believe many experimental observations take place in systems that are perturbed *out* of chemical equilibrium, a hypothesis supported by our results from *Generation I*. We again test this proposition by evaluating our systems for the two membrane geometries under study at various relaxation ratios, η_i (or

degrees of transbilayer diffusion), and comparing the trends in protein localization on the bilayer as obtained from our theory with those observed experimentally by our collaborators. Our findings again substantiate our claim by the good agreement between theoretical and experimental results when the former are calculated using a value for the relaxation ratio less than that which marks equilibrium (free exchange, η_i^*). Recall from *Section 4.6*, for $\eta_i < \eta_i^*$ the concentration of the lipid species i in an expanded(compressed) leaflet of the bilayer is below(above) that required for the equality of $\mu_{i,L}$ across the membrane, due to insufficient lipid transbilayer diffusion. In this state, the expanded membrane leaflet experiences relief in the lateral pressure entropically generated by the membrane's hydrophobic lipid chains, granting enhanced opportunity for its internalization of nearby proteins *(see Section 7.3 for all Generation II Results)*.

The expression for the chemical potential of a lipid of species i in the δ leaflet of the bilayer is obtained by differentiating the system's equilibrium potential *(Equation 6.54)* with respect to the total number of lipid molecules of the same species and leaflet, holding constant the temperature, T, system volume, V, average membrane area, A, number of molecules of all other membrane components, $N_{j\neq i}$ and $N_{i,\delta'\neq\delta}$, and chemical potentials of the mobile species in solution, μ_m:

$$\mu_{i,\delta} = \left(\frac{\partial \Phi_{\text{S.G.}}^{equilib}}{\partial N_{i,\delta}} \right)_{T,V,A,N_{j\neq i},N_{i,\delta'\neq\delta},\mu_m} \tag{6.61}$$

$$\beta\mu_{i,L,\delta}(\mathbf{c}) = \ln\left[\frac{x_{i,L}\, x_{i,L,\delta}(\mathbf{c})\lambda_{i,L}^2}{a(0)} \right] - \sum_{\omega}^{n_{i,L}^{tails}} \ln\left[q_{i,L-t,\omega,\delta}(\mathbf{c}) \right] - \ln\left[q_{i,L-h,\delta}(\mathbf{c}) \right] \tag{6.62}$$

CHAPTER 7
GENERATION II THEORY: LIPIDATED PROTEINS DISCRIMINATE MEMBRANES OF DIFFERENT GEOMETRY

7.1 THE GAUSS-BONNET THEOREM AND GAUSSIAN CURVATURE

Morphological plasticity of biological membranes is essential for all facets of cellular life. The polymorphism among the hundreds of different species of lipids comprising the membrane, and among the varied types of membranes enclosing cells and cellular compartments, confers specific functionalities to each unique lipid macrostructure. In *Generation I* we investigated the effects of changes in *lipid type* and *liposome size* on the membrane's ability to recruit membrane-integrated proteins. In the present study, using the *Generation II* model, we seek to discover how membrane *geometry* modulates protein–membrane interactions and the driving mechanisms at work, with specific consideration of the individual contributions from each type of curvature: mean and Gaussian.

We begin this chapter with a continuation of the discussion on curvature theory that we began in *Section 4.5*. The two membrane geometries of primary interest in this work, spherical and cylindrical, have mean and Gaussian curvatures that are constant over the entire surface:

$$H_{cyl} = \frac{1}{2R_{cyl}} \qquad \begin{matrix} \textit{mean curvature of} \\ \textit{a cylindrical surface} \end{matrix} \tag{7.1}$$

$$H_{sph} = \frac{1}{R_{sph}} \qquad \begin{matrix} \textit{mean curvature of} \\ \textit{a spherical surface} \end{matrix} \tag{7.2}$$

$$K_{G,cyl} = 0 \qquad \begin{matrix} \textit{Gaussian curvature of} \\ \textit{a cylindrical surface} \end{matrix} \tag{7.3}$$

$$K_{G,sph} = \frac{1}{R_{sph}^2} \qquad \begin{matrix} \textit{Gaussian curvature of} \\ \textit{a spherical surface} \end{matrix} \tag{7.4}$$

If one were interested in comparing a sphere and a cylinder with the same mean curvature, then the radius of the cylinder would be half that of the sphere. Given all other properties are the same, such a comparison would isolate the contribution from Gaussian curvature to any curvature-dependent property.

An important aspect of the *Generation I* study is the elucidation of the membrane's lateral pressure profile as an important underlying molecular mechanism influencing the trends observed in the lipidated protein adsorption isotherms. This theme is generalized by the results from our expanded *Generation II* model. Traditionally, emphasis has been placed on curvature-induced lipid packing defects at the hydrophobic–hydrophilic interface – in other words, changes in molecular surface area – as the biophysical mechanism that drives protein–membrane interactions [281, 283, 314, 315]. Such surface analyses have been illuminating in the context of peripheral protein adsorption to the membrane,

offering insight regarding how membrane composition and curvature synergistically regulate selective recruitment of proteins that anchor via shallow insertion of amphipathic helices. However, in regard to integral membrane proteins, which insert deeper into the targeted monolayer or through the bilayer, detailed information about the atomic-scale variation of membrane properties, such as packing density and lateral pressure, *through* the depth of the host membrane leaflet(s) is necessary.

In the same vein, curvature analyses of lipid bilayers have often been conducted under the treatment of the membrane as a two-dimensional, infinitely thin sheet. Under this assumption, analysis based purely on the topology and boundary of such a surface would be appropriate. This is the approach taken with the all-too common application of the Gauss-Bonnet theorem to the physics of membrane curvature [176, 316]:

$$\int_S K_G dA + \oint_{\partial S} k_g ds = 2\pi\chi(S) = 4\pi\left(1 - g(S)\right) \qquad \begin{matrix} Gauss\text{ - }Bonnet \\ theorem \end{matrix} \qquad (7.5)$$

where $\chi(S)$ is the Euler-Poincaré characteristic of the surface S, k_g is the geodesic curvature at the boundary, ∂S, of the surface, and $g(S)$ is an integer based on the number of holes formed in the system, referred to as the genus, described as:

$$g(S) = \frac{2 - \chi(S)}{2} \qquad (7.6)$$

which is equal to zero for spheres and equal to one for a single cylinder. The

Gauss-Bonnet expression is often used in the Helfrich Hamiltonian, describing the change in free energy upon bending the membrane *(Equation 4.47)*, to evaluate the surface integral over the Gaussian term. Since the integral over the surface is a topological invariant, it is concluded that neither the Gaussian energy nor its associated modulus, $\overline{\kappa}$, have any meaningful contribution to membrane energetics, unless there is a change in boundary (including interfaces between different membrane phases of differing Gaussian curvature moduli) or topology (such as during cellular fission or fusion) during the bending process.

Herein lies the problem, rather than an infinitely thin, two-dimensional sheet, the bilayer is realistically a three-dimensional structure with a depth that, despite being exceedingly small (on the order of a few nanometers), features incredible physical heterogeneity, which in turn confers significant variation to local thermodynamic and chemical properties and the bilayer's ensuing functionality. In any formation that has a thickness, the Gaussian curvature is a function of depth into that thickness; properly accounting for such, especially at high curvatures, captures an imperative part of the fundamental physics, otherwise lost with the inapropos dismissal of the Gaussian curvature contribution.

In the *Results II.I* section at the end of this chapter, we illustrate differences in the degree to which lipidated proteins localize on spherical versus cylindrical

lipid bilayers, the two most predominant cellular morphologies. Our theoretical analyses, together with quantitative, comparative experiments performed by our collaborators at the University of Copenhagen and North Carolina State University, assess membranes of equivalent mean curvatures in the two geometries (with different Gaussian curvatures), revealing a 67% geometry-driven disparity in protein adsorption and, consequently, the crucial contribution from Gaussian curvature that, to our knowledge, has yet been undocumented.

7.2 PROTEIN ADSORPTION ON THE MEMBRANE

We introduced the general concept of membrane-bound proteins in the introduction of Chapter 5 and began our discussion specifically regarding lipidated proteins in *Section 5.1*. The mathematical methods laid out in *Section 5.2*, detailing the addition of a lipidated protein's anchor to the model membrane system within the framework of the *Generation I* theory, also apply to the *Generation II* model. We refer the reader to these sections for the background regarding lipidated proteins and the detailed theoretical methodology used to integrate them into our theory. The physics of the anchor insertion is captured in the expression for the anchor's chemical potential, $\mu_{A,\delta}(\mathbf{c})$, which has the same functional form in *Generation II* as was derived in *Equation 5.20*:

$$\beta\mu_{A,\delta}(\mathbf{c}) = \ln\left[\rho_{A,\delta}(\mathbf{c})\lambda_A^2\right] - \ln\left[q_{palmitoyl,\delta}(\mathbf{c}) \cdot q_{farnesyl,\delta}(\mathbf{c})\right] \qquad (5.20)$$

It is the expression for the partition functions of the anchor molecule's palmitoyl and farnesyl chains that brings about the divergence between the two theoretical models:

$$q_{A,\omega,\delta}(\mathbf{c}) = \sum_{\varsigma_{A,\omega,\delta}} \exp\left[\begin{array}{l} -\beta\varepsilon(\varsigma_{A,\omega,\delta}) \\ +\dfrac{\beta J_{L-t} x_L}{a(0) v_{CH_2}} \displaystyle\int_{-l}^{l} \xi_{A,\omega,\delta}(\varsigma_{A,\omega,\delta}, r) \sum_{\delta'} x_{L,\delta'}(\mathbf{c}) \left\langle \xi_{L-t,\delta'}(r,\mathbf{c}) \right\rangle dr \\ -\beta\varepsilon_{L-t} \displaystyle\int_{-l}^{l} \overline{n}_{A,\omega,\delta}^{hydrophobic}(\varsigma_{A,\omega,\delta}, r, \mathbf{c}) \sum_{\delta'} \left\langle \phi_{L-t,\delta'} r, \mathbf{c}) \right\rangle dr \\ -\displaystyle\int_{-\infty}^{\infty} \psi(r,\mathbf{c}) \overline{n}_{A,\omega,\delta}(\varsigma_{A,\omega,\delta}, r, \mathbf{c}) z_{A,\omega,\delta}(\varsigma_{A,\omega,\delta}, r, \mathbf{c}) dr \\ -\beta \displaystyle\int_{-\infty}^{\infty} \pi(r,\mathbf{c}) \overline{v}_{A,\omega,\delta}(\varsigma_{A,\omega,\delta}, r, \mathbf{c}) dr \end{array}\right] \tag{7.7}$$

The potential energy of the protein's anchor is modulated by the mean-fields generated by the incumbent lipid constituents of the membrane, which, in the *Generation II* theory, include the additional attractive component to the energy from the hydrophobic effect and electrostatic interactions. Furthermore, the fields tied to the incompressibility constraint are now bound to the volume fractions of the solution components. Recall that, unless applied to the study of ordered phases of the membrane, the Maier-Saupe ordering term is not needed, though we include it here for generality. Also note that the electrostatic term in the partition function of the protein's anchor is not relevant in the present analysis because the protein of interest, N-Ras, inserts uncharged hydrocarbon chains as its method of interaction with the bilayer.

The solutions obtained for the attractive, osmotic, and electrostatic fields of the lipid membrane system, without the presence of the protein, are used as inputs to evaluate the protein–membrane system by means of Widom's Potential Distribution Theorem, as detailed in *Section 5.2*. Equating the expressions for the chemical potentials of the membrane-inserted protein anchor in a planar (or locally near-planar) bilayer and in a bilayer of a defined curvature satisfies the requirement for equilibrium. We thereby calculate the relative adsorption densities of the protein's anchor in a membrane leaflet, as a function of membrane curvature, by means of the corresponding ratio of the anchor's partition functions; for tN-Ras, this depends on evaluation of the partition functions of its palmitoyl and farnesyl chains, as was shown in *Equation 5.23*:

$$\frac{\rho_{A,\delta}(\mathbf{c})}{\rho_{A,\delta}(\mathbf{c}=0)} = \frac{q_{palmitoyl,\delta}(\mathbf{c}) \cdot q_{farnesyl,\delta}(\mathbf{c})}{q_{palmitoyl,\delta}(\mathbf{c}=0) \cdot q_{farnesyl,\delta}(\mathbf{c}=0)} \qquad (5.23)$$

For direct comparison of theoretical results with the findings obtained experimentally, we use this methodology to calculate tN-Ras density in membranes of a given geometry over a range of diameters, all relative to the protein density on (nearly flat) membranes of 400 nm in diameter, plotted against the error-weighted fitting of the experimental tN-Ras density data obtained under the same conditions. These ratios are referred to as the *relative recruitment ratios*, *RR*; specifically, the ratio evaluated at a diameter D = 40 nm, RR^{40}, is used as a

measure of the efficiency by which lipidated proteins are able to sense membrane curvature and, more pointedly in the *Generation II* study, the efficiency by which lipidated proteins discriminate between the two different membrane geometries considered here, cylinders and spheres. Experimental data are obtained using the procedures described briefly in *Section 5.2* and, for more detail, in [317].

7.3 Results II.I: The Effects of Membrane Geometry and the Contribution of Gaussian Curvature to Membrane Thermodynamics and Protein Adsorption

This Chapter presents the results for the equilibrium lateral pressure distributions, energy profiles, and all other structural and thermodynamic properties of interest, obtained from self-consistently solving the set of coupled, nonlinear equations constructed from the equilibrium expressions derived in Chapter 6. The subsection below illustrates findings obtained for a planar, symmetric DOPC lipid membrane residing in an aqueous ionic medium. The subsections that follow demonstrate findings regarding curved DOPC membranes in the same environment, drawing comparisons between cylindrical and spherical membrane systems and establishing how membrane geometry regulates the spatial segregation of lipidated proteins.

Planar, Symmetric Bilayer in an Ionic, Aqueous Solution

Structural details of our system components are illustrated in *Figure 7.1.*

Here we consider the lateral pressure profile of a planar model membrane in a salt solution and the volume fraction distributions of all species in the system. These distributions correspond to an equilibrium area per molecule and bilayer hydrophobic width of 69.5955 $Å^2$ and 28.0 Å, respectively, for a tensionless DOPC lipid membrane; the temperature is set to be constant throughout the system at 298 K, the surrounding 'bulk' aqueous reservoir has a specified pH of 7.0, with a bulk pK_w of 14.0, and the bulk salt concentration is set to 0.1 M. The *NaCl* salt included in our system is taken to be completely ionized.

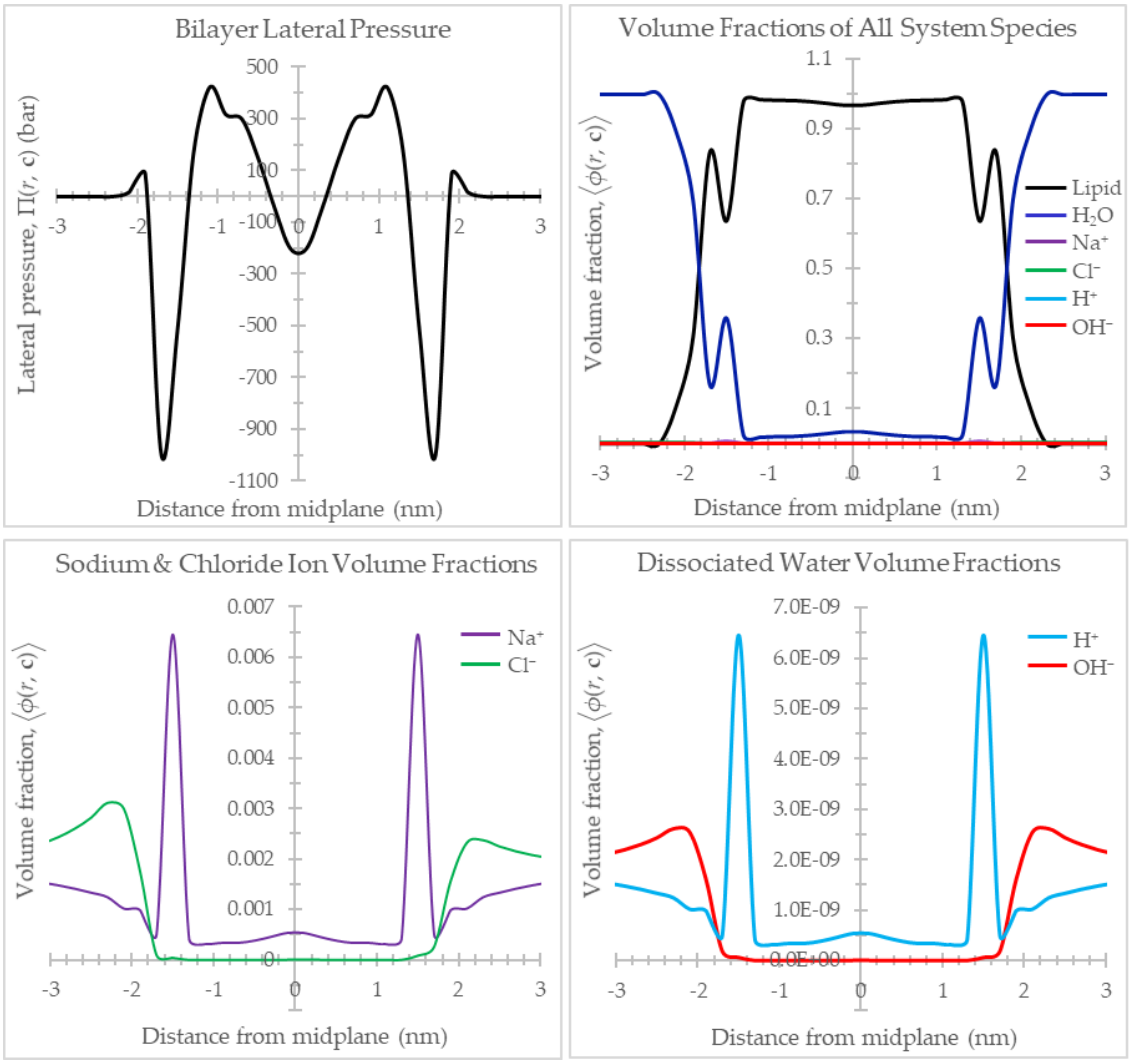

Figure 7.1) **Structural-mechanical distributions of system components.** ***Top left:*** Lateral pressure profile through a pure DOPC, symmetric, planar bilayer in ionic solution. ***Top right:*** Volume fraction distributions through a planar bilayer of all system components: DOPC lipids *(black)*, water *(dark blue)*, sodium ions *(purple)*, chloride ions *(green)*, hydronium ions *(light blue)*, and hydroxide ions *(red)*. ***Bottom panel:*** The ions are at much lower concentrations than the lipids and undissociated water in and around the membrane region, thus, in the bottom two graphs, we have isolated and magnified the volume fraction distributions of sodium *(left, purple)* and chloride *(left, green)* ions, and the hydronium *(right, light blue)* and hydroxide *(right, red)* ions from dissociated water.

The volume fractions of the system components are bound by the

incompressibility constraint to sum to unity over each discretization length of 2 Å along the axis perpendicular to the bilayer (horizontal axes in *Figure 7.1*). The peak in lipid volume fraction in *Figure 7.1, top right (black line)* at around ±1.7 nm (distance from the bilayer midplane) corresponds to the region where the lipid headgroups contribute, on average, most of their volume due to their energetically driven aggregation to shield the hydrophobic lipid tails from exposure to solvent. This mirrors the precipitous elevation in compression lateral pressure (negative values) in this region in *Figure 7.1, top left*. The shape of the lipid volume fraction curve within the range of ±1.4 to ±2.2 nm from the midplane *(Figure 7.1, top right)* is dictated by the volumes of the phosphate/glycerol and choline moieties (161.06 $Å^3$ and 99.93 $Å^3$, respectively) and the probabilities of the choline's conformational states. The distribution indicates that the probability of the headgroup moieties extending linearly, parallel to the bilayer normal, is relatively small, while higher conformational probability is afforded to a bent configuration, where a substantial portion of the phosphate and choline moieties exist in the same plane. This is consistent with data in the literature on lipid headgroup orientation [318, 319].

Undissociated water *(dark blue line)* largely fills the gaps between the bulky headgroup moieties, with a small concentration of water permeating the hydrophobic region. The remainder of the available volume is occupied by a smaller concentration of dissociated salt and water ions. The plots in *Figure 7.1,*

bottom panel magnify the volume fractions of the dissociated *NaCl (left)* and water ions *(right)*. The peaks in the Na^+ *(purple line)* and H^+ *(light blue line)* volume fractions, above their values in the bulk reservoir, show where they accumulate around the static, negative charge of the phosphate moiety of the lipid headgroup, near the hydrophobic–hydrophilic membrane interface. This region is accompanied by a depression in the volume fractions of the negatively charged Cl^- *(green line)* and OH^- *(red line)* ions, relative to their bulk values. The broader peaks of the Cl^- and OH^- volume fraction distributions illustrate the attraction of the negative ion cloud to the mobile, positively charged choline moiety at the extremum of the lipid headgroup, which repulses the positive ions, causing a depression in their volume fractions in this region. Outside the membrane domain, the salt and dissociated water ions approach their bulk volume fractions, $\sim 1.81\times10^{-3}$ and $\sim 1.81\times10^{-9}$, respectively, corresponding to the bulk salt concentration of 0.1 M and p*H* of 7.0, set as inputs to the system.

The net and individual component charge density distributions, as functions of the distance from the bilayer midplane, are also captured by the molecular theory, illustrated below in *Figure 7.2*. Analogous to the volume fraction distributions, the charge densities of the counter ions deviate from their values in the bulk close to the water–membrane interface due to the zwitterionic lipid headgroups. The model operates under the constraint of global charge neutrality,

thus, the area under the net charge distribution curve, depicted in *Figure 7.2, top left*, sums to zero.

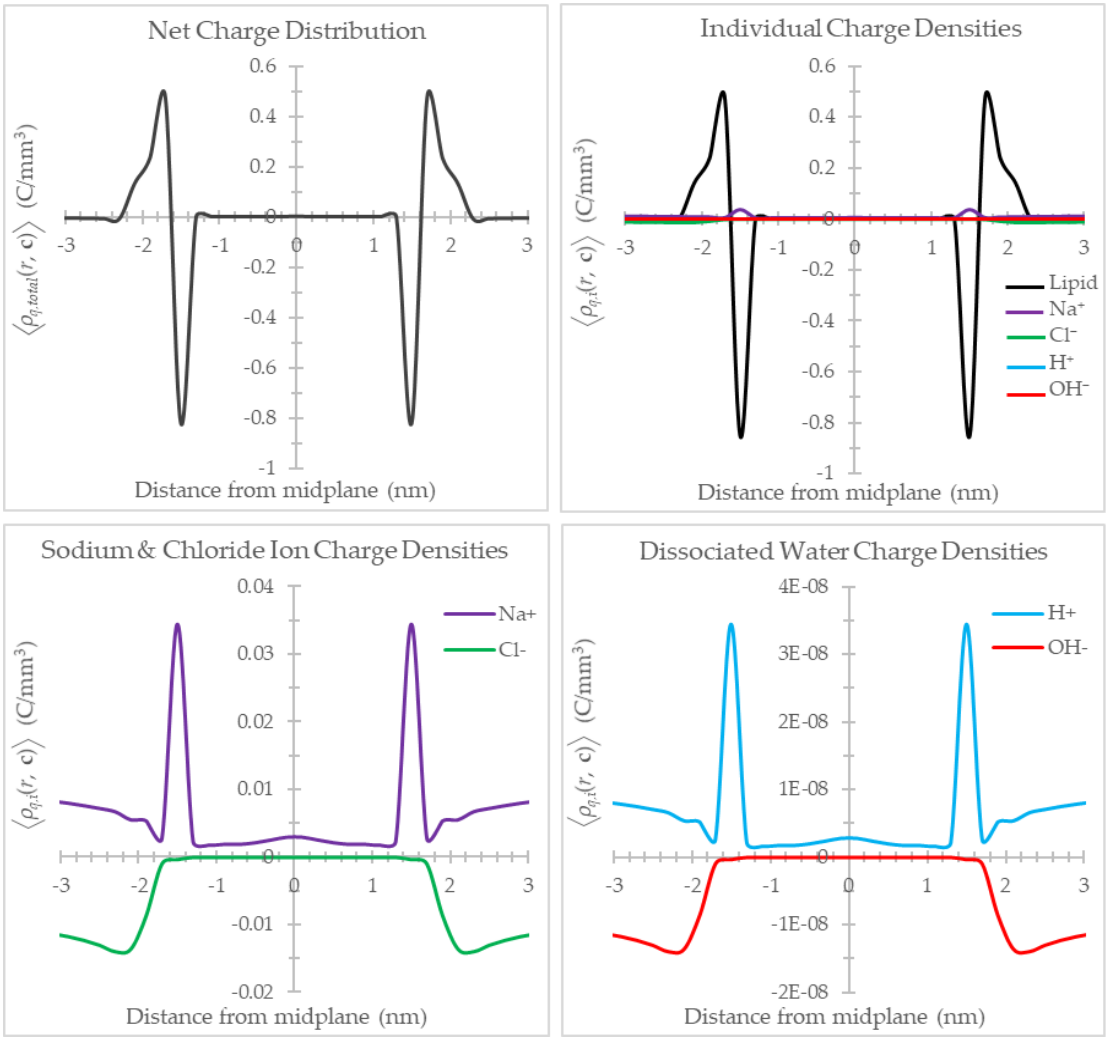

Figure 7.2) **Charge density distributions of system components.** ***Top left:*** Net charge distribution through the system contributed by all charged system species. Due to the global charge neutrality constraint, the area under the curve sums to zero. ***Top right:*** This plot depicts the individual charge distributions for each charged species, including the DOPC lipid constituents of the membrane, which have polar headgroups *(black)*, sodium ions *(purple)*, chloride ions *(green)*, and dissociated water ions, hydronium *(light blue)* and hydroxide *(red)*. The graph portrays the dominant contribution of the lipid headgroups to the overall charge distribution in the headgroup region. ***Bottom left:*** Magnified sodium and chloride ion charge density distributions. ***Bottom right:*** Magnified hydronium and hydroxide ion charge density distributions.

PC lipid headgroups are capable of undergoing acid-base equilibrium reactions, depending on the local p*H* of the aqueous medium. As shown in *Figure 7.3*, the p*H* profile through our system does not exceed 7.8, nor fall below 6.4; thus, the lipid phosphate group, which has a pK_a of ~2, maintains its deprotonated form with a charge of −1, and the lipid choline group, with pK_a of ~9, remains protonated with a charge of +1.

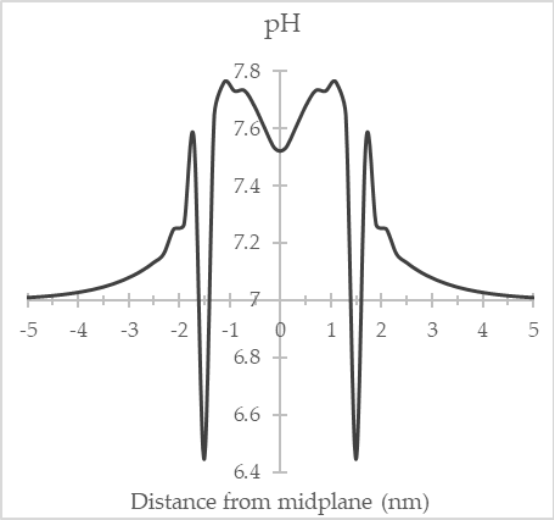

Figure 7.3) **p*H* profile through the system.** The local p*H* of the aqueous medium surrounding the lipid membrane deviates from its bulk value of 7.0 due to the local distribution of hydronium ions that congregate or deplete, as governed by the total electrostatic potential, predominantly influenced by the negative phosphate and positive choline moieties, respectively, of the lipid headgroups.

Physiological p*H* is tightly regulated to range between 7.35 and 7.45, as measured in the arterial blood – though p*H* varies widely in different fluids and tissues in the body. For instance, the p*H* along the gastrointestinal tract alone changes from highly acidic in the lower stomach cavity (p*H* ~1-2) [320-322] to moderately alkaline in parts of the small intestine (p*H* ~7.5) [320, 323]. Though charge

regulation equations for the membrane's lipid constituents are unnecessary for our purposes in this work, they may easily be incorporated for lipid studies focusing on areas of the body with p*H* values closer to the extrema of the p*H*-scale or when incorporating lipids with headgroups that more readily participate in acid-base reactions in media with a p*H* closer to neutral.

The distribution of the electrostatic potential as a function of distance from the bilayer's midplane is obtained from the solutions to the Poisson equation, derived via functional minimization in *Equation 6.53*. The total electrostatic potential, shown in *Figure 7.4*, is largely dominated by the charge distribution of the lipid headgroups.

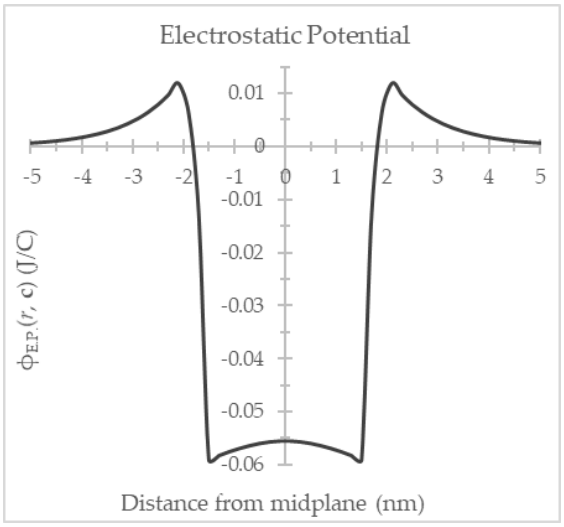

Figure 7.4) **Electrostatic potential profile through the system.** The electrostatic potential is calculated using the molecular theory through a planar, symmetric DOPC bilayer, within an aqueous ionic medium, approaching a constant value of zero in the bulk solution due to the charge-neutral requirement and boundary condition imposed on the system.

As the distance from the membrane increases and solution components approach their values in the 'bulk' aqueous medium, the number of positive and negative ions in the system balance at each location, resulting in a homogenous, net charge-neutral environment. Thus, far from the membrane's surface, the electrostatic potential approaches a constant value, which is set to zero (as $r \rightarrow \pm\infty$) as a boundary condition we impose on the system. The electrostatic potential is relatively constant inside the hydrophobic core of the planar, symmetric bilayer due to the near absence of ions within this region. The decay rate of the electrostatic potential profile from the surface of the membrane to its value of zero in the bulk solution is mediated by the bulk concentration of the salt ions (0.1 M) and the p*H* of the bulk solution (7.0). Decreasing the concentration of salt counterions, which screen the polar surface of the bilayer, and raising the p*H*, increases the influence of the bilayer's surface charge on the electrostatic potential (and corresponds to an increase in Debye length and a shallower decay of the potential).

Geometry-Driven Effects on Molecular Properties of the Membrane

We use the lipid properties and above distributions found for the planar membrane system as points of reference for our analysis of the effects caused by curving the membrane out of planarity. Earlier we introduced a parameter defined as the relaxation ratio, η_i, which specifies the mole fraction of a given

species of lipid in the expanded leaf of a bilayer with curvature, **c**, and hydrophobic thickness, *l (Equation 4.51)*. We have chosen a relaxation ratio of 0.40 for all results in this section, as this value produces a bending modulus of ~21k_BT for DOPC, matching the averaged experimental values reported in the literature *(as explained in Section 4.7)*. As the concentration of lipids in each leaflet is dependent on both principal curvatures, $C_i = {}^1/_{R_i}$, which differ between spherical and cylindrical bilayers $\left(C_1 = C_2 = {}^1/_R\right)$ and $\left(C_1 = {}^1/_R, C_2 = 0\right)$, respectively, membranes of the two different geometries with the same radius will have different lipid concentrations in the expanded and compressed leaflets. Similarly, the area per lipid is subject to the membrane's principal curvatures, with the additional dependency on the distance from the bilayer midplane, as described by *Equation 4.3*. *Figure 7.5, top panel* demonstrates how the hydrophobic–hydrophilic interfacial area per lipid (at ±1.3 nm from the midplane) *(left)* and lipid mole fraction *(right)* diverge from their planar membrane values when the bilayer is curved into spherical and cylindrical forms of varied diameter. *Figure 7.5, bottom left* illustrates the change in molecular area through the bilayer in a membrane curved to a diameter of 40 nm in both geometries (note that positive values on the horizontal axis represent distance from the bilayer midplane, passing through the expanded leaf, and negative values represent distance through the compressed leaf). The driving factor for lipid transbilayer diffusion from the compressed to

the expanded membrane leaf is the deviation in chemical potential that arises between lipids in the opposing leaflets upon bending the bilayer out of the chemical equilibrium maintained in its planar form. This chemical potential difference is shown in *Figure 7.5, bottom right* as a function of diameter in spherical and cylindrical membranes.

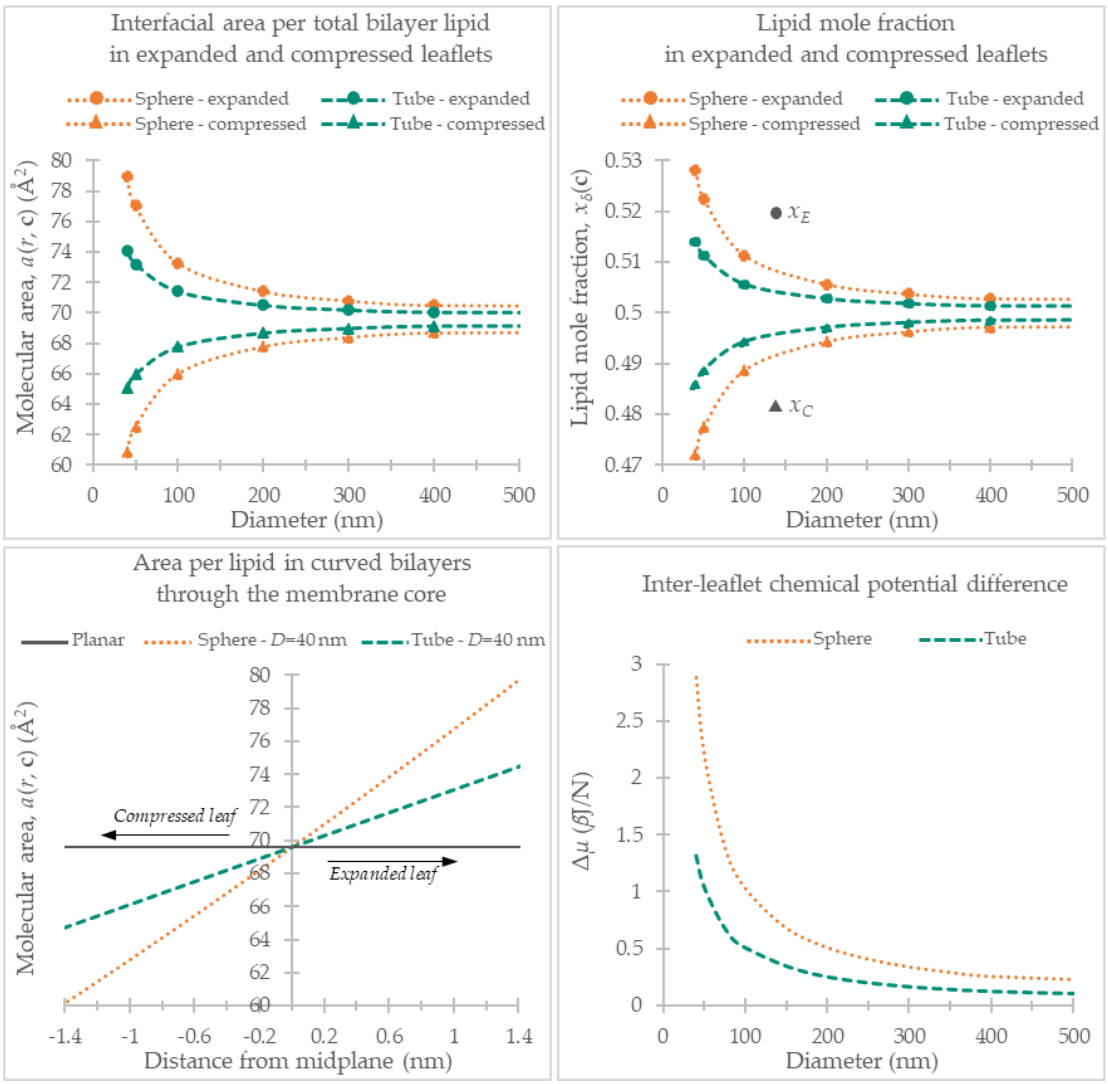

Figure 7.5) **Theoretically calculated physical and chemical membrane properties in spherical *versus* cylindrical bilayers.** ***Top panel:*** Changes in the molecular area at the hydrophobic–hydrophilic interfaces ***(left)*** and the lipid mole fraction (for a relaxation ratio of 0.40) ***(right)*** as a function of diameter for spherical *(orange)* and cylindrical *(turquoise)* bilayers in the expanded leaflet *(circles)* and in the compressed leaflet *(triangles)*. ***Bottom left:*** Changes in the molecular area through the membrane core as a function of distance from the bilayer midplane. Planar bilayers *(black horizontal line)* have constant molecular area at all points along the bilayer normal, while increasingly positive(negative) deviations from the planar value occurs in curved bilayers with increasing distance from the midplane into the expanded(compressed) membrane leaf. ***Bottom right:*** The change in chemical potential between the compressed and expanded membrane leaflets in curved bilayers, for a relaxation ratio of 0.40. Curvature effects are calculated using spherical *(orange)* and cylindrical *(turquoise)* membranes.

Analogous to the volume fraction plots in *Figure 7.1*, *Figure 7.6* features the lipid/water *(left)* and cation/anion *(right)* volume fraction profiles through the system, with the changes in the distributions indicated for spherical and cylindrical membranes, 40 nm in diameter.

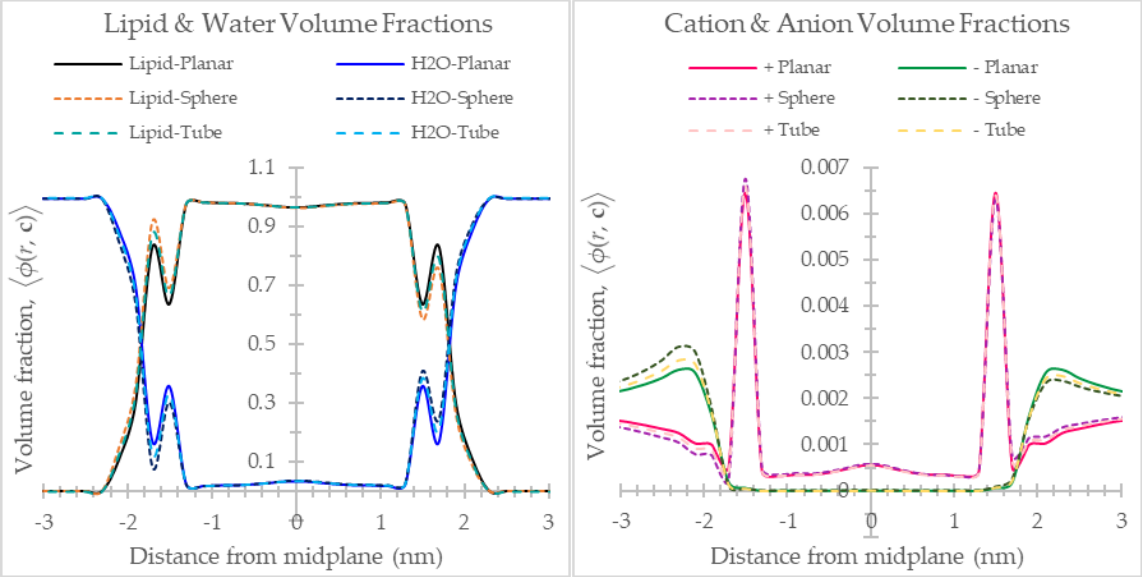

Figure 7.6) **Effect of membrane curvature on the volume fraction distributions of all system species.** The plots show the differences in the volume fraction distributions of the system's species as the membrane curves out of planarity to spherical and cylindrical geometries, 40 nm in diameter. ***Left:*** the membrane's lipid constituents *(planar: black; spherical: orange; cylindrical: turquoise)* and water *(planar: royal blue; spherical: dark blue; cylindrical: pale blue*) and ***Right:*** cations – sodium plus hydronium *(planar: bright pink; spherical: purple; cylindrical: pale pink)* and anions – chloride plus hydroxide *(planar: green; spherical: dark green; cylindrical: yellow)*. As the membrane's hydrophobic region is exceedingly dense, it is nearly impermeable to solution components, resulting in very low concentrations of water and salts through the membrane core. Negative values on the horizontal axis represent distance into the compressed leaflet of the curved membrane; positive values on the horizontal axis represent distance into the expanded leaflet. The midplane is where the horizontal axis = 0.

Notably, though the lipid concentration in the expanded leaf of a curved membrane, x_E *(Figure 7.5, top right)*, increases as a result of the chemical potential-driven transbilayer diffusion of lipids, the overall volume fraction of lipids actually decreases in the bilayer's expanded leaf *(positive values of the horizontal axis, Figure 7.6, left)*, relative to its planar value, due to the influx of the more readily available water molecules. This is intuitive considering the large energy barrier posed to lipids diffusing from one bilayer leaflet to another (a reason for our conclusion that η^{bio} settles at a value less than η^*) when compared to the influx of small, unimpeded water molecules directly adjacent to the curvature-induced spatial vacancies at the membrane-water interface.

Figure 7.7 shows the differences in the distributions of the electrostatic potential *(left)* and the net charge density *(right)*, as functions of distance from the bilayer midplane, between planar, spherical, and cylindrical membranes. The diminished(augmented) peak amplitudes exhibited in these profiles within the expanded(compressed) leaf of the bilayer in the curved membrane systems, relative to the planar, mirror the changes in lipid volume fraction due to curvature, reflecting the dominance of the lipid contribution above that of other system species on these properties within the membrane region.

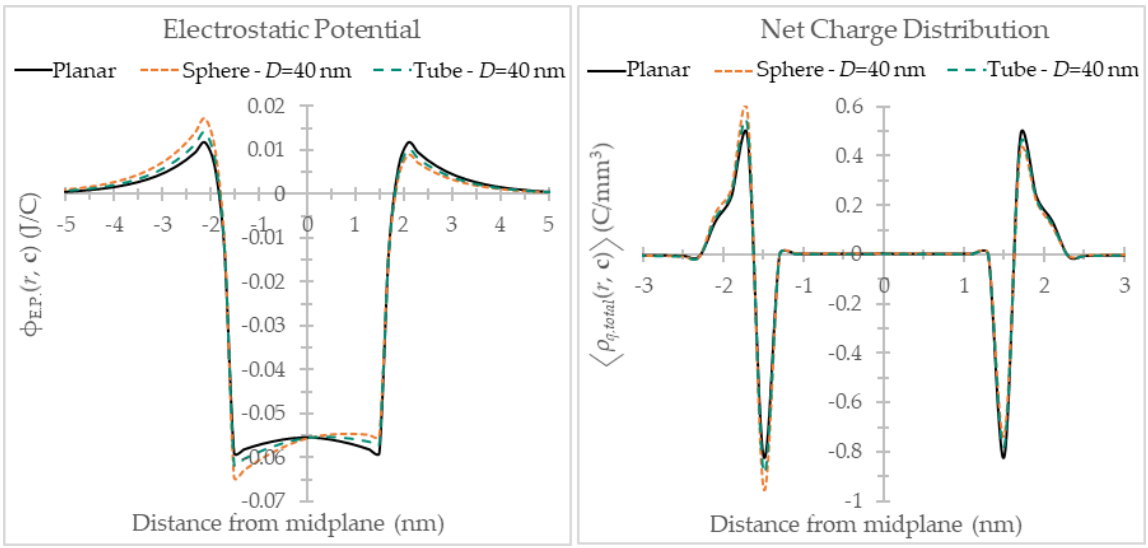

Figure 7.7) **Effect of membrane curvature on the distributions of the electrostatic potential and total charge density through the system.** The plots show the differences in the electrostatic potential ***(left)*** and charge density ***(right)*** distributions when they are curved out of planarity to spherical *(orange)* and cylindrical *(turquoise)* geometries, 40 nm in diameter. Negative values on the horizontal axis represent distance into the compressed leaflet of the curved membrane; positive values on the horizontal axis represent distance into the expanded leaflet. The midplane is where the horizontal axis = 0.

A trend revealed in all profiles displayed in this section is the stronger response induced by bending the bilayer into spherical form than when it is curved to a cylindrical geometry with the same diameter, given by the differential shifts in the curves relative to their planar distributions.

Geometry-Driven Effects on Interactions between the Membrane and Lipidated Proteins

Analogous to the results presented in *Section 5.3* using the *Generation I* model, in *Figure 7.8* we demonstrate the relative adsorption density of tN-Ras on curved DOPC membranes of varying diameter, now residing in an aqueous, ionic

solution, using the *Generation II* model. The plots recapitulate our previous findings [177] of preferential protein adsorption to membranes of high curvature; however, with our side-by-side comparison of protein localization on both spherical and cylindrical bilayers, we now reveal the additional ability of the protein to sense and target membranes of specific geometries.

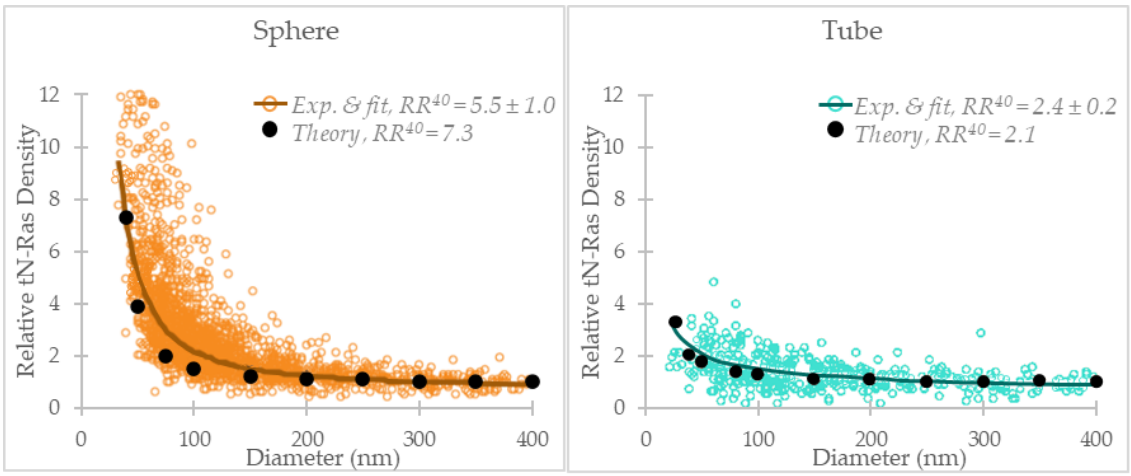

Figure 7.8) **Side-by-side comparison of the normalized tN-Ras density on spherical and cylindrical membranes as a function of membrane diameter.** Open symbols indicate the normalized density of membrane-adsorbed tN-Ras protein, measured by experiment, on spherical bilayers *(**left**, orange)* and cylindrical bilayers *(**right**, turquoise)* of various diameters. The solid lines are the error-weighted fits to the experimental data. Molecular field theory calculations of normalized tN-Ras adsorption density as a function of diameter are given by black markers, demonstrating excellent agreement with experimental results. Data demonstrate higher recruitment of the protein by spherical membranes, relative to cylindrical membranes.

Of the two shapes, comparing membranes of the same diameter over the range of diameters studied (from planar to highly curved at 20 nm), spherical bilayers act as significantly more effective recruiters of the tN-Ras protein. This can also be clearly recognized from the ratio of adsorption densities on spherical-

to-cylindrical bilayers, illustrated as a color-landscape encompassing a range of diameters for the two membrane geometries, presented in *Figure 7.9*. The orange region indicates enhanced adsorption on spherical membranes, while turquois values represent higher density on cylindrical membranes; the black, dashed line guides the eye along the spherical/cylindrical bilayer diameters where the protein portrays no preference for either geometry.

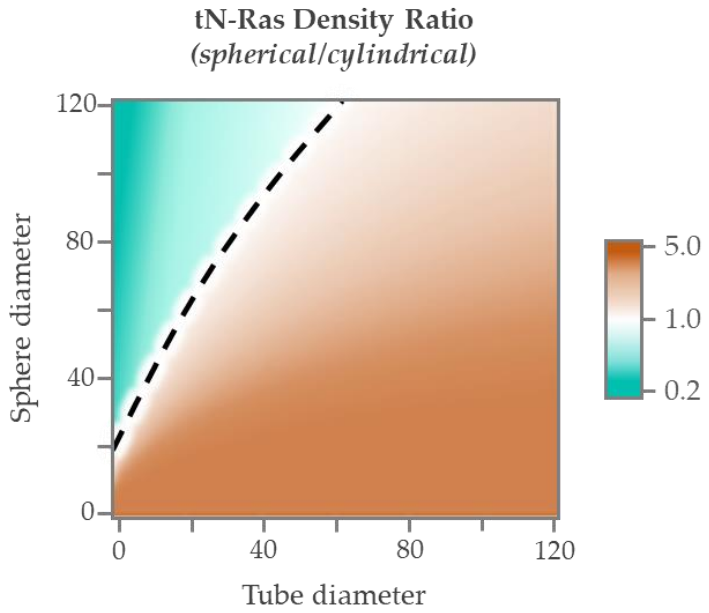

Figure 7.9) **Relative equilibrium adsorption density of tN-Ras on the membrane over a curvature landscape comprising a range of spherical and cylindrical membrane geometries.** The color landscape depicts the experimentally determined tN-Ras density as the ratio of values for spherical membranes to those for cylindrical membranes. Orange values represent increased density on spherical bilayers; turquoise values represent increased density on cylindrical bilayers. The black dashed line is a guide to the eye representing the sphere/tube diameters at which there is no net preference of the protein for one of the membrane shapes.

In the *Generation I* model, we identified one important mechanism by which tN-Ras senses membrane curvature and differentiates membrane composition as

the relief in lateral pressure through the bilayer's expanded leaf, caused by bending the membrane into spherical liposomes of decreasing diameter, effectively reducing the amount of work needed by the protein to insert into the membrane's hydrophobic region *(see Section 5.3)*. In *Generation II*, we seek to expand the assessment by investigating how changes in membrane shape, and particularly in Gaussian curvature, influence the membrane's lateral pressure distribution and if this translates to a means of predicting the localization behavior of lipidated proteins on geometry-variant bilayers. Considering *Equations 7.7* and *6.58*, we see that the partition function of the protein's anchor, which dictates the relative density of protein in a curved bilayer, explicitly depends on the three dominant, curvature-mediated elements composing the lateral pressure, integrated over the depth of the bilayer leaflet in contact with the protein. These are the $\pi(r,\mathbf{c})$, $\langle\phi_{L\text{-}t,\delta}(r,\mathbf{c})\rangle$, and (for proteins with charged elements in proximity to the membrane) $\Psi(r,\mathbf{c})$ fields that contain the contributions from the excluded volume (repulsive), hydrophobic (attractive), and electrostatic interactions, respectively. First, we note the correlations between the differences in both the theoretical and experimental relative adsorption densities of tN-Ras in the geometrically varied membrane systems, presented in *Figure 7.8* above, and the corresponding differences in the membrane's lateral pressure, illustrated in *Figure 7.10* below.

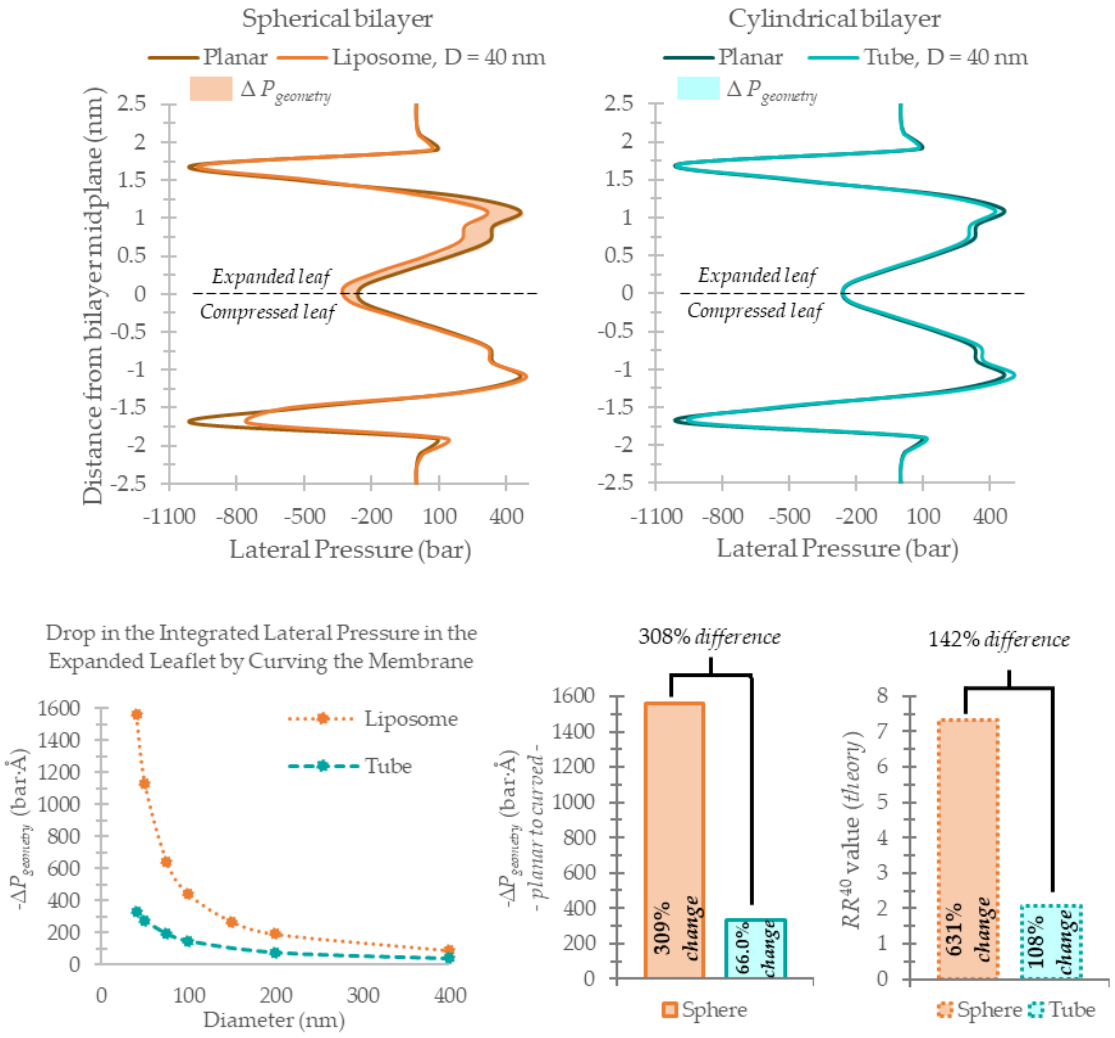

Figure 7.10) **Effects of spherical *versus* cylindrical membrane geometries on membrane properties, as calculated by the molecular theory.** ***Top panel:*** Theoretically calculated lateral pressure profiles along the bilayer normal (through the bilayer's width), for a planar bilayer *(**left**, dark orange or **right**, dark turquoise)* and a spherical *(**left**, bright orange)* or cylindrical *(**right**, bright turquoise)* bilayer. The shaded region between the curves indicates the degree of relief in lateral pressure ($\Delta P_{geometry}$) in the expanded membrane leaf when the membrane bends out of planarity to a 40 nm in diameter sphere *(**left**, pale orange)* or cylinder *(**right**, pale turquoise)*. ***Bottom left:*** The change in the integrated lateral pressure, $\Delta P_{geometry}$, from bending the membrane from planar form to a sphere *(orange)* or to a cylinder *(turquoise)* as a function of membrane diameter. ***Bottom center:*** $\Delta P_{geometry}$ between planar and curved bilayers 40 nm in diameter. ***Bottom right:*** Theoretically calculated recruitment ratio at $D = 40$ nm (RR^{40}).

In the top two plots of *Figure 7.10* the reader can visualize the degree of curvature-induced relief in lateral pressure through the hydrophobic and headgroup regions of the expanded membrane leaf (positive values on the vertical axis) as the shaded region between the lateral pressure profile of the planar bilayer *(dark line)* and that of a curved bilayer, 40 nm in diameter *(pale line)*, noting the differences between spherical *(left)* and cylindrical *(right)* membranes. The augmented curvature-induced localization of tN-Ras on spherical DOPC membranes, compared with the less impressive adsorption density curve of tN-Ras on the cylindrical DOPC membranes from *Figure 7.8*, corresponds with the more pronounced relief in lateral pressure in the expanded leaflet of the membrane when transformed from a flat to a spherical, compared to a cylindrical, geometry, as indicated in *Figure 7.10*. The bottom set of graphs in *Figure 7.10* quantify these curvature-induced lateral pressure drops for the two curved membrane geometries with the change in the integrated lateral pressure, $\Delta P_{geometry}$, as a function of membrane diameter *(left)* and for a diameter of 40 nm *(center)*, to compare with the differential localization exhibited by tN-Ras between the two membrane shapes at D = 40 nm using the RR^{40} value *(right)*.

The results of this section thus far demonstrate the regulatory effect of membrane geometry on the physicochemical characteristics and thermodynamic properties of the membrane, as well as on the spatial segregation of lipidated

membrane-inserting proteins. For the same membrane diameter, spherical bilayers incite a stronger response in all elements studied than do cylindrical bilayers under identical system conditions. We discussed earlier two physical parameters that, together, define the local morphology at a point on a given surface – the mean and Gaussian curvatures. The latter is often neglected in theoretical models that treat the lipid bilayer as an infinitely thin, two-dimensional sheet, where the contribution from the Gaussian curvature is rendered irrelevant to membrane energetics *(see Sections 4.5 and 7.1)*. The following set of results demonstrates that Gaussian curvature does in fact have a significant impact on membrane functionality and is important to the understanding of geometry-function correlations – a revelation identified by consideration of the atomic-scale heterogeneity through the membrane's width.

To highlight the influence of Gaussian curvature on membrane properties, we compare spherical bilayers of a given radius with cylindrical bilayers of half that radius, thereby equating the mean curvatures of the two geometries $\left(H_{sph} = {}^{1}/_{R}, H_{cyl} = {}^{1}/_{2R}\right)$ and isolating the contribution from Gaussian curvature $\left(K_{G,sph} = {}^{1}/_{R^2}, K_{G,cyl} = 0\right)$. First, we can visualize how the lateral pressure through the bilayer is affected, specifically by Gaussian curvature, by plotting the distribution of the change in lateral pressure between cylindrical and spherical bilayers, of diameter ${}^{D}/_{2}$ and D, respectively, as a function of bilayer depth. We

demonstrate this distribution for a 'low curvature regime' (D_{sph} = 200 nm, D_{cyl} = 100 nm), a 'mid-range curvature regime' (D_{sph} = 150 nm, D_{cyl} = 75 nm), and 'high curvature regime' (D_{sph} = 40 nm, D_{cyl} = 20 nm) to feature the growing influence of the Gaussian curvature contribution as curvature increases in *Figure 7.11*.

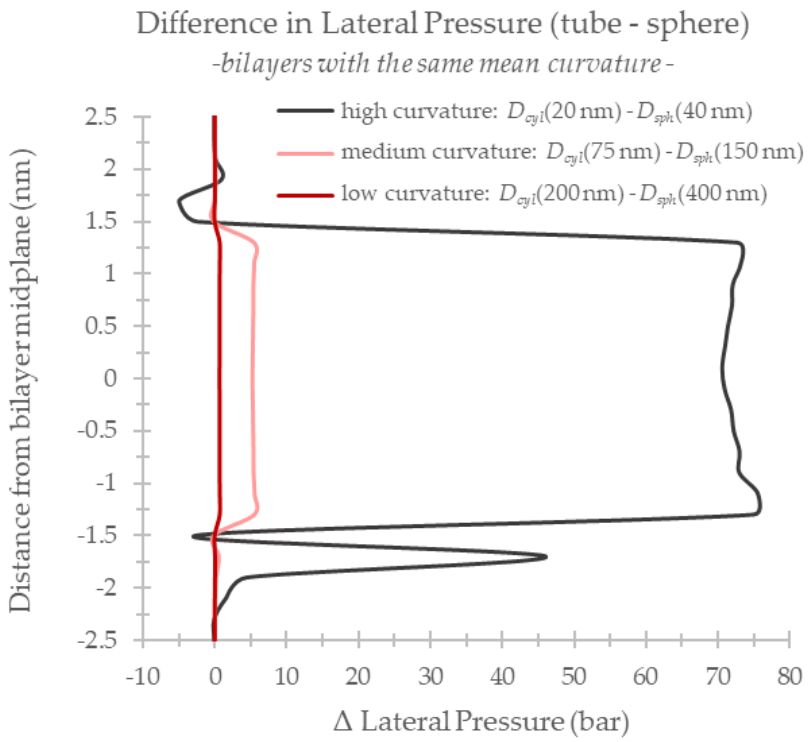

Figure 7.11) **Isolated effect of Gaussian curvature on the lateral pressure distribution.** Theoretically calculated distribution of the Gaussian curvature-mediated change in the lateral pressure, from a cylindrical membrane of a given diameter, *D*, to a spherical membrane of twice that diameter, for a low curvature *(red)* and a high curvature *(dark grey)* regime, as a function of distance from the bilayer midplane, along the bilayer normal.

The plot indicates that the impact of Gaussian curvature on the lateral pressure profile in pure DOPC membranes is dispersed relatively uniformly through the hydrophobic thickness and is dramatically augmented in the high curvature

regime.

Previously we noted that to detect the influence of Gaussian curvature on the thermodynamics in a lipid bilayer, consideration of the membrane's thickness is necessary. We demonstrate this point by examining the effect of Gaussian curvature on a surface (two-dimensional) property, such as the membrane's average interfacial area per lipid, compared with its effect on a (three-dimensional) property dependent on the structural details through the membrane's core, such as the integrated lateral pressure. The influence of membrane curvature on many properties of interest in the biosciences is generally attributed to its modulation of lipid packing in the membrane, which is represented in our theory by changes in these two elements within a given leaf of the bilayer. We calculate the change (planar to curved) in (1) the expanded leaflet's interfacial area per total bilayer lipid, (2) the interfacial area per number of lipids in the expanded leaf, with a relaxation ratio of 0.40, and (3) the lateral pressure, integrated over the width of the bilayer's expanded leaf, $A(r=l, \mathbf{c})/_{N}$, $A(r=l, \mathbf{c})/_{N_E}$, and $\Delta P_{geometry}$, respectively. In *Figure 7.12*, we plot these as ratios of the given property in spherical bilayers with diameter, D, to cylindrical bilayers with half that diameter (membranes of the same mean curvature), as a function of D.

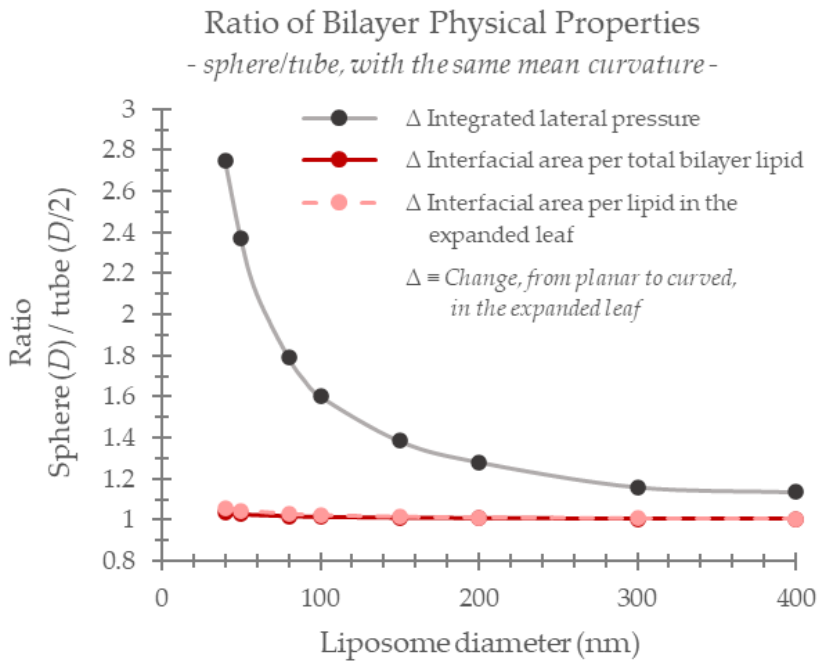

Figure 7.12) **Effects mediated by Gaussian curvature in a three-dimensional membrane property.** Theoretically calculated change (Δ, from planar to curved bilayers) in the integrated lateral pressure *(dark grey markers)*, interfacial area per total number of bilayer lipids *(dark red markers)*, and interfacial area per number of lipids in the expanded leaf *(pale red)*, all calculated for the expanded membrane leaf, plotted as ratios of the values in spherical liposomes of a given diameter, *D*, to cylindrical membranes of half that diameter (membranes of the same mean curvature), as a function of *D*. Lines through the data points are to guide the eye. Deviation from unity indicates the isolated effect of Gaussian curvature. The integrated lateral pressure, which depends on bilayer thickness, demonstrates a distinct dependency on Gaussian curvature, while the interfacial area does not.

We discover that the change in the interfacial molecular area, either on a 'per total lipid' or 'per number of lipids in the expanded leaf' basis, has little response to changes in Gaussian curvature, deviating a maximum of only ~3% and ~5%, respectively, from unity. Any property that is purely two-dimensional, such as the interfacial molecular area, will not show a considerable dependence on

Gaussian curvature, which, in tandem with its generally smaller magnitude relative to the mean curvature for all but very small radii, contributes to the apparent shortage of scientific studies involving the effects of Gaussian curvature in lipid membrane physics up to this point. The calculation of the same ratio using $\Delta P_{geometry}$ as a function of membrane diameter, however, shows distinct increasing deviation from unity with decreasing diameter, and thus an express dependency on Gaussian curvature, with a 22% increase at D = 150 nm and up to a 142% increase at D = 40 nm. Given the importance of $\Delta P_{geometry}$ in predicting curvature sensing in lipidated proteins, established from the *Generation I* results, this dependency suggests that Gaussian curvature might be an important metric in predicting how these proteins sense membranes of different geometries. To detect this influence, consideration of the bilayer's thickness is necessary, hence the error in purely surface analyses, or interpretation of the bilayer as a two-dimensional sheet.

To determine if the localization of lipidated proteins on membranes of varied geometry is indeed similarly affected by Gaussian curvature, independently of mean curvature, we plot the ratio of both the experimental and theoretical tN-Ras adsorption densities on spherical membranes, with diameter, D, to cylindrical membranes, with diameter, $D/2$, in *Figure 7.13.*

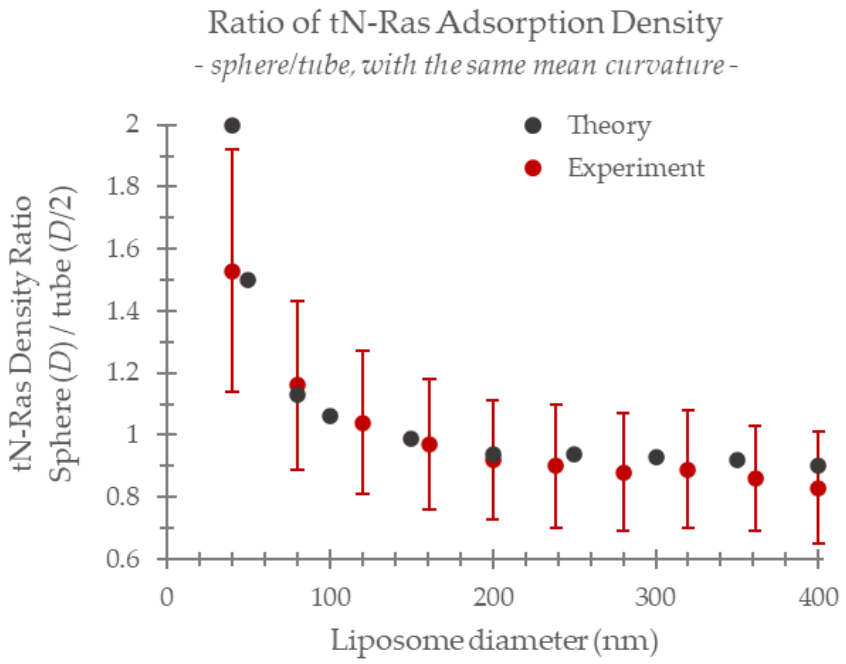

Figure 7.13) **Impact of Gaussian curvature on tN-Ras adsorption on lipid membranes.** tN-Ras adsorption density on curved membranes, plotted as a ratio of density values on spherical membranes of a given diameter, *D*, to cylindrical membranes of half that diameter (membranes of the same mean curvature), as a function of spherical liposome diameter, *D*. Excellent agreement is found between experimental *(dark red)* and theoretical *(dark grey)* results. Deviation from unity demonstrate the non-negligible contribution from Gaussian curvature to membrane–protein interactions.

Under the estimation of negligible Gaussian curvature employed by traditional theoretical membrane models, protein localization is predicted to be identical on similar bilayers of different geometries with the same mean curvature, which would result in values of unity at all diameters in the plot above. Both the experimental and theoretical results presented here reveal deviation from unity, with a more pronounced influence from Gaussian curvature on tN-Ras adsorption at higher curvatures (diameters < 150 nm), as was observed with the integrated

lateral pressure curve from *Figure 7.12*. The data indicate that the lateral pressure profile, integrated over the width of the leaflet in contact with membrane-inserting proteins, is a valuable physical parameter that underlies geometry discrimination of these proteins and that the differential contribution by Gaussian curvature to the lateral pressure in geometry-variant bilayers is an important indicator of the proteins' curvature-sensing behavior.

Membranes are, in fact, widely varied in morphology, taking forms everywhere between the planar, cylindrical, and spherical geometries we have examined thus far. Theoretical descriptions of biological systems are uniquely efficacious for delineating behaviors and properties for which no experimental technique for direct measurement exists and for exploring systems under certain conditions that are currently unattainable experimentally. Given the excellent agreement between our theoretical results presented in this work and those obtained experimentally by our collaborators, we believe our molecular model can be used to make reliable quantitative predictions for a range of membrane geometrical forms that are presently beyond the reach of experimental approaches.

The study of a lipidated protein's integration with the membrane, particularly N-Ras, is an apt representative example for this purpose because of the protein's interaction with various membrane formations along its intracellular pathway, from those of the tightly folded ER and Golgi, to the membranes of small,

spherical transport vesicles, and ultimately to the plasma membrane [286, 324]. The plasma membrane is reported to develop highly curved inward protrusions that are identified with Ras localization called caveolae [272, 325], as illustrated in *Figure 4.1*. *Figure 7.14* offers a depiction of three stages of the progressive development, or budding, of a caveola formation, and includes corresponding membrane-adsorption densities of tN-Ras, normalized to the density on a planar bilayer, represented by superimposed color maps. Such illustrations demonstrate the uninterrupted adaptation in tN-Ras localization, prompted solely by continuous, gradual geometrical transformations of the model bilayer that reflect the complex morphological diversity of real biological membranes. We find a more than 16-fold upregulation in the tN-Ras normalized density, spanning from the constricted saddle-type regions that depress protein–membrane interaction to the broad sphere-like surfaces of the budding membrane that enhance successful protein insertion.

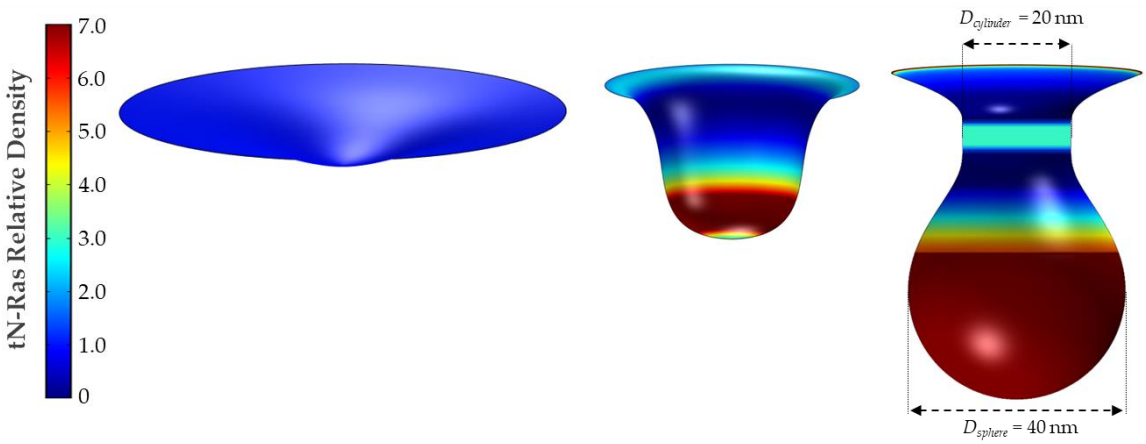

Figure 7.14) **Quantitative theoretical prediction of tN-Ras localization due to the complex geometrical transformations associated with vesicle budding, or caveolae formation.** ***Left to right:*** progressive deformation of a planar membrane to the 'inverse omega' shape commonly adopted by budding vesicles and caveolae. The color scale shows the density of tN-Ras, relative to that on a planar membrane. The models for spherical and cylindrical regions of the membrane surface are validated experimentally in this work, while the model for saddle points has no experimental comparison. Local variations in the mean and Gaussian curvature of these complex geometries give rise to the depicted equilibrium protein density patterns.

The equilibrium normalized density distribution of tN-Ras quantified in the above figure manifests from the combined influence of mean and Gaussian curvature on local membrane behavior. How the values of these two geometrical properties themselves change with shape transitions, corresponding to the budding caveola portrayed in *Figure 7.14*, is quantitatively and visually depicted in *Figure 7.15*.

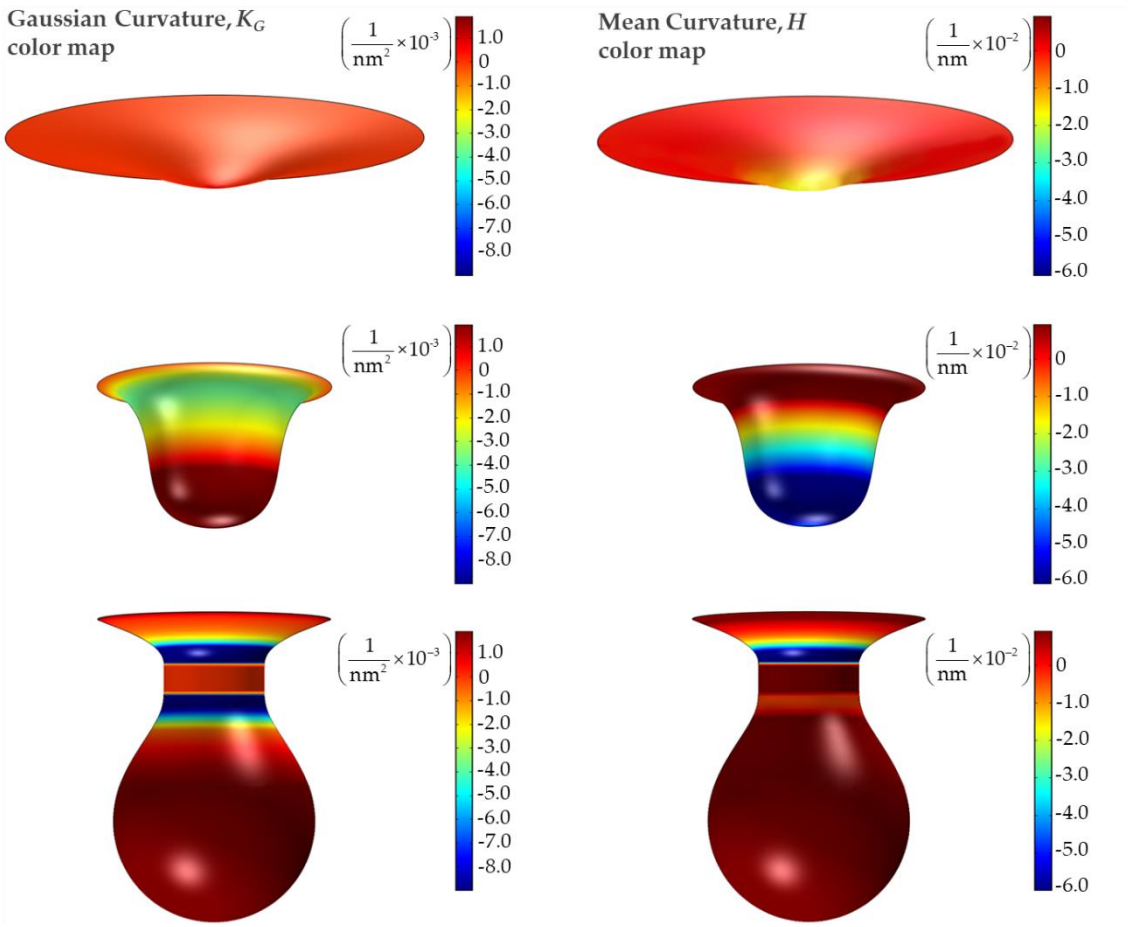

Figure 7.15) **Calculated Gaussian and mean curvatures for complex membrane formations.** The calculated distribution of Gaussian ***(left column)*** and mean ***(right column)*** curvatures, in units of nm^{-2} and nm^{-1}, respectively, for the geometries used to generate the tN-Ras adsorption densities in *Figure 7.14*.

We use the COMSOL Multiphysics (v. 4.3b) program to mathematically map the surface geometry and project a color gradient overlay, with wavelength proportional to the value of the curvature of interest (mean or Gaussian), for each of the three depicted stages of the budding 'caveola' membrane. Each figure is constructed as a three-dimensional simulation in the SolidWorks CAD program, with specified dimensions, and subsequently imported into COMSOL for surface

analysis. Mean and Gaussian curvature values illustrated in *Figure 7.15* are calculated in nm^{-1} and nm^{-2}, respectively, and applied as inputs in the molecular theory to determine the relative adsorption densities of tN-Ras at each point on the surfaces of the budding membranes; these densities are used for the construction of the mapping presented in *Figure 7.14*.

We have focused on the enhanced ability of the membrane to recruit lipidated proteins, facilitated by its flexible nature, as it bends into various forms. However, curvature of the membrane can just as easily diminish protein adsorption, relative to a planar geometry, in areas of local concavity, or compression. The darkest blue regions of the center and right-most buds in *Figure 7.14* demonstrate such downregulation of tN-Ras adsorption. These regions correspond to *hyperbolic points* of the surface, that is, points where the values of the local principal curvatures are of opposite sign and the surface is locally saddle shaped. True *saddle-points* are those defined by principal curvatures which are equal and opposite. An example of tN-Ras membrane-adsorption behavior in the presence of locally saddle-shaped DOPC membranes is provided in *Figure 7.16* below, as a function of local membrane diameter, along with the corresponding adsorption trends on spherical and cylindrical membranes for comparison[16].

[16] Note that in *Figures 7.14* and *7.16*, protein densities are normalized to the planar membrane value. All other density calculations presented throughout this work are normalized to the values at diameters of 400 nm for a given geometry, for direct comparisons with the experimental results.

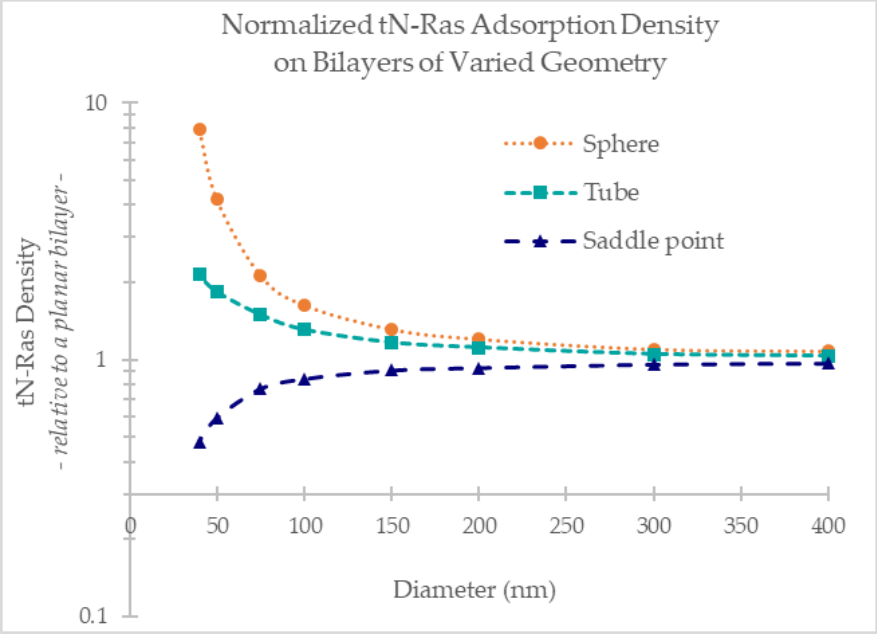

Figure 7.16) **Effect of membrane geometry on the normalized adsorption density of tN-Ras.** Theoretically calculated tN-Ras adsorption density, relative to the density on a planar bilayer, on membranes of various geometries: spherical *(orange)*, cylindrical *(turquois)*, and saddle point *(dark blue)*. The combined influence of mean and Gaussian curvature creates complex formations and affects the adsorption behavior of lipidated proteins.

In conclusion, the purpose of this work is to inform the reader about the direct and diverse role cellular membranes play in biology, to discuss important inherent elements of lipid membranes, and to extend the scientific community's understanding regarding the structure-to-function relationship between lipid membranes and lipidated proteins. These themes are discussed within a more general message highlighting the value of molecular theoretical models, rigorous enough to capture essential energetic and entropic contributions to the system that

There is almost no difference between the two, as a spherical or cylindrical bilayer with a diameter of 400 nm is nearly planar at the molecular scale.

emerge at the atomic scale, yet sufficiently simple as to enhance the comprehension of mechanistic motivations within the system while avoiding large computational expenses. Such molecular theories are capable of shedding light on sub-nanometer properties that have a large influence on biophysical characteristics/processes, yet which are inaccessible to current experimental techniques.

We have disclosed the significant control that local structural properties of the membrane, and the lipids it comprises, have on the preferential adsorption behavior of lipidated proteins; we have also revealed a synergistic coupling among them that mediates the membrane's interaction with the proteins in a non-trivial manner. These properties include lipid type (which encompasses variations in the degree of lipid tail saturation, membrane thickness, and size of the lipid headgroup), local membrane curvature (with a detailed examination into the contributions from both mean and Gaussian curvature), and compositional asymmetry between membrane leaflets, caused by the curvature-induced transbilayer diffusion of membrane lipids. Our findings have implications regarding how the membranes of cellular compartments purposefully fine-tune their composition and shape to affect the sorting, trafficking, and functionality of membrane-inserting proteins throughout the entire secretory pathway.

In addition to reporting on these correlations as observed by theory and

experiment, a major contribution of this work is the delineation of the underlying mechanisms driving them. We find that the amplification of tN-Ras sensitivity to a decrease in liposome diameter when increasing lipid chain saturation, decreasing bilayer thickness (shorter lipid chain length), or decreasing the concentration of conically-shaped DOPE lipids (smaller headgroup-to-tail cross-sectional area ratio) is ubiquitously engendered by the heterogeneous relief in lateral pressure through the depth of the membrane leaf expanded during the size transition. The mechanistic role of the bilayer's lateral pressure is also found to extend to the distinct adsorption trends exhibited by tN-Ras with transitions in membrane geometry. The study leads to the important revelation that changes in the local Gaussian curvature of the bilayer, independent of mean curvature, motivates a substantial response in the lateral pressure distribution, which translates to the observed differences in the density isotherms of the protein. Therefore, the width of the bilayer is an imperative dimension to be considered in scientific research regarding membrane curvature. Though we have shown that the structural heterogeneity that exists at a nanoscopic scale through the membrane's core provokes macroscopic consequences that are non-negligible, the bilayer is often approximated as an infinitely thin, two-dimensional sheet, lending one reason as to why the contribution of Gaussian curvature has been previously unaccounted for in membrane biophysics.

We anticipate our findings will expand the reader's insight into the esoteric relationships that link cellular functionality with the membrane's molecular properties and polymorphism and relate to a wide range of disciplines within the biosciences, with the potential to lend meaningful contributions to the bioengineering and biomedical sectors.

REFERENCES

1. Singer SJ, Nicolson GL. The fluid mosaic model of the structure of cell membranes: Cell membranes are viewed as two-dimensional solutions of oriented globular proteins and lipids. *Science*. (1972) Feb 18; 175(4023):720-31. doi: 10.1126/science.175.4023.720.

2. Karp G. Cell and Molecular Biology: Concepts and Experiments, 6th ed. John Wiley & Sons; (2009) Oct 19.

3. Phillips MC, Ladbrooke BD, Chapman D. Molecular interactions in mixed lecithin systems. *Biochim Biophys Acta*. (1970) Jan 6; 196(1):35-44. doi: 10.1016/0005-2736(70)90163-x.

4. Shimshick EJ, McConnell HM. Lateral phase separation in phospholipid membranes. *Biochemistry*. (1973) Jun 5; 12(12):2351-60. doi: 10.1021/bi00736a026.

5. Grant CW, Wu SH, McConnell HM. Lateral phase separations in binary lipid mixtures: correlation between spin label and freeze-fracture electron microscopic studies. *Biochim Biophys Acta*. (1974) Sep 6; 363(2):151-8. doi: 10.1016/0005-2736(74)90055-8.

6. Lentz BR, Barenholz Y, Thompson TE. Fluorescence depolarization studies of phase transitions and fluidity in phospholipid bilayers. 2 Two-component phosphatidylcholine liposomes. *Biochemistry*. (1976) Oct 5; 15(20):4529-37. doi: 10.1021/bi00665a030.

7. Schmidt CF, Barenholz Y, Thompson TE. A nuclear magnetic resonance study of sphingomyelin in bilayer systems. *Biochemistry*. (1977) Jun 14; 16(12):2649-56. doi: 10.1021/bi00631a011.

8. Meder D, Moreno MJ, Verkade P, Vaz WL, Simons K. Phase coexistence and connectivity in the apical membrane of polarized epithelial cells. *Proc*

Natl Acad Sci USA. (2006) Jan 10; 103(2):329-34. doi: 10.1073/pnas.0509885103.

9. Sorre B, Callan-Jones A, Manneville JB, Nassoy P, Joanny JF, Prost J, *et al*. Curvature-driven lipid sorting needs proximity to a demixing point and is aided by proteins. *Proc Natl Acad Sci USA*. (2009) Apr 7; 106(14):5622-6. doi: 10.1073/pnas.0811243106.

10. Dietrich C, Volovyk ZN, Levi M, Thompson NL, Jacobson K. Partitioning of Thy-1, GM1, and cross-linked phospholipid analogs into lipid rafts reconstituted in supported model membrane monolayers. *Proc Natl Acad Sci USA.* (2001) Sep 11; 98(19):10642-7. doi: 10.1073/pnas.191168698.

11. Dietrich C, Yang B, Fujiwara T, Kusumi A, Jacobson K. Relationship of lipid rafts to transient confinement zones detected by single particle tracking. *Biophys J*. (2002) Jan; 82(1 Pt 1):274-84. doi: 10.1016/S0006-3495(02)75393-9.

12. Danielsen EM, Hansen GH. Lipid raft organization and function in the small intestinal brush border. *J Physiol Biochem*. (2008) Dec; 64(4):377-82. doi: 10.1007/BF03174093.

13. Engel S, Scolari S, Thaa B, Krebs N, Korte T, Herrmann A, *et al*. FLIM-FRET and FRAP reveal association of influenza virus haemagglutinin with membrane rafts. *Biochem J*. (2010) Jan 15; 425(3):567-73. doi: 10.1042/BJ20091388.

14. Bagatolli LA, Mouritsen OG. Is the fluid mosaic (and the accompanying raft hypothesis) a suitable model to describe fundamental features of biological membranes? What may be missing? *Front Plant Sci*. (2013) Nov 13; 4:457. doi: 10.3389/fpls.2013.00457.

15. Gebhardt C, Gruler H, Sackmann E. On domain structure and local curvature in lipid bilayers and biological membranes. *Z Naturforsch C Biosci*. (1977) Jul-Aug; 32(7-8):581-96. doi: 10.1515/znc-1977-7-817.

16. Rao M, Mayor S. Active organization of membrane constituents in living cells. *Curr Opin Cell Biol*. (2014) Aug; 29:126-32. doi: 10.1016/j.ceb.2014.05.007.

17. Marcelja S. Lipid-mediated protein interaction in membranes. *Biochim Biophys Acta.* (1976) Nov 11; 455(1):1-7. doi: 10.1016/0005-2736(76)90149-8.

18. Mouritsen OG, Bloom M. Mattress model of lipid-protein interactions in membranes. *Biophys J.* (1984) Aug; 46(2):141-53. doi: 10.1016/S0006-3495(84)84007-2.

19. Pagano RE, Cherry RJ, Chapman D. Phase transitions and heterogeneity in lipid bilayers. *Science*. (1973) Aug 10; 181(4099):557-9. doi: 10.1126/science.181.4099.557.

20. Träuble H. Membrane Electrostatics. In: Abrahamsson S, Pascher I. (eds) Structure of Biological Membranes. Nobel Foundation Symposia, Vol 34. Boston, MA: Springer; (1977). 509-550 p. doi: 10.1007/978-1-4684-8127-3_29.

21. Op den Kamp JA. Lipid asymmetry in membranes. *Annu Rev Biochem*. (1979); 48:47-71. doi: 10.1146/annurev.bi.48.070179.000403.

22. Thompson TE, Tillack TW. Organization of glycosphingolipids in bilayers and plasma membranes of mammalian cells. *Annu Rev Biophys Biophys Chem*. (1985); 14:361-86. doi: 10.1146/annurev.bb.14.060185.002045.

23. Vaz WL, Almeida PF. Phase topology and percolation in multi-phase lipid bilayers: is the biological membrane a domain mosaic? *Curr Opin Struct Biol.* (1993) Aug 1; 3(4):482-8. doi: 10.1016/0959-440X(93)90071-R.

24. Simons K, van Meer G. Lipid sorting in epithelial cells. *Biochemistry*. (1988) Aug 23; 27(17):6197-202. doi: 10.1021/bi00417a001.

25. Simons K, Ikonen E. Functional rafts in cell membranes. *Nature*. (1997) Jun 5; 387(6633):569-72. doi: 10.1038/42408.

26. Mouritsen OG, Zuckermann MJ. What's so special about cholesterol? *Lipids.* (2004) Nov; 39(11):1101-13. doi: 10.1007/s11745-004-1336-x.

27. Naito T, Ercan B, Krshnan L, Triebl A, Koh DHZ, Wei FY, *et al*. Movement of accessible plasma membrane cholesterol by the GRAMD1 lipid transfer protein complex. *Elife*. (2019) Nov 14; 8:e51401. doi: 10.7554/eLife.51401.

28. Ipsen JH, Karlström G, Mouritsen OG, Wennerström H, Zuckermann MJ. Phase equilibria in the phosphatidylcholine-cholesterol system. *Biochim Biophys Acta*. (1987) Nov 27; 905(1):162-72. doi: 10.1016/0005-2736(87)90020-4.

29. Veatch SL, Keller SL. Seeing spots: complex phase behavior in simple membranes. *Biochim Biophys Acta*. (2005) Dec 30; 1746(3):172-85. doi: 10.1016/j.bbamcr.2005.06.010.

30. Elliott R, Katsov K, Schick M, Szleifer I. Phase separation of saturated and mono-unsaturated lipids as determined from a microscopic model. *J Chem Phys*. (2005) Jan 22; 122(4):44904. doi: 10.1063/1.1836753.

31. Ben-Shaul A. Molecular Theory of Chain Packing, Elasticity and Lipid-protein Interaction in Lipid Bilayers. In: Lipowsky R, Sackmann E. (eds) Handbook of Biological Physics, Vol 1. North-Holland: Elsevier Science B.V.; (1995) Jan 1. 359-401 p. doi: 10.1016/S1383-8121(06)80024-2.

32. Blosser MC, Starr JB, Turtle CW, Ashcraft J, Keller SL. Minimal effect of lipid charge on membrane miscibility phase behavior in three ternary systems. *Biophys J*. (2013) Jun 18; 104(12):2629-38. doi: 10.1016/j.bpj.2013.04.055.

33. Davis JH, Clair JJ, Juhasz J. Phase equilibria in DOPC/DPPC-d62/cholesterol mixtures. *Biophys J*. (2009) Jan; 96(2):521-39. doi: 10.1016/j.bpj.2008.09.042.

34. Edidin M. Lipids on the frontier: a century of cell-membrane bilayers. *Nat Rev Mol Cell Biol*. (2003) May; 4(5):414-8. doi: 10.1038/nrm1102.

35. Elliott R, Szleifer I, Schick M. Phase diagram of a ternary mixture of cholesterol and saturated and unsaturated lipids calculated from a microscopic model. *Phys Rev Lett*. (2006) Mar 10; 96(9):098101. doi: 10.1103/PhysRevLett.96.098101.

36. Brown DA, London E. Functions of lipid rafts in biological membranes. *Annu Rev Cell Dev Biol*. (1998); 14:111-36. doi: 10.1146/annurev.cellbio.14.1.111.

37. Nagle JF. Introductory lecture: basic quantities in model biomembranes. *Faraday Discuss*. (2013); 161:11-29; discussion 113-50. doi: 10.1039/c2fd20121f.

38. Ohvo-Rekilä H, Ramstedt B, Leppimäki P, Slotte JP. Cholesterol interactions with phospholipids in membranes. *Prog Lipid Res*. (2002) Jan; 41(1):66-97. doi: 10.1016/s0163-7827(01)00020-0.

39. Pereira CS, Hünenberger PH. Interaction of the sugars trehalose, maltose and glucose with a phospholipid bilayer: a comparative molecular dynamics study. *J Phys Chem B*. (2006) Aug 10; 110(31):15572-81. doi: 10.1021/jp060789l.

40. Schick M. Membrane heterogeneity: manifestation of a curvature-induced microemulsion. *Phys Rev E Stat Nonlin Soft Matter Phys*. (2012) Mar; 85(3 Pt 1):031902. doi: 10.1103/PhysRevE.85.031902.

41. Shlomovitz R, Schick M. Model of a raft in both leaves of an asymmetric lipid bilayer. *Biophys J*. (2013) Sep 17; 105(6):1406-13. doi: 10.1016/j.bpj.2013.06.053.

42. Uline MJ, Longo GS, Schick M, Szleifer I. Calculating partition coefficients of chain anchors in liquid-ordered and liquid-disordered phases. *Biophys J*. (2010) May 19; 98(9):1883-92. doi: 10.1016/j.bpj.2010.01.036.

43. Uline MJ, Schick M, Szleifer I. Phase behavior of lipid bilayers under tension. *Biophys J*. (2012) Feb 8; 102(3):517-22. doi: 10.1016/j.bpj.2011.12.050.

44. Uline MJ, Szleifer I. Mode specific elastic constants for the gel, liquid-ordered, and liquid-disordered phases of DPPC/DOPC/cholesterol model lipid bilayers. *Faraday Discuss*. (2013); 161:177-91; discussion 273-303. doi: 10.1039/c2fd20091k.

45. Veatch SL, Polozov IV, Gawrisch K, Keller SL. Liquid domains in vesicles investigated by NMR and fluorescence microscopy. *Biophys J*. (2004) May; 86(5):2910-22. doi: 10.1016/S0006-3495(04)74342-8.

46. Sackmann E. Biological Membranes. Architecture and Function. In: Lipowsky R, Sackmann E. (eds) Handbook of Biological Physics, Vol 1.

Amsterdam: Elsevier B.V.; (1995). 1–63 p. doi: 10.1016/S1383-8121(06)80018-7.

47. Baumgart T, Hammond AT, Sengupta P, Hess ST, Holowka DA, Baird BA, *et al*. Large-scale fluid/fluid phase separation of proteins and lipids in giant plasma membrane vesicles. *Proc Natl Acad Sci USA*. (2007) Feb 27; 104(9):3165-70. doi: 10.1073/pnas.0611357104.

48. Veatch SL, Keller SL. Separation of liquid phases in giant vesicles of ternary mixtures of phospholipids and cholesterol. *Biophys J*. (2003) Nov; 85(5):3074-83. doi: 10.1016/S0006-3495(03)74726-2.

49. Collins MD. Interleaflet coupling mechanisms in bilayers of lipids and cholesterol. *Biophys J*. (2008) Mar 1; 94(5):L32-4. doi: 10.1529/biophysj.107.124362.

50. Uppamoochikkal P, Tristram-Nagle S, Nagle JF. Orientation of tie-lines in the phase diagram of DOPC/DPPC/cholesterol model biomembranes. *Langmuir.* (2010) Nov 16; 26(22):17363-8. doi: 10.1021/la103024f.

51. Jain MK, White HB 3rd. Long-range order in biomembranes. *Adv Lipid Res*. (1977); 15:1-60. doi: 10.1016/b978-0-12-024915-2.50007-4.

52. Israelachvili JN. Refinement of the fluid-mosaic model of membrane structure. *Biochim Biophys Acta*. (1977) Sep 5; 469(2):221-5. doi: 10.1016/0005-2736(77)90185-7.

53. Sviridov D, Miller YI, Ballout RA, Remaley AT, Bukrinsky M. Targeting lipid rafts-a potential therapy for COVID-19. *Front Immunol*. (2020) Sep 29; 11:574508. doi: 10.3389/fimmu.2020.574508.

54. Veatch SL, Cicuta P, Sengupta P, Honerkamp-Smith A, Holowka D, Baird B. Critical fluctuations in plasma membrane vesicles. *ACS Chem Biol*. (2008) May 16; 3(5):287-93. doi: 10.1021/cb800012x.

55. Veatch SL, Soubias O, Keller SL, Gawrisch K. Critical fluctuations in domain-forming lipid mixtures. *Proc Natl Acad Sci USA*. (2007) Nov 6; 104(45):17650-5. doi: 10.1073/pnas.0703513104.

56. Idema T, van Leeuwen JM, Storm C. Phase coexistence and line tension in ternary lipid systems. *Phys Rev E Stat Nonlin Soft Matter Phys*. (2009) Oct; 80(4 Pt 1):041924. doi: 10.1103/PhysRevE.80.041924.

57. Anderson TG, McConnell HM. Condensed complexes and the calorimetry of cholesterol-phospholipid bilayers. *Biophys J*. (2001) Nov; 81(5):2774-85. doi: 10.1016/S0006-3495(01)75920-6.

58. Marsh D. Elastic curvature constants of lipid monolayers and bilayers. *Chem Phys Lipids*. (2006) Nov-Dec; 144(2):146-59. doi: 10.1016/j.chemphyslip.2006.08.004.

59. Lee WC, Huang H, Feng G, Sanes JR, Brown EN, So PT, *et al*. Dynamic remodeling of dendritic arbors in GABAergic interneurons of adult visual cortex. *PLoS Biol*. (2006) Feb; 4(2):e29. doi: 10.1371/journal.pbio.0040029.

60. Megías M, Molist P, Pombal MA. Animal tissues. *Atlas of Plant and Animal Histology*. (2019). http://mmegias.webs.uvigo.es/index.html [Accessed June 12, 2022].

61. Britannica, The Editors of Encyclopaedia. Red blood cell. *Encyclopedia Britannica*, (2020) May 26. https://www.britannica.com/science/red-blood-cell. [Accessed June 12, 2022].

62. Britannica, The Editors of Encyclopaedia. Smooth muscle. *Encyclopedia Britannica*, (2022) Feb 6. https://www.britannica.com/science/smooth-muscle. [Accessed June 12, 2022].

63. Diez-Silva M, Dao M, Han J, Lim CT, Suresh S. Shape and biomechanical characteristics of human red blood cells in health and disease. *MRS Bull*. (2010) May; 35(5):382-388. doi: 10.1557/mrs2010.571.

64. Sickle cell disease at a glance. *New England Regional Genetics Network, Institute on Disability*. (2020) May. https://www.negenetics.org/gemss/conditions/sickle-cell-disease. [Accessed June19, 2022].

65. Day KJ, Staehelin LA, Glick BS. A three-stage model of Golgi structure and function. *Histochem Cell Biol*. (2013) Sep; 140(3):239-49. doi: 10.1007/s00418-013-1128-3.

66. Terasaki M, Shemesh T, Kasthuri N, Klemm RW, Schalek R, Hayworth KJ, *et al*. Stacked endoplasmic reticulum sheets are connected by helicoidal membrane motifs. *Cell*. (2013) Jul 18; 154(2):285-96. doi: 10.1016/j.cell.2013.06.031.

67. Heald R, Cohen-Fix O. Morphology and function of membrane-bound organelles. *Curr Opin Cell Biol*. (2014) Feb; 26:79-86. doi: 10.1016/j.ceb.2013.10.006.

68. Gomes LC, Di Benedetto G, Scorrano L. During autophagy mitochondria elongate, are spared from degradation and sustain cell viability. *Nat Cell Biol*. (2011) May; 13(5):589-98. doi: 10.1038/ncb2220.

69. Wang T, Ingram C, Weisshaar JC. Model lipid bilayer with facile diffusion of lipids and integral membrane proteins. *Langmuir*. (2010) Jul 6; 26(13):11157-64. doi: 10.1021/la101046r.

70. Almeida PF, Vaz WL, Thompson TE. Lipid diffusion, free area, and molecular dynamics simulations. *Biophys J*. (2005) Jun 1; 88(6):4434-8. doi: 10.1529/biophysj.105.059766.

71. Contreras FX, Sánchez-Magraner L, Alonso A, Goñi FM. Transbilayer (flip-flop) lipid motion and lipid scrambling in membranes. *FEBS Lett*. (2010) May 3; 584(9):1779-86. doi: 10.1016/j.febslet.2009.12.049.

72. Nelson DL, Cox MM. Lehninger Principles of Biochemistry: International Edition. India: WH Freeman & Co Ltd; (2017).

73. Hankins HM, Baldridge RD, Xu P, Graham TR. Role of flippases, scramblases and transfer proteins in phosphatidylserine subcellular distribution. *Traffic*. (2015) Jan; 16(1):35-47. doi: 10.1111/tra.12233.

74. Andersen JP, Vestergaard AL, Mikkelsen SA, Mogensen LS, Chalat M, Molday RS. P4-ATPases as Phospholipid flippases-structure, function, and enigmas. *Front Physiol*. (2016) Jul 8; 7:275. doi: 10.3389/fphys.2016.00275.

75. Bevers EM, Comfurius P, Zwaal RF. Changes in membrane phospholipid distribution during platelet activation. *Biochim Biophys Acta*. (1983) Dec 7; 736(1):57-66. doi: 10.1016/0005-2736(83)90169-4.

76. Lentz BR. Exposure of platelet membrane phosphatidylserine regulates blood coagulation. *Prog Lipid Res*. (2003) Sep; 42(5):423-38. doi: 10.1016/s0163-7827(03)00025-0.

77. Fadok VA, Voelker DR, Campbell PA, Cohen JJ, Bratton DL, Henson PM. Exposure of phosphatidylserine on the surface of apoptotic lymphocytes triggers specific recognition and removal by macrophages. *J Immunol*. (1992) Apr 1; 148(7):2207-16.

78. Bratton DL, Fadok VA, Richter DA, Kailey JM, Guthrie LA, Henson PM. Appearance of phosphatidylserine on apoptotic cells requires calcium-mediated nonspecific flip-flop and is enhanced by loss of the aminophospholipid translocase. *J Biol Chem*. (1997) Oct 17; 272(42):26159-65. doi: 10.1074/jbc.272.42.26159.

79. Schlegel RA, Williamson P. Phosphatidylserine, a death knell. *Cell Death Differ*. (2001) Jun; 8(6):551-63. doi: 10.1038/sj.cdd.4400817.

80. Bruckner RJ, Mansy SS, Ricardo A, Mahadevan L, Szostak JW. Flip-flop-induced relaxation of bending energy: implications for membrane remodeling. *Biophys J*. (2009) Dec 16; 97(12):3113-22. doi: 10.1016/j.bpj.2009.09.025.

81. Steck TL, Ye J, Lange Y. Probing red cell membrane cholesterol movement with cyclodextrin. *Biophys J*. (2002) Oct; 83(4):2118-25. doi: 10.1016/S0006-3495(02)73972-6.

82. Garg S, Porcar L, Woodka AC, Butler PD, Perez-Salas U. Noninvasive neutron scattering measurements reveal slower cholesterol transport in model lipid membranes. *Biophys J*. (2011) Jul 20; 101(2):370-7. doi: 10.1016/j.bpj.2011.06.014.

83. Yu T, Zhou G, Hu X, Ye S. Transport and organization of cholesterol in a planar solid-supported lipid bilayer depend on the phospholipid flip-flop rate. *Langmuir*. (2016) Nov 8; 32(44):11681-11689. doi: 10.1021/acs.langmuir.6b02560.

84. Bennett WF, MacCallum JL, Hinner MJ, Marrink SJ, Tieleman DP. Molecular view of cholesterol flip-flop and chemical potential in different membrane environments. *J Am Chem Soc*. (2009) Sep 9; 131(35):12714-20. doi: 10.1021/ja903529f.

85. Bennett WFD, Tieleman DP. Molecular simulation of rapid translocation of cholesterol, diacylglycerol, and ceramide in model raft and nonraft membranes. *J Lipid Res*. (2012) Mar; 53(3):421-429. doi: 10.1194/jlr.M022491.

86. Parisio G, Sperotto MM, Ferrarini A. Flip-flop of steroids in phospholipid bilayers: effects of the chemical structure on transbilayer diffusion. *J Am Chem Soc*. (2012) Jul 25; 134(29):12198-208. doi: 10.1021/ja304007t.

87. Parisio G, Ferrarini A, Sperotto MM. Model studies of lipid flip-flop in membranes. Int *J Adv Eng Sci Appl Math*. (2016); 8(2):134-146. doi: 10.1007/s12572-015-0155-9.

88. Choubey A, Kalia RK, Malmstadt N, Nakano A, Vashishta P. Cholesterol translocation in a phospholipid membrane. *Biophys J*. (2013) Jun 4; 104(11):2429-36. doi: 10.1016/j.bpj.2013.04.036.

89. Jo S, Rui H, Lim JB, Klauda JB, Im W. Cholesterol flip-flop: insights from free energy simulation studies. *J Phys Chem B*. (2010) Oct 28; 114(42):13342-8. doi: 10.1021/jp108166k.

90. Helfrich W. Elastic properties of lipid bilayers: theory and possible experiments. *Z Naturforsch C*. (1973) Nov-Dec; 28(11):693-703. doi: 10.1515/znc-1973-11-1209.

91. Markin VS, Albanesi JP. Membrane fusion: stalk model revisited. *Biophys J*. (2002) Feb; 82(2):693-712. doi: 10.1016/S0006-3495(02)75432-5.

92. Kozlovsky Y, Kozlov MM. Membrane fission: model for intermediate structures. *Biophys J*. (2003) Jul; 85(1):85-96. doi: 10.1016/S0006-3495(03)74457-9.

93. Reynwar BJ, Illya G, Harmandaris VA, Müller MM, Kremer K, Deserno M. Aggregation and vesiculation of membrane proteins by curvature-

mediated interactions. *Nature*. (2007) May 24; 447(7143):461-4. doi: 10.1038/nature05840.

94. Davies SM, Epand RM, Kraayenhof R, Cornell RB. Regulation of CTP: phosphocholine cytidylyltransferase activity by the physical properties of lipid membranes: an important role for stored curvature strain energy. *Biochemistry*. (2001) Sep 4; 40(35):10522-31. doi: 10.1021/bi010904c.

95. Olusanya TOB, Haj Ahmad RR, Ibegbu DM, Smith JR, Elkordy AA. Liposomal drug delivery systems and anticancer drugs. *Molecules*. (2018) Apr 14; 23(4):907. doi: 10.3390/molecules23040907.

96. Liu Y, Castro Bravo KM, Liu J. Targeted liposomal drug delivery: a nanoscience and biophysical perspective. *Nanoscale Horiz*. (2021) Feb 1; 6(2):78-94. doi: 10.1039/d0nh00605j.

97. Xing H, Tang L, Yang X, Hwang K, Wang W, Yin Q, *et al*. Selective delivery of an anticancer drug with aptamer-functionalized liposomes to breast cancer cells *in vitro* and *in vivo*. *J Mater Chem B*. (2013) Oct 21; 1(39):5288-5297. doi: 10.1039/C3TB20412J.

98. Cao Z, Tong R, Mishra A, Xu W, Wong GC, Cheng J, *et al.* Reversible cell-specific drug delivery with aptamer-functionalized liposomes. *Angew Chem Int Ed Engl*. (2009); 48(35):6494-8. doi: 10.1002/anie.200901452.

99. Gaber BP, Schnur JM, Chapman D. (eds) Biotechnical Applications of Lipid Microstructures, 1st ed. New York, NY: Springer; (1988). doi: 10.1007/978-1-4684-7908-9.

100. Heath GR, Li M, Rong H, Radu V, Frielingsdorf S, Lenz O, *et al*. Multilayered lipid membrane stacks for biocatalysis using membrane enzymes. *Adv Funct Mater*. (2017) May; 27(17):1606265. **doi: 10.1002/adfm.201606265**.

101. Kim YR, Jung S, Ryu H, Yoo YE, Kim SM, Jeon TJ. Synthetic biomimetic membranes and their sensor applications. *Sensors (Basel)*. (2012); 12(7):9530-50. doi: 10.3390/s120709530.

102. Song W, Tu YM, Oh H, Samineni L, Kumar M. Hierarchical optimization of high-performance biomimetic and bioinspired membranes. *Langmuir*. (2019) Jan 22; 35(3):589-607. doi: 10.1021/acs.langmuir.8b03655.

103. Hall DO, Rao KK. Immobilized photosynthetic membranes and cells for the production of fuels and chemicals. *Adv Exp Med Biol*. (1988); 238:225-45. doi: 10.1007/978-1-4684-7908-9_18.

104. Yallapu MM, Katti KS, Katti DR, Mishra SR, Khan S, Jaggi M, *et al*. The roles of cellular nanomechanics in cancer. *Med Res Rev*. (2015) Jan; 35(1):198-223. doi: 10.1002/med.21329.

105. Cannon DM, Pacholski ML, Winograd N, Ewing AG. Molecule specific imaging of freeze-fractured, frozen-hydrated model membrane systems using mass spectrometry. *J Am Chem Soc*. (2000) Feb 2; 122(4):603-10. doi: 10.1021/ja992078p.

106. Suwalsky M, Espinoza MA, Sánchez I, Villena F. X-ray studies on phospholipid bilayers. XI. Interactions with chloramphenicol. *Z Naturforsch C J Biosci*. (1991) Jul-Aug; 46(7-8):647-55. doi: 10.1515/znc-1991-7-823.

107. Suwalsky M, Villena F, Montoya G, Garrido C, Sánchez I, Neira F. X-ray studies on phospholipid bilayers. XII. Interactions of pentachlorophenol with myelin. *Z Naturforsch C J Biosci*. (1992) Jul-Aug; 47(7-8):601-7. doi: 10.1515/znc-1992-7-818.

108. Robertson JD. The molecular structure and contact relationships of cell membranes. *Prog Biophys Mol Biol*. (1960); 10:343-418.

109. Zhong S, Pochan DJ. Cryogenic transmission electron microscopy for direct observation of polymer and small-molecule materials and structures in solution. *Polym Rev*. (2010) Jul 27; 50(3):287-320. doi: 10.1080/15583724.2010.493254.

110. Kunding AH, Mortensen MW, Christensen SM, Stamou D. A fluorescence-based technique to construct size distributions from single-object measurements: application to the extrusion of lipid vesicles. *Biophys J*. (2008) Aug; 95(3):1176-88. doi: 10.1529/biophysj.108.128819.

111. Menger FM, Caran KL, Apkarian RP. In-lens cryo-high-resolution scanning electron microscopy of large vesicles. *Langmuir*. (2000) Jan 11; 16(1):98-101. doi: 10.1021/la9905620.

112. Robson AL, Dastoor PC, Flynn J, Palmer W, Martin A, Smith DW, *et al*. Advantages and limitations of current imaging techniques for characterizing liposome morphology. *Front Pharmacol*. (2018) Feb 6; 9:80. doi: 10.3389/fphar.2018.00080.

113. Liang X, Mao G, Ng KY. Mechanical properties and stability measurement of cholesterol-containing liposome on mica by atomic force microscopy. *J Colloid Interface Sci*. (2004) Oct 1; 278(1):53-62. doi: 10.1016/j.jcis.2004.05.042.

114. Ruozi B, Tosi G, Forni F, Fresta M, Vandelli MA. Atomic force microscopy and photon correlation spectroscopy: two techniques for rapid characterization of liposomes. *Eur J Pharm Sci*. (2005) May; 25(1):81-9. doi: 10.1016/j.ejps.2005.01.020.

115. Ruozi B, Tosi G, Leo E, Vandelli MA. Application of atomic force microscopy to characterize liposomes as drug and gene carriers. *Talanta*. (2007) Aug 15; 73(1):12-22. doi: 10.1016/j.*Talanta*.2007.03.031.

116. Qian S, Sharma VK, Clifton LA. Understanding the structure and dynamics of complex biomembrane interactions by neutron scattering techniques. *Langmuir*. (2020) Dec 22; 36(50):15189-15211. doi: 10.1021/acs.langmuir.0c02516.

117. Léonard A, Escrive C, Laguerre M, Pebay-Peyroula E, Néri W, Pott T, *et al*. Location of cholesterol in DMPC membranes. A comparative study by neutron diffraction and molecular mechanics simulation. *Langmuir*. (2001) Mar 23; 17(6):2019-30. doi: 10.1021/la001382p.

118. Maier O, Oberle V, Hoekstra D. Fluorescent lipid probes: some properties and applications (a review). *Chem Phys Lipids*. (2002) Jun; 116(1-2):3-18. doi: 10.1016/s0009-3084(02)00017-8.

119. Chong PL, Sugár IP. Fluorescence studies of lipid regular distribution in membranes. *Chem Phys Lipids*. (2002) Jun; 116(1-2):153-75. doi: 10.1016/s0009-3084(02)00025-7.

120. Goswami D, Gowrishankar K, Bilgrami S, Ghosh S, Raghupathy R, Chadda R, *et al*. Nanoclusters of GPI-anchored proteins are formed by cortical actin-driven activity. *Cell*. (2008) Dec 12; 135(6):1085-97. doi: 10.1016/j.cell.2008.11.032.

121. Vyas N, Goswami D, Manonmani A, Sharma P, Ranganath HA, VijayRaghavan K, *et al*. Nanoscale organization of hedgehog is essential for long-range signaling. *Cell*. (2008) Jun 27; 133(7):1214-27. doi: 10.1016/j.cell.2008.05.026.

122. Pincet F, Adrien V, Yang R, Delacotte J, Rothman JE, Urbach W, *et al*. FRAP to characterize molecular diffusion and interaction in various membrane environments. *PLoS One*. (2016) Jul 7; 11(7):e0158457. doi: 10.1371/journal.pone.0158457.

123. Ben-Shaul A, Szleifer I, Gelbart WM. Chain organization and thermodynamics in micelles and bilayers. I. Theory. *J Chem Phys*. (1985) Oct 1; 83(7):3597-611. doi: 10.1063/1.449166.

124. Szleifer I, Ben-Shaul A, Gelbart WM. Chain organization and thermodynamics in micelles and bilayers. II. Model calculations. *J Chem Phys*. (1985) Oct 1; 83(7):3612-20. doi: 10.1063/1.449167.

125. Szleifer I, Ben-Shaul A, Gelbart WM. Chain statistics in micelles and bilayers: effects of surface roughness and internal energy. *J Chem Phys*. (1986) Nov 1; 85(9):5345-58. doi: 10.1063/1.451679.

126. Szleifer I, Kramer D, Ben-Shaul A, Gelbart WM, Safran SA. Molecular theory of curvature elasticity in surfactant films. *J Chem Phys*. (1990) Jun 1; 92(11):6800-17. doi: 10.1063/1.458267.

127. Ben-Shaul A, Gelbart WM. Statistical Thermodynamics of Amphiphile Self-assembly: Structure and Phase Transitions in Micellar Solutions. In: Micelles, Membranes, Microemulsions, and Monolayers. New York, NY: Springer; (1994) 1-104 p.

128. Fattal DR, Ben-Shaul A. Lipid chain packing and lipid-protein interaction in membranes. *Physica A*. (1995) Oct 15; 220(1-2):192-216. doi: 10.1016/0378-4371(95)00117-P.

129. Putzel GG, Uline MJ, Szleifer I, Schick M. Interleaflet coupling and domain registry in phase-separated lipid bilayers. *Biophys J*. (2011) Feb 16; 100(4):996-1004. doi: 10.1016/j.bpj.2011.01.021.

130. Longo GS, Schick M, Szleifer I. Stability and liquid-liquid phase separation in mixed saturated lipid bilayers. *Biophys J*. (2009) May 20; 96(10):3977-86. doi: 10.1016/j.bpj.2009.02.043.

131. Grillo D, de la Cruz MO, Szleifer I. Theoretical studies of the phase behavior of DPPC bilayers in the presence of macroions. *Soft Matter.* (2011); 7(10):4672-9. **doi: 10.1039/C1SM05061C**.

132. Ben-Shaul A, Szleifer I, Gelbart WM. Statistical thermodynamics of amphiphile chains in micelles. *Proc Natl Acad Sci USA*. (1984) Jul; 81(14):4601-5. doi: 10.1073/pnas.81.14.4601.

133. Szleifer I, Kramer D, Ben-Shaul A, Roux D, Gelbart WM. Curvature elasticity of pure and mixed surfactant films. *Phys Rev Lett*. (1988) May 9; 60(19):1966-1969. doi: 10.1103/PhysRevLett.60.1966.

134. Szleifer I, Ben-Shaul A, Gelbart WM. Statistical thermodynamics of molecular organization in mixed micelles and bilayers. *J Chem Phys*. (1987) Jun 15; 86(12):7094-109. doi: 10.1063/1.452359.

135. Nap R, Gong P, Szleifer I. Weak polyelectrolytes tethered to surfaces: effect of geometry, acid–base equilibrium and electrical permittivity. *J Polym Sci, Part B: Polym Phys*. (2006) Sep 15; 44(18):2638-62. **doi: 10.1002/polb.20896**.

136. Szleifer I, Carignano MA. Tethered polymer layers. *Adv Chem Phys*. (1996); 94:165-260.

137. Szleifer I. Statistical thermodynamics of polymers near surfaces. *Curr Opin Colloid Interface Sci*. (1996) Jun 1; 1(3):416-23. doi: 10.1016/S1359-0294(96)80142-7.

138. Gong P, Szleifer I. Interactions between charged surfaces and functionalized grafted polymer layers. *Ind Eng Chem Res*. (2006) Aug 2; 45(16):5466-76. doi: 10.1021/ie0510977.

139. Gong P, Genzer J, Szleifer I. Phase behavior and charge regulation of weak polyelectrolyte grafted layers. *Phys Rev Lett*. (2007) Jan 5; 98(1):018302. doi: 10.1103/PhysRevLett.98.018302.

140. Tagliazucchi M, de la Cruz MO, Szleifer I. Self-organization of grafted polyelectrolyte layers via the coupling of chemical equilibrium and physical interactions. *Proc Natl Acad Sci USA*. (2010) Mar 23; 107(12):5300-5. doi: 10.1073/pnas.0913340107.

141. Tagliazucchi M, Azzaroni O, Szleifer I. Responsive polymers end-tethered in solid-state nanochannels: when nanoconfinement really matters. *J Am Chem Soc*. (2010) Sep 8; 132(35):12404-11. doi: 10.1021/ja104152g.

142. Gong P, Wu T, Genzer J, Szleifer I. Behavior of surface-anchored poly (acrylic acid) brushes with grafting density gradients on solid substrates: 2. Theory. *Macromolecules*. (2007) Nov 27; 40(24):8765-73. doi: 10.1021/ma071018y.

143. Pogodin S, Baulin VA. Coarse-grained models of phospholipid membranes within the single chain mean field theory. *Soft Matter*. (2010); 6(10):2216-26. **doi: 10.1039/B927437E**.

144. Pogodin S, Baulin VA. Can a carbon nanotube pierce through a phospholipid bilayer? *ACS Nano*. (2010) Sep 28; 4(9):5293-300. doi: 10.1021/nn1016549.

145. Pogodin S, A Baulin V. Equilibrium insertion of nanoscale objects into phospholipid bilayers. *Curr Nanosci*. (2011) Oct 1; 7(5):721-6. doi: 10.2174/157341311797483871.

146. Brownholland DP, Longo GS, Struts AV, Justice MJ, Szleifer I, Petrache HI, *et al*. Phase separation in binary mixtures of bipolar and monopolar lipid dispersions revealed by 2H NMR spectroscopy, small angle x-ray scattering, and molecular theory. *Biophys J*. (2009) Nov 18; 97(10):2700-9. doi: 10.1016/j.bpj.2009.06.058.

147. Ting CL, Wang ZG. Interactions of a charged nanoparticle with a lipid membrane: implications for gene delivery. *Biophys J*. (2011) Mar 2; 100(5):1288-97. doi: 10.1016/j.bpj.2010.11.042.

148. Flory PJ. Foundations of rotational isomeric state theory and general methods for generating configurational averages. *Macromolecules*. (1974) May; 7(3):381-92. doi: 10.1021/ma60039a022.

149. Israelachvili JN. Intermolecular and Surface Forces. Academic press; (2011) Jul 22. doi: 10.1016/C2009-0-21560-1.

150. Small DM. Lateral chain packing in lipids and membranes. *J Lipid Res*. (1984) Dec 15; 25(13):1490-500. doi: 10.1016/S0022-2275(20)34422-9.

151. Reiss-Husson F, Luzzati V. The structure of the micellar solutions of some amphiphilic compounds in pure water as determined by absolute small-angle X-ray scattering techniques. *J Phys Chem*. (1964) Dec; 68(12):3504-11. doi: 10.1021/j100794a011.

152. Tardieu A, Luzzati V, Reman FC. Structure and polymorphism of the hydrocarbon chains of lipids: a study of lecithin-water phases. *J Mol Biol*. (1973) Apr 25; 75(4):711-33. doi: 10.1016/0022-2836(73)90303-3.

153. Nagle JF, Tristram-Nagle S. Structure of lipid bilayers. *Biochim Biophys Acta*. (2000) Nov 10; 1469(3):159-95. doi: 10.1016/s0304-4157(00)00016-2.

154. Flory PJ, Volkenstein M. Statistical mechanics of chain molecules. *Biopolymers* (1969) 8:699-700. doi: 10.1002/bip.1969.360080514.

155. Maier W, Saupe A. Eine einfache molekular-statistische Theorie der nematischen kristallinflüssigen Phase. Teil l[1]. *Z Naturforsch A*. (1959) Oct 1; 14(10):882-9. doi: 10.1515/zna-1959-1005.

156. Maier W, Saupe A. Eine einfache molekular-statistische Theorie der nematischen kristallinflüssigen Phase. Teil II. *Z Naturforsch A*. (1960) Apr 1; 15(4):287-92. doi: 10.1515/zna-1960-0401.

157. Gruen DW. A statistical mechanical model of the lipid bilayer above its phase transition. *Biochim Biophys Acta*. (1980) Jan 25; 595(2):161-83. doi: 10.1016/0005-2736(80)90081-4.

158. Schmid F. Self-consistent-field theories for complex fluids. *J Phys: Condens Matter*. (1998) Sep 21; 10(37):8105. doi: 10.1088/0953-8984/10/37/002.

159. Marcelja S. Chain ordering in liquid crystals. II. Structure of bilayer membranes. *Biochim Biophys Acta*. (1974) Oct 29; 367(2):165-76. doi: 10.1016/0005-2736(74)90040-6.

160. Gullingsrud J, Schulten K. Lipid bilayer pressure profiles and mechanosensitive channel gating. *Biophys J*. 2004 Jun; 86(6):3496-509. doi: 10.1529/biophysj.103.034322.

161. Sodt AJ, Venable RM, Lyman E, Pastor RW. Nonadditive compositional curvature energetics of lipid bilayers. *Phys Rev Lett*. (2016) Sep 23; 117(13):138104. doi: 10.1103/PhysRevLett.117.138104.

162. Orsi M, Essex JW. Physical properties of mixed bilayers containing lamellar and nonlamellar lipids: insights from coarse-grain molecular dynamics simulations. *Faraday Discuss*. (2013); 161:249-72; discussion 273-303. doi: 10.1039/c2fd20110k.

163. Rowlinson JS, Widom B. Molecular Theory of Capillarity. New York: Dover Publications; (1982).

164. Larsen JB, Jensen MB, Bhatia VK, Pedersen SL, Bjørnholm T, Iversen L, *et al*. Membrane curvature enables N-Ras lipid anchor sorting to liquid-ordered membrane phases. *Nat Chem Biol*. (2015) Mar; 11(3):192-4. doi: 10.1038/nchembio.1733.

165. Carrillo-Tripp M, Feller SE. Evidence for a mechanism by which omega-3 polyunsaturated lipids may affect membrane protein function. *Biochemistry*. (2005) Aug 2; 44(30):10164-9. doi: 10.1021/bi050822e.

166. Sonne J, Hansen FY, Peters GH. Methodological problems in pressure profile calculations for lipid bilayers. *J Chem Phys*. (2005) Mar 22; 122(12):124903. doi: 10.1063/1.1862624.

167. Lindahl E, Edholm O. Spatial and energetic-entropic decomposition of surface tension in lipid bilayers from molecular dynamics simulations. *J Chem Phys*. (2000) Sep 1; 113(9):3882-93. doi: 10.1063/1.1287423.

168. Patra M. Lateral pressure profiles in cholesterol-DPPC bilayers. *Eur Biophys J*. (2005) Dec; 35(1):79-88. doi: 10.1007/s00249-005-0011-0.

169. Cantor RS. Lipid composition and the lateral pressure profile in bilayers. *Biophys J*. (1999) May; 76(5):2625-39. doi: 10.1016/S0006-3495(99)77415-1.

170. Harries D, Ben-Shaul A. Conformational chain statistics in a model lipid bilayer: comparison between mean field and Monte Carlo calculations. *J Chem Phys*. (1997) Jan 22; 106(4):1609-19. doi: 10.1063/1.473283.

171. Xiang TX, Anderson BD. Molecular distributions in interphases: statistical mechanical theory combined with molecular dynamics simulation of a model lipid bilayer. *Biophys J*. (1994) Mar; 66(3 Pt 1):561-72. doi: 10.1016/s0006-3495(94)80833-1.

172. Goetz R, Lipowsky R. Computer simulations of bilayer membranes: self-assembly and interfacial tension. *J Chem Phys*. (1998) May 1; 108(17):7397-409. doi: 10.1063/1.476160.

173. Venturoli M, Smit B. Simulating the self-assembly of model membranes. *PhysChemComm*. (1999); 2(10):45-9. doi: 10.1039/A906472I.

174. van den Brink-van der Laan E, Killian JA, de Kruijff B. Nonbilayer lipids affect peripheral and integral membrane proteins via changes in the lateral pressure profile. *Biochim Biophys Acta*. (2004) Nov 3; 1666(1-2):275-88. doi: 10.1016/j.bbamem.2004.06.010.

175. Szleifer I. (1988) Statistical Thermodynamics of amphiphilic aggregates. [Doctoral Dissertation]. [Jerusalem, Israel]: Hebrew University of Jerusalem.

176. Hu M, Briguglio JJ, Deserno M. Determining the Gaussian curvature modulus of lipid membranes in simulations. *Biophys J*. (2012) Mar 21; 102(6):1403-10. doi: 10.1016/j.bpj.2012.02.013.

177. Larsen JB, Kennard C, Pedersen SL, Jensen KJ, Uline MJ, Hatzakis NS, *et al*. Membrane Curvature and lipid composition synergize to regulate N-Ras anchor recruitment. *Biophys J*. (2017) Sep 19; 113(6):1269-1279. doi: 10.1016/j.bpj.2017.06.051.

178. Pan J, Tristram-Nagle S, Kucerka N, Nagle JF. Temperature dependence of structure, bending rigidity, and bilayer interactions of dioleoylphosphatidylcholine bilayers. *Biophys J*. (2008) Jan 1; 94(1):117-24. doi: 10.1529/biophysj.107.115691.

179. Gracia RS, Bezlyepkina N, Knorr RL, Lipowsky R, Dimova R. Effect of cholesterol on the rigidity of saturated and unsaturated membranes: fluctuation and electrodeformation analysis of giant vesicles. *Soft Matter.* (2010); 6(7):1472-82. **doi: 10.1039/B920629A**.

180. Arriaga LR, López-Montero I, Monroy F, Orts-Gil G, Farago B, Hellweg T. Stiffening effect of cholesterol on disordered lipid phases: a combined neutron spin echo + dynamic light scattering analysis of the bending elasticity of large unilamellar vesicles. *Biophys J*. (2009) May 6; 96(9):3629-37. doi: 10.1016/j.bpj.2009.01.045.

181. Kucerka N, Liu Y, Chu N, Petrache HI, Tristram-Nagle S, Nagle JF. Structure of fully hydrated fluid phase DMPC and DLPC lipid bilayers using X-ray scattering from oriented multilamellar arrays and from unilamellar vesicles. *Biophys J*. (2005) Apr; 88(4):2626-37. doi: 10.1529/biophysj.104.056606.

182. Kucerka N, Tristram-Nagle S, Nagle JF. Structure of fully hydrated fluid phase lipid bilayers with monounsaturated chains. *J Membr Biol*. (2005) Dec; 208(3):193-202. doi: 10.1007/s00232-005-7006-8.

183. Chu N, Kucerka N, Liu Y, Tristram-Nagle S, Nagle JF. Anomalous swelling of lipid bilayer stacks is caused by softening of the bending modulus. *Phys Rev E Stat Nonlin Soft Matter Phys*. (2005) Apr; 71(4 Pt 1):041904. doi: 10.1103/PhysRevE.71.041904.

184. Pabst G, Katsaras J, Raghunathan VA, Rappolt M. Structure and interactions in the anomalous swelling regime of phospholipid bilayers. *Langmuir*. (2003) Mar 4; 19(5):1716-22. doi: 10.1021/la026052e.

185. Rheinstädter MC, Häussler W, Salditt T. Dispersion relation of lipid membrane shape fluctuations by neutron spin-echo spectrometry. *Phys Rev Lett*. (2006) Jul 28; 97(4):048103. doi: 10.1103/PhysRevLett.97.048103.

186. Nagle JF. Experimentally determined tilt and bending moduli of single-component lipid bilayers. *Chem Phys Lipids*. (2017) Jun; 205:18-24. doi: 10.1016/j.chemphyslip.2017.04.006.

187. Petrache HI, Gouliaev N, Tristram-Nagle S, Zhang R, Suter RM, Nagle JF. Interbilayer interactions from high-resolution x-ray scattering. *Phys Rev E*. (1998) Jun 1; 57(6):7014. doi: 10.1103/PhysRevE.57.7014.

188. Rawicz W, Olbrich KC, McIntosh T, Needham D, Evans E. Effect of chain length and unsaturation on elasticity of lipid bilayers. *Biophys J*. (2000) Jul; 79(1):328-39. doi: 10.1016/S0006-3495(00)76295-3.

189. Petrache HI, Tristram-Nagle S, Harries D, Kucerka N, Nagle JF, Parsegian VA. Swelling of phospholipids by monovalent salt. *J Lipid Res*. (2006) Feb; 47(2):302-9. doi: 10.1194/jlr.M500401-JLR200.

190. Henriksen JR, Ipsen JH. Measurement of membrane elasticity by micro-pipette aspiration. Eur Phys J E *Soft Matter.* (2004) Jun; 14(2):149-67. doi: 10.1140/epje/i2003-10146-y.

191. Tian A, Capraro BR, Esposito C, Baumgart T. Bending stiffness depends on curvature of ternary lipid mixture tubular membranes. *Biophys J*. (2009) Sep 16; 97(6):1636-46. doi: 10.1016/j.bpj.2009.07.012.

192. Brochard F, Lennon JF. Frequency spectrum of the flicker phenomenon in erythrocytes. *J Phys*. (1975) Nov 1; 36(11):1035-47. doi: 10.1051/jphys:0197500360110103500.

193. Bouvrais H. Bending Rigidities of Lipid Bilayers: Their Determination and Main Inputs in Biophysical Studies. In: Advances in Planar Lipid Bilayers and Liposomes, Vol 15. Academic Press; (2012) Jan 1. 1-75 p. doi: 10.1016/B978-0-12-396533-2.00006-9.

194. Dimova R. Recent developments in the field of bending rigidity measurements on membranes. *Adv Colloid Interface Sci*. 2014 Jun;208:225-34. doi: 10.1016/j.cis.2014.03.003.

195. Bouvrais H, Duelund L, Ipsen JH. Buffers affect the bending rigidity of model lipid membranes. *Langmuir*. (2014) Jan 14; 30(1):13-6. doi: 10.1021/la403565f.

196. Nagle JF, Jablin MS, Tristram-Nagle S, Akabori K. What are the true values of the bending modulus of simple lipid bilayers? *Chem Phys Lipids*. (2015) Jan; 185:3-10. doi: 10.1016/j.chemphyslip.2014.04.003.

197. Vitkova V, Genova J, Mitov MD, Bivas I. Sugars in the aqueous phase change the mechanical properties of lipid mono-and bilayers. *Mol Cryst Liq Cryst*. (2006) Jul 1; 449(1):95-106. doi: 10.1080/15421400600582515.

198. Genova J, Zheliaskova A, Mitov MD. The influence of sucrose on the elasticity of SOPC lipid membrane studied by the analysis of thermally induced shape fluctuations. *Colloids Surf, A*. (2006) Jul 20; 282:420-2. doi: 10.1016/j.colsurfa.2005.11.065.

199. Genova J, Zheliaskova A, Mitov MD. Monosaccharides (fructose, glucose) and disaccharides (sucrose, trehalose) influence the elasticity of SOPC membranes. *J Optoelectron Adv Mater*. (2007) Feb 1; 9(2):427-30.

200. Shchelokovskyy P, Tristram-Nagle S, Dimova R. Effect of the HIV-1 fusion peptide on the mechanical properties and leaflet coupling of lipid bilayers. *New J Phys*. (2011) Feb; 13:25004. doi: 10.1088/1367-2630/13/2/025004.

201. Nagle JF, Jablin MS, Tristram-Nagle S. Sugar does not affect the bending and tilt moduli of simple lipid bilayers. *Chem Phys Lipids*. (2016) Mar; 196:76-80. doi: 10.1016/j.chemphyslip.2016.01.003.

202. Jablin MS, Akabori K, Nagle JF. Experimental support for tilt-dependent theory of biomembrane mechanics. *Phys Rev Lett*. (2014) Dec 12; 113(24):248102. doi: 10.1103/PhysRevLett.113.248102.

203. Liu Y, Nagle JF. Diffuse scattering provides material parameters and electron density profiles of biomembranes. *Phys Rev E Stat Nonlin Soft Matter Phys*. (2004) Apr; 69(4 Pt 1):040901. doi: 10.1103/PhysRevE.69.040901.

204. Jablin MS. (2015) Tilt-dependent analysis of diffuse X-ray scattering from oriented stacks of fluid phase lipid bilayers [Doctoral dissertation]. [Pittsburgh, PA]: Carnegie Mellon University.

205. Li DP, Hu SX, Li M. Full q-space analysis of x-ray scattering of multilamellar membranes at liquid-solid interfaces. *Phys Rev E Stat Nonlin Soft Matter Phys*. (2006) Mar; 73(3 Pt 1):031916. doi: 10.1103/PhysRevE.73.031916.

206. Lyatskaya Y, Liu Y, Tristram-Nagle S, Katsaras J, Nagle JF. Method for obtaining structure and interactions from oriented lipid bilayers. *Phys Rev E Stat Nonlin Soft Matter Phys*. (2001) Jan; 63(1 Pt 1):011907. doi: 10.1103/PhysRevE.63.011907.

207. Bouvrais H, Pott T, Bagatolli LA, Ipsen JH, Méléard P. Impact of membrane-anchored fluorescent probes on the mechanical properties of lipid bilayers. *Biochim Biophys Acta*. (2010) Jul; 1798(7):1333-7. doi: 10.1016/j.bbamem.2010.03.026.

208. Pakkanen KI, Duelund L, Qvortrup K, Pedersen JS, Ipsen JH. Mechanics and dynamics of triglyceride-phospholipid model membranes: Implications for cellular properties and function. *Biochim Biophys Acta*. (2011) Aug; 1808(8):1947-56. doi: 10.1016/j.bbamem.2011.04.006.

209. Henriksen J, Rowat AC, Ipsen JH. Vesicle fluctuation analysis of the effects of sterols on membrane bending rigidity. *Eur Biophys J*. (2004) Dec; 33(8):732-41. doi: 10.1007/s00249-004-0420-5.

210. Bouvrais H, Méléard P, Pott T, Jensen KJ, Brask J, Ipsen JH. Softening of POPC membranes by magainin. *Biophys Chem*. (2008) Sep; 137(1):7-12. doi: 10.1016/j.bpc.2008.06.004.

211. Salditt T, Vogel M, Fenzl W. Thermal fluctuations and positional correlations in oriented lipid membranes. *Phys Rev Lett*. (2003) May 2; 90(17):178101. doi: 10.1103/PhysRevLett.90.178101.

212. Méléard P, Gerbeaud C, Pott T, Fernandez-Puente L, Bivas I, Mitov MD, *et al*. Bending elasticities of model membranes: influences of temperature and sterol content. *Biophys J*. (1997) Jun; 72(6):2616-29. doi: 10.1016/S0006-3495(97)78905-7.

213. Duwe HP, Kaes J, Sackmann E. Bending elastic moduli of lipid bilayers: modulation by solutes. *J Phys*. (1990) May 1; 51(10):945-61. doi: 10.1051/jphys:019900051010094500.

214. Vitkova V, Méléard P, Pott T, Bivas I. Alamethicin influence on the membrane bending elasticity. *Eur Biophys J*. (2006) Feb; 35(3):281-6. doi: 10.1007/s00249-005-0019-5.

215. Fernandez-Puente L, Bivas I, Mitov MD, Méléard P. Temperature and chain length effects on bending elasticity of phosphatidylcholine bilayers. *EPL (Europhys Lett)*. (1994) Oct 20; 28(3):181.

216. Storck EM, Serwa RA, Tate EW. Chemical proteomics: a powerful tool for exploring protein lipidation. *Biochem Soc Trans*. (2013) Feb 1; 41(1):56-61. doi: 10.1042/BST20120283.

217. Synthesis of glycosylphosphatidylinositols (GPIs). *Max Planck Institute of Colloids and Interfaces*. (2022). https://www.mpikg.mpg.de/189227/GPIs [Accessed June 21, 2022].

218. Resh MD. Regulation of cellular signalling by fatty acid acylation and prenylation of signal transduction proteins. *Cell Signal*. (1996) Sep; 8(6):403-12. doi: 10.1016/s0898-6568(96)00088-5.

219. Resh MD. Trafficking and signaling by fatty-acylated and prenylated proteins. *Nat Chem Biol*. (2006) Nov; 2(11):584-90. doi: 10.1038/nchembio834.

220. Resh MD. Covalent lipid modifications of proteins. *Curr Biol*. (2013) May 20; 23(10):R431-5. doi: 10.1016/j.cub.2013.04.024.

221. Hanna CC, Kriegesmann J, Dowman LJ, Becker CFW, Payne RJ. Chemical synthesis and semisynthesis of lipidated proteins. *Angew Chem Int Ed Engl*. (2022) Apr 4; 61(15):e202111266. doi: 10.1002/anie.202111266.

222. Cox AD, Der CJ. Ras history: The saga continues. *Small GTPases*. (2010) Jul; 1(1):2-27. doi: 10.4161/sgtp.1.1.12178.

223. Hobbs GA, Der CJ, Rossman KL. RAS isoforms and mutations in cancer at a glance. *J Cell Sci*. (2016) Apr 1; 129(7):1287-92. doi: 10.1242/jcs.182873.

224. Santos E, Tronick SR, Aaronson SA, Pulciani S, Barbacid M. T24 human bladder carcinoma oncogene is an activated form of the normal human homologue of BALB- and Harvey-MSV transforming genes. *Nature*. (1982) Jul 22; 298(5872):343-7. doi: 10.1038/298343a0.

225. Der CJ, Krontiris TG, Cooper GM. Transforming genes of human bladder and lung carcinoma cell lines are homologous to the Ras genes of Harvey and Kirsten sarcoma viruses. *Proc Natl Acad Sci USA*. (1982) Jun; 79(11):3637-40. doi: 10.1073/pnas.79.11.3637.

226. Parada LF, Tabin CJ, Shih C, Weinberg RA. Human EJ bladder carcinoma oncogene is homologue of Harvey sarcoma virus Ras gene. *Nature*. (1982) Jun 10; 297(5866):474-8. doi: 10.1038/297474a0.

227. Taparowsky E, Suard Y, Fasano O, Shimizu K, Goldfarb M, Wigler M. Activation of the T24 bladder carcinoma transforming gene is linked to a single amino acid change. *Nature.* (1982) Dec 23; 300(5894):762-5. doi: 10.1038/300762a0.

228. Reddy EP, Reynolds RK, Santos E, Barbacid M. A point mutation is responsible for the acquisition of transforming properties by the T24 human bladder carcinoma oncogene. *Nature*. (1982) Nov 11; 300(5888):149-52. doi: 10.1038/300149a0.

229. Tabin CJ, Bradley SM, Bargmann CI, Weinberg RA, Papageorge AG, Scolnick EM, *et al*. Mechanism of activation of a human oncogene. *Nature.* (1982) Nov 11; 300(5888):143-9. doi: 10.1038/300143a0.

230. Rauen KA. The RASopathies. *Annu Rev Genomics Hum Genet*. (2013); 14:355-69. doi: 10.1146/annurev-genom-091212-153523.

231. Mejuch T, Waldmann H. Synthesis of lipidated proteins. *Bioconjug Chem*. (2016) Aug 17; 27(8):1771-83. doi: 10.1021/acs.bioconjchem.6b00261.

232. Smit VT, Boot AJ, Smits AM, Fleuren GJ, Cornelisse CJ, Bos JL. KRAS codon 12 mutations occur very frequently in pancreatic adenocarcinomas.

Nucleic Acids Res. (1988) Aug 25; 16(16):7773-82. doi: 10.1093/nar/16.16.7773.

233. Almoguera C, Shibata D, Forrester K, Martin J, Arnheim N, Perucho M. Most human carcinomas of the exocrine pancreas contain mutant c-K-Ras genes. *Cell*. (1988) May 20; 53(4):549-54. doi: 10.1016/0092-8674(88)90571-5.

234. Bos JL, Fearon ER, Hamilton SR, Verlaan-de Vries M, van Boom JH, van der Eb AJ, *et al*. Prevalence of Ras gene mutations in human colorectal cancers. *Nature*. (1987) May 28-Jun 3; 327(6120):293-7. doi: 10.1038/327293a0.

235. Forrester K, Almoguera C, Han K, Grizzle WE, Perucho M. Detection of high incidence of K-Ras oncogenes during human colon tumorigenesis. *Nature*. (1987) May 28-Jun 3; 327(6120):298-303. doi: 10.1038/327298a0.

236. Rodenhuis S, van de Wetering ML, Mooi WJ, Evers SG, van Zandwijk N, Bos JL. Mutational activation of the K-Ras oncogene. A possible pathogenetic factor in adenocarcinoma of the lung. *N Engl J Med*. (1987) Oct 8; 317(15):929-35. doi: 10.1056/NEJM198710083171504.

237. Siegel RL, Miller KD, Fuchs HE, Jemal A. Cancer statistics. *CA Cancer J Clin*. (2021) Jan; 71(1):7-33. doi: 10.3322/caac.21654.

238. Castellano E, Santos E. Functional specificity of Ras isoforms: so similar but so different. *Genes Cancer*. (2011) Mar ;2(3):216-31. doi: 10.1177/1947601911408081.

239. Harvey JJ. An unidentified virus which causes the rapid production of tumours in mice. *Nature*. (1964) Dec 12; 204:1104-5. doi: 10.1038/2041104b0.

240. Kirsten WH, Mayer LA. Morphologic responses to a murine erythroblastosis virus. *J Natl Cancer Inst*. (1967) Aug; 39(2):311-35. doi: 10.1093/jnci/39.2.311.

241. Marshall CJ, Hall A, Weiss RA. A transforming gene present in human sarcoma cell lines. *Nature*. (1982) Sep 9; 299(5879):171-3. doi: 10.1038/299171a0.

242. Hall A, Marshall CJ, Spurr NK, Weiss RA. Identification of transforming gene in two human sarcoma cell lines as a new member of the Ras gene family located on chromosome 1. *Nature*. (1983) Jun 2-8; 303(5916):396-400. doi: 10.1038/303396a0.

243. Shimizu K, Goldfarb M, Suard Y, Perucho M, Li Y, Kamata T, *et al*. Three human transforming genes are related to the viral Ras oncogenes. *Proc Natl Acad Sci USA*. (1983) Apr; 80(8):2112-6. doi: 10.1073/pnas.80.8.2112.

244. Lal R, Harris D, Postel-Vinay S, de Bono J. Reovirus: Rationale and clinical trial update. *Curr Opin Mol Ther*. (2009) Oct; 11(5):532-9.

245. Fu X, Tao L, Cai R, Prigge J, Zhang X. A mutant type 2 herpes simplex virus deleted for the protein kinase domain of the ICP10 gene is a potent oncolytic virus. *Mol Ther*. (2006) May; 13(5):882-90. doi: 10.1016/j.ymthe.2006.02.007.

246. Thirukkumaran C, Morris DG. Oncolytic Viral therapy using Reovirus. *Methods Mol Biol*. (2015); 1317:187-223. doi: 10.1007/978-1-4939-2727-2_12.

247. Bunda S, Burrell K, Heir P, Zeng L, Alamsahebpour A, Kano Y, *et al.* Inhibition of SHP2-mediated dephosphorylation of Ras suppresses oncogenesis. *Nat Commun*. (2015) Nov 30; 6:8859. doi: 10.1038/ncomms9859.

248. Astorgues-Xerri L, Riveiro ME, Tijeras-Raballand A, Serova M, Neuzillet C, Albert S, *et al*. Unraveling galectin-1 as a novel therapeutic target for cancer. *Cancer Treat Rev*. (2014) Mar; 40(2):307-19. doi: 10.1016/j.ctrv.2013.07.007.

249. Nussinov R, Tsai CJ, Jang H. Oncogenic Ras isoforms signaling specificity at the membrane. *Cancer Res*. (2018) Feb 1; 78(3):593-602. doi: 10.1158/0008-5472.CAN-17-2727.

250. Haigis KM, Kendall KR, Wang Y, Cheung A, Haigis MC, Glickman JN, *et al*. Differential effects of oncogenic K-Ras and N-Ras on proliferation, differentiation and tumor progression in the colon. *Nat Genet*. (2008) May; 40(5):600-8. doi: 10.1038/ng.115.

251. Rocks O, Peyker A, Kahms M, Verveer PJ, Koerner C, Lumbierres M, *et al*. An acylation cycle regulates localization and activity of palmitoylated Ras isoforms. *Science*. (2005) Mar 18; 307(5716):1746-52. doi: 10.1126/science.1105654.

252. Simanshu DK, Nissley DV, McCormick F. RAS proteins and their regulators in human disease. *Cell*. (2017) Jun 29; 170(1):17-33. doi: 10.1016/j.cell.2017.06.009.

253. Erwin N, Sperlich B, Garivet G, Waldmann H, Weise K, Winter R. Lipoprotein insertion into membranes of various complexity: lipid sorting, interfacial adsorption and protein clustering. *Phys Chem Chem Phys*. (2016) Apr 7; 18(13):8954-62. doi: 10.1039/c6cp00563b.

254. Wittinghofer A, Waldmann H. Ras-A molecular switch involved in tumor formation. *Angew Chem Int Ed Engl*. (2000) Dec 1; 39(23):4192-4214. doi: 10.1002/1521-3773(20001201)39:23<4192::AID-ANIE4192>3.0.CO;2-Y.

255. Gelb MH, Brunsveld L, Hrycyna CA, Michaelis S, Tamanoi F, Van Voorhis WC, *et al*. Therapeutic intervention based on protein prenylation and associated modifications. *Nat Chem Biol*. (2006) Oct; 2(10):518-28. doi: 10.1038/nchembio818.

256. Cho KJ, van der Hoeven D, Zhou Y, Maekawa M, Ma X, Chen W, *et al*. Inhibition of acid sphingomyelinase depletes cellular phosphatidylserine and mislocalizes K-Ras from the plasma membrane. *Mol Cell Biol*. (2015) Nov 16; 36(2):363-74. doi: 10.1128/MCB.00719-15.

257. van der Hoeven D, Cho KJ, Ma X, Chigurupati S, Parton RG, Hancock JF. Fendiline inhibits K-Ras plasma membrane localization and blocks K-Ras signal transmission. *Mol Cell Biol*. (2013) Jan; 33(2):237-51. doi: 10.1128/MCB.00884-12.

258. Kattan WE, Hancock JF. RAS Function in cancer cells: translating membrane biology and biochemistry into new therapeutics. *Biochem J*. (2020) Aug 14; 477(15):2893-2919. doi: 10.1042/BCJ20190839.

259. Hancock JF. Ras proteins: different signals from different locations. *Nat Rev Mol Cell Biol*. (2003) May; 4(5):373-84. doi: 10.1038/nrm1105.

260. Hancock JF, Parton RG. Ras plasma membrane signalling platforms. *Biochem J*. (2005) Jul 1; 389(Pt 1):1-11. doi: 10.1042/BJ20050231.

261. Hatzakis NS, Bhatia VK, Larsen J, Madsen KL, Bolinger PY, Kunding AH, *et al*. How curved membranes recruit amphipathic helices and protein anchoring motifs. *Nat Chem Biol*. (2009) Nov; 5(11):835-41. doi: 10.1038/nchembio.213.

262. McMahon HT, Gallop JL. Membrane curvature and mechanisms of dynamic cell membrane remodelling. *Nature*. (2005) Dec 1; 438(7068):590-6. doi: 10.1038/nature04396.

263. Lemmon MA. Membrane recognition by phospholipid-binding domains. *Nat Rev Mol Cell Biol*. (2008) Feb; 9(2):99-111. doi: 10.1038/nrm2328.

264. Yeung T, Gilbert GE, Shi J, Silvius J, Kapus A, Grinstein S. Membrane phosphatidylserine regulates surface charge and protein localization. *Science*. (2008) Jan 11; 319(5860):210-3. doi: 10.1126/science.1152066.

265. McLaughlin S, Murray D. Plasma membrane phosphoinositide organization by protein electrostatics. *Nature*. (2005) Dec 1; 438(7068):605-11. doi: 10.1038/nature04398.

266. Linder ME, Deschenes RJ. Palmitoylation: policing protein stability and traffic. *Nat Rev Mol Cell Biol*. (2007) Jan; 8(1):74-84. doi: 10.1038/nrm2084.

267. Manneville JB, Casella JF, Ambroggio E, Gounon P, Bertherat J, Bassereau P, *et al*. COPI coat assembly occurs on liquid-disordered domains and the associated membrane deformations are limited by membrane tension. *Proc Natl Acad Sci USA*. (2008) Nov 4; 105(44):16946-51. doi: 10.1073/pnas.0807102105.

268. Widom B. Potential-distribution theory and the statistical mechanics of fluids. *J Phys Chem*. (1982) Mar; 86(6):869-72. doi: 10.1021/j100395a005.

269. Bhatia VK, Madsen KL, Bolinger PY, Kunding A, Hedegård P, Gether U, *et al*. Amphipathic motifs in BAR domains are essential for membrane curvature sensing. *EMBO J*. (2009) Nov 4; 28(21):3303-14. doi: 10.1038/emboj.2009.261.

270. Verkade P, Simons K. Robert Feulgen Lecture 1997. Lipid microdomains and membrane trafficking in mammalian cells. *Histochem Cell Biol*. (1997) Sep; 108(3):211-20. doi: 10.1007/s004180050161.

271. Mukherjee S, Maxfield FR. Role of membrane organization and membrane domains in endocytic lipid trafficking. Traffic. (2000) Mar; 1(3):203-11. doi: 10.1034/j.1600-0854.2000.010302.x.

272. Prior IA, Harding A, Yan J, Sluimer J, Parton RG, Hancock JF. GTP-dependent segregation of H-Ras from lipid rafts is required for biological activity. *Nat Cell Biol*. (2001) Apr; 3(4):368-75. doi: 10.1038/35070050.

273. Prior IA, Hancock JF. Compartmentalization of Ras proteins. *J Cell Sci*. (2001) May; 114(Pt 9):1603-8. doi: 10.1242/jcs.114.9.1603.

274. Bankaitis VA, Morris AJ. Lipids and the exocytotic machinery of eukaryotic cells. *Curr Opin Cell Biol*. (2003) Aug; 15(4):389-95. doi: 10.1016/s0955-0674(03)00076-0.

275. van Meer G, Sprong H. Membrane lipids and vesicular traffic. *Curr Opin Cell Biol*. (2004) Aug; 16(4):373-8. doi: 10.1016/j.ceb.2004.06.004.

276. Plowman SJ, Hancock JF. Ras signaling from plasma membrane and endomembrane microdomains. *Biochim Biophys Acta*. (2005) Dec 30; 1746(3):274-83. doi: 10.1016/j.bbamcr.2005.06.004.

277. Simons K, Gerl MJ. Revitalizing membrane rafts: new tools and insights. *Nat Rev Mol Cell Biol*. (2010) Oct; 11(10):688-99. doi: 10.1038/nrm2977.

278. Janosi L, Li Z, Hancock JF, Gorfe AA. Organization, dynamics, and segregation of Ras nanoclusters in membrane domains. *Proc Natl Acad Sci USA*. (2012) May 22; 109(21):8097-102. doi: 10.1073/pnas.1200773109.

279. Campelo F, Kozlov MM. Sensing membrane stresses by protein insertions. *PLoS Comput Biol*. (2014) Apr 10; 10(4):e1003556. doi: 10.1371/journal.pcbi.1003556.

280. Antonny B, Huber I, Paris S, Chabre M, Cassel D. Activation of ADP-ribosylation factor 1 GTPase-activating protein by phosphatidylcholine-

derived diacylglycerols. *J Biol Chem*. (1997) Dec 5; 272(49):30848-51. doi: 10.1074/jbc.272.49.30848.

281. Pinot M, Vanni S, Pagnotta S, Lacas-Gervais S, Payet LA, Ferreira T, *et al*. Lipid cell biology. Polyunsaturated phospholipids facilitate membrane deformation and fission by endocytic proteins. *Science*. (2014) Aug 8; 345(6197):693-7. doi: 10.1126/science.1255288.

282. Bigay J, Gounon P, Robineau S, Antonny B. Lipid packing sensed by ArfGAP1 couples COPI coat disassembly to membrane bilayer curvature. *Nature*. (2003) Dec 4; 426(6966):563-6. doi: 10.1038/nature02108.

283. Vanni S, Hirose H, Barelli H, Antonny B, Gautier R. A sub-nanometre view of how membrane curvature and composition modulate lipid packing and protein recruitment. *Nat Commun*. (2014) Sep 15; 5:4916. doi: 10.1038/ncomms5916.

284. Kučerka N, Nieh MP, Katsaras J. Fluid phase lipid areas and bilayer thicknesses of commonly used phosphatidylcholines as a function of temperature. *Biochim Biophys Acta*. (2011) Nov; 1808(11):2761-71. doi: 10.1016/j.bbamem.2011.07.022.

285. Elvas F, Stroobants S, Wyffels L. Phosphatidylethanolamine targeting for cell death imaging in early treatment response evaluation and disease diagnosis. *Apoptosis*. (2017) Aug; 22(8):971-987. doi: 10.1007/s10495-017-1384-0.

286. Apolloni A, Prior IA, Lindsay M, Parton RG, Hancock JF. H-Ras but not K-Ras traffics to the plasma membrane through the exocytic pathway. *Mol Cell Biol*. (2000) Apr; 20(7):2475-87. doi: 10.1128/MCB.20.7.2475-2487.2000.

287. van Meer G, de Kroon AI. Lipid map of the mammalian cell. *J Cell Sci*. (2011) Jan 1; 124(Pt 1):5-8. doi: 10.1242/jcs.071233.

288. Tokarev AA, Alfonso A, Segev N. Overview of Intracellular Compartments and Trafficking Pathways. In: Trafficking Inside Cells. Molecular Biology Intelligence Unit. New York, NY: Springer; (2009) 3-14 p. doi: 10.1007/978-0-387-93877-6_1.

289. Brandizzi F, Barlowe C. Organization of the ER-Golgi interface for membrane traffic control. *Nat Rev Mol Cell Biol*. (2013) Jun; 14(6):382-92. doi: 10.1038/nrm3588.

290. Fadeel B, Xue D. The ins and outs of phospholipid asymmetry in the plasma membrane: roles in health and disease. *Crit Rev Biochem Mol Biol*. (2009) Sep-Oct; 44(5):264-77. doi: 10.1080/10409230903193307.

291. Prior IA, Hancock JF. Ras trafficking, localization and compartmentalized signalling. Semin Cell Dev Biol. (2012) Apr; 23(2):145-53. doi: 10.1016/j.semcdb.2011.09.002.

292. Mitra K, Ubarretxena-Belandia I, Taguchi T, Warren G, Engelman DM. Modulation of the bilayer thickness of exocytic pathway membranes by membrane proteins rather than cholesterol. *Proc Natl Acad Sci USA*. (2004) Mar 23; 101(12):4083-8. doi: 10.1073/pnas.0307332101.

293. Andersen OS, Koeppe RE 2nd. Bilayer thickness and membrane protein function: an energetic perspective. *Annu Rev Biophys Biomol Struct*. (2007); 36:107-30. doi: 10.1146/annurev.biophys.36.040306.132643.

294. Bigay J, Casella JF, Drin G, Mesmin B, Antonny B. ArfGAP1 responds to membrane curvature through the folding of a lipid packing sensor motif. *EMBO J*. (2005) Jul 6; 24(13):2244-53. doi: 10.1038/sj.emboj.7600714.

295. Mesmin B, Drin G, Levi S, Rawet M, Cassel D, Bigay J, *et al*. Two lipid-packing sensor motifs contribute to the sensitivity of ArfGAP1 to membrane curvature. *Biochemistry*. (2007) Feb 20; 46(7):1779-90. doi: 10.1021/bi062288w.

296. Zimmerberg J, Kozlov MM. How proteins produce cellular membrane curvature. *Nat Rev Mol Cell Biol*. (2006) Jan; 7(1):9-19. doi: 10.1038/nrm1784.

297. Iversen L, Mathiasen S, Larsen JB, Stamou D. Membrane curvature bends the laws of physics and chemistry. *Nat Chem Biol*. (2015) Nov; 11(11):822-5. doi: 10.1038/nchembio.1941.

298. Stachowiak JC, Brodsky FM, Miller EA. A cost-benefit analysis of the physical mechanisms of membrane curvature. *Nat Cell Biol*. (2013) Sep; 15(9):1019-27. doi: 10.1038/ncb2832.

299. Rafelski SM, Marshall WF. Building the cell: design principles of cellular architecture. *Nat Rev Mol Cell Biol*. (2008) Aug; 9(8):593-602. doi: 10.1038/nrm2460.

300. Nap RJ, Tagliazucchi M, Szleifer I. Born energy, acid-base equilibrium, structure and interactions of end-grafted weak polyelectrolyte layers. *J Chem Phys*. (2014) Jan 14; 140(2):024910. doi: 10.1063/1.4861048.

301. Wang D, Nap RJ, Lagzi I, Kowalczyk B, Han S, Grzybowski BA, *et al*. How and why nanoparticle's curvature regulates the apparent pKa of the coating ligands. *J Am Chem Soc*. (2011) Feb 23; 133(7):2192-7. doi: 10.1021/ja108154a.

302. Nap RJ, Szleifer I. How to optimize binding of coated nanoparticles: coupling of physical interactions, molecular organization and chemical state. *Biomater Sci*. (2013) Aug 1; 1(8):814-823. doi: 10.1039/C3BM00181D.

303. Ren CL, Nap RJ, Szleifer I. The role of hydrogen bonding in tethered polymer layers. *J Phys Chem B*. (2008) Dec 18; 112(50):16238-48. doi: 10.1021/jp8080904.

304. Mbamala EC, Fahr A, May S. Electrostatic model for mixed cationic-zwitterionic lipid bilayers. *Langmuir*. (2006) May 23; 22(11):5129-36. doi: 10.1021/la060180b.

305. Hasted JB, Ritson DM, Collie CH. Dielectric properties of aqueous ionic solutions. Parts I and II. *J Chem Phys*. (1948) Jan; 16(1):1-21. doi: 10.1063/1.1746645.

306. Vequi-Suplicy CC, Riske KA, Knorr RL, Dimova R. Vesicles with charged domains. *Biochim Biophys Acta*. (2010) Jul; 1798(7):1338-47. doi: 10.1016/j.bbamem.2009.12.023.

307. Marsh D. Handbook of lipid bilayers, 2nd ed. CRC press; (2013) Feb 15. doi: 10.1201/b11712.

308. Templer RH, Castle SJ, Curran AR, Rumbles G, Klug DR. Sensing isothermal changes in the lateral pressure in model membranes using di-pyrenyl phosphatidylcholine. *Faraday Discuss*. (1998); (111):41-53; discussion 69-78. doi: 10.1039/a806472e.

309. Loura LMS, Prates Ramalho JP. Fluorescent membrane probes' behavior in lipid bilayers: insights from molecular dynamics simulations. *Biophys Rev*. (2009) Sep; 1(3):141. doi: 10.1007/s12551-009-0016-5.

310. Curdová J, Capková P, Plásek J, Repáková J, Vattulainen I. Free pyrene probes in gel and fluid membranes: perspective through atomistic simulations. *J Phys Chem B*. (2007) Apr 12; 111(14):3640-50. doi: 10.1021/jp065956w.

311. Siminovitch DJ, Ruocco MJ, Makriyannis A, Griffin RG. The effect of cholesterol on lipid dynamics and packing in diether phosphatidylcholine bilayers. X-ray diffraction and 2H-NMR study. *Biochim Biophys Acta*. (1987) Jul 23; 901(2):191-200. doi: 10.1016/0005-2736(87)90115-5.

312. Lindahl E, Hess B, Van Der Spoel D. GROMACS 3.0: a package for molecular simulation and trajectory analysis. *J Mol Model*. (2001) Aug; 7(8):306-17. doi: 10.1007/s008940100045.

313. Wüstner D, Sklenar H. Atomistic Monte Carlo simulation of lipid membranes. *Int J Mol Sci*. (2014) Jan 24; 15(2):1767-803. doi: 10.3390/ijms15021767.

314. Vamparys L, Gautier R, Vanni S, Bennett WF, Tieleman DP, Antonny B, *et al*. Conical lipids in flat bilayers induce packing defects similar to that induced by positive curvature. *Biophys J*. (2013) Feb 5; 104(3):585-93. doi: 10.1016/j.bpj.2012.11.3836.

315. Cui H, Lyman E, Voth GA. Mechanism of membrane curvature sensing by amphipathic helix containing proteins. *Biophys J*. (2011) Mar 2; 100(5):1271-9. doi: 10.1016/j.bpj.2011.01.036.

316. Boal D, Boal DH. Mechanics of the Cell, 2nd ed. Cambridge, England: Cambridge University Press; (2012). doi: 10.1017/CBO9781139022217.

317. Larsen JB, Rosholm KR, Kennard C, Pedersen SL, Munch HK, Tkach V, *et al.* How membrane geometry regulates protein sorting independently of mean curvature. *ACS Cent Sci*. (2020) Jul 22; 6(7):1159-1168. doi: 10.1021/acscentsci.0c00419.

318. Le CT, Houri A, Balage N, Smith BJ, Mechler A. Interaction of small ionic species with phospholipid membranes: The role of metal coordination. *Front Mater*. (2019) Jan 7; 5:80. doi: 10.3389/fmats.2018.00080.

319. Vernier PT, Ziegler MJ, Dimova R. Calcium binding and head group dipole angle in phosphatidylserine-phosphatidylcholine bilayers. *Langmuir*. (2009) Jan 20; 25(2):1020-7. doi: 10.1021/la8025057.

320. Evans DF, Pye G, Bramley R, Clark AG, Dyson TJ, Hardcastle JD. Measurement of gastrointestinal pH profiles in normal ambulant human subjects. *Gut*. (1988) Aug; 29(8):1035-41. doi: 10.1136/gut.29.8.1035.

321. Russell TL, Berardi RR, Barnett JL, Dermentzoglou LC, Jarvenpaa KM, Schmaltz SP, *et al*. Upper gastrointestinal pH in seventy-nine healthy, elderly, North American men and women. *Pharm Res*. (1993) Feb; 10(2):187-96. doi: 10.1023/a:1018970323716.

322. Dressman JB, Berardi RR, Dermentzoglou LC, Russell TL, Schmaltz SP, Barnett JL, *et al*. Upper gastrointestinal (GI) pH in young, healthy men and women. *Pharm Res*. (1990) Jul; 7(7):756-61. doi: 10.1023/a:1015827908309.

323. Fallingborg J. Intraluminal pH of the human gastrointestinal tract. *Dan Med Bull*. (1999) Jun; 46(3):183-96.

324. Choy E, Chiu VK, Silletti J, Feoktistov M, Morimoto T, Michaelson D, *et al.* Endomembrane trafficking of Ras: the CAAX motif targets proteins to the ER and Golgi. *Cell*. (1999) Jul 9; 98(1):69-80. doi: 10.1016/S0092-8674(00)80607-8.

325. Anderson RG. The caveolae membrane system. *Annu Rev Biochem*. (1998); 67:199-225. doi: 10.1146/annurev.biochem.67.1.199.